MARCH 1956

A.I.Ch.E. JOURNAL

Published by the American Institute of Chemical Engineers

CONTENTS

UNIV. OF MICHIGAN
APR 18 1956
EAST ENGINEERING LIBRARY

Entrainment from Bubble-cap Trays	P. T. Atteridg, E. J. Lemieux, W. C. Schreiner, and R. A. Sundback
A Generalized Correlation of Diffusion Coefficients	J. R. Fair and B. J. Lerner
Correlation of Bubble-cap Fractionating-column Plate Efficiencies	E. D. Oliver and C. C. Watson
Rate of Nitration of Benzene with Mixed Acid	R. D. Biggs and R. R. White
An Algebraic Approach to Calculating the Solvent Extraction of Complex Mixtures	H. F. Hopp, Jr., and R. B. Smith
Prediction of Ideal-stage Requirements in Complex Liquid-liquid Extraction Systems	H. C. Peterson and G. H. Beyer
Heat Transfer Through a Homogeneous Isotropic Turbulent Field	T. J. Hanratty
Catalytic Hydrogenation of Carbon Monoxide and Dioxide over Steel	B. D. Smith and R. R. White
Mechanics of Steady State Single-phase Fluid Displacement from Porous Media	D. U. von Rosenberg
Analysis of Kinetic Data for Heterogeneous Reactions	Sol Weller
Kinetics on Ideal and Real Surfaces	Michel Boudart
Adsorption Phase-equilibrium Correlations: Light-hydrocarbon Vapors on Activated Charcoal	L. D. Etherington, R. E. D. Haney, W. A. Herbst, and H. W. Scheeline
Regeneration of Fluidized Cracking Catalysts	W. F. Pansing
Performance of an Internally Baffled Multistage Extraction Column	E. G. Scheibel
Pressure Drop Through Porous Media, Part V	L. E. Brownell, D. C. Gami, R. A. Miller, and W. F. Nekarvis
Distribution of Temperature in 1-2— and 1-4—pass Heat Exchangers	H. T. Bates
Prediction of Specific Heat of Organic Liquids	B. C. Sakiadis and Jesse Coates
Determination of Relative Permeability Under Simulated Reservoir Conditions	J. W. Wilson
Mass Transfer in a Wetted-wall Column: Turbulent Flow	W. H. Schwarz and H. E. Hoelscher
Analysis of Crystal-size Distribution in Mixed Suspensions	W. C. Saeman
Properties of Evaporated Metal Films Related to Their Use for Surface Temperature Measurements	T. B. Simpson and C. C. Winding
Chemical Reactor Stability and Sensitivity, Part II	Olegh Bilous and N. R. Amundson
Forces Acting in Flowing Beds of Solids	J. W. Delaplaine

Foote
LITHIUM HYDROXIDE

The basic lithium salt for industrial use, Foote lithium hydroxide provides chemically unique properties which are being applied to a host of products ranging from ceramic formulations to multi-purpose grease manufacture and welding rod coatings. Many other industrial uses of lithium are in the development stage.

Foote's integrated lithium facilities—raw material, production, research—are your assurance of an abundant supply of lithium for you and all industry.

We invite you to investigate and apply the unusual properties of lithium hydroxide and its derivatives in your products or processes.

Write for technical data sheets.

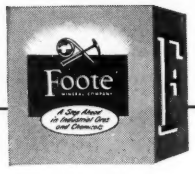

LITHIUM HYDROXIDE FOR INDUSTRY

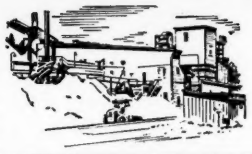

Kings Mountain, N.C. . . . where Foote is mining large deposits of spodumene.

Sunbright, Va. . . . the world's largest lithium chemical plant.

FOOTE MINERAL COMPANY

448 Eighteen West Chelten Building, Philadelphia 44, Pa.

RESEARCH LABORATORIES: Berwyn, Pa. • PLANTS: Exton, Pa.; Kings Mountain, N.C.; Sunbright, Va.

A.I.Ch.E. JOURNAL

MARCH 1956 · VOL. 2, NO. 1

PUBLISHER
F. J. Van Antwerpen

EDITOR
Harding Bliss

ADVISORY BOARD

C. M. Cooper, O. E. Dwyer, W. C. Edmister, E. R. Gilliland, A. N. Hixson, W. R. Marshall, Jr., R. H. Newton, R. L. Pigford, J. M. Smith, Theodore Vermeulen, R. R. White, R. H. Wilhelm

The A. I. Ch. E. Journal, an official publication of the American Institute of Chemical Engineers, is devoted in the main to theoretical developments and research in chemical engineering and allied branches of engineering and science. Manuscripts should be submitted to the New York office.

How Not to Alleviate the Shortage of Engineers 1

Entrainment from Bubble-cap Trays . *P. T. Atteridg, E. J. Lemieux, W. C. Schreiner, and R. A. Sundback* 3

A Generalized Correlation of Diffusion Coefficients . . . . . *J. R. Fair and B. J. Lerner* 13

Correlation of Bubble-cap Fractionating-column Plate Efficiencies . . . . . *E. D. Oliver and C. C. Watson* 18

Rate of Nitration of Benzene with Mixed Acid . . . . . *R. D. Biggs and R. R. White* 26

An Algebraic Approach to Calculating the Solvent Extraction of Complex Mixtures *H. F. Hopp, Jr., and R. B. Smith* 34

Prediction of Ideal-stage Requirements in Complex Liquid-liquid Extraction Systems *H. C. Peterson and G. H. Beyer* 38

Heat Transfer Through a Homogeneous Isotropic Turbulent Field . . . . . *T. J. Hanratty* 42

Catalytic Hydrogenation of Carbon Monoxide and Dioxide over Steel . . . . *B. D. Smith and R. R. White* 46

Mechanics of Steady State Single-phase Fluid Displacement from Porous Media . . . *D. U. von Rosenberg* 55

Analysis of Kinetic Data for Heterogeneous Reactions . . . . . *Sol Weller* 59

Kinetics on Ideal and Real Surfaces . . . . . *Michel Boudart* 62

Adsorption Phase-equilibrium Correlations: Light-hydrocarbon Vapors on Activated Charcoal *L. D. Etherington, R. E. D. Haney, W. A. Herbst, and H. W. Scheeline* 65

Regeneration of Fluidized Cracking Catalysts . . . . . *W. F. Pansing* 71

Performance of an Internally Baffled Multistage Extraction Column . . . . . *E. G. Scheibel* 74

Pressure Drop Through Porous Media, Part V *L. E. Brownell, D. C. Gami, R. A. Miller, and W. F. Nekarvis* 79

Distribution of Temperature in 1-2— and 1-4—pass Heat Exchangers . . . . . *H. T. Bates* 82

Prediction of Specific Heat of Organic Liquids . . . . . *B. C. Sakiadis and Jesse Coates* 88

Determination of Relative Permeability Under Simulated Reservoir Conditions . . . . . *J. W. Wilson* 94

Mass Transfer in a Wetted-wall Column: Turbulent Flow . . . . . *W. H. Schwarz and H. E. Hoelscher* 101

Analysis of Crystal-size Distribution in Mixed Suspensions . . . . . *W. C. Saeman* 107

Properties of Evaporated Metal Films Related to Their Use for Surface Temperature Measurements *T. B. Simpson and C. C. Winding* 113

Chemical Reactor Stability and Sensitivity, Part II . . . . . *Olegh Bilous and N. R. Amundson* 117

Forces Acting in Flowing Beds of Solids . . . . . *J. W. Delaplaine* 127

Books 139

Publication Office, Richmond, Virginia. Published quarterly in March, June, September, and December by the American Institute of Chemical Engineers, 25 West 45 Street, New York 36 New York. Manuscripts and other communications should be sent to the New York office. Correspondence with the editor may be addressed to him at Yale University, 225 Prospect Street, New Haven 11, Connecticut. Statements and opinions in the *A.I.Ch.E. Journal* are those of the contributors, and the American Institute of Chemical Engineers assumes no responsibility for them. Subscriptions: one year, member $4.50, nonmember $9.00; two years, member $7.50, nonmember $16.00; additional yearly postage, Canada 50 cents, Pan American Union $1.50, other foreign $2.00 (foreign subscriptions payable in advance). Single copies: $3.00. Second-class mail privileges authorized at Richmond, Virginia.

Copyright 1956 by the American Institute of Chemical Engineers.

CEC increases the scope of

industrial mass spectrometry

through two great instruments for process monitoring and control

Consolidated's Model 21-610 mass-spectrometer and its companion, the new Model 21-620, far excel all other instruments of comparable price in performance capabilities and reliability in industrial environment. The extreme sensitivity of the 21-610—accurate to a few parts per million—qualify it for highly critical purity studies as well as process monitoring and control applications. Fitted with an accessory hand-held probe, either model serves as a leak detector for any gas within its mass-range. The 21-620's resolving power up to mass 150 further extends the applicability of an industrial mass-spectrometer to research laboratories and medical centers, as well as to plants of chemical, petro-chemical, petroleum and gas industries. Nearly identical in appearance, the 21-610 features the Diatron ion analyzer and the 21-620, a new cycloidal focusing analyzer.

21-620 Except for slightly less sensitivity, the 21-620 has all the capabilities of the 21-610 plus many others. Where the task is to analyze "heavy" gases or liquids, either in plant locations or in the laboratory, the 21-620 process monitor mass-spectrometer is the ideal control instrument.

21-610 The 21-610 is completely self-contained, needing only 110 volts and a small quantity of cooling water for operation. Moderately priced, easily movable, and economical to operate, the 21-610 is industry's ideal instrument for chemical research, process control and leak detection.

CEC Service Engineers quick change of ion analyzers (right) adds flexibility to Consolidated's two process monitoring mass-spectrometers. A cycloidal focusing analyzer assembly of the 21-620 type is being mounted in the vacuum rack in place of the Diatron analyzer of the 21-610.

The basic instrument can be augmented by many available accessories, thus broadening its application scope. At the far right, are a gas or light-liquid sample inlet system and chart recorder.

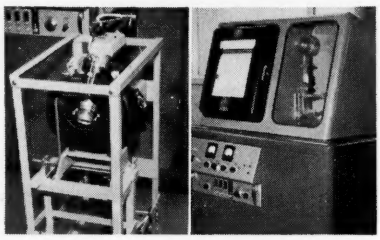

Consolidated Electrodynamics

CORPORATION

formerly Consolidated Engineering Corporation

ELECTRONIC INSTRUMENTS FOR MEASUREMENT AND CONTROL

300 No. Sierra Madre Villa, Pasadena, California

Sales and Service Offices in: Albuquerque, Atlanta, Boston, Buffalo, Chicago, Dallas, Detroit, New York, Pasadena, Philadelphia, San Francisco, Seattle, Washington, D. C.

Investigate the application of industrial mass-spectrometry to your business. For full details about CEC's two companion process monitoring mass-spectrometers, send for Bulletin CEC 1824A-X33

A.I.Ch.E. JOURNAL

How Not to Alleviate the Engineer Shortage

Great shortages periodically confront our nation, and each seems more critical than the last. Rubber, oil, iron ore, tin—each in turn has been scarce, and now scientists and engineers are in short supply. Congressmen and commissioners, business executives and labor leaders have come forth with suggestions designed to solve this problem with dispatch so that we may turn our attention to the next crisis secure in our belief that the shortage is a thing of the past and that all is well. Actually, of course, the shortage is real and it is serious, because the world in which we find ourselves is particularly in need of special scientific and technical skills, and there is no sign that this need will ever be lessened to any significant degree. Since the problem is real and serious, careful attention should be paid to the suggestions which have been made, many of which have merit. However, some proposals are open to considerable criticism and two in particular should be viewed with some skepticism.

The first of these is the suggestion or belief that all can be solved by opening the Federal treasury for scholarship money so that more students will be attracted to engineering or science. This proposal is a poor excuse for facing the facts. In the first place, there is no real evidence that lack of scholarship assistance deters students from these fields. On the contrary, there is much evidence that students are attracted by the ultimate financial rewards in these professions, rewards which are themselves a consequence of the current shortage. But the major objection to this proposal is that it misses completely these paramount points: (1) who will teach the greater numbers of students? and (2) in what laboratories will they be taught? A scholarship program which does not provide means to acquire better laboratories and to attract more and better teachers is doomed to failure. Indeed, it poses a real threat to the educational standards of science and engineering. The country will profit little, if at all, from a larger number of poorer quality engineers. While the shortage is roundly condemned on all sides, it has had its beneficial effects, and one of them is the upgrading of engineers to positions consistent with their excellent training and abilities. We have a fine group of superior engineers at present, and we must guard against lowering our standards.

The second suggestion open to serious question is that the necessary teachers be brought from industry to instruct the larger numbers of pupils. One year has been mentioned as a suitable period for the industralist to be excused from his duties to help with the teaching. Let us give the proponents of this scheme an *A* for effort but an *F* for diplomacy! Although we strongly disapprove of the professional pedagogue who ranks the teaching art and technique above the subject matter, it must be admitted, nonetheless, that there are aspects of teaching the subject matter which are different from its application. Certainly there must be a liking for teaching, an interest in and affection for students, sympathy, firmness, and an approach to the subject at hand which is quite different from personal mastery of it. Above all, there must be, for the successful teacher, teaching experience. These things are not learned and put into practice in one year or, for that matter, in a few years. There are many people in industry who could lend assistance by lecture tours, by counseling, by bringing the attractions of science and engineering home to the students, but the number who can do the actual day-to-day teaching must be rather small. There are a lot of teaching positions open and there are very few "comers." Also, a possible unforeseen consequence of this plan is widespread nervous collapses on the part of the teacher-industrialists. After all, it is often said that the purpose of sabbatical years for professors is to permit them to have their coronaries off campus.

If the shortage of scientists and engineers is to be alleviated, it can be done only by a fundamental attack on the problem. Means must be found to make teaching more remunerative and to provide more laboratory facilities. This will attract more and better teachers. Nothing else will. Halfway and stop-gap devices will not meet the problem. And only more and better teaching will attract more and better students.

H. B.

SPECIFY EIMCO FILTERS FOR MAXIMUM PERFORMANCE & PROFIT

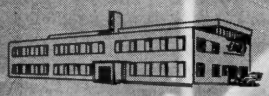

Research and Development Center — a fully equipped pilot plant for research on solids-liquid separation through filtration.

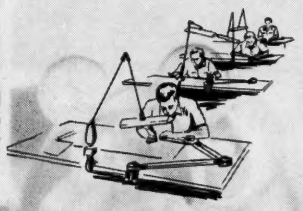

Engineering — Designed with individual attention towards customer's requirements.

Facilities — includes foundries, fabrication and machine shops covering 26 acres.

Service — for the life of the machine, includes calls by trained personnel. Operational tips and consultation are part of the purchase price.

Eimco Vacuum and Pressure Filters are working in many industries increasing production at lower cost. These industries include: Metallurgical and Chemical Plants; Paint, Varnish and Pigment Plants; Sewage and Industrial Wastes; Pharmaceutical Laboratories; Foods; Coal; Petroleum; Tanneries; Pickle Liquors and Other Wastes; Beet and Cane Sugar; Paper; Steel Mills; Starch, Corn and Potato; Salts and Sand; Water Treatment and many others.

Selecting the unit for the solid-liquids separation problem in your plant is one of your most difficult decisions.

Testing samples under your own conditions, with the numerous variables of materials and equipment available today can be an endless research job.

Eimco's suggestion to companies with problems on solids-liquids separation is that they avail themselves of the data already gathered at Eimco's own Research and Development Center devoted to problems of this type.

Filters of all types are manufactured by Eimco and data on filterability of a product is available on each type of filter to which it is applicable.

Eimco engineers have this exclusive reservoir of experience, gained through more than half a century of service to the processing industries, and the facilities of Eimco's vast manufacturing plants where filters of standard or specialized design are built for each customer's requirements.

Eimco has gained the confidence of many of the world's top processing organizations through suggestions made to simplify flow sheet layouts, plant design or to cut operating costs. These contributions to the processing industry are made possible by new developments in filtration.

Eimco's engineers will be happy to consult with you regarding filtration problems. If further research or test work would seem to be indicated, Eimco equipment is available for test purposes in the customer's plant, on a rental or lease basis with funds thus expended applicable on production size equipment.

THE EIMCO CORPORATION

Salt Lake City, Utah—U.S.A. • **Export Offices: Eimco Bldg., 52 South St., New York City**

New York, N. Y. Chicago, Ill. San Francisco, Calif. El Paso, Tex. Birmingham, Ala. Duluth, Minn. Kellogg, Ida. Baltimore, Md. Pittsburgh, Pa. Seattle, Wash. Pasadena, Calif. Houston, Texas Vancouver, B. C. London, England Gateshead, England Paris, France Milan, Italy Johannesburg, South Africa

EIMCO

B183

Entrainment from Bubble-cap Trays

P. T. ATTERIDG, E. J. LEMIEUX, W. C. SCHREINER, and R. A. SUNDBACK

The M. W. Kellogg Company, New York, New York

Data on liquid entrainment are reported for rectangular-cap bubble trays on 24-in. tray spacing for an air-water system. Several tray variations were studied, and entrainment is given for trays containing eight, twelve, and sixteen caps a tray. Some hydraulic characteristics (pressure drop, liquid backup, minimum vapor velocity, and downflow froth height) are also reported. It was found in this study that decreasing liquid path length increased the entrainment from a bubble-cap tray and increasing tray bubbling area decreased entrainment. It was also found that decreasing slot area generally had no effect on liquid entrainment over the range investigated.

In recent years the design of fractionation towers has become highly competitive. Designers are faced with the problems of designing trays with higher vapor and liquid loadings than ever before. In both the petroleum and the chemical industries better fractionation is required to produce purer chemicals, as well as better grades of petroleum products. In order to obtain better fractionation with more heavily loaded bubble-cap trays, various chemical and petroleum engineering companies have instigated development programs to study bubble-cap tower hydraulics, as well as the various factors which affect fractionation. A tower development program was begun several years ago by The M. W. Kellogg Company to study the hydraulics of its rectangular-bubble-cap trays, including the factors which affect the entrainment of liquid between trays.

Some of the data obtained in the more recent development program on rectangular-bubble-cap trays were previously reported in a paper by Houghland and Schreiner (*5*). This paper dealt exclusively with bubble-tray hydraulics and contained data that were obtained on 18-in. tray spacing with one- and two-tray operation. Since these were published, an additional bubble-cap tray was added to the experimental tower and tray performance was studied at other tray spacings.

This paper presents the information taken with trays which had eight, twelve, and sixteen rectangular bubble caps a tray and which were spaced 24 in. apart. These trays were 18 in. wide by 63 in. long and were equivalent to the center section of a 7-ft.-diam. commercial bubble-cap tower. The first section of the paper gives the hydraulic characteristics of these trays and supplements the previous paper by Houghland and Schreiner (*5*). The second section presents entrainment data.

The amount of entrainment data available in the literature is fairly limited, being for the most part reported for fairly small experimental towers with round-cap bubble trays under a limited range of vapor and liquid rates. In the past 10 or 15 years very few additional entrainment data have been published, although entrainment has become more and more

important as a factor in good tower and tray design. Furthermore, no data have ever been published for rectangular- or tunnel-cap trays of the type used in this study. The studies that were concluded on a commercial-size section of a 7-ft.-diam. tray were made to determine the effects of tray and cap modifications on liquid entrainment, as well as on tray hydraulics. The present paper, although limited to one tray spacing, 24 in., shows the effects on entrainment of bubbling area, length of liquid path, and slot area. Owing to the size of the trays used, it was also possible to study entrainment, as well as the hydraulics of rectangular trays under a wide range of vapor and liquid loadings.

Entrainment data based on various means of measurement on several types of trays have been reported in the literature. Strang (*12*), Sherwood and Jenny (*10*), Volante (*14*), Pyott, Jackson, and Huntington (*8*), and Chillas and Weir (*2*) measured entrainment from bubble-cap trays using an air-water system. Ashraf, Cubbage, and Huntington (*1*) reported experimental work on three differently sized gas absorbers. Holbrook and Baker (*4*) obtained entrainment data using a steam-salt water system. Peavy and Baker (*7*), using an ethanol-water system, measured entrainment colorimetrically. Thomson (*13*) also used an ethanol-water system, and Rhodes and Slachman (*9*) used a benzene-toluene system. Souders and Brown (*11*) pointed out in their paper that entrainment in fractionating columns affects plate efficiency and limits the maximum vapor velocity that gives satisfactory operation.

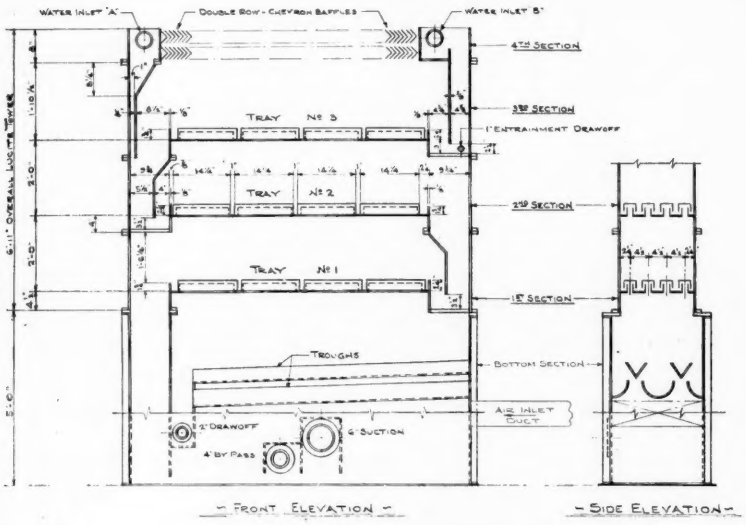

Fig. 1. Experimental-tower drawing.

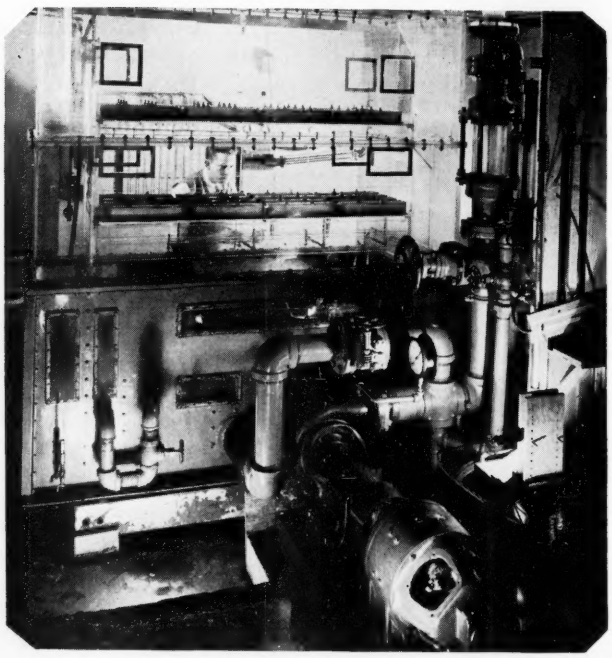

Fig. 2. Experimental tower.

EXPERIMENTAL COLUMN

The experimental column consisted of a 6 ft. 10¾ in. by 1 ft. 6 in. rectangular box-like shell. That portion of the shell which held the trays was made of Lucite plastic to permit visual observation of all phases of tray operation. This construction was strong and could be disassembled easily to provide for the necessary changes in tray layout. The size of the shell was chosen to provide a tray which had a length of path which could be compared directly to a commercial-size tower. The tower shell consisted of flanged sections which could be removed so that the number of trays, as well as the tray spacing, could be varied fairly easily. In this study the tower contained five sections: a bottom section which contained a collection tank for the recirculation of water and semicircular troughs which could be used to collect liquid dumping from the risers; a top section which contained a double row of angle baffles to minimize splashing from the top of the tower; and three tray sections, each of which contained an 18- by 63-in. bubble-cap tray. Figure 1 gives the front elevation of the experimental tower. Figure 2 is a photograph which shows two tray sections of the tower and the water-pumping equipment. Water was pumped from the collection tank to the top of the tower by a centrifugal pump. Calibrated rotameters measured the water flow to the unit. Water could be pumped to either the middle or the top tray, depending on the type of operation that was desired. Air was blown to the bottom of the tower below the first tray section through either of two ducts by means of a 6,000 cu. ft./min. centrifugal blower powered by a 60-hp., 440-volt electric motor. Two interchangeable ducts were used: one 12¼ in. in diameter, the other 5¾ in. In either case the air flow was measured by a calibrated Pitot tube at the center of the duct. The smaller duct was calibrated at four rates and the larger at three. Paired traverses agreed within 1%. The plot of duct flow (by traverse) with the specific station reading showed a fit to linearity of within 1%. The manometer reading was good to 0.01 in.

Suitable lines were provided for collecting entrainment to the top tray. Entrainment rate was determined by drawing off liquid from the dry upper tray during the entrainment runs. Pressures at various sections of the tower were measured with vertical or inclined manometers. All temperatures were measured with ordinary Fahrenheit thermometers.

The trays were constructed of No. 12 U.S. Standard gauge, 12% Cr, type-410 stainless steel and consisted of 1¼ by 13⅜ in. No. 14 U.S. Standard gauge risers that were fitted with 2¾ by 14¼ in. No. 16 U.S. Standard gauge rectangular bubble caps. Details of the bubble-cap trays and the rectangular bubble caps used in this study are given in Figures 3 and 4, respectively.

EXPERIMENTAL PROCEDURE

Three types of tower operation were used in the experimental tower study, depending on the type of data that was desired. Dry-tray pressure-drop runs were made by blowing air to the bottom of the tower and measuring the differential pressure drop across each tray section. During the measurement of dry-tray pressure drop no water was present on any of the trays. Downcomers were sealed by filling seal pots with water.

Bubble-cap-tray hydraulic data, pressure drop, seal-pot level, and downflow static and froth levels were obtained by blowing air to the bottom of the tower at a predetermined Pitot reading. Water was introduced in the seal pot of the top tray. The pressure drop across each tray was measured by differential manometers, as was the downflow static level. Downflow froth heights were measured visually.

Normally the air flow was set at the lowest value of interest and the liquid flow was increased in steps from 300 to 18,000 gal./hr. Readings were taken, usually, at the following water rates: 300, 1,000, 1,800, 4,000, 6,000, 9,000, 12,000, 15,000 and 18,000 gal./hr. This series of observations was then repeated for several higher air rates, up to the maximum capacity of the blower.

Entrainment data were obtained by measuring the water which was collected on the top tray. For this type of operation water was pumped to the middle tray, the top tray acting solely as an entrainment collector. Air and water rates were varied in a manner similar to the tray hydraulic operation. Only two entrainment measurements were required at each condition since reproducibility of the results was excellent. In many instances successive measurements of entrainment rates were made. Analyses of these weighings (twenty-eight conditions consisting of four quadruplicates, ten triplicates, and fourteen duplicates for a total of forty-six degrees of freedom) show the observed standard error of measurement about each mean to be 3.6%. Therefore 95% of single measurements should be within ±7.2% of the correct weight, and 95% of the means of duplicate measurements within ±5.1%. The value of entrainment shown in the data is the average of the measurements made at any given condition.

The air rate necessary to make all caps bubble, as well as all slots of all caps bubble, was also determined with three operating trays. At a fixed water rate the air rate was varied to determine the bubbling from the cap slots. The opening of the slots of the caps on either side of the tower was observed.

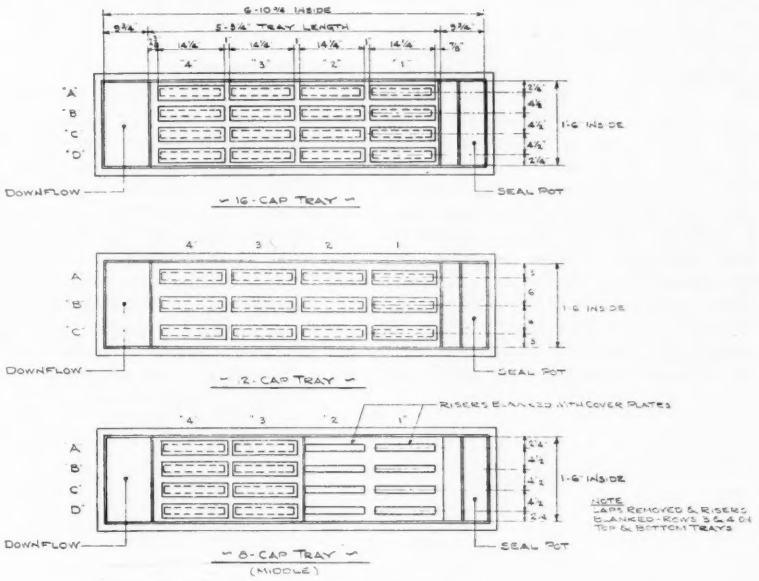

Fig. 3. Detail of trays.

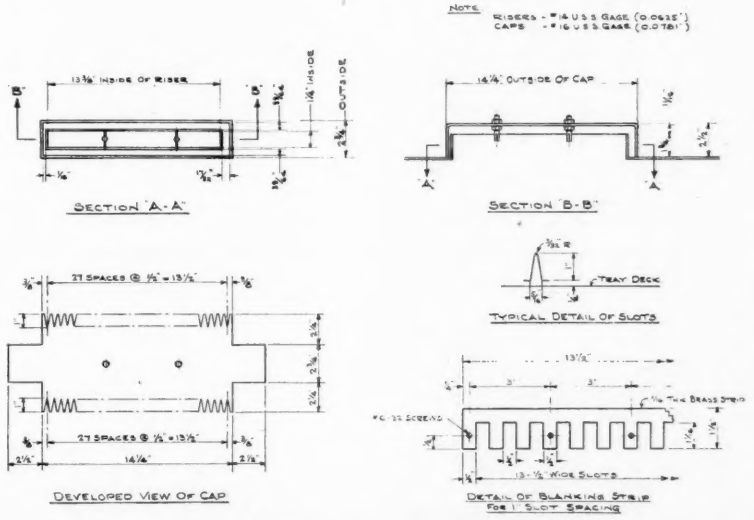

Fig. 4. Detail of rectangular bubble cap.

RESULTS

Bubble-cap-tray Hydraulics

Bubble-cap-tray hydraulics were studied in the experimental tower to obtain the various factors which determine capacity and stability. The capacity of a tray is determined primarily by the height of froth which can exist in the downcomer without causing flooding. Satisfactory bubbling of cap slots usually gives a good indication of tray stability. All the data presented on bubble-cap-tray hydraulics were obtained with trays on 24-in. tray spacing.

When vapor distribution becomes unbalanced because of the hydraulic gradient, there is set up a cross flow of vapor from the downstream end to the upstream. This cross flow would flood a tray well before the flooding loads predicted by existing theory. Houghland and Schreiner (5) showed the existence of this

behavior with a tray having no support beam. The magnitude of the effect of vapor cross flow is not predictable. Observations from one- or two-tray tests applied to multitrays would be in error if this effect were cumulative. The data presented on pressure drop, froth height, and entrainment show that this unbalance was not important on a 24-in. tray spacing in the test tower; therefore, the data are as correct for an infinite number of trays as for one.

The pressure drop across a bubble-cap tray is fundamentally the most important factor determining tray operation. Excessive pressure drop through bubble caps will result in tower flooding due to backup of liquid in the downcomers. Too small a pressure drop will result in inactive caps (caps not bubbling) and may permit liquid dumping through the risers at high liquid rates. These conditions will affect the tray efficiency adversely by allowing vapor by-passing and a decrease in contact between the vapor and liquid.

Tray capacity is limited by the amount of liquid a downflow can handle. As liquid flows over the downflow weir, vapor is entrained into the downflow. This entrained vapor lowers the density of the downflow liquid. When downflow froth level reaches the top of the downflow weir, pressure drop across the tray increases rapidly and the tray floods. The height of aerated liquid (froth height) which exists in the downflow under any vapor and liquid load is therefore important to the tray designers. This height can be obtained only if a relationship is known between the static liquid and aerated liquid heights in the downflow. The static liquid height is equal to the sum of the seal-pot liquid level, the tray pressure drop, and the loss due to flow through the downflow. This last item is negligible for all practical purposes.

In order to obtain good contacting between vapor and liquid, as well as stable tray operation and uniform froth distribution over a tray, there is a minimum vapor velocity below which a given bubble-cap tray should not be operated. Operations below minimum vapor velocity usually result in a decrease in contact between vapor and liquid. Owing to the liquid gradient over any bubble-cap tray, the vapors have a greater tendency to flow across the downstream end of the tray, thus by-passing the upstream end of the tray. Under heavy liquid loads and low vapor rates, liquid dumping (leakage) can occur from the upstream risers. Such a condition can have serious effects on tray efficiency. Vapor velocities are expressed as Z_F or Z_R, that is, as the ratio of the vapor velocity in the tray free area or riser area, feet per second, to allowable velocity. Souders and Brown (*11*) derived an allowable velocity for reasonable entrainment as equal to $c(\rho_L - \rho_V/\rho_V)^{1/2}$ where c was an arbitrary constant different for each tray spacing. Designers have come to use less conservative values for c and to apply the allowable velocity to the free area (or bubbling area) of a tray, rather than to the superficial area. Converting Souders and Brown's original relationship to linear velocity at a 24-in. tray spacing and taking free area as 80% of the tower area yields an allowable velocity in the free area of $0.227 (\rho_L - \rho_V/\rho_V)^{1/2}$. The ratio of actual velocity through the free area of a tray to allowable velocity, $0.227 (\rho_L - \rho_V/\rho_V)^{1/2}$, is designated as Z_F. The ratio of riser velocity to allowable velocity, $0.227 (\rho_L - \rho_V/\rho_V)^{1/2}$, is designated as Z_R.

Dry-tray Pressure Drop

At various times during the experimental program dry-tray pressure drop was measured for the sixteen-cap tray and the twelve-cap tray with cap slots on ½-in. spacing (56 slots per cap) and also for one tray with cap slots on 1-in. spacing (28 slots per cap). One-inch slot spacing was obtained by blanking off every alternate slot on all the caps of the middle tray. Details of the blanking strips are shown on Figure 4. Figure 5 shows the plot of dry-tray pressure drop in inches of water against air rate expressed as a

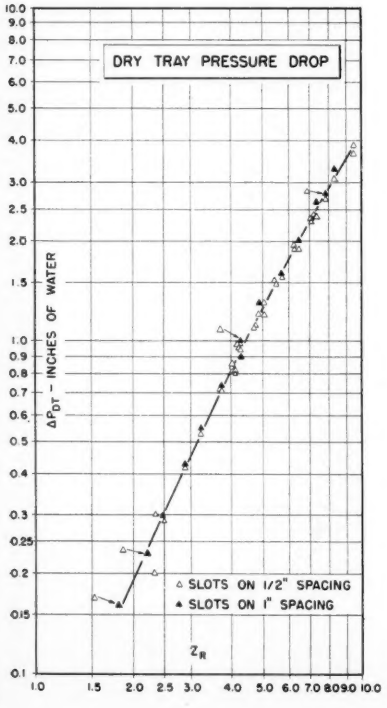

Fig. 5.

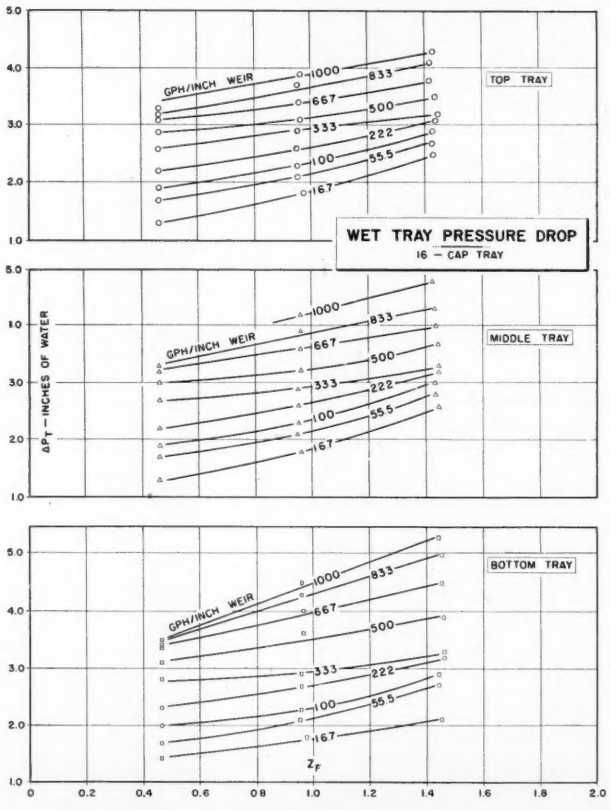

Fig. 6.

TABLE 1. TRAY DETAILS

	16-Cap Tray	12-Cap Tray	8-Cap Tray
Dimensions of downflow from tray			
Upper section	←	9¾×18 in.	→
Lower section	←	5½×18 in.	→
Height of downflow weir above tray	←	1¾ in.	→
Height of seal-pot dam above tray	←	2¼ in.	→
Size of risers	←	1¼×13⅜ in.	→
Height of risers above tray	←	1¾ in.	→
Size of caps	←	2¾×14¼ in.	→
Number of slots per cap	←	56	→
Number of slots per tray	896	672	448
Tray "free" area, sq. ft.	←	7.906	→ 4.10
Total area per tray, sq. ft.			
Inside riser	1.858	1.391	0.929
Riser reversal	2.14	1.60	1.07
Riser annular	1.993	1.492	0.997
Slots alone	1.50	1.12	.075
Below slots and teeth	0.793	0.594	0.397
Clearance between caps			
Long side	1¾ in.	3¼ in.	1¾ in.
Short side	←	1 in.	→

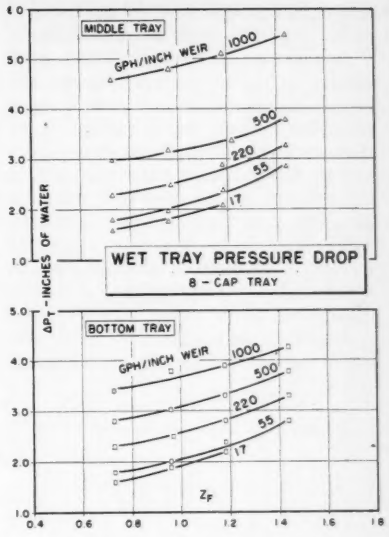

Fig. 8.

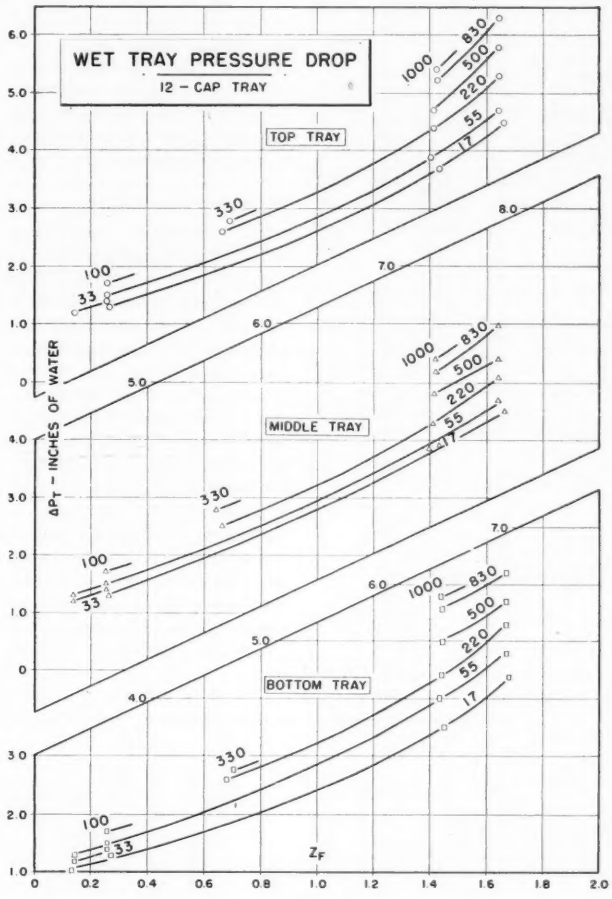

Fig. 7.

percentage of an arbitrarily defined allowable velocity. It can be seen from Figure 5 that the differences in dry-tray pressure drop between a tray with cap slots on ½-in. spacing and one with cap slots on 1-in. spacing are negligible.

Wet-tray Pressure Drop

Pressure drop was measured in the experimental bubble-cap tower with a dynamic air-water system. Figure 6 is a plot of the total pressure drop across each of the three trays for the sixteen-cap tray. Details of this tray are given in Table 1. A cross plot of these data at Z_F of 1.4 and 1.0 indicates that pressure drop for the three trays is about equal up to 400 gal./(hr.)(in. of weir). Above this value the bottom tray has a higher pressure drop than either the middle or the top tray. The top tray has the lowest pressure drop. At a Z_F of 0.5 the pressure drop across the bottom tray is the highest at all liquid rates; the top tray the lowest. Pressure drops across the three operating bubble-cap trays have to be reported individually in this study, owing to the vapor distribution which is different for the three trays. This is indicated by differences in pressure drop under certain vapor and liquid rates. Data (*6*) taken with a static liquid level on the trays gave identical pressure-drop readings across all trays, showing that vapor distribution was excellent. Figure 7 shows the pressure drop for the twelve-cap tray arrangement; Figure 8, for the eight-cap tray arrangement. Details of the twelve- and eight-cap trays are also given in Table 1.

Downflow Level

In order to obtain a relationship between the height of static liquid in the downflow and the height of froth, the static and froth downflow levels were measured for the sixteen-cap tray operation at various air and water rates. Downflow static level was measured by installing a gauge glass at the bottom of the second tray seal pot; downflow froth level was measured visually. All measurements were made from the tray floor. Downflow static level was measured by a gauge glass open to the atmosphere. The correct static level reading was obtained by subtracting from the observed gauge reading the pressure drop across the splash baffles. Figure 9 shows the variation of downflow static and froth heights with air and liquid loading. As it is possible to calculate the unaerated liquid backup, if the pressure drop across the tray and the liquid level in the seal pot are known, downflow froth

height can be obtained if the ratio of static height to froth height is known. This ratio is also equal to the froth density divided by the liquid density and gives a measure of the amount of vapor which is present in the downflow. Figure 10 shows a plot of the ratio of static height to froth height against water rate at three air rates. It can be seen that the ratio decreases very rapidly with increasing water rates, indicating that, owing to increasing amounts of entrained air in the downflow, froth height is increasing rapidly. At lower water rates the ratio approaches 1 as a limit. This figure also shows the effect of air rate on the static-to-froth-downflow-height ratio. At a constant water rate the ratio would pass through a minimum which would occur at about a Z_F of 0.96. The scattering of the data in Figure 10 is due to the difficulties of measurement. The accuracy of the visual measurement of downflow froth height and the gauge readings of static downflow height is about ±10%.

Seal-pot Level

Figure 11 presents a plot of seal-pot level vs. water rate for three air rates for the sixteen-cap tray. This figure gives the froth level on the upstream side of the seal-pot dam for the middle tray. It can be seen from this figure that seal-pot level varies with air rate, as well as with water rate. It can also be noticed that a common curve could be used for Z_F's from 0.95 to 1.44 without too great an error. Seal-pot level, as measured in this study, is the actual height of liquid upstream of the seal dam. A portion of this curve, up to about 330 gal./(hr.)(in.), is a solid liquid level. Observation of tray operations has shown that at the lower liquid rates no vapor is trapped in the downcomer. Vapor entrained in the downcomer disengages and returns to the vapor space. At higher liquid rates vapor is carried under the downflow plate. Under these conditions liquid in the seal pot has a lower density than the unaerated liquid. This gives an increase in seal-pot level. As downflow-froth levels are calculated on the basis of unaerated liquid in the seal pot, portions of the curves on Figure 11 cannot be used in calculating backup in the downflow. For this study, as downflow static height has been measured, the seal-pot level (unaerated) can be calculated; it is equal to the downflow static height minus the pressure drop across the tray above.

Minimum Vapor Rate

Two minimum vapor rates were recorded for the sixteen- and the eight-cap trays: (1) the air rate to maintain at least one slot on every cap bubbling and (2) the air rate to maintain all slots of all caps bubbling. For the twelve-cap tray the latter condition was obtained. These data are shown on Figures 12, 13, and 14. It can be seen from these figures that the middle tray requires the lowest air rate to obtain cap bubbling and that the bottom tray needs the highest. Figure 15 is a plot of the minimum air rate to maintain all slots of all caps bubbling for the eight-, twelve-, and sixteen-cap trays. This figure shows that minimum air rate depends on the length of liquid travel. A greater air rate is needed for the sixteen-

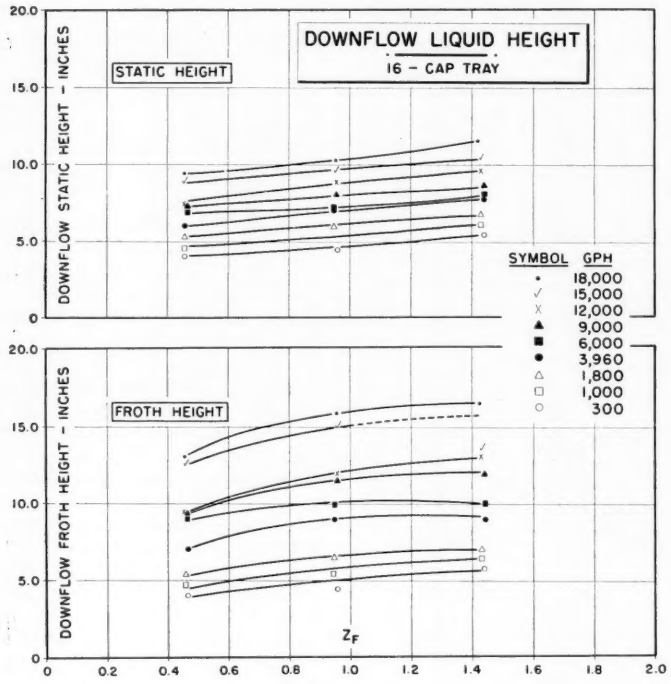

Fig. 9.

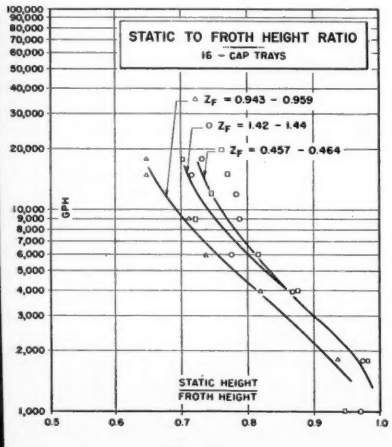

Fig. 10.

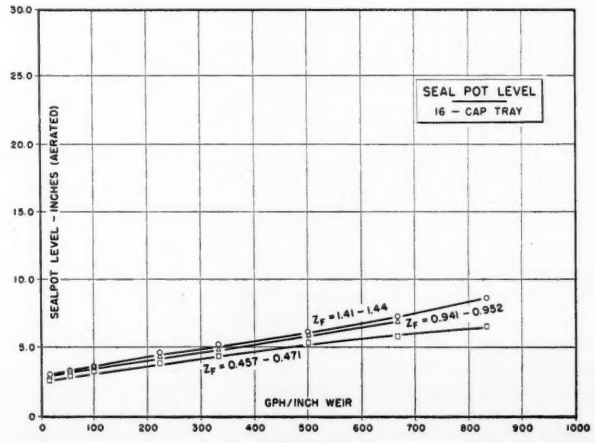

Fig. 11.

cap tray than for the eight-cap tray at the same water rate. This figure also shows that at the same length of liquid travel placing caps on a greater cap spacing has lowered the air rate at which all slots of all caps are bubbling.

Entrainment

In recent years the study of entrainment has become more and more important as the design of fractionating towers has become more competitive, necessitating operation at higher vapor and liquid loads.

Entrainment has been shown theoretically to be a factor in limiting good fractionation. Colburn (*3*) has shown that the effect of entrainment in a plate column is to reduce the apparent efficiency to a new value, according to the equation

$$\frac{E_v}{1 + [(eE_v)/(L/V)]}$$

A tower can be designed to operate at any tray spacing if sufficient trays are added to compensate for the adverse effects of entrainment on efficiency and if the tray is given sufficient capacity to handle the liquid and vapor loads. Some towers can operate with considerable entrainment without any appreciable effect on the efficiency of fractionation (towers with low apparent efficiency operating under high reflux ratios), and other towers can sustain only a small amount of entrainment without a considerable lowering of efficiency (towers with high apparent efficiencies operating under low reflux ratios). In order to obtain the most economical tower design and a tower that will do the fractionation that is required, a judicious choice of tower diameter, tray spacing, and number of trays must be made. The most important factor which influences this choice is entrainment.

Entrainment was studied in the experimental tower with an air-water system using three rectangular-cap bubble trays. Water was pumped to the seal pot of the middle tray, and air was blown under the bottom tray; the top tray was used for the collection of entrainment, which was withdrawn from the seal pot and measured. Wall effect, although not a function of the method of measuring entrainment, was investigated simply by inserting a false wall the full length of the tray so that only three longitudinal rows of caps were active instead of the four rows normally present on the test tray. Thus a significant change in the ratio of wall space to tower volume was effected, but the measured entrainments were not significantly different.

Effect of Length of Liquid Path

Entrainment was measured for the sixteen- and the eight-cap trays. The eight-cap tray was obtained by removing eight caps from the sixteen-cap tray and blanking the risers. Plastic weirs and

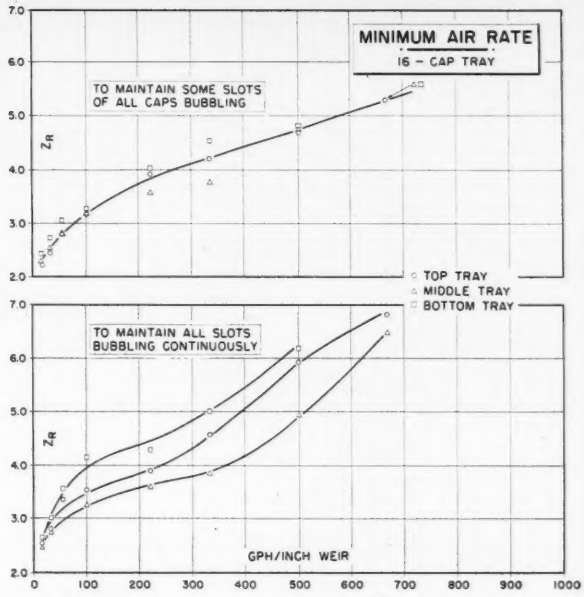

Fig. 12.

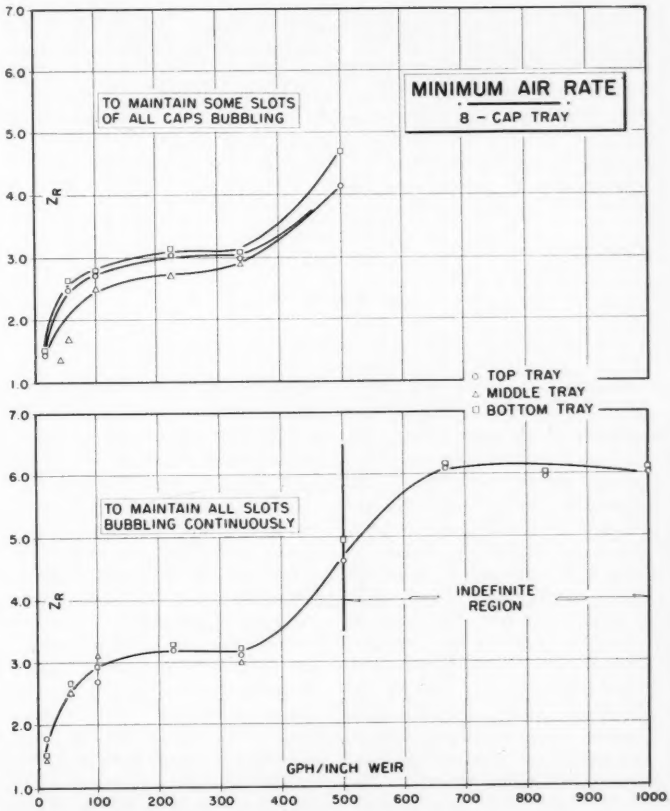

Fig. 13.

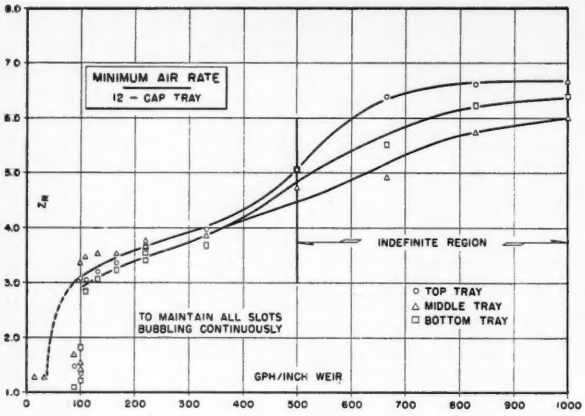

Fig. 14.

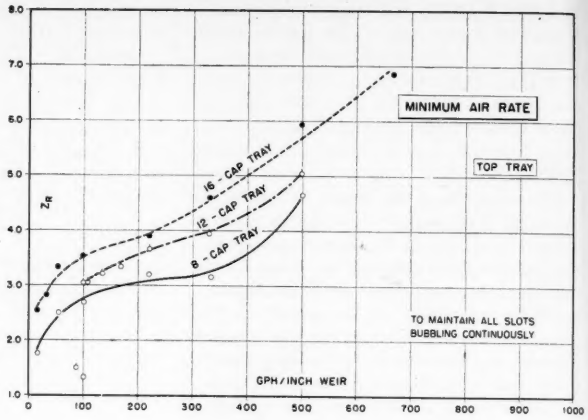

Fig. 15.

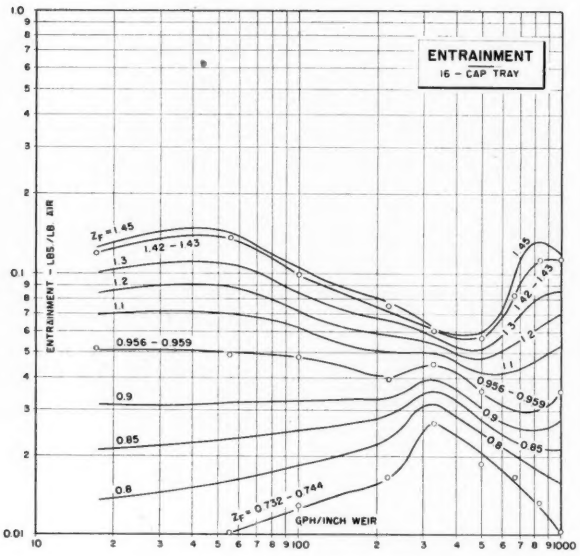

Fig. 16.

seal-pot dams were added to the trays. Figure 16 shows the effect of liquid rate on entrainment at air rates from a Z_F of 0.75 to 1.45 for the sixteen-cap tray. This series of curves contains all the actual measurements, as well as values obtained from a cross plot of entrainment vs. air rate expressed as Z_F. Values of entrainment were obtained at three air rates and nine water rates. As can be seen from the plot of the data, the shape of the curves at the three air rates studied is well defined and the cross plot is used solely to interpolate among the data in order to obtain a series of curves that can be used for obtaining entrainment at any air and liquid rate. The maximum air rate obtained was a Z_F of 1.43. The maximum Z_F obtainable was limited, not only by the capacity of the blower, but also by the amount of pressure the Lucite tower could withstand. It can also be noticed from Figure 16 that there is a definite minimum which occurs at a water rate of about 500 gal./(hr.)(in.) at Z_F's of 1.1 to 1.43. Some of the curves below a Z_F of 1.1 have both a maximum and a minimum. No satisfactory explanation is available for this behavior.

Figure 17 gives a plot of data for entrainment from the eight-cap tray, as well as the lines at other air rates obtained from a cross plot of entrainment and air rate. Figure 18 is a plot of entrainment vs. water rate for the sixteen- and eight-cap trays for Z_F's of 1.38, 1.135, and 0.922. The curves for the sixteen-cap tray were obtained from cross plots; the lines for the eight-cap tray, from the data. It can be seen from Figure 18 that there is an appreciable difference in entrainment between a tray with a length of path of 63 in. and one with 30 in. The tray with the shorter length of liquid path has higher entrainment for a Z_F of 1.38 and 1.135 at all water rates. At a Z_F of 0.922 the eight-cap tray generally has lower entrainment. It can be noticed that as air rate is increased, the difference in entrainment between the sixteen- and the eight-cap trays also increases.

Effect of Slot Spacing

In order to study the effect of slot spacing on entrainment, alternate slots on all caps of the middle tray of the sixteen-cap tray were blanked. The blanking of these slots decreased the number of open slots on the middle tray from 896 to 448. The details of the metal blanking strips are shown in Figure 4. The top and bottom trays remained unchanged and each contained 896 slots per tray. Figure 19 shows the plot of entrainment for the sixteen-cap tray with all slots open and with alternate slots on the middle tray blanked. This figure shows that for Z_F's of 1.43 and 0.955 there are no differences in entrainment between the sixteen-cap tray with or without alternate slots blanked. At a Z_F of 0.72 blanking slots has somewhat increased entrainment, below a water rate of 500 gal./(hr.)(in. of weir).

Effect of Bottom Tray

Entrainment was measured in the sixteen-cap-tray tower with and without caps on the bottom tray in order to determine what effects, if any, the bottom tray had on entrainment from the middle tray. In the first arrangement the caps on the bottom tray were retained. In the second arrangement the bubble caps were removed from the bottom tray, leaving the sixteen risers open. The data for these arrangements are plotted on Figure 20. Only two air rates were studied with caps on the bottom tray: Z_F equal to 0.959 and 0.744. It can be seen from Figure 20 that

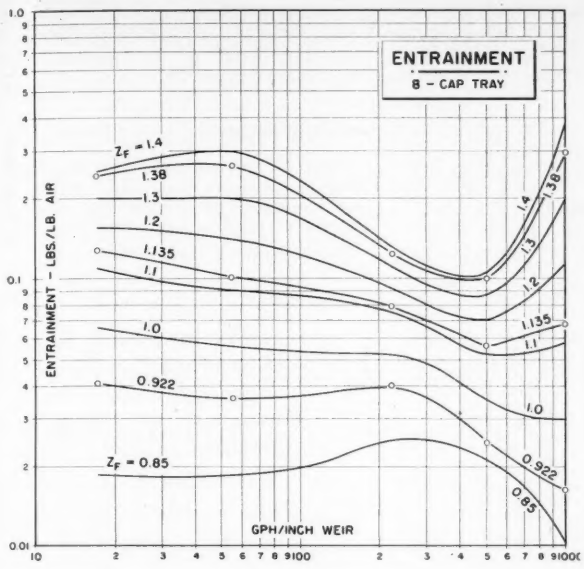

Fig. 17.

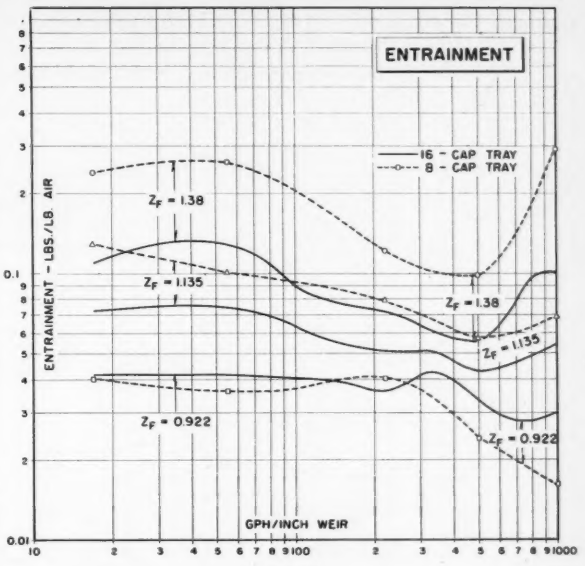

Fig. 18.

removing caps from the bottom tray has had no effect on the entrainment from the middle tray.

Effect of Cap Spacing

Tests were made in the laboratory tower to determine the effect of cap spacing on entrainment. Preliminary tests (*6*) were made by attaching 3/16-in. Lucite strips on the outside of the caps above the slots. These tests indicated that decreasing cap spacing increased entrainment. These Lucite strips reduced the bubbling area between caps and effectively changed cap spacing from 4½ to 4⅛ in. This small reduction of bubbling area increased entrainment substantially. More conclusive tests were made on a bubble-cap tray with twelve caps. This tray had caps on 6-in. spacing, which increased bubbling area from 37.7% of the free area for the sixteen-cap tray to 52.3%. Figure 21 shows a plot of entrainment vs. water rate at four air rates. Curves have also been drawn at various air rates by use of a cross plot. Figure 22 shows comparisons between entrainment with the sixteen-cap tray and the twelve-cap tray at Z_F's of 0.73, 0.968, 1.23, and 1.43. It can be seen that increasing cap bubbling area by increasing cap spacing has decreased entrainment at all air rates and all water rates, except for a Z_F of 1.43 at water rates above 220 gal./(hr.) (in. of weir), where the twelve-cap tray entrainment is slightly higher.

CONCLUSIONS

Although some of the results of this study confirm those previously obtained by other investigators, the following new and basic conclusions on entrainment can be drawn. These are possibly applicable to most bubble-cap-tray designs.

1. Entrainment increases with a decrease in liquid-path length.

2. Entrainment decreases with increasing cap spacing.

3. Decreasing number of slots while maintaining bubbling area constant has negligible effect on entrainment.

4. Increasing or decreasing liquid rate may increase or decrease entrainment, as most entrainment curves have a maxi-

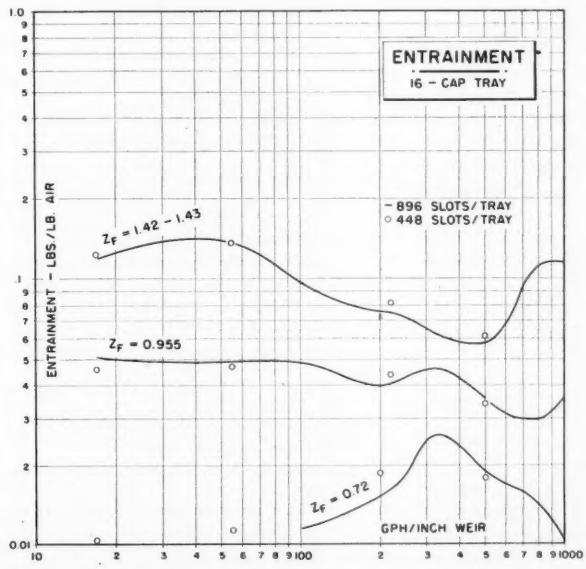

Fig. 19.

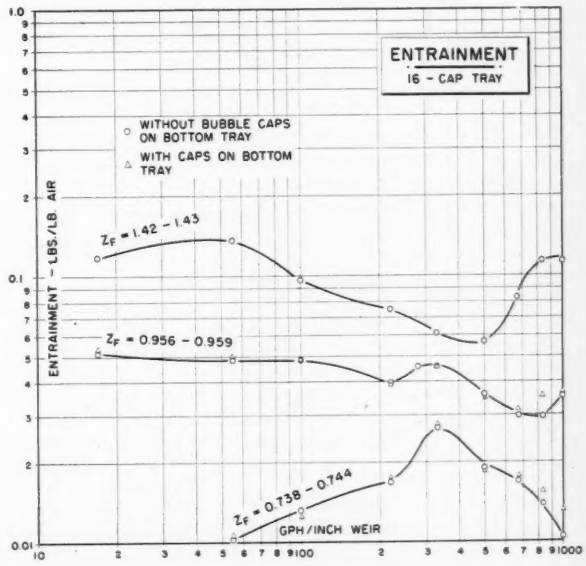
ENTRAINMENT
16 - CAP TRAY
WITHOUT BUBBLE CAPS ON BOTTOM TRAY
WITH CAPS ON BOTTOM TRAY
ENTRAINMENT - LBS./LB. AIR
GPH/INCH WEIR
Z_F = 1.42 - 1.43
Z_F = 0.956 - 0.959
Z_F = 0.738 - 0.744

Fig. 20.

mum and/or a minimum at any given air rate.

Owing to the differences in the type of cap used in this study, comparisons with the data of previous investigators would be meaningless and have not been presented. As the conclusions of this study were derived from data taken on a section of a commercial-size tower, they should represent an important contribution to the knowledge of entrainment from bubble-cap trays.

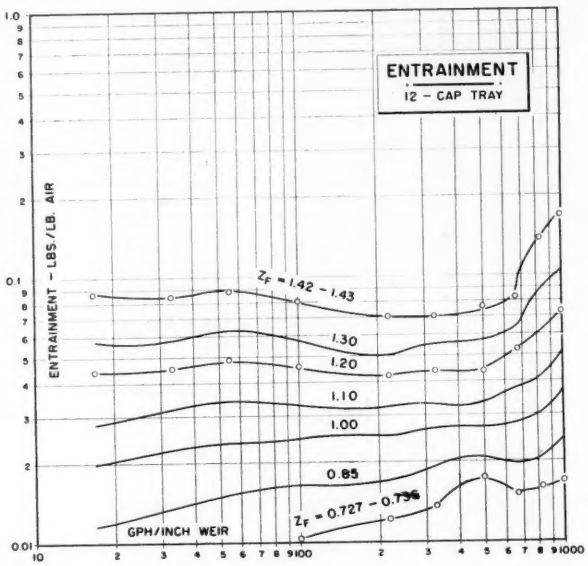

Fig. 21.

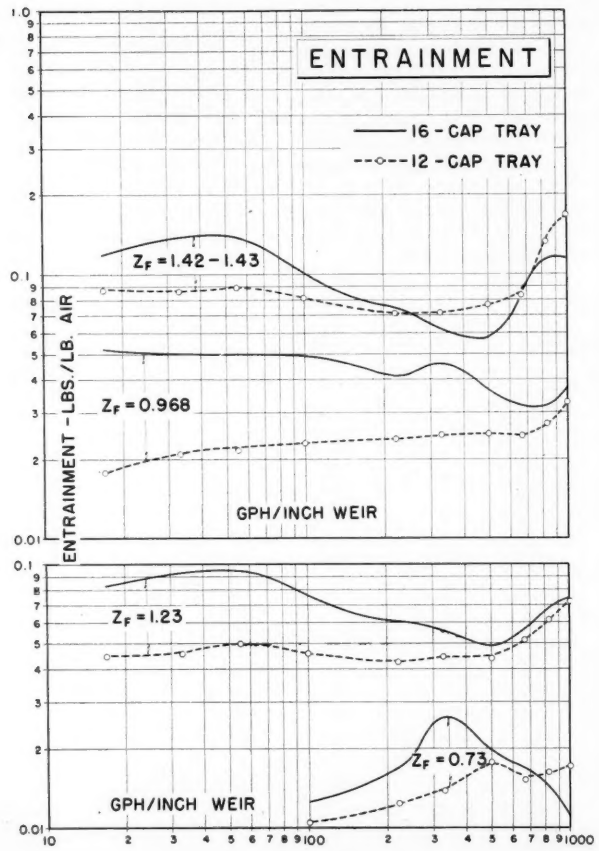

Fig. 22.

ACKNOWLEDGMENT

The authors wish to thank The M. W. Kellogg Company, New York, New York, for permission to publish the data and Walter E. Lobo and Leo Friend for their guidance in preparing the paper.

NOTATION

e = liquid entrainment lb./lb. air
E_a = efficiency with entrainment
E_v = efficiency without entrainment
L/V = reflux ratio, lb. of liquid/lb. of vapor

$$Z_F = \frac{\text{true vapor velocity in free area, ft./sec.}}{0.227\sqrt{\frac{\rho_L - \rho_V}{\rho_V}}}$$

$$Z_R = \frac{\text{true vapor velocity in riser area, ft./sec.}}{0.227\sqrt{\frac{\rho_L - \rho_V}{\rho_V}}}$$

Greek Symbols

ΔP = pressure drop, in. of water
ΔP_{DT} = total dry-tray pressure drop, in. of water
ΔP_T = total wet-tray pressure drop, in. of water
ρ_L = liquid density, lb./cu. ft.
ρ_V = true vapor density, lb./cu. ft.

LITERATURE CITED

1. Ashraf, F. A., T. L. Cubbage, and R. L. Huntington, *Ind. Eng. Chem.*, **26**, 1068 (1934).
2. Chillas, R. B., and H. M. Weir, *loc. cit.*, **22**, 206 (1930).
3. Colburn, A. P., *loc. cit.*, **28**, 526 (1935).
4. Holbrook, G. E., and E. M. Baker, *loc. cit.*, **26**, 1063 (1934).
5. Houghland, G. S., and W. C. Schreiner, *Proc. Natl. Conf. Ind. Hydraulics*, **4**, 75 (1950).
6. Kellogg Company, The M. W., unpublished data.
7. Peavy, C. C., and E. M. Baker, *Ind. Eng. Chem.*, **29**, 1056 (1937).
8. Pyott, W. T., C. A. Jackson, and R. L. Huntington, *loc. cit.*, **27**, 821 (1935).
9. Rhodes, F. H., and P. G. Slachman, *loc. cit.*, **29**, 51 (1937).
10. Sherwood, T. K., and F. J. Jenny, *loc. cit.*, **27**, 265 (1935).
11. Souders, M. J., and G. G. Brown, *loc. cit.*, **26**, 98 (1934).
12. Strang, L. C., *Trans. Inst. Chem. Engrs. (London)*, **12**, 169 (1934).
13. Thomson, A. K. G., *loc. cit.*, **14**, 119 (1936).
14. Volante, M. A., bachelor's thesis, Mass. Inst. Technol. (1929).

Presented at A.I.Ch.E. St. Louis meeting

A Generalized Correlation of Diffusion Coefficients

J. R. FAIR and B. J. LERNER

The University of Texas, Austin, Texas

Graphical correlations of binary gas diffusion coefficients are developed based on the Hirschfelder-Bird-Spotz diffusion equation and the theorem of corresponding states. A critical diffusion coefficient is defined and is used in turn for a definition of a "reduced" coefficient. The reduced diffusion coefficient is correlated graphically in generalized form in terms of the reduced properties of the diffusing gas. Using air as a reference "barrier" gas, the authors compared critical diffusion coefficients for various gases diffusing through a single barrier gas with the critical coefficients for these gases through air. This ratio, termed the *barrier gas ratio*, was found to be independent of the properties of the diffusing gas. A graphical correlation of the barrier gas ratio enables rapid estimation of a binary diffusion coefficient with a minimum of information.

While the importance of gaseous diffusion coefficients in chemical engineering calculations is well recognized, the availability of experimental data is limited and desired values must usually be estimated. This paper discusses the problems attendant on gaseous-diffusion-coefficient estimation and presents a generalized estimating technique which is both reliable and simple, particularly when applied to repetitive calculations.

Early theoretical work by Sutherland (*13*) and Gilliland (*5*) led to diffusion coefficient equations which had several recognized shortcomings. The equations were not applicable over wide temperature and pressure ranges, and the required calculations were sometimes tedious and cumbersome, particularly in their application to multicomponent systems. In general, the equations were based on a somewhat primitive kinetic theory of molecular collision, with empirical or semiempirical correction factors obtained from a meager supply of reliable experimental information.

Chapman and Cowling (*2*) made use of a realistic and correct approach to molecular interaction by taking into account the potential field surrounding a molecule. Hirschfelder and coworkers (*4, 6, 7, 8*) then utilized the Chapman and Cowling model, applied the Lennard-Jones 6–12 equation for the energy profile on close approach of two molecules, and arrived at basic equations for each of the transport properties of a gas. Mathematical analysis of the intermolecular forces resulting from close molecular approach involved an evaluation of a complex function, called the collision integral ϕ. This function serves as a correction factor for the familiar expressions derived from the simple kinetic theory. Thus the modified diffusion equation derived by Hirschfelder, Bird, and Spotz (*7*) (hereafter called the H-B-S equation) for binary pairs of spherical, nonpolar molecules is as follows:

$$D_{AB} = \frac{(1.492 \times 10^{-3})T^{3/2}}{P r_{AB}^{\ 2} \phi_{AB}} \cdot \left(\frac{1}{M_A} + \frac{1}{M_B}\right)^{1/2} \quad (1)$$

where A and B are the diffusing and barrier gases, respectively.

The collision integral ϕ as evaluated by Hirschfelder, Bird, and Spotz may be plotted as a function of the group kT/ϵ as shown in Figure 1. A simple analytical expression is not easily fitted to a relationship of this kind, as Scheibel (*12*) indicated in his discussion of the collision integral function involved in the viscosity expression for gases. It is of interest to note, however, that the slope varies from about -0.1 to about -0.5 over the normal range of engineering calculations. Thus the net dependence of D_{AB} on T in Equation (1) is of the order of the 1.6 to 2.0 power, which agrees with most experimental findings.

The proper use of Equation (1) involves determination of the mean molecular diameter, evaluation of the collision integral, and assumption of linear dependency of the diffusion coefficient on total pressure. Because of ternary and higher order collisions, this last named assumption breaks down at elevated pressures approaching the critical, but linear extrapolation with pressure is permissible in pressure ranges for which binary collisions predominate. Within these limitations it was suggested by Hirschfelder (*7*) that in the absence of reliable experimental data on molecular diameters and interaction energy, the diameter be estimated by the equation

$$r_A = 3.30(V_{cA})^{1/3} \quad (2)$$

The arithmetic average of the diameters of the diffusing and barrier molecules, obtained by use of Equation (2), is taken

---

J. R. Fair is at present with Shell Development Company, Emeryville, California, and B. J. Lerner with Gulf Research and Development Company, Pittsburgh, Pennsylvania.

as the collision diameter. The characteristic ratio ϵ_{AB}/k may be taken as the geometric mean of ϵ_A/k and ϵ_B/k. These values may be obtained from viscosity measurements or second virial coefficients or may be estimated from the equation

$$\epsilon_A/k = 0.75T_{c_A} \qquad (3)$$

The H-B-S equation is generally recognized as the best means presently available for estimating binary diffusion coefficients in the gas phase. It is not difficult to use for occasional calculations, although a table of collision integrals is required. When many coefficients must be evaluated, however, the procedure becomes time consuming, and a simplified yet accurate technique becomes desirable. Accordingly, graphical correlations are developed in this paper which have as their basis Equations (1), (2), and (3) above.

CRITICAL DIFFUSION COEFFICIENT

In a recent monograph Hougen (*9*) pointed out that generalized graphical correlations based on the theorem of corresponding states had been developed for both viscosity and thermal conductivity in terms of reduced properties but that no comparable correlation had as yet been devised for diffusion coefficients. As all gas transport properties may be related to essentially identical molecular interaction mechanisms, it is logical to assume that a graphical correlation with reduced properties can be developed for the diffusion coefficient.

Inasmuch as the H-B-S transport equations were used successfully by Bromley and Wilke (*1*) in the generalization of gas viscosity in terms of reduced properties, it appeared to the authors that a parallel development for diffusion coefficients on the same basis would be in order. Diffusion coefficients however present a unique situation with regard to correlation, because it is necessary to deal initially with a binary system rather than a pure substance, as is the case with other transport properties. As a starting point for the prediction of diffusion coefficients by means of reduced properties of a binary system, it was therefore necessary to define a critical diffusion coefficient as a reference point for a particular gas diffusing through another gas. This was done by means of Equation (1), the *critical diffusion coefficient* for A diffusing through B being arbitrarily defined as

$$D_{c_{AB}} = \frac{(1.492 \times 10^{-3})T_{c_A}^{3/2}}{P_{c_A}r_{AB}^{2}\phi_{c_{AB}}} \cdot \left(\frac{1}{M_A} + \frac{1}{M_B}\right)^{1/2} \qquad (4)$$

where $\phi_{c_{AB}}$ is evaluated with the aid of Equation (3) at the critical temperature of A.

The foregoing equation, of course, introduces the difficulty that the critical diffusion coefficient so defined loses some physical significance, since it is possible for the binary collision basis of Equation (1) to be violated at conditions approaching the critical. If the critical properties of the diffusing gas are employed, the critical diffusion coefficient of A through B is not equal to that of B through A, as is the case for "ordinary" diffusion coefficients. Rather, the critical coefficients are related by the equation

$$\frac{D_{c_{AB}}}{D_{c_{BA}}} = \left(\frac{T_{c_A}}{T_{c_B}}\right)^{3/2}\left(\frac{P_{c_B}}{P_{c_A}}\right)\left(\frac{\phi_{c_{BA}}}{\phi_{c_{AB}}}\right) \qquad (5)$$

The inequality of the two critical diffusion coefficients is due to the arbitrary use of the critical properties of the diffusing gas as system conditions in Equation (4); the only properties of the barrier gas affecting the equation directly are its molecular weight, molecular diameter, and its contribution to the collision integral. A further qualification must be introduced in that the critical diffusion coefficient has no meaning when the barrier material is not in the gaseous state at the critical temperature and pressure of the diffusing gas. In spite of this limitation, the concept of the critical diffusion coefficient has been found to be quite convenient as a datum, and its further application presents no serious practical problems as long as the inherent limitations are borne in mind.

REDUCED DIFFUSION COEFFICIENT

In view of the definition of the critical diffusion coefficient given above, a reduced diffusion coefficient may now be defined as follows:

$$D_{R_{AB}} = \frac{D_{AB}}{D_{c_{AB}}} = \left(\frac{T_A^{1.5}}{P_A\phi_{AB}}\right)\Big/\left(\frac{T_{c_A}^{1.5}}{P_{c_A}\phi_{c_{AB}}}\right) = \frac{T_{R_A}^{1.5}}{P_{R_A}\phi_{R_{AB}}} \qquad (6)$$

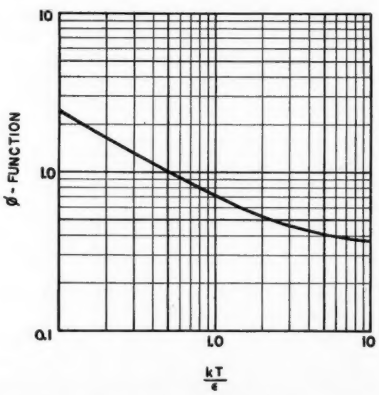

Fig. 1. Collision integral as function of group (kT/ϵ).

where

$$\phi_{R_{AB}} = \frac{\phi_{AB}}{\phi_{c_{AB}}} = \frac{f\left(\frac{kT_A}{\epsilon_{AB}}\right)}{f\left(\frac{kT_{c_A}}{\epsilon_{AB}}\right)}$$

Table 1—Critical Data and Barrier Gas Ratios

Gas A	$D_{c_{A-air}}$ sq. ft./hr.	$\frac{D_{c_{(x-A)}}}{D_{c_{(x-air)}}}$
Acetic acid	0.0253	0.48
Acetone	0.0218	0.47
Acetylene	0.0110	0.82
Air	0.00462	1.00
Aniline	0.0280	0.36
Ammonia	0.0126	1.04
Argon	0.00435	0.90
Benzene	0.0223	0.40
Bromine	0.0130	0.42
Bromobenzene	0.0266	0.30
Butadiene 1,3	0.0179	0.49
*Iso*butane	0.0183	0.46
n-Butane	0.0190	0.46
Butene-1	0.0182	0.48
Carbon dioxide	0.00846	0.73
Carbon disulfide	0.0156	0.46
Carbon monoxide	0.00496	0.98
Carbon tetrachloride	0.0214	0.35
Chlorine	0.0116	0.55
Chloroform	0.0182	0.38
Cyclohexane	0.0241	0.37
Cyclopentane	0.0210	0.42
Dimethyl ether	0.0142	0.55
Ethane	0.0120	0.71
Ethyl acetate	0.0240	0.38
Ethyl alcohol	0.0192	0.54
Ethyl chloride	0.0171	0.48
Ethyl ether	0.0217	0.41
Ethylene	0.0110	0.79
Ethylene oxide	0.0157	0.60
Fluorobenzene	0.0231	0.38
Freon-11	0.0177	0.38
Freon-12	0.0148	0.42
Freon-113	0.0211	0.32
n-Heptane	0.0296	0.32
n-Hexane	0.0261	0.35
Hydrogen	0.00365	4.08
Hydrogen chloride	0.0111	0.91
Hydrogen cyanide	0.0224	0.69
Iodobenzene	0.0293	0.29
Methane	0.00789	1.11
Methyl acetate	0.0208	0.43
Methyl alcohol	0.0187	0.60
Methyl chloride	0.0134	0.58
Nitric oxide (NO)	0.00510	0.10
Nitrogen	0.00470	0.99
Nitrogen dioxide (NO_2)	0.0116	0.70
Nitrous oxide (N_2O)	0.00885	0.72
n-Octane	0.0329	0.28
Oxygen	0.00459	0.97
Ozone	0.00755	0.74
n-Pentane	0.0227	0.39
Phosgene	0.0150	0.44
Propane	0.0157	0.55
Propionic acid	0.0247	0.41
n-Propyl acetate	0.0270	0.34
n-Propyl alcohol	0.0221	0.45
Propylene	0.0146	0.58
Sulfur dioxide	0.0122	0.56
Sulfur trioxide	0.0135	0.51
Toluene	0.0256	0.35
Trimethylamine	0.0184	0.45
Trimethyl benzene-1,2,3	0.0358	0.29
Water	0.0158	1.03

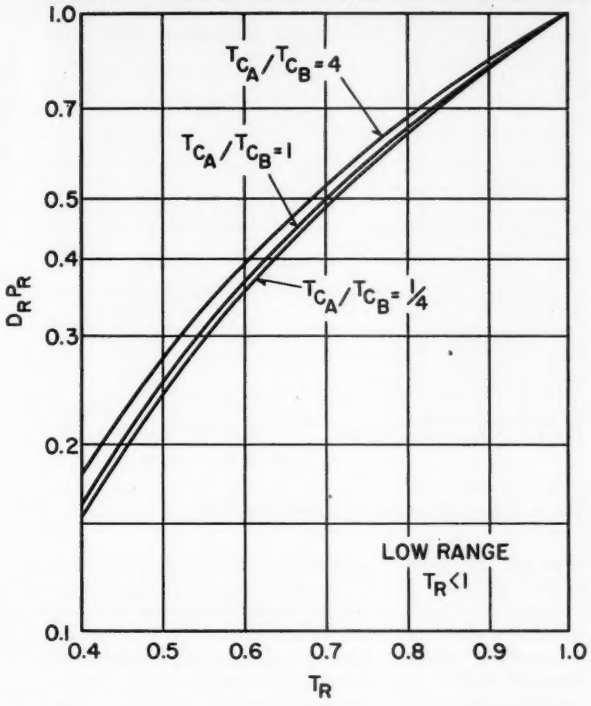

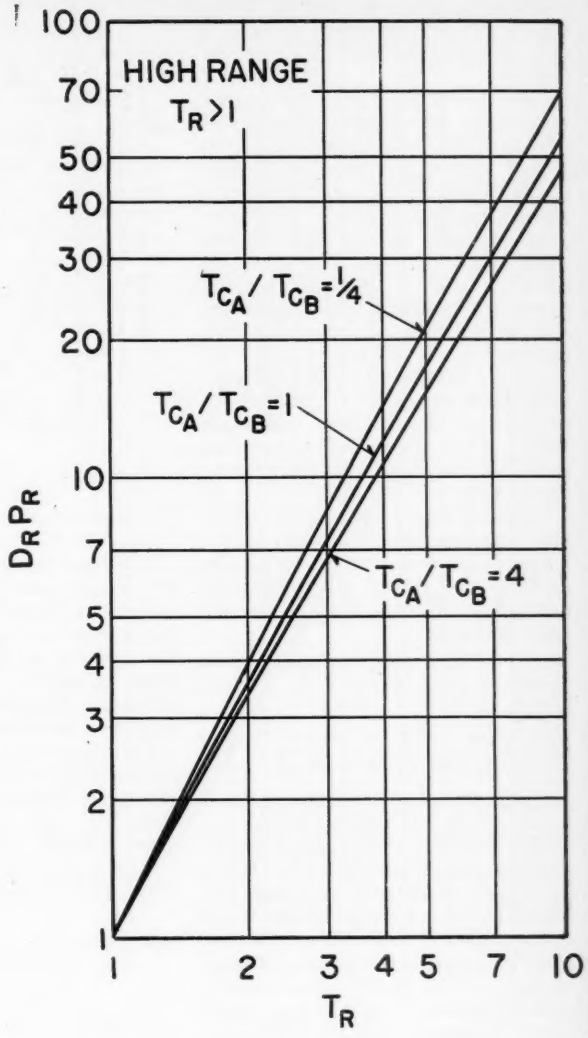

Fig. 2. Reduced diffusion coefficient correlation: $A\uparrow$, low range; B, high range.
$\rightarrow$

and $f(kT/\epsilon)$ is shown graphically in Figure 1. From Equation (3) and the geometric mean definition of ϵ_{AB}/k,

$$\phi_{R_{AB}} = \frac{f\left[\dfrac{kT_A}{0.75(T_{c_A}T_{c_B})^{0.5}}\right]}{f\left[\dfrac{kT_{c_A}}{0.75(T_{c_A}T_{c_B})^{0.5}}\right]} \quad (7)$$

or

$$\phi_{R_{AB}} = \frac{f\left[\dfrac{kT_{R_A}}{0.75}\left(\dfrac{T_{c_A}}{T_{c_B}}\right)^{0.5}\right]}{f\left[\dfrac{k}{0.75}\left(\dfrac{T_{c_A}}{T_{c_B}}\right)^{0.5}\right]} \quad (8)$$

Thus $\phi_{R_{AB}}$ should be a function of T_{R_A} and the ratio of the critical temperatures of the gases under consideration. Inspection of Equations (6) and (8) indicated that it would be possible to plot $D_R P_R$ against T_R on logarithmic coordinates, by use of (T_{c_A}/T_{c_B}) as a parameter. This was done by calculating $D_R P_R$ for many combinations of gases (by use of tabulated ϕ values from reference *6*), and the results are shown in Figure 2*A* and *B*. It should be noted that Figure 2 is a graphical presentation of the H-B-S diffusion equation with parameters derived from an approximation of the collision integral and does not represent experimental data directly. However, the H-B-S equation has been used to detect errors in experimental results, and so Figure 2 may be taken as a tentative standard chart in lieu of extensive and precise experimental data on diffusion coefficients.

EXAMPLE

The use of Figure 2 may be illustrated by means of the following problem.

Estimate the diffusion coefficient for carbon dioxide through air at 1.0 atm. total pressure and a temperature of 900°R.

From Table 1

for carbon dioxide

D_c (through air) = 0.00846 sq. ft./hr.
T_c = 548 °R.
P_c = 72.9 atm.

and for air,

T_c = 238 °R.

from which

T_R (carbon dioxide) = 1.64
P_R (carbon dioxide) = 0.0137
T_{c_A}/T_{c_B} = 2.3

Then, from Figure 2*B*, for $T_R = 1.64$ and the parameter value of 2.3,

$$D_R P_R = 2.43$$

whence

$$D = D_R D_c = \frac{(2.43)(D_c)}{P_R}$$

$$= \frac{(2.43)(0.00846)}{0.0137}$$

$$= 1.50 \text{ sq. ft./hr.}$$

which agrees with the value of 1.50 sq. ft./hr. calculated by means of the H-B-S equation.

BARRIER GAS RATIO

In the foregoing example it is apparent that the utility of Figure 2 for rapid estimation of diffusion coefficients is limited by the necessity for first calculating the critical diffusion coefficient for A through B. Indeed, the whole purpose of the graph is defeated if it requires direct use of Equation (1) for this calculation. A graphical estimation technique therefore

hinges on a means for arriving at the critical diffusion coefficient quickly, a requirement best satisfied by a graphical method.

Tabulation of initial calculations on the value of the critical diffusion coefficient as related to binary-system properties showed that any graphical estimation method would require specification of a reference barrier gas. In order to systematize comparison, air was chosen as the reference gas. Although it is a slightly variable mixture in itself, air has the advantages of suitable critical properties and also of frequent occurrence in actual problems as the diffusion barrier. By means of Equation (4), critical diffusion coefficients for a number of gases through air were calculated. These values are listed in Table 1. Values of other critical properties were taken from the compilation by Kobe and Lynn (*10*).

Critical diffusion coefficients for various gases diffusing through a single barrier gas were compared with the coefficients for these gases through air. Comparison was made on the basis of the barrier gas ratio, defined as

$$\frac{D_{cAB}}{D_{cA-air}} = \left(\frac{r_{A-air}}{r_{AB}}\right)^2 \left(\frac{\phi_{cA-air}}{\phi_{cAB}}\right) \cdot \left(\frac{M_A + M_B}{M_A + M_{air}}\right)^{0.5} \left(\frac{M_{air}}{M_B}\right)^{0.5} \quad (9)$$

A large number of calculations revealed that the barrier gas ratio was *independent of the properties of the diffusing gas.* This may be illustrated by a single series of calculations involving the coefficients of randomly chosen gases diffusing through carbon dioxide and the coefficients of the same gases diffusing through air. The results of these calculations are presented in Table 2, where it may be observed that the barrier gas ratio is essentially independent of the properties of the diffusing gas, with a maximum difference of the order of $\pm 4\%$.

It is thus possible to characterize the barrier diffusion behavior of all gases relative to air by the assignment to each gas of a dimensionless barrier ratio number. The characteristic barrier numbers were calculated by taking the same series of twenty-five diffusing gases listed in Table 2 through each barrier gas. The resulting average values of the ratios are tabulated in Table 1. It was obvious that if the barrier ratio could be generally related to the molecular properties of the barrier gas, then the use of the reduced diffusion chart would require information only on D_{cA-air}.

The correlating terms for the barrier ratio were obtained from an analysis of Equation (9). Of the several correlations derived, only Figure 3 represents the most successful generalization of the barrier ratio as a function of molecular properties. The data points of Figure 3 include all the gases listed in Table 1 with the exception of hydrogen.

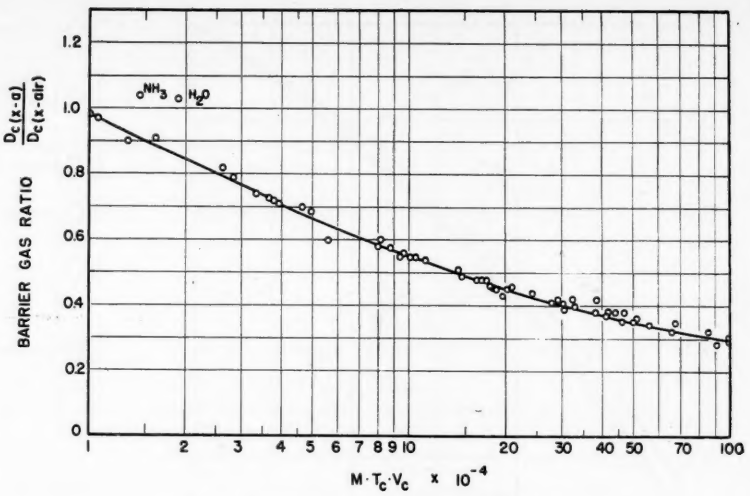

Fig. 3. Barrier gas ratio as function of MT_cV_c.

As pointed out by Cook and Rowlinson (*3*), certain gases possess electronic arrangements which will cause them to deviate from any generalization based on the theorem of corresponding states. Since structural anomalies would be reflected in measured values of the critical properties, deviations from the correlation of Figure 3 are to be expected, particularly for molecules which have a strong tendency for hydrogen bonding. Thus, H_2O, NH_3, and CH_3OH are all off the curve of Figure 3. Caution should therefore be exercised in applying the correlation to other molecules which are highly associated in the liquid state. With this reservation, the correlation of Figure 3 may be used to estimate the barrier gas ratio when direct data are unavailable. Because D_{cAB} for any barrier gas B can thus be obtained by simply multiplying the barrier gas ratio by D_{cA-air}, the value of D_{cA-air} may be viewed as a fundamental property of a gas of equal rank with its other critical transport or molecular properties.

Table 2—Diffusion of Gases Through Carbon Dioxide

Gas A	D_{cA-CO_2}, sq. ft./hr.	D_{cA-air}, sq. ft./hr.	$\frac{D_{cA-CO_2}}{D_{cA-air}}$
Acetic acid	0.0187	0.0253	0.74
Acetone	0.0159	0.0218	0.73
Acetylene	0.00822	0.0110	0.75
Aniline	0.0205	0.0280	0.73
Ammonia	0.0096	0.0126	0.76
Benzene	0.0162	0.0223	0.73
Bromine	0.00920	0.0130	0.71
Bromobenzene	0.0191	0.0266	0.72
n-Butane	0.0139	0.0190	0.73
Carbon disulfide	0.0115	0.0156	0.74
Carbon tetrachloride	0.0152	0.0214	0.71
Chlorine	0.00832	0.0116	0.72
Chloroform	0.0130	0.0182	0.71
Cyclopentane	0.0152	0.0210	0.72
Dimethyl ether	0.0105	0.0142	0.74
Ethyl acetate	0.0174	0.0240	0.73
Ethyl alcohol	0.0142	0.0192	0.74
Ethyl chloride	0.0124	0.0171	0.73
Ethylene oxide	0.0115	0.0157	0.73
Freon-11	0.0127	0.0177	0.72
n-Heptane	0.0214	0.0296	0.72
Hydrogen chloride	0.00805	0.0111	0.73
Hydrogen cyanide	0.0170	0.0224	0.76
Iodobenzene	0.0208	0.0293	0.71
Methane	0.00590	0.00789	0.75
		Average	0.73

CALCULATION PROCEDURE

It should be reiterated that the correlations presented in this paper are based on the Hirschfelder-Bird-Spotz equation, which in turn is valid only for nonpolar-nonpolar and polar-nonpolar pairs of gases. On this basis the calculation procedure may be summarized briefly as follows:

1. Considering the diffusion of A through B, the value of D_c for A through air is obtained from Table 1. The barrier gas ratio for B is also obtained from Table 1. These values are multiplied together to obtain D_{cAB}.
2. From the values of T_{RA} and P_{RA} and the critical temperature ratio T_{cA}/T_{cB}, $D_{RA}P_{RA}$ is read from Figure 2.
3. D_{AB} is obtained by multiplying D_{RA} by D_{cAB}.

If the necessary barrier ratio is not listed in Table 1, then the correlation of Figure 3 may be used. If neither of the gases is included in Table 1, it will be necessary to calculate one of the critical diffusion coefficients (through air) by means of Equation (4).

Binary Examples

Example 1

Calculate the diffusion coefficient for ethylene through methane at 100 lb./sq. in. gauge (7.80 atm. abs. pressure) and 120° F. (580°R.).

From Table 1

for ethylene,

D_c (through air) = 0.0110 sq. ft./hr.
T_c = 508 °R.
P_c = 50 atm.

and for methane,

T_c = 344 °R.
Barrier ratio = 1.11

Then

D_c (ethylene–methane) = 1.11(0.0110) = 0.0122 sq. ft./hr.
T_{cA}/T_{cB} = 1.48

From Figure 2*B*, for $T_R = 1.14$, $P_R = 0.156$

$$D_R P_R = 1.26$$

whence

$$D = \frac{1.26(0.0122)}{0.156}$$

$$= 0.0988 \text{ sq. ft./hr.}$$

which may be compared with a value of 0.0950 calculated by means of the H-B-S equation.

When D_{cA-ei}, for the diffusing gas is not listed in Table 1 and its value for the barrier gas is known, advantage may be taken of the fact that $D_{AB} = D_{BA}$, as shown in the following example:

Example 2

Estimate the diffusion coefficient for 1,2-dichloroethane through hydrogen chloride at 2.0 atm. total pressure and 200°F. (660°R.).

1,2-dichloroethane is not listed in Table 1. Consider it as the barrier gas. From Table 1 and from reference *11*

	HCl	$C_2H_4Cl_2$
D_c (through air), sq. ft./hr.,	0.0111	
T_c, °R.,	584	1,011
P_c, atm.,	81.6	53
V_c, cu. ft./lb.-mole,	—	3.78

For 1,2-dichloroethane, $MT_cV_c = 99(1{,}011)(3.78) = 37.8 \times 10^4$ for which, from Figure 3, the barrier ratio is 0.37.
Then

$$D_c(\text{HCl} - C_2H_4Cl_2) = 0.37(0.0111)$$

$$= 0.00411 \text{ sq. ft./hr.}$$

from Figure 2*B*, for $T_R = 1.13$, $T_{cA}/T_{cB} = 0.58$, $P_R = 0.0245$

$$D_R P_R = 1.28$$

whence

$$D = \frac{0.00411(1.28)}{0.0245}$$

$$= 0.214 \text{ sq. ft./hr.}$$

which may be compared with a value of 0.216 sq. ft./hr. calculated by means of the H-B-S equation.

MULTICOMPONENT SYSTEMS

It has been shown by Wilke (*14*) that the effective diffusion coefficient for gas A through a mixture of gases $B, C, D, \ldots, n$ may be obtained from the expression

$$D_A' = \frac{1 - y_A}{\sum_{i=B}^{n} \frac{y_i}{D_{A-i}}} \qquad (10)$$

where

D_A' = effective diffusion coefficient for A in a multicomponent system
y = mole fraction in the gas

Thus the number of separate binary coefficients to be determined equals the number of binary gases. The direct use of the H-B-S equation for this situation, particularly when a range of temperatures is involved, becomes somewhat tedious. The graphical correlations presented here offer a rapid and simple means for multicomponent diffusion calculations and lend themselves readily to elementary desk-calculator computation. The time-saving advantages inherent in the present correlation may be illustrated by the following example.

Multicomponent Example

Estimate the effective diffusion coefficient for methane at a temperature of 200°F. and a total pressure of 3.0 atm. in a mixture of the following composition:

	Mole %
Methane	16.0
Ethane	20.0
Propane	12.0
n-Butane	40.0
n-Pentane	12.0
	100.0

The details of the estimation procedure are tabulated below.

For methane:

T_{cA} = 344°R. P_{cA} = 45.8 atm.
T_{RA} = 1.92 P_{RA} = 0.0655

From Table 1

$D_c(CH_4\text{-air})$ = 0.00789 sq. ft./hr.

	C_2H_6	C_3H_8	C_4H_{10}	C_5H_{12}
T_{cB}, °R.	550	666	765	846
T_{cA}/T_{cB}	0.63	0.52	0.45	0.41
D_RP_R (Fig. 2*B*)	3.55	3.58	3.62	3.65
D_R	54.2	54.7	55.3	55.7
Barrier ratio (Table 1)	0.710	0.550	0.460	0.390
D_{cAB}	0.00560	0.00434	0.00363	0.00310
$D_i = (D_R)(D_{cAB})$	0.304	0.237	0.201	0.171

$$D_A' = \frac{0.840}{\frac{0.200}{0.304} + \frac{0.120}{0.237} + \frac{0.400}{0.201} + \frac{0.120}{0.171}}$$

$$= 0.218 \text{ sq. ft./hr.}$$

ACKNOWLEDGMENT

The assistance of Mr. E. J. Cullen in the initial phases of correlation and calculation work is gratefully acknowledged.

NOTATION

D = gaseous diffusion coefficient, sq. ft./hr. D_{AB} = diffusion coefficient for A diffusing through B. D_A' = effective diffusion coefficient for A diffusing through a mixture.
D_c = critical diffusion coefficient, sq. ft./hr.
D_R = reduced diffusion coefficient, D/D_c
k = Boltzmann constant, ergs/°R.-molecule
M = molecular weight
P = pressure, atm. abs.
P_c = critical pressure, atm. abs.
P_R = reduced pressure, P/P_c
r = molecular diameter, Angstroms
r_{AB} = collision diameter for molecules A and B, Angstroms
T = temperature, °R.
T_c = critical temperature, °R.
T_R = reduced temperature, T/T_c
V_c = critical volume, cu. ft./lb.-mole
x = any gas diffusing through A (Table 1)
y = mole fraction

Greek Letters

ϵ = minimum interaction energy, ergs
ϕ = collision function
ϕ_c = collision function evaluated at critical temperature

Subscripts

A,B = gases in the binary system under consideration
c = a critical property
R = a reduced property

LITERATURE CITED

1. Bromley, L. A., and C. R. Wilke, *Ind. Eng. Chem.*, **43**, 1641 (1951).
2. Chapman, S., and T. G. Cowling, "Mathematical Theory of Non-Uniform Gases," Cambridge University Press, Teddington (1939).
3. Cook, D., and J. S. Rowlinson, *Proc. Royal Soc. (London)*, **A219**, 405 (1953).
4. Curtiss, C. F., and J. O. Hirschfelder, *J. Chem. Phys.*, **17**, 550 (1949).
5. Gilliland, E. R., *Ind. Eng. Chem.*, **26**, 681 (1934).
6. Hirschfelder, J. O., R. B. Bird, and E. L. Spotz, *J. Chem. Phys.*, **16**, 968 (1948).
7. ———, *Chem. Rev.*, **44**, 205 (1949).
8. ———, *Trans. Am. Soc. Mech. Engrs.*, **71**, 921 (1949).
9. Hougen, O. A., *Chem. Eng. Progr. Monograph Ser.*, No. 1, **47** (1951).
10. Kobe, K. A., and R. E. Lynn, *Chem. Rev.*, **52**, 117 (1953).
11. Landolt-Bornstein, "Physikalisch-Chemische Tabellen," 5th ed., **1**, 254, Springer-Verlag, Berlin (1923).
12. Scheibel, E. G., *Ind. Eng. Chem.*, **46**, 2008 (1954).
13. Sutherland, W., *Phil. Mag.*, **38**, 1 (1894).
14. Wilke, C. R., *Chem. Eng. Progr.*, **46**, 95 (1950).

Presented at A.I.Ch.E. Houston meeting

Correlation of Bubble-cap Fractionating-column Plate Efficiencies

EARL D. OLIVER and C. C. WATSON

University of Wisconsin, Madison, Wisconsin

A method of estimating the true conditions of operation of a bubble-cap tray is presented. Intermediate between the Murphree and the Lewis methods, which represent the extremes of actual operation, this method involves the use of a correlation to determine the degree of liquid mixing on the tray and the use of new relations between the Murphree vapor efficiency, the Lewis case I efficiency, and the true local efficiency. For the last, partial liquid mixing is taken into account.

Data were obtained on an 18-in. O.D. three-tray bubble-cap tower containing ten 3-in. bubble caps a tray. Partial liquid mixing was correlated for changes in vapor and liquid rates, pressure, temperature, and weir height for the system ethylene dichloride–toluene.

Efficiency data on acetone-water, ethanol-water, and ethylene dichloride–toluene showed the following effects: (1) low concentration of low boiler usually, but not always, resulted in low true local efficiencies, always with high Murphree efficiencies; (2) vapor velocity effects are more intimately connected with slot velocity than superficial velocity (and hence entrainment); (3) raising the pressure gives higher efficiencies; (4) an increase in liquid depth increases the true local efficiency but may have no effect on the Murphree efficiency.

THEORETICAL DEVELOPMENT

Murphree (*11*) assumed that the liquid on bubble-cap trays was completely mixed. Lewis (*10*) assumed that it was completely unmixed in the direction of flow. Actually, significant but incomplete liquid mixing was found in this study. The data were correlated by analogy to the well-known relation that the degree of mixing is a unique function of the power input per unit volume for a given geometrical shape and a given system. This led to a dimensionless mixing parameter,

$$F = f_1\left(\frac{u_G^2 w_G v_L}{2 q_L^2 \mu_L}\right) \qquad (1)$$

In this parameter, $U_G^2 w_G/2q_L$ is considered the power input per unit volume of liquid per unit time, v_L/q_L is the residence time of the liquid, and μ_L is the resistance to mixing.

The Murphree vapor efficiency is, for Murphree's model, the ratio of actual to theoretical enrichment. Thus

$$E_{MV} = \frac{y_n - y_{n+1}}{y_n^* - y_{n+1}} \qquad (2)$$

Lewis (*10*) for his case I assumed (1) perfect vertical liquid mixing, (2) no horizontal liquid mixing (that is, in the direction of net cross flow), and (3) perfect mixing of entering vapor. On this model a material balance may be written for a differential slab between two vertical planes perpendicular to the direction of liquid flow, through which a differential amount of vapor dG rises. For constant molal overflow,

$$L\,dx = (y_n' - y_{n+1})\,dG$$
$$= E_{OG}(y^* - y_{n+1})\,dG \qquad (3)$$

If E_{OG} is constant for the entire plate,

$$E_{OG} = \frac{L}{G}\int_{x_n}^{x_{n-1}} \frac{dx}{y^* - y_{n+1}} \qquad (4)$$

If the equilibrium line is straight for the concentration range involved,

$$E_{OG} = \frac{L}{mG} \ln \frac{y_{n-1}^* - y_{n+1}}{y_n^* - y_{n+1}} \qquad (5)$$

Combining with a material balance leads to

$$E_{OG} = \frac{y_n - y_{n+1}}{(y^* - y_{n+1})_{lm}} \qquad (6)$$

The denominator, which is the theoretical enrichment, is the logarithmic mean of the possible enrichment for the inlet and outlet liquid concentrations.

Lewis derived a relationship between his case I efficiency and the Murphree efficiency for a straight equilibrium line, as follows:

$$E_{OG} = \frac{\ln(1 + \lambda E_{MV})}{\lambda} \qquad (7)$$

In this work, for ethanol-water the integration of Equation (4) was performed by expressing the equilibrium data with Clark (*4*) equations and substituting for y^* in terms of x. Clark expressed binary equilibrium data by the equations

$$Y = AX + B \qquad (8a)$$

$$Y' = A'X' + B' \qquad (8b)$$

where

$$Y = y^*/(1 - y^*) = 1/Y'$$

$$X = x/(1 - x) = 1/X'$$

Equation (8*a*) is applicable above the conjugate, $X = \sqrt{A'B/AB'}$; Equation (8*b*) is applicable below. Both equations give an identical form to the integral, but the constants differ. Above the conjugate

$$E_{OG} = \frac{L}{G}\frac{1}{A_c}\left[A_a(x_{n-1} - x_n) + \frac{A}{A_c}\ln\frac{A_c x_{n-1} + A_d}{A_c x_n + A_d}\right] \qquad (9a)$$

where

$$A_a = A - B - 1$$

$$A_c = A - B - (A - B - 1)y_{n+1}$$

$$A_d = B - (B + 1)y_{n+1}$$

Below the conjugate

$$E_{OG} = \frac{L}{G}\frac{1}{A_c'}\left[A_a'(x_{n-1} - x_n) + \frac{A'}{A_c'}\ln\frac{A_c' x_{n-1} + A_d'}{A_c' x_n + A_d'}\right] \qquad (9b)$$

where

$$A_a' = 1 - A' + B'$$

$$A_c' = 1 - (1 - A' + B')y_{n+1}$$

$$A_d' = -A' y_{n+1}$$

For ethylene dichloride and toluene, y^* was related to x by an assumed constant relative volatility. Substitution and integration yield

Earl D. Oliver is with Shell Development Company, Emeryville, California.

Original data are contained in the Ph.D. thesis of Earl D. Oliver, which is obtainable on loan from the Memorial Library, University of Wisconsin, 728 State Street, Madison, Wisconsin.

$$E_{OG} = \frac{L}{G}\left[\frac{\alpha}{(C_1)^2}\ln\frac{C_1x_{n-1} - y_{n+1}}{C_1x_n - y_{n+1}} + \frac{(\alpha - 1)(x_{n-1} - x_n)}{C_1}\right] \quad (10)$$

where $C_1 = \alpha - (\alpha - 1)_{n+1}$.

For the system acetone-water, molal overflow was far from constant. An analysis similar to that resulting in Equation (3), but with all terms in the energy balance considered, yields for the top plate

$$\int_0^G \frac{E_{OG}\,dG}{L} = -\int_{x_0}^{x_1}\frac{dx}{y^* - y_2 - \dfrac{(H' - H_2)(y' - x)}{E_{OG}(H' - h)}} \quad (11)$$

The last term is considered a small correction term, and an average value is taken. Other approximations make possible the solution

$$E_{OG} = \frac{2}{G_2\left(\dfrac{1}{L_0} + \dfrac{1}{L_1}\right)} \cdot \int_{x_1}^{x_0}\frac{dx}{y^* - \left[y_2 + \dfrac{(H_1 - H_2)(y_1 - x_{1_{ave}})}{E_{OG}(H_1 - h_{1_{ave}})}\right]} \quad (12)$$

which is evaluated as in Equation (9).

On an actual plate a liquid concentration traverse would make possible a plot of y^* vs. distance across the plate, from which the theoretical enrichment could be derived. The ratio of the actual enrichment to the theoretical is the true local efficiency.

If only the total fractional mixing F is known, the assumption that the rate of mixing is uniform across the plate makes possible a solution analogous to Equation (4):

$$E_{OGT} = \frac{L}{G(1 - F)}\int_{x_n}^{x_0}\frac{dx}{y^* - y_{n+1}} \quad (13)$$

The previous integrations may be applied, or if the equilibrium line is straight, Equation (6) still holds, provided x_e is used in place of x_{n-1} for finding the inlet equilibrium value. Alternatively, the true local efficiency may be derived from the Murphree efficiency as follows:

$$E_{OGT} = \frac{\ln\left[1 + \lambda(1 - F)E_{MV}\right]}{\lambda(1 - F)} \quad (14)$$

This equation reduces to the Lewis relation for $F = 0$, and, by L'Hôpital's rule, to $E_{OGT} = E_{MV}$ for $F = 1$.

The two-film theory of packed columns was extended to bubble-plate fractionating columns by Gerster et al. (*5*). Important equations may be combined in the following form:

$$N_{OG} = -\ln(1 - E_{OGT}) = \int_{y'_{n+1}}^{y'_n}\frac{dy'}{y^* - y'} = \frac{zK_{OG}a}{G} \quad (15)$$

Where liquid mixing occurs, the true local efficiency should be used as the measure of the actual number of transfer units. The composition y' represents the instantaneous bulk value for a single bubble, and y^* is the corresponding value in equilibrium with the adjacent liquid. Analogous relations may be written for the individual gas and liquid film resistances.

Certain limitations of Equation (15) should be carefully noted. In the first place the validity of the relation between N_{OG} and E_{OGT} depends on vertical constancy of liquid composition (and hence y^*). Direct determinations of point liquid compositions would present extreme experimental difficulties.

Second, the constancy of the transfer coefficient is doubtful, as, for example, the equations

$$\frac{1}{K_{OG}} = \frac{1}{k_G} + \frac{m}{k_L} \quad (16)$$

$$\frac{1}{N_{OG}} = \frac{1}{N_G} + \frac{mG}{L}\cdot\frac{1}{N_L} \quad (17)$$

The slope m is constant if the liquid composition is vertically constant. But the film transfer coefficients would be expected to depend on film properties. With interface equilibrium assumed in the two-film theory, the film concentration is necessarily variable.

Third, terms affecting interfacial area are not necessarily constant in bubble-plate columns.

Thus the two-film theory should not be thought of as basically sound. The simple flow pattern assumed in the derivation does not exist; nevertheless, the use of the two-film theory is a promising method of correlating efficiency data.

If efficiency data are to be generalized by the two-film theory, means must be available for predicting the interfacial area terms and transfer coefficient of Equation (15). No such means is available for the interfacial area terms, but the data of van Krevelen and Hoftijzer (*19*) suggest relative constancy at a given vapor rate on a given tray. Their data also indicate that the friction factor of a rising bubble is constant at high rates.

Variations of coefficients may be estimated by the Chilton-Colburn (*3*) modification of the Reynolds analogy. Thus

$$\frac{k_G}{G}\left(\frac{\mu_G}{\rho_G D_G}\right)^{2/3} = j_M = \frac{f}{2} \quad (18)$$

Generally the relation holds for skin friction, but not form drag. However, a bubble does not have a fixed shape, and its dimensions oscillate rapidly. Presumably both friction and mass transfer are increased by the greater turbulence.

If the mass transfer factor is assumed constant, one may obtain

$$k_G = C_2\frac{\rho_G u_G}{M_G}\left(\frac{\mu_G}{\rho_G D_G}\right)^{-2/3} \quad (19)$$

This assumption gives a much more reasonable function of the viscosity than does the assumption that mass transfer data for solid particles apply. Such data make the mass transfer factor proportional to the $-\frac{1}{2}$ power of Reynolds number, which would nearly cancel the effect of viscosity shown in Equation (19).

For constant-rate data on a given system, with the perfect gas law assumed and diffusivity taken proportional to the temperature to the $\frac{3}{2}$ power divided by the pressure, Equation (19) reduces to

$$k_G = C_3 p_t^{1/3}\left(\frac{\mu_G}{\rho_G}\right)^{-2/3} \quad (20)$$

For the liquid film, in the same way,

$$k_L = C_4\frac{\rho_L u_L}{M_L}\left(\frac{\mu_L}{\rho_L D_L}\right)^{-2/3} \quad (21)$$

For constant-rate data

$$k_L = \frac{C_5}{V_L}\left(\frac{\mu_L}{\rho_L D_L}\right)^{-2/3} \quad (22)$$

Frequently for a liquid $D\mu/T$ is constant. If so,

$$k_L = \frac{C_6}{V_L}\left(\frac{\mu_L^2}{\rho_L T}\right)^{-2/3} \quad (23)$$

It is not clear whether the velocities in these equations are rising bubble velocities, relative velocities of vapor to liquid, or some other velocities. Frequent reports of relatively constant efficiency over a wide range of velocity suggest that whatever velocities are effective are often constant in this range.

Also, fairly successful correlations which neglect design factors suggest that efficiencies may be generalized by consideration of the effects of Equations (20) and (22) only.

EXPERIMENTAL WORK

Apparatus

A fractionating column of 18-in. O.D. and 300 lb./sq. in. gauge rating was used. It contained three trays at 2-ft. spacing, with ten 3-in. bubble caps a tray on 4½-in. equilateral triangular centers. The equipment was originally the same as was used by Shilling, Beyer, and Watson (*18*), and further constructional details may be obtained from their paper. Changes made in their equipment will be noted.

The sampling arrangements intended to measure point efficiencies directly proved entirely inadequate at rates higher than those used in the prior work, probably because of the unpredictable blowing of the liquid away from the sampler. The vapor chimney was therefore removed and the vapor sampler made movable, to make vapor-composition traverses possible. Late in the work the liquid sampler (Shilling x_e)

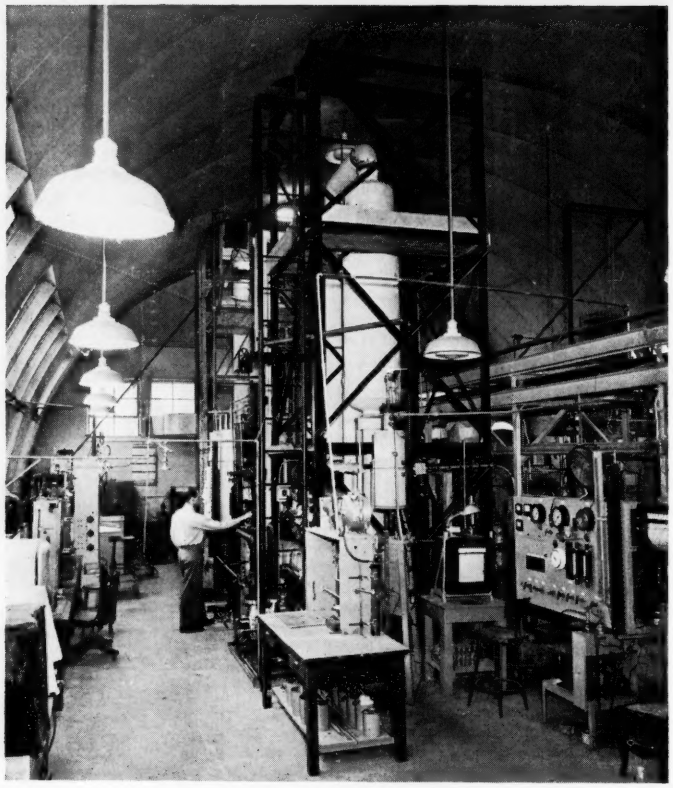

Fig. 1. Over-all view of apparatus.

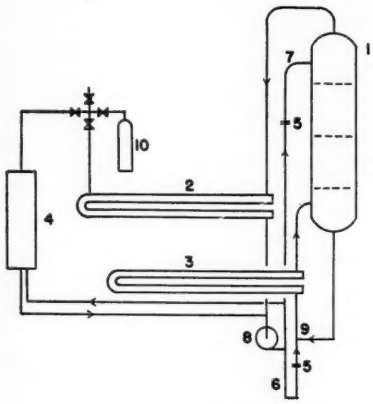

Fig. 2. Flow diagram.

1. Fractionating column
2. Condenser
3. Reboiler
4. Surge tank
5. Orifice meters
6. Product line
7. Reflux line
8. Reflux pimp
9. Jet pump connection
10. Nitrogen supply

was moved so as to draw liquid from just downstream of the inlet weir. The composition of this sample was the basis of the fractional mixing.

For some of the later runs a hinged gate was installed above the outlet weir on the middle tray only. In the closed position it raised the weir height to 2 in. Weir length was reduced to 6 in. to allow room for the supports.

For studying the effect of vapor velocity, the relation between slot velocity and superficial velocity was changed markedly by blocking flow through 40% of the slots. All the liquid was still forced to flow past the active slots. The top two trays were modified identically. The three caps on the east side (weirs were on north and south sides) were plugged in the risers, and a sheet-metal dam was installed to prevent liquid from flowing past these caps. On the west side the two caps nearer the outlet weir had half their slots facing outward blanked. Dams were built to prevent liquid flow past the inactive slots. Sheet-metal inserts in the risers for these half-blanked caps cut the flow area in half. Asbestos rope was used to seal the dams.

Changes and additions to auxiliary equipment increased the capacity for condensation, reboiler circulation, and pumping.

A general view of the equipment is shown in Figure 1.

Procedures

Figure 2 is a flow diagram of the equipment as operated. With this arrangement steady conditions were possible at either total or partial reflux without a large inventory of charge stock.

Reflux temperature was controlled by a steam jacket on the reflux, the steam being controlled by a globe valve. To make the top plate comparable to the middle plate, it was attempted to return reflux at just below the bubble-point temperature. When this condition could not be achieved, and it appeared that top-plate efficiencies were adversely affected, they were not plotted with the others. Pressure was controlled by opening the condenser vents to the atmosphere for operation or by closing the vents and introducing nitrogen for other pressures. Flows were controlled by globe valves. Rates were determined from the pressure drops across orifices, as measured by mercury manometers. Valves in the manometer leads were opened early in the run to ensure that liquid in the leads was the same as reflux.

Samples were drawn at rates which were small fractions of the total rates, so as not to disturb the steady-state conditions. Unless something interfered, all runs were checked by separate sets of samples and readings of instruments at least ½ hr. apart. The first set of samples was generally not taken until conditions had been reasonably steady for at least 1 hr. It was necessary to adjust flows and heat input by trial to get the desired conditions.

Ethanol–water samples were analyzed by density, which was measured by a Westphal balance of chainomatic type at room temperature. Errors due to change in composition during this operation and during sampling were shown experimentally to be insignificant. Data from Perry (*14*) were used to find the composition.

Acetone–water samples were also analyzed by density, with the same balance, but at 0°C. to minimize errors due to the higher volatility. Data of Schwers (*17*) were used to find the concentration corresponding to a given density.

Ethylene dichloride–toluene samples were analyzed by means of an Abbé refractometer. Data of Jones et al. (*8*), together with direct experimental data, were used to determine the composition from the refractive index.

CALCULATIONS

Ethanol-water

Flow rates for all systems were calculated from standard orifice equations, with upstream velocity head considered, a discharge coefficient of 0.61, which was determined by calibration, being used. Liquid in the manometer leads was assumed to be reflux at room temperature. Flowing liquid temperature was measured, and the density at that temperature used. Reflux and "product" rates were obtained in this way; other rates were calculated by material and energy balances.

Slot velocities were based on total slot area, as the slots were generally fully open, and major interest was in conditions where they were. "Allowable" velocities were calculated by the method outlined in Perry (*14*).

It has often been pointed out that the equilibrium data used in calculating plate

efficiencies are fully as important as the experimental data themselves. Consequently much effort was directed toward examining and comparing data from different sources. Rao (*15*) has obtained excellent averaging of all available equilibrium data on the ethanol-water system, using Clark equations developed by the method of least squares. In addition, he tested the equations by calculating temperatures and using the Gibbs-Duhem relation. His equations are

$$Y = 0.8853X + 0.9701 \text{ (above conjugate)}$$

$$Y' = 0.07755X' + 0.5709 \text{ (below conjugate)}$$

The conjugate point is at $x = 0.2796$.

Another test made by the authors was based on the thermodynamic equation

$$\int_0^1 \ln \frac{\gamma_1}{\gamma_2} dx = 0$$

This expression has the advantage of not requiring evaluation of any slopes, which makes results of the usual Gibbs-Duhem form uncertain. The value of the integral was 0.0045 instead of zero. Thus, if the error is constant for the whole composition range, γ_1/γ_2 is high by 0.45%. This is the error in relative volatility, with the error in y^* being smaller yet. Apparently Rao's equations give the best representation of ethanol-water equilibrium now available.

Another advantage of this manner of expressing data is that the mathematical form allows direct evaluation of the integral of Equation (4). In collaboration with Rao, the authors computed values of this integral for various arbitrary values of the parameters and plotted them as illustrated in Figure 3. The value of the integral between any two points for a given y is quickly found as the difference between the corresponding ordinates on the plot. A more detailed large-scale plot was used in the actual calculations of Lewis case I efficiencies by Equation (4).

A Ponchon-Savarit diagram was constructed for the ethanol-water system by transposing the data of White (*20*) to a molar basis. Murphree vapor-plate efficiencies were calculated by use of the Ponchon-Savarit diagram to find the vapor compositions from the liquid compositions, which were found to be more reliable than measured vapor concentrations, and by use of the Clark equations to find the equilibrium values.

Acetone-water

Data of the International Critical Tables (*7*) were used to construct a Ponchon-Savarit diagram, employed to find enthalpy values as well as vapor compositions.

Clark equations were developed by averaging the data of Brunjes and Bogart (*1*); Othmer, Friedland, and Scheibel (*13*); Othmer and Benenati (*12*); and York and Holmes (*21*). The results were

$$Y = 1.151X + 4.485 \text{ (above conjugate)}$$

$$Y' = 0.02553X' + 0.1532 \text{ (below conjugate)}$$

The conjugate is at $x = 0.4464$.

Testing with the Gibbs-Duhem equation indicated that these equations are slightly less consistent than the best experimental data. The value of

$$\int_0^1 \ln \frac{\gamma_1}{\gamma_2} dx$$

was 0.053. The error is unfortunately large, but the calculated curve falls within the experimental-data band at all concentrations. Because of the convenience of the expressions, they were used.

Figure 4 gives the integral of Equation (4) for the acetone-water system.

Other calculations were parallel to those for the ethanol-water system, except that Equation (12), or its equivalent for the middle tray, was used to find the Lewis case I efficiency. Equation (6) was used for the true local efficiency for actual liquid concentrations, which was spot-checked by Equation (13).

Ethylene Dichloride–toluene

This system was assumed ideal wherever enthalpy data were required. Necessary data were obtained from Perry (*14*), Lange (*9*), and A.P.I. Project 44 (*2*).

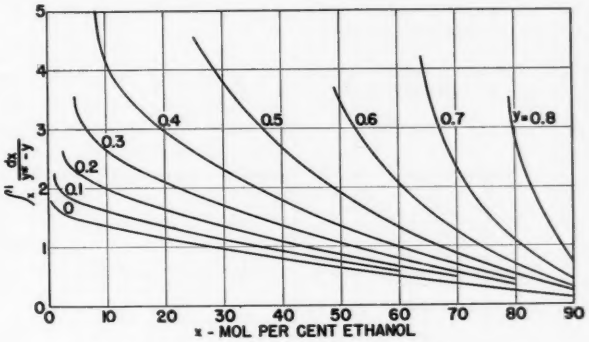

Fig. 3. $\int_x' dx/(y^* - y)$ for ethanol–water system.

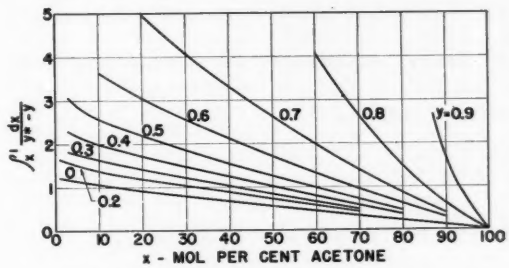

Fig. 4. $\int_x' dx/(y^* - y)$ for acetone–water system.

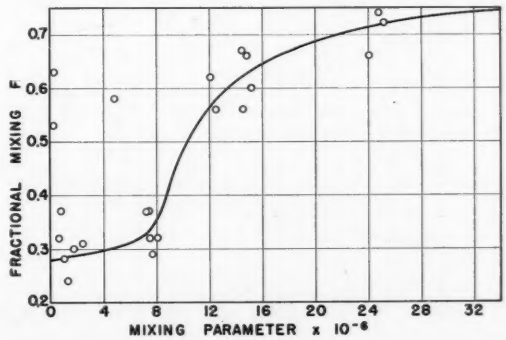

Fig. 5. Effect of the mixing parameter [Equation (1)] on fractional mixing for the ethylene dichloride–toluene runs.

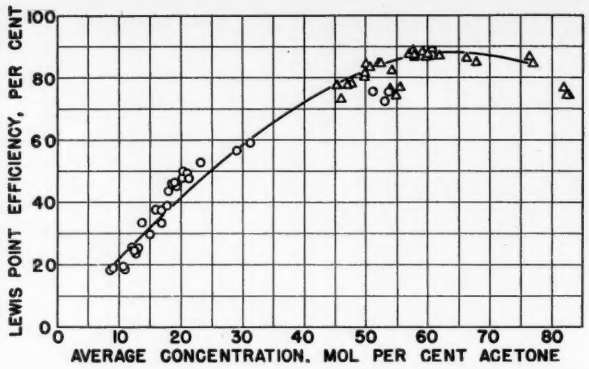

Fig. 6. Acetone–water runs, concentration study. Triangles are for top plate, circles for middle plate; reflux ratio $L_0/D = \frac{1}{2}$; atmospheric pressure; vapor rate about 24 lb.-moles/hr.; Lewis case I assumptions made; static seal $\frac{1}{2}$ in.

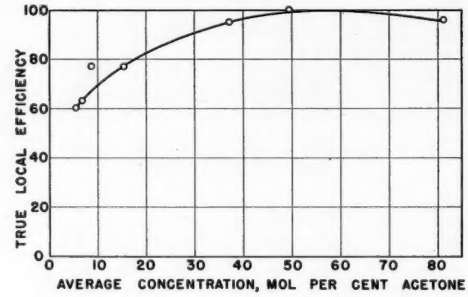

Fig. 7. Effect of concentration of acetone on true local efficiency.

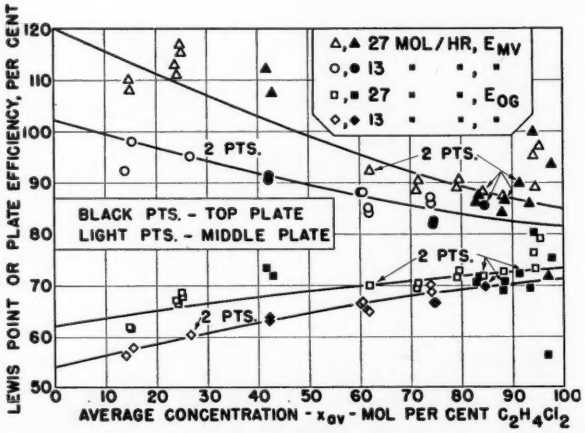

Fig. 8. Effect of concentration of ethylene dichloride on Lewis point efficiency and on plate efficiency.

Jones, Schoenborn, and Colburn (*8*) found that this system follows Raoult's law. Accordingly for atmospheric pressure, equilibrium data were calculated with ideal mixtures and ideal gas vapors assumed. For higher pressures corrections to vaporization equilibrium constants were combined as a correction to relative volatility by use of the generalized charts of Hougen and Watson (6). Relative volatilities were plotted and used to calculate point efficiencies by Equation (10).

Vapor compositions were found from liquid compositions by a McCabe-Thiele diagram.

When the composition just downstream of the inlet weir was available, the true local efficiency of the middle tray was calculated by Equation (13) and/or (14).

The vapor velocity for the mixing correlation was based on the plate free area, defined as the total area between the weirs minus the area of the caps.

The liquid holdup on the tray was assumed to be the plate free area times the height of the weir. The true holdup is probably roughly proportional to this term for a plate having a baffle by the outlet weir, as this one did.

RESULTS

Mixing of Liquid

Figure 5 shows that the mixing of the liquid was always between one quarter and three quarters complete on this tray; that is, the concentration change across the inlet weir was one quarter to three quarters the total between the two plates. (This maximum mixing held to a value of the mixing parameter of 140 million, which is well beyond the range plotted.) The fractional mixing F may theoretically vary from zero to one. Zero corresponds to a Lewis plate; one to a Murphree plate. Such data were obtained for the system ethylene dichloride–toluene only, for one particular tray. Conditions which were varied included vapor and liquid flow rates, pressure, temperature, and weir height.

The accuracy of the mixing correlation is questionable. The band of points is rather wide, but this is more likely the result of experimental errors than of ascribing the wrong effects to the different variables. Thus instantaneous concentrations at a point were found, under some conditions, to vary 5% or more within a matter of seconds. Eddying is known to occur near weirs, and there is no assurance that the sampler was in the same position in the eddy under different conditions. This correlation should not be applied indiscriminately to other trays until the effect of tray size and geometry is studied. The evidence is strong, however, that under no normal operating conditions does this plate resemble either a Murphree or a Lewis plate. It is in between the two.

Mixing of Vapor

Variations in the composition of the vapor entering a tray appear to have little effect. Although composition traverses under conditions of appreciable liquid entrainment gave erratic results, lower rate runs showed nearly uniform composition. Vapor composition may vary more for plate spacings less than the 2 ft. of this column. The Lewis case III plate, however, in which the vapor is assumed unmixed, generally shows little advantage over the case I plate, in which the vapor is assumed completely mixed.

Concentration

Acetone-water. A low concentration of acetone in water gives a low Lewis case I efficiency, as shown in Figure 6. The drop at low concentrations has been attributed to the increase in the liquid film resistance from the higher liquid viscosity and larger value of the slope of the equilibrium line. The larger slope is analogous to a lower solubility of acetone vapor. Equation (16) shows its effect.

The effect of concentration of acetone on true local efficiency, in which liquid mixing is taken into account, is less pronounced, as shown in Figure 7. Thus the large variation of Lewis case I efficiency is the result not only of the effect of the slope m on the liquid-film resistance, but also of the effect of slope m on the calculation of efficiencies from experimental measurements.

The data of Shilling, Beyer, and Watson (*18*) confirm this conclusion. Their plot of point efficiencies, i.e., those determined from liquid and vapor samples at the center of the tray, shows much less variation than does the plot of local efficiencies, i.e., those determined from exit liquid samples by means of the Lewis analysis.

The curve in Figure 7 was derived by assuming that the liquid was three quarters mixed, which was indicated by the mixing correlation based on ethylene dichloride and toluene data. A few points falling on the Lewis case I curve were recalculated to give the new curve. Both the ordinate and abscissa for a given run will be different from those in Figure 6. The abscissa is the average liquid composition on the tray, consistent with the assumptions used in deriving the efficiencies. The assumption that local efficiency is constant across the tray, which was necessary to perform the integration, is obviously not true, because composition may vary widely across the tray. This method of plotting is intended to cancel out as much of the error introduced as possible. It has the property of moving points out much farther from the ordinate axis at low concentrations than when exit liquid concentration is the abscissa.

Lewis case I efficiencies are easiest to correlate, because the spread of liquid composition is the greatest. Hence the average value of the equilibrium vapor composition is least dependent on experimental liquid compositions.

Ethylene Dichloride–toluene. The curves of Figure 8 show the trends anticipated from the two-film theory and the Lewis analysis. Thus a large slope of the equilibrium line (low concentration) corresponds to a large Murphree efficiency but a small Lewis case I efficiency. Equation (7) predicts the former effect; Equations (17) and (15) predict the latter.

A plot of true local efficiencies, as in Figure 9, however, is quite surprising. The 27 moles/hr. data show that this efficiency is definitely higher at low concentrations than at high. Equation (17) is unable to predict this. One must assume that the interfacial area terms of Equation (15) are responsible. In contrast to the 27 moles/hr. data, the 13 moles/hr. data show the expected trend.

To find whether the 27 moles/hr. trend might be explained by errors in the experimental mixing data used, the true local efficiencies at 0 and 100% ethylene dichloride were calculated from extrapolated Lewis case I efficiencies and the mixing correlation. These true local efficiencies were 0.91 and 0.81, respectively, confirming the previous conclusion. The extrapolation, however, was somewhat uncertain.

Vapor Velocity

Acetone-water. The slot velocity appears to be more important than superficial column velocity to plate performance, as shown in Figures 10 and 11. They include efficiencies in the concentration range of 60 to 75% acetone, where the effect of concentration was small. Also, the mixing correlation indicates that the liquid was about three quarters mixed in all these runs. Hence it is permissible to show the trends by plotting any convenient efficiency.

Figure 10 is derived from the traditional method of finding the capacity of a column, based on the idea that entrainment causes the loss in efficiency above the normal operating range. The plot shows very clearly that more is involved than entrainment, because otherwise a single line should be obtained for both sets of data. The comparability of the two sets of data is established by the check obtained at low rates.

Figure 11 is based on the idea that "coning," the pushing back of liquid from the slots, is more likely to be the limiting condition. Here the two sets of data form a single line, establishing $\rho_G V_S^2$ as a better criterion of the effect of vapor velocity on efficiency.

Ethanol-water. The preferability of the slot-velocity-head criterion is confirmed by Figure 12. The data fall near a single curve. They would not for a superficial velocity-head criterion. For a given slot velocity head, the superficial velocity head is 36% as much for partial slot operation as for total slot operation.

The efficiencies plotted were for the concentration range of 30 to 40% ethanol, where concentration has little effect. The

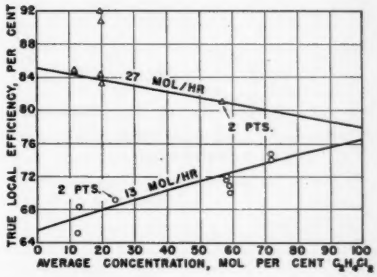

Fig. 9. Effect of concentration of ethylene dichloride on true local efficiency.

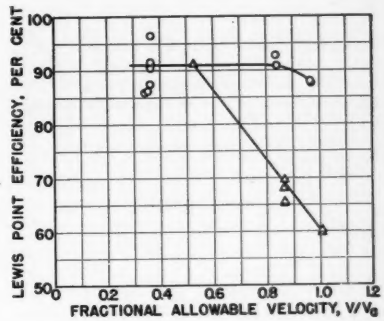

Fig. 10. Effect of slot velocity on Lewis point efficiency.

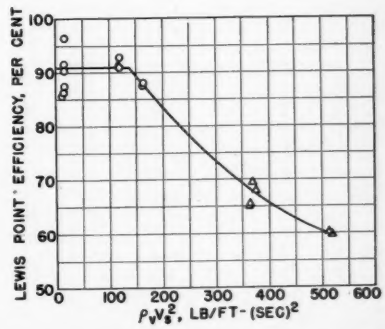

Fig. 11. Acetone–water runs, vapor velocity study. For circles, all slots were active; for triangles, 40% of slots were blocked; same data as Fig. 10.

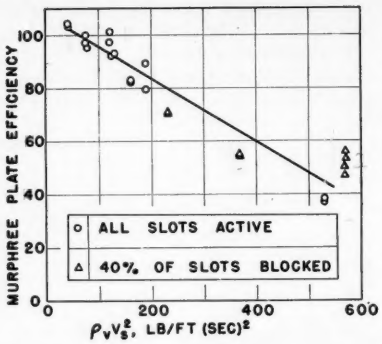

Fig. 12. Correlation of Murphree plate efficiency for ethanol–water with slot-velocity head.

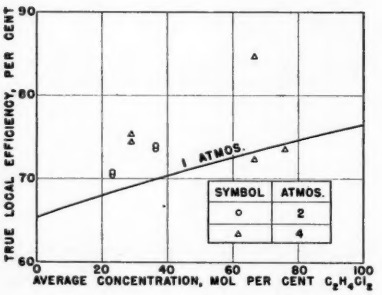

Fig. 13. Effect of pressure on true local efficiency for ethylene dichloride–toluene.

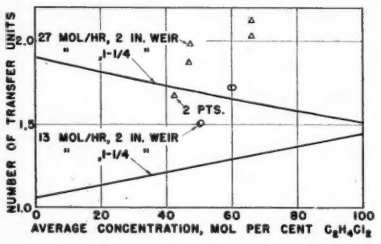

Fig. 14. Effect of liquid depth on true local efficiency for ethylene dichloride–toluene.

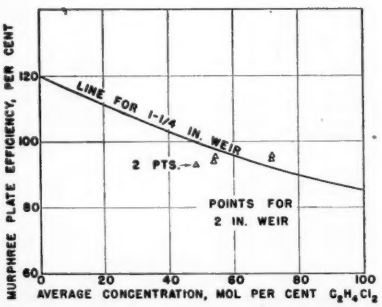

Fig. 15. Effect of liquid depth on Murphree plate efficiency for ethylene dichloride–toluene.

low reflux ratios used, which were necessary to get enough reboiler circulation, reduced the accuracy of these data.

At the highest slot velocity heads, total slot operation gave lower efficiencies. The greater entrainment was no doubt responsible.

Ethylene Dichloride–toluene. Efficiencies are higher at 27 moles/hr. (two thirds the "allowable") than at 13 moles/hr., as shown in Figures 8 and 9. This is in contrast to some other systems. Data taken in the study of pressure confirm that higher rates give higher efficiencies when the column is well below capacity.

Pressure

Increasing the pressure increases the true local efficiencies at constant rate and composition for the system ethylene dichloride–toluene, as shown in Figure 13 and Table 1.* This effect is attributed mainly to the lower kinematic viscosities of both the liquid and vapor phases. The slope, m, becomes lower at low concentrations, but higher at high concentrations as pressure rises. Figure 13 also gives the atmospheric pressure lines from Figure 9, with the points omitted to avoid confusion.

This study was hampered by the inability to get the desired vapor rates at the lower reboiler temperature differences and by the difficulties of operating at the ultimate heat transfer capacity. The experimental mixing data were erratic for the superatmospheric pressure runs, and so the correlation values of mixing were used in calculating the true local efficiencies.

Some anomalies appear in the data. These are mainly in the low separation regions of high concentration, where accuracy is poor. Also, the 2-atm. 27 moles/hr. data are not consistently above the 1-atm. data in this plot. Use of the experimental mixing values in place of the correlation on values, however, would make the 2-atm. data higher.

Because of the large effects of vapor rate and concentration, pressure effects should not be inferred unless the other conditions are constant.

Liquid Depth

Increasing the liquid depth increases the true local efficiency. The number of transfer units is shown in Figure 14 for two weir heights, namely, 1¼ and 2 in. The corresponding static seals are ½ and 1¼ in.

Gilliland (*16*) has suggested that the number of transfer units should be taken as proportional to the square root of the average slot submergence. This is not a bad approximation for these data.

The efficiency that really counts, however, was not increased at all for the 27 moles/hr. runs. The degree of mixing increased as well as the true local efficiency, and so the Murphree vapor efficiency received no net benefit. From an operational standpoint, the higher weir would be of no advantage. To illustrate this point, the 2-in. weir data are plotted in Figure 15 together with the 1¼-in. weir line from Figure 8.

*See footnote on page 18.

QUANTITATIVE CORRELATIONS OF RESULTS

Equations from the section on theoretical development have been successfully used to predict variations of performance for constant vapor velocity data. Illustrations are given below for changes in composition and pressure.

A single efficiency point cannot be separated into individual film resistances and Equation (17) applied. However, if the modes of variation of resistances are known, the resistances at another point may be expressed in terms of those of the first, and the two equations may be solved simultaneously.

In total reflux runs the vapor entering a tray has the same composition as the liquid leaving the tray. These compositions are used to estimate properties in the following calculations.

For analysis of the 13 moles/hr. data of Figure 12, subscript 0 refers to conditions at 0% ethylene dichloride. Equation (17) becomes

$$0.943 = \frac{1}{N_{GO}} + 2.12\left(\frac{1}{N_{LO}}\right) \quad (24)$$

Subscript 1 identifies any other condition for the constant rate data. Equations (20) and (22) lead to the relation

$$\frac{1}{N_{OG_1}} = \frac{1}{N_{G_0}}\left(\frac{P_{t_0}}{P_{t_1}}\right)^{1/3}\left(\frac{\nu_{G_1}}{\nu_{G_0}}\right)^{2/3} + \frac{m_1 G_1}{L_1}\left(\frac{1}{N_{L_0}}\right)\left(\frac{V_{L_1}}{V_{L_0}}\right)\left(\frac{\nu_{L_1} D_{L_0}}{\nu_{L_0} D_{L_1}}\right)^{2/3} \quad (25)$$

Assuming liquid diffusivities constant and substituting numerical values at 100% ethylene dichloride yield

$$0.690 = \frac{1}{N_{G_0}}\left(\frac{3.20}{3.05}\right)^{2/3} + 0.435\left(\frac{1}{N_{L_0}}\right)\left(\frac{84.0}{118}\right)\left(\frac{0.35}{0.32}\right)^{2/3} \quad (26)$$

Solving Equations (24) and (26) simultaneously gives values for $1/N_{L_0}$ of 0.153 and for $1/N_{G_0}$ of 0.618.

If these values are used, Equation (25) will predict for 50% ethylene dichloride.

$$\frac{1}{N_{OG_1}} = 0.618\left(\frac{3.12}{3.05}\right)^{2/3} + 0.856(0.153)\left(\frac{101}{118}\right)\left(\frac{0.34}{0.32}\right)^{2/3} = 0.743$$

The corresponding value of E_{OGT} is 0.740, compared with the experimental value of 0.715.

This type of comparison is obviously dependent on the values used for the physical properties. Lack of knowledge about liquid diffusivities makes the liquid-phase resistance uncertain. This resistance is indicated, however, to vary from 35% of the total at 0% concentration down to 10% at 100% concentration.

For these data, liquid- and gas-phase kinematic viscosities varied in about the same ratio. A better check on the effect of kinematic viscosity will be to compare data at different pressures but at the same composition, provided the relative phase resistances are reasonably accurate. Because of the compressibility of the gas, its kinematic viscosity falls much more rapidly than that of the liquid. Variations of diffusivity can be predicted when only the temperature and pressure change.

The 27 moles/hr., 2-atm. curve is chosen to compare with the 13 moles/hr. atmospheric curve, because it is at about the same volumetric vapor rate. By Equations (20) and (23),

$$\frac{1}{N_{OG_1}} = \frac{1}{N_{G_o}}\left(\frac{P_{t_o}}{P_{t_1}}\right)^{1/3}\left(\frac{v_{G_1}}{v_{G_o}}\right)^{2/3} + \frac{m_1 G_1}{L_1}\left(\frac{1}{N_{L_o}}\right)\left(\frac{V_{L_1}}{V_{L_o}}\right)\left(\frac{\rho_{L_o} T_0}{\rho_{L_1} T_1}\right)^{2/3}\left(\frac{\mu_{L_1}}{\mu_{L_o}}\right)^{4/3} \qquad (22)$$

When the atmospheric values already determined at 0% ethylene dichloride are used, the over-all resistance at 2 atm. would be predicted as

$$\frac{1}{N_{OG}} = 0.618\left(\frac{1}{2}\right)^{1/3}\left(\frac{1.62}{3.05}\right)^{2/3} + 1.905(0.153)\left(\frac{123}{118}\right)\cdot\left[\left(\frac{0.781}{0.746}\right)\left(\frac{384}{410}\right)\right]^{2/3}\left(\frac{0.20}{0.25}\right)^{4/3} = 0.544$$

$$E_{OGT} = 0.841$$

The mixing correlation indicates that F is 0.30. The predicted Murphree vapor efficiency by Equation (14) is 155%, which may be compared with the extrapolated experimental value of 152%.

This research indicates that at least three types of data should be taken in future work, if possible: first, plate efficiencies; second, mixing data; and third, interfacial areas.

ACKNOWLEDGMENT

Financial support of the Shell Fellowship Committee, the Chemical Engineering Department of the University of Wisconsin, and the Wisconsin Alumni Research Foundation is gratefully acknowledged.

M. N. Rao helped in the treatment of equilibrium data and collaborated in the evaluation of integral functions for the system ethanol–water.

NOTATION

a = surface area per unit volume, sq. ft./cu. ft.
A, A', B, B' = constants in Clark equations
$A_a, A_b, A_c, A_d, B_d, B_b, B_c, B_d, c_1$, etc. = constants as defined
D = diffusivity
E_{MV} = Murphree vapor plate efficiency
E_{OG} = local efficiency by Lewis case I analysis
E_{OGT} = true local efficiency
f = Fanning friction factor
f_1, etc. = function
F = fractional mixing, concentration change across inlet weir divided by total change across plate,

$$F = \frac{X_n - X_e}{X_n - X_{n+1}}$$

G = mass velocity of vapor, lb.-moles/(hr.)(sq. ft.)
h = enthalpy of liquid, B.t.u./mole
H = enthalpy of vapor, B.t.u./mole
j_M = mass transfer factor
k_G = mass transfer coefficient, moles/(hr.)(sq. ft.)$(y_i - y)$
k_L = mass transfer coefficient, moles/(hr.)(sq. ft.)$(x - x_i)$
k_{OG} = mass transfer coefficient, moles/(hr.)(sq. ft.)$(y^* - y)$
L = mass velocity of liquid, lb.-moles/(hr.)(sq. ft.)
m = dy^*/dx, slope of equilibrium line
M = molecular weight
N_G = number of gas-phase transfer units
N_L = number of liquid-phase transfer units
N_{OG} = number of over-all transfer units, based on gas phase
P_t = total pressure
P_1 = vapor pressure, low boiler
P_2 = vapor pressure, high boiler
q = volumetric flow rate, cu. ft./sec.
T = absolute temperature
u = local velocity
V = superficial column velocity, ft./sec.
V_a = allowable superficial column velocity, ft./sec.
V_S = slot velocity, ft./sec.
V_G = molal volume, gas
V_L = molal volume, liquid
v_L = volume of liquid holdup on tray, cu. ft.
w = mass flow rate, lb./sec.
x = mole fraction, liquid
x_e = mole fraction in liquid, just downstream of inlet weir
X = mole ratio, liquid
y = mole fraction, vapor, average
y' = mole fraction, vapor, at a point
y^* = mole fraction, vapor, in equilibrium with liquid at that point
Y = mole ratio, vapor
Z = distance, vertical direction, ft.
α = relative volatility
γ_1 = activity coefficient, low boiler
γ_2 = activity coefficient, high boiler
λ = mG/L
μ = viscosity (dynamic)
ρ_V = density, vapor
ρ_L = density, liquid
ν = viscosity, kinematic

Subscripts

0, 1, 2, 3 = reflux, top, middle, bottom tray, for flow quantities, thermodynamic functions, and concentrations
n = number of tray, down from top
L = liquid
G = gas
OG = over-all, based on gas film
V = vapor
i = interface between phases
avg = average
l.m. = logarithmic mean
e = entering plate
$'$ = (prime) point condition

LITERATURE CITED

1. Brunjes, A. S., and M. J. P. Bogart, *Ind. Eng. Chem.*, **35**, 255 (1943).
2. Bur. Standards, "Selected Values of Properties of Hydrocarbons," U. S. Govt. Printing Office, Washington (1947).
3. Chilton, T. H., and A. P. Colburn, *Ind. Eng. Chem.*, **26**, 1183 (1934).
4. Clark, A. M., *Trans. Faraday Soc.*, **41**, 718 (1945); **42**, 742 (1946).
5. Gerster, J. A., A. P. Colburn, W. E. Bonnet, and T. W. Carmody, *Chem. Eng. Progr.*, **45**, 716 (1949).
6. Hougen, O. A., and K. M. Watson, "Chemical Process Principles," John Wiley and Sons, New York (1947).
7. "International Critical Tables," McGraw-Hill Book Company, Inc., New York (1926).
8. Jones, C. A., E. M. Schoenborn, and A. P. Colburn, *Ind. Eng. Chem.*, **35**, 666 (1943).
9. Lange, N. A., "Handbook of Chemistry," 4 ed., Handbook Publishers, Inc., Sandusky, Ohio (1941).
10. Lewis, W. K., *Ind. Eng. Chem.*, **28**, 399 (1936).
11. Murphree, E. V., *Ind. Eng. Chem.*, **17**, 747 (1925).
12. Othmer, D. F., and R. F. Benenati, *Ind. Eng. Chem.*, **37**, 299 (1945).
13. ———, D. Friedland, and E. G. Scheibel, unpublished paper.
14. Perry, J. H., "Chemical Engineers' Handbook," 3 ed., McGraw-Hill Book Company, Inc., New York (1950).
15. Rao, M. N., private communication, Andhra University, Waltair, India.
16. Robinson, C. S., and E. R. Gilliland, "Elements of Fractional Distillation," 4 ed., McGraw-Hill Book Company, Inc., New York (1950).
17. Schwers, F., *J. chim. phys.*, **9**, 15 (1911).
18. Shilling, G. D., G. H. Beyer, and C. C. Watson, *Chem. Eng. Progr.*, **49**, 128 (1953).
19. Van Krevelen, D. W., and P. J. Hoftijzer, *Chem. Eng. Progr.*, **46**, 29 (1950).
20. White, R. R., *Petroleum Processing*, **1**, 147 (1946).
21. York, R., and R. C. Holmes, *Ind. Eng. Chem.*, **34**, 345 (1942).

Presented at A.I.Ch.E. Houston meeting

Rate of Nitration of Benzene with Mixed Acid

R. D. BIGGS and R. R. WHITE

University of Michigan, Ann Arbor, Michigan

The rates of nitration of benzene by nitric acid in mixed acid to produce mononitrobenzene have been measured in well-emulsified reaction mixtures in the temperature range from 34° to 54°C. The acid-phase compositions ranged from 1.6 mole % nitric acid and 27 mole % sulfuric acid to 35 mole % nitric acid and zero % sulfuric acid; the organic-phase composition ranged from 4 to 95 mole % benzene, and the relative extent of the acid and organic phases was varied from 25 to 80 volume % acid phase.

The reaction rate based on the total volume of the reacting mixture is shown to be a function of the phase compositions, temperature, and volume % of acid phase.

The nitration of aromatic hydrocarbons has been the subject of numerous investigations since nitrobenzene was first synthesized in 1834 from benzene and fuming nitric acid (*13*). However, only a few recent investigators have determined data which are useful for engineering applications (*3, 4, 8, 9, 11, 12, 14*). The uncertainties inherent in the reaction-rate data available at the present time led to this investigation of the variables affecting the rate of nitration of benzene in a continuous, stirred-pot reaction system.

EXPERIMENTAL EQUIPMENT

A continuous-flow, stirred-pot reaction system was used to study the variables affecting the rate of nitration of benzene with mixed acid. This type of apparatus possesses certain advantages that a batch reaction system does not have: that is, (1) large samples can be collected without affecting the reacting system, and (2) neither the reaction rate nor the reactor compositions change with time when steady state conditions are achieved, the reaction rate being calculated from the steady state material balance. Figure 1 is a flow diagram of the apparatus.

As shown in Figure 1, mixed acid and benzene flowed by gravity from the constant-head reservoirs (*12*), *A* and *B*, through the flow meters *C* and *D* and dripped into the feed lines *E* and *F*. The Pyrex-glass capillary-tube flow meters *C* and *D* were used to indicate instantaneous flow rates of the benzene and acid feeds for control purposes. The feeds drained through the feed lines into the reactor *G*. The stirrer,

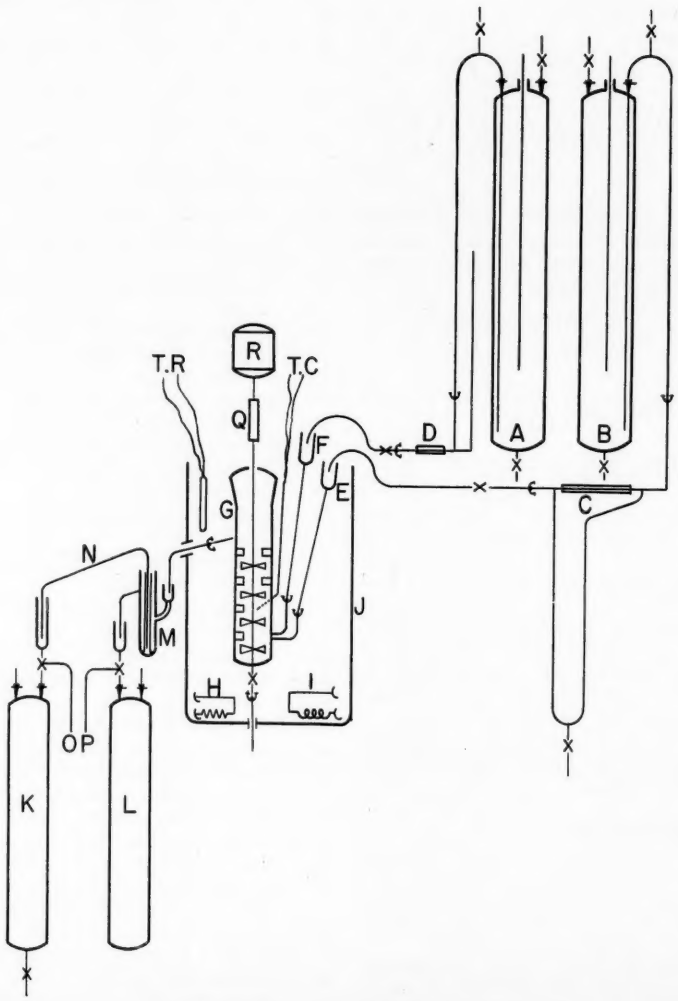

Fig. 1. Schematic diagram of equipment.

R. D. Biggs is with Ethyl Corporation, Baton Rouge, Louisiana.

driven by a variable-speed motor R through a sleeve bearing Q, kept the acid and organic phases in the reactor well emulsified. The product from the reactor overflowed into the separator M, where the two phases separated completely. The lighter organic phase rose to the top in the separator and overflowed into the organic-product receiver L. The heavier acid phase settled to the bottom in the separator, where it was drained by the syphon tube N into the acid-product reservoir K.

A large glass battery jar J contained water which was maintained at a constant temperature by circulating cooling water through the coils I and by intermittently heating with an electric heater H. The reactor temperature was measured by a copper-constantan thermocouple TC which extended into the center of the reactor.

With the exception of the stirrer assembly in the reactor all the apparatus was constructed of glass. Flow rates were determined by measuring the difference in volume over a measured period of time in each of the calibrated reservoirs. Samples of the feed streams were taken from the drain in the bottom of each feed reservoir. Product samples were taken through the side tubes O and P.

A detailed drawing of the reactor is shown in Figure 2. The reactor was constructed of Pyrex glass and was designed to maintain a uniform emulsion of the acid and organic phases and a high degree of circulation of the contents.

MATERIALS

Reagent-grade sulfuric and nitric acids manufactured by the J. T. Baker Chemical Company were mixed with distilled water to obtain the desired feed-acid concentration. The nitric acid was water white and contained no lower oxides of nitrogen detectable by chemical analysis.

Reagent-grade benzene manufactured by the General Chemical Division of Allied Chemical and Dye Corporation was used in all the experiments. The minimum freezing point reported by the manufacturer corresponds to a minimum purity of 99.53 mole %.

Table 1. Operating Conditions

Run	Reaction liquid volume, Mi	Acid phase in reaction mixture: Reactor vol., %	Acid phase in reaction mixture: Overflow vol., %	Acid feed rate, g./hr.	Benzene feed rate, g./hr.	Acid product rate, g./hr.	Organic product rate, g./hr.	Reaction rate, g.-mole/(hr.)(liter) total vol.
1*	416	59.2	58.5	690	228	625	301	3.17
2*	396	73.5	58.2	674	211	594	291	3.54
3*	403	58.8	58.4	585	191	521	252	2.98
4*	413	56.4	58.0	642	205	564	277	3.08
5*	402	56.1	58.8	660	212	600	285	3.22
6*	404	57.4	57.5	1,103	431	1,067	462	1.398
7*	405	59.5	60.8	686	234	667	255	0.957
8*	341	30.2	33.5	294	288	270	314	1.323
9*	350	40.0	41.8	401	266	358	302	1.780
10	355	51.2	53.5	596	219	516	306	4.57
11	345	52.7	54.0	609	214	519	303	4.86
12	350	62.0	63.4	729	239	714	249	0.249
13	324	55.6	54.8	487	217	457	254	1.175
14	323	50.8	53.5	416	215	404	233	0.503
15	322	58.7	58.0	570	253	562	265	0.265
16	327	60.4	60.4	772	284	753	304	0.575
17	344	58.2	62.2	534	194	527	211	0.771
18	328	42.6	46.8	443	274	433	289	0.666
19	336	78.6	78.2	940	139	927	164	1.155
20	324	35.5	42.1	302	229	299	240	0.468
21	323	25.0	31.7	302	345	287	357	0.470
22	337	60.8	63.5	567	175	549	198	1.138
23	328	65.5	64.4	575	184	551	213	0.995
24	318	64.4	63.4	429	159	426	162	0.0648
25	332	55.4	56.8	561	198	503	254	2.91
26	324	61.1	60.4	544	194	534	206	0.424
27	312	64.1	61.8	506	185	494	194	0.289
28	334	54.5	54.5	548	197	473	274	4.57
29	326	52.8	53.0	501	203	434	264	2.73
30	341	70.7	72.3	741	118	670	192	3.70
31	306	26.1	28.1	324	405	294	443	2.09
32	312	32.7	36.8	421	319	376	368	2.69
33	339	77.6	80.2	806	80.6	747	142	2.86
34	299	29.8	35.5	481	412	431	472	3.33

*Runs 1 to 9 were made with old reactor.

EXPERIMENTAL PROCEDURE

In each experimental run the reaction system was brought to steady state conditions by operation for about 2½ hr. at a constant reactor temperature and with constant feed rates. The approach of the or-

ganic-product density to a constant value within ±0.1% served as an indication of the approach to steady state conditions.

After steady state conditions had been achieved, samples of the acid- and organic-product streams were collected for density measurement and analysis. After the samples were collected, the total volume of the emulsion and the volume of the acid phase in the reactor were measured.

Standard methods for analysis were used for the total acid, nitrous acid (*15*), and nitric acid (*10*). The sulfuric acid was calculated as the difference between the percentage of total acid and the percentage of nitric acid. The organic-product sample was washed with water, and the benzene was determined by density measurement after the sample was dried with calcium chloride. A qualitative test was made for dinitrobenzene (*2*, *6*). The nitric and sulfuric acid content of the organic product was determined from the wash water by the foregoing methods.

Neither nitrous acid nor dinitrobenzene was detected in any of the runs.

EXPERIMENTAL RESULTS

The effects of agitation, phase composition, phase ratio, and temperature on the rate of nitration of benzene with mixed acid were investigated. Among the thirty-four runs the agitator speed was varied from 1,290 to 2,810 rev./min., the volume percentage of acid phase from 25 to 79, and the temperature from 34.6° to 53.7°C. The acid-phase composition was varied from 35 mole % nitric acid and 0% sulfuric acid to 1.6 mole % nitric acid and 27 mole % sulfuric acid. The organic-phase composition ranged from 4 to 97 mole % benzene.

Table 2. Analytical Data

	Acid feed composition, mole %		Acid-product composition, mole %		Organic-product composition, mole %				Benzene, mole % acid-free
Run	HNO_3	H_2SO_4	HNO_3	H_2SO_4	HNO_3	H_2SO_4*	C_6H_6	$C_6H_5NO_2$	basis
1	15.4	23.8	5.36	24.1	9.21	trace	48.8	42.0	53.8
2	15.0	24.5	4.70	24.9	8.91	0.005	43.8	47.3	48.1
3	15.1	24.6	4.64	24.9	8.69	trace	44.8	46.5	49.1
4	15.0	24.7	4.59	24.9	8.22	0.052	47.1	44.6	51.4
5	15.0	24.7	4.64	25.1	8.31	0.062	47.6	44.0	52.0
6	5.72	24.9	3.32	24.9	1.76	0.033	88.2	9.99	89.8
7	5.69	24.7	3.08	24.6	1.85	0.028	85.5	12.6	87.2
8	12.1	24.8	4.11	25.0	2.52	0.054	85.4	12.0	87.7
9	12.1	24.8	4.17	25.0	3.45	0.068	78.8	17.7	81.7
10	18.0	27.1	3.06	27.2	7.37	0.029	39.0	53.6	41.7
11	18.0	27.1	3.15	27.2	7.80	0.010	35.8	56.4	38.8
12	15.5	14.0	14.7	14.0	2.92	0.019	94.2	2.87	97.0
13	35.7	4.29	30.5	4.19	10.2	0.027	77.5	12.3	86.3
14	38.9	0	35.1	0	5.79	0	88.7	5.56	94.2
15	36.2	0	34.3	0	3.79	0	93.7	2.53	97.4
16	23.3	10.1	21.4	10.1	4.70	0.026	90.4	4.92	94.8
17	9.70	21.0	7.07	21.1	3.18	0.034	86.4	10.4	89.3
18	9.64	21.0	7.19	21.1	2.45	0.008	91.5	6.06	93.8
19	9.39	20.7	7.38	20.9	5.78	0.033	73.8	20.4	78.4
20	9.73	20.9	7.06	20.7	2.14	0.022	92.8	5.06	94.8
21	9.41	21.2	7.00	22.2	1.96	trace	94.7	3.38	96.4
22	9.73	21.2	6.11	21.0	4.06	trace	79.5	16.4	82.9
23	39.0	0	34.2	0	9.08	0	78.3	12.6	86.2
24	29.7	0	29.1	0	1.88	0	97.1	1.00	99.0
25	13.9	23.1	4.96	23.4	7.06	trace	57.5	35.4	61.9
26	13.9	15.0	12.4	15.1	3.42	0.052	91.2	5.33	94.5
27	24.3	6.69	23.6	6.49	3.52	trace	92.9	3.56	96.2
28	15.6	26.3	1.59	26.6	4.14	trace	38.3	57.6	39.9
29	19.6	17.6	9.83	18.1	11.0	trace	58.7	30.3	65.9
30	15.3	24.8	5.84	25.0	15.9	0.086	13.4	70.7	15.9
31	15.4	24.8	4.38	25.6	2.90	0.012	85.1	12.0	87.6
32	15.4	24.8	4.66	25.2	4.14	trace	76.3	19.6	79.4
33	14.2	24.5	7.43	24.2	21.3	0.016	4.34	74.4	5.59
34	16.1	24.8	5.03	25.2	4.36	trace	77.6	18.1	81.1

*Any quantity <0.005 wt. % was reported trace.

ANALYSES

The following analyses were made:

A. Acid feed
   1. Total acid
   2. Nitric acid

B. Acid product
   1. Total acid
   2. Nitric acid
   3. Nitrous acid

C. Organic product
   1. Total acid
   2. Nitric acid
   3. Nitrobenzene
   4. Dinitrobenzene (qualitative test)

Tables 1 and 2 present the operating conditions and analytical results, respectively, which were calculated for the thirty-four runs. Material balances for the over-all material flow, sulfur, and nitrogen were calculated for each run. The maximum deviation for the nitrogen balance was 4.1%. The majority of all the material balance deviations was less than 2.0%. Detailed sample calculations of the experimental data recorded in Tables 1 and 2 are available (*1*).

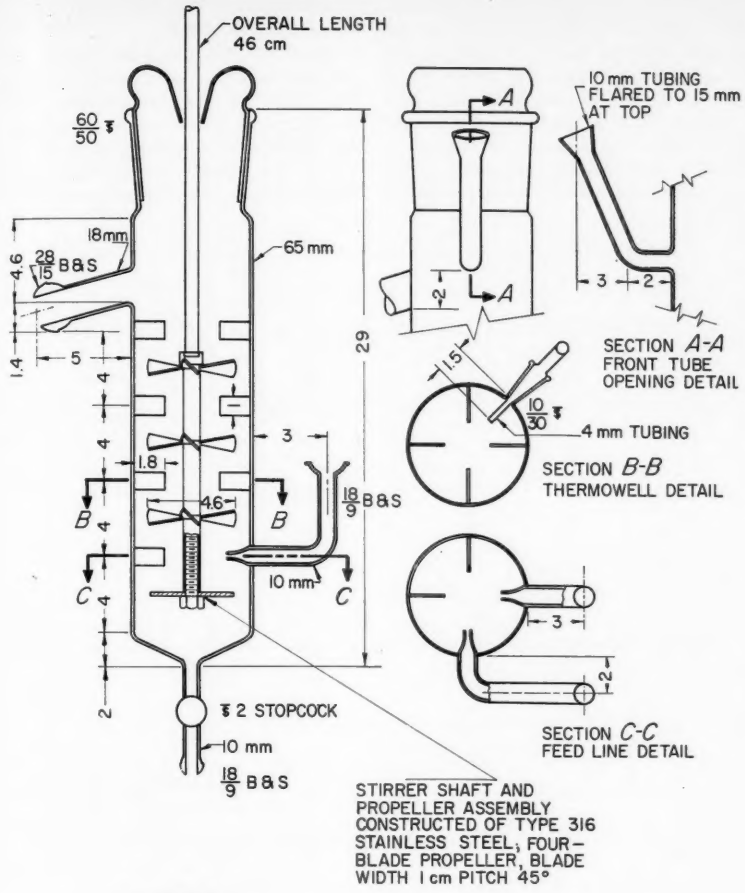

Fig. 2. Reactor.

DISCUSSION

Test for Steady State Conditions

Run 1 served to justify the basis for steady state conditions used for the majority of the runs. After the densities of two successive organic samples agreed within the set limits for steady state operation, samples were taken of the organic and the acid products. The operation of the equipment was continued for an additional hour, whereupon a second set of samples was collected.

The uniformity of the emulsion in the reactor during steady state operation is indicated by the agreement for most of the runs of the volume percentage of acid phase measured in the reactor and that calculated from the product streams. Further evidence of uniformity was the agreement of the analyses of acid-phase samples from the reactor and from the acid-product stream.

Effect of Agitation

The over-all reaction between benzene and nitric acid in mixed acid is the sum of the homogeneous reactions in the acid and the organic phases. Previous studies of aromatic nitration (*11, 12*) indicated that the reaction is essentially irreversible; therefore, the over-all reaction may be written

$$R = R_A + R_O \tag{1}$$

$$R = k_A a_{AN} a_{AB} \frac{V_A}{100} + k_O a_{ON} a_{OB} \frac{V_O}{100} \tag{2}$$

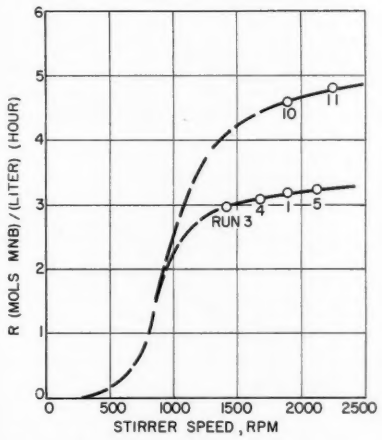

Fig. 3. Effect of agitation upon reaction rate.

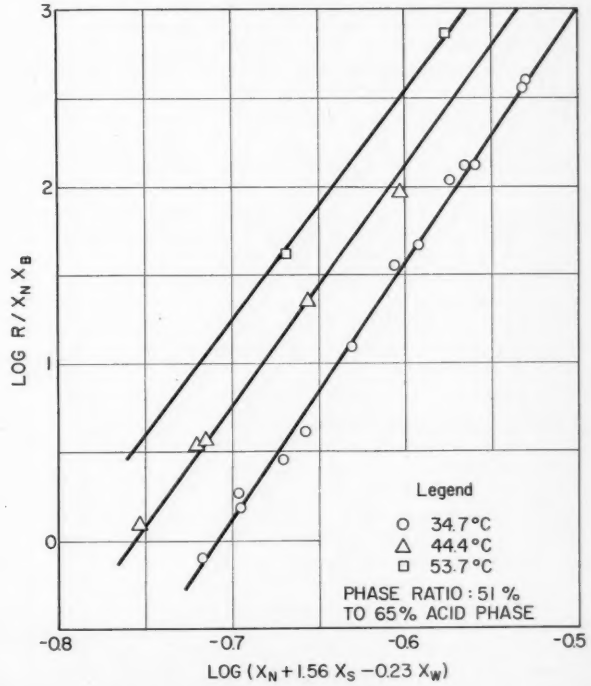

Fig. 4. Reaction-rate–composition correlation.

Under steady state conditions benzene transfers into the acid phase at the same rate as it is consumed in that phase by chemical reaction. Similarly, the nitric acid transfers into the organic phase at the same rate as it is consumed in the organic phase. This situation can be expressed mathematically as

$$R_O = K_N(a_{AN} - a_{ON}) \qquad (3)$$

$$R_A = K_B(a_{OB} - a_{AB}) \qquad (4)$$

Equation (3) represents the mass transfer of nitric acid, and Equation (4) represents the mass transfer of benzene.

Substituting Equations (3) and (4) into (2) gives

$$R = \left[k_A a_{AN}\left(a_{OB} - \frac{R_A}{K_B}\right)\right]\frac{V_A}{100} + \left[k_O a_{OB}\left(a_{AN} - \frac{R_O}{K_N}\right)\right]\frac{V_O}{100} \qquad (5)$$

Since the terms in the brackets in Equation (5) represent R_A and R_O respectively, Equation (5) may be written

$$R = \frac{a_{AN}a_{OB}}{100}\left[\frac{V_A}{\left(\frac{1}{k_A} + \frac{a_{AN}}{K_B}\right)} + \frac{V_O}{\left(\frac{1}{k_O} + \frac{a_{OB}}{K_N}\right)}\right] \qquad (6)$$

Increasing the degree of agitation by increasing the stirrer speed will reduce the resistance terms to mass transfer in (6) by increasing the transfer coefficients K_B and K_N (5, 7). Thus if the stirrer speed is increased until the terms a_{AN}/K_B and a_{OB}/K_N become negligible with respect to $1/k_A$ and $1/k_O$ respectively, Equation (6) reduces to

$$R = a_{AN}a_{OB}\frac{(k_A V_A + k_O V_O)}{100} \qquad (7)$$

which gives the over-all reaction rate expressed in terms of activities of nitric acid and benzene in the acid and organic phases respectively.

As $a = \gamma X$ Equation (7) may be written in terms of activity coefficients and mole fractions as

$$R = X_{AN}X_{OB}\gamma_{AN}\gamma_{OB}\left(\frac{k_A V_A + k_O V_O}{100}\right) \qquad (8)$$

also as

$$\frac{V_O}{100} = 1 - \frac{V_A}{100}$$

$$R = (X_{AN}X_{OB})(\gamma_{AN}\gamma_{OB}k_A)\cdot\left[\left(1 - \frac{k_O}{k_A}\right)\frac{V_A}{100} + \frac{k_O}{k_A}\right] \qquad (9)$$

The effect of agitation on the reaction rate is illustrated in Figure 3, where the reaction rates for runs 1, 3, 4, 5, 10, and 11 are plotted against the stirrer speed. One curve is for the reactor in which runs 1 through 9 were made and the second curve is for the reactor (illustrated in Figure 2) in which the remainder of the runs were made. Each curve represents approximately constant phase compositions and phase ratio.

Figure 3 indicates that above 2,200 rev./min. in either reactor the resistance terms to mass transfer were made sufficiently small to eliminate the stirrer speed as a variable affecting the reaction rate. The great majority of the thirty-four runs were made at stirrer speeds above 2,200 rev./min.

CORRELATION OF REACTION RATES

Composition Correlation

Equation (9) suggests that if mass transfer between the phases is eliminated as a variable, the reaction rate can be correlated as a function of temperature, the nitric acid concentration in the acid phase, the benzene concentration in the organic phase, the volume percentage of acid phase, and some function of the phase compositions. The latter variable is included because, in general, the term $(\gamma_{AN}\gamma_{OB})$ is a function of composition.

In Figure 4 the values of log $R/X_N X_B$ are plotted as a function of log $(X_N + 1.56X_S - 0.23X_W)$ for all the data with a volume percentage of acid phase between 50 and 65%. All the data points at a common temperature fall close to a

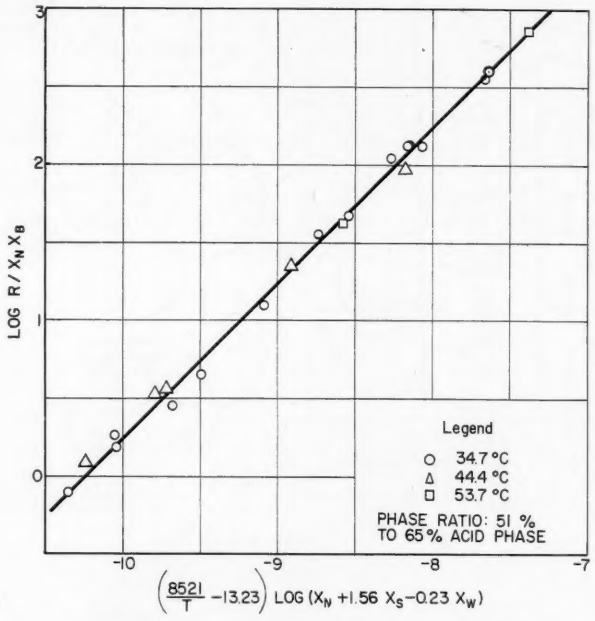

Fig. 5. Reaction-rate–composition–temperature correlation.

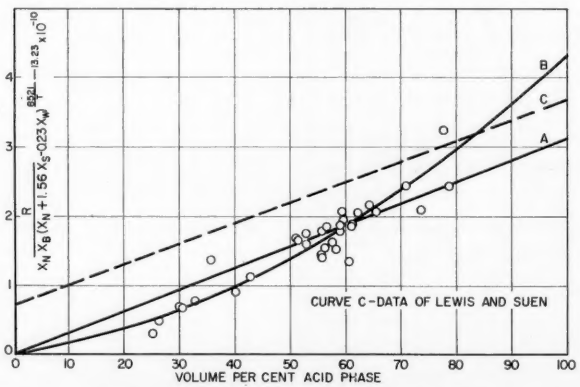

Fig. 6. Effect of phase ratio upon reaction rate.

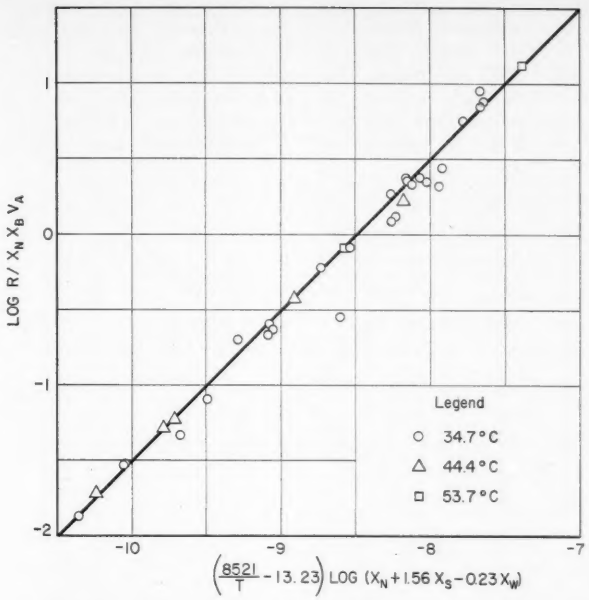

Fig. 7. Correlation including effect of phase ratio as a linear function.

straight line represented by the equation

$$\log \frac{R}{X_N X_B} = P \log (X_N + 1.56X_S - 0.23X_W) + \log I \quad (10)$$

or

$$R = I(X_N + 1.56X_S - 0.23X_W)^P X_N X_B \quad (11)$$

where P is the slope of the line, a function of temperature, and log I is the intercept when the straight line is extrapolated to a value of log $(X_N + 1.56X_S - 0.23X_W)$ equal to zero. This general form of correlation was previously used to relate the rate of nitration of toluene with the phase compositions (*3*).

The empirical function $(X_N + 1.56X_S - 0.23X_W)^P$ correlates the effect of the temperature as well as an effect of composition and can be considered as representing the product of the activity coefficients of benzene and nitric acid and the rate constant k_A, as indicated by Equation (9). The term

$$\left[\left(1 - \frac{k_O}{k_A}\right)V_A + \frac{k_O}{k_A}\right]$$

of Equation (9) is insensitive to temperature over the 6% variation in absolute temperature covered in this investigation. Furthermore, the effect of phase ratio on the reaction rate indicates that k_O is probably small as compared with k_A.

The correlation was presented in terms of the mole fraction of benzene in the organic phase on an acid-free basis for convenience only, as it makes little difference in the correlation whether the actual mole fraction or the acid-free mole fraction is used.

Composition-temperature Correlation

The three straight lines in Figure 4 may be extrapolated to a common intercept, and the slope P of each line is found to be a function of temperature. The family of curves can be represented by the equation

$$\log \frac{R}{X_N X_B} = \left(\frac{8521}{T} - 13.23\right) \log (X_N + 1.56X_S - 0.23X_W) + 10.24 \quad (12)$$

Equation (12) can be rearranged to give

$$R = (1.73 \times 10^{10}) X_N X_B \cdot e^{8521/T - 13.23 \ln (X_N + 1.56X_S - 0.23X_W)} \quad (13)$$

The exponential function in Equation (13) is an empirical representation of the product $(\gamma_{AN}\gamma_{OB}k_A)$ in Equation (9).

The data in Figure 4 are represented as a single straight line in Figure 5 by Equation (12). As previously noted, Equations (12) and (13) are valid only for a volume percentage of acid phase in the range from 50 to 65% acid phase.

Effect of Phase Ratio

In an attempt to evaluate the extent of the nitration reaction in each phase, the volume percentage of acid phase was varied from 25 to 79. It was impractical to hold the phase composition constant while the relative amounts of the phases were varied, and it became necessary to correct the data for these differences. It was assumed that the effect of composition and temperature at constant phase ratio was expressed by Equation (12) and that the effect of phase ratio could be accounted for as in Equation (9); the resulting expression was

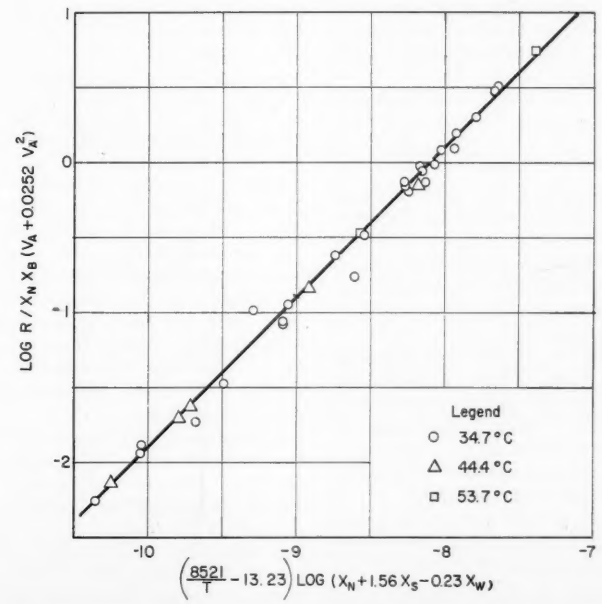

Fig. 8. Correlation including effect of phase ratio as a quadratic function.

$$R = x_N x_B[(x_N + 1.56x_S - 0.23x_W)^{8521/T-13.23}] \cdot \left[\left(1 - \frac{k_O}{k_A}\right)V_A + \frac{k_O}{k_A}\right] \quad (14)$$

The quantity $R/x_N x_B(x_N + 1.56x_S - 0.23x_W)^{8521/T-13.23}$ was plotted against the volume percentage of acid phase V_A in Figure 6.

According to Equation (14), the data plotted in Figure 6 should fall on a straight line, the intercept being equal to k_O/k_A and the slope being equal to $(1 - k_O/k_A)$. This means that the slope can take on any value, positive or negative, and that the intercept must be greater than or equal to zero.

The straight line which most nearly satisfies the theoretical requirements is labeled as curve A on Figure 6. This indicates that the reaction rate in the organic phase is negligibly small compared with the reaction rate in the acid phase. Figure 7 shows a final correlation based on curve A of Figure 6. The equation of the straight line representing the data in Figure 7 is

$$R = (3.12 \times 10^8)x_N x_B V_A(x_N + 1.56x_S - 0.23x_W)^{8521/T-13.23} \quad (15)$$

Although it was contrary to Equation (14), a parabola, curve B, was drawn through the data in Figure 6. Curve B gives a better representation of the data below, and a satisfactory representation of the data above, 50% acid phase. Figure 8 shows a final correlation based on curve B of Figure 6. The equation for the correlation of Figure 8 is

$$R = (1.233 \times 10^8)x_N x_B(V_A + 0.0252V_A^2)(x_N + 1.56x_S - 0.23x_W)^{8521/T-13.23} \quad (16)$$

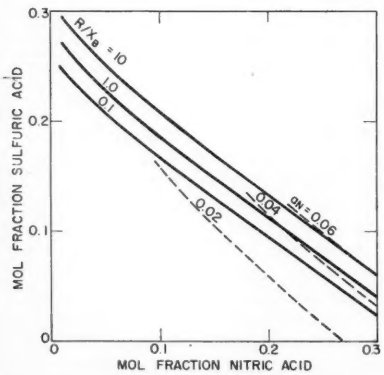

Fig. 9. Comparison of activity of nitric acid with rate of nitration of benzene.

Suen (*16*) reports that in the emulsion the acid phase is continuous above 33% acid phase and the organic phase is continuous below 33% acid phase. This inversion of phases might explain the fact that the data points below 50% acid phase in Figure 6 fail to substantiate Equation (14). It is possible that the agitation supplied failed to produce a sufficiently fine emulsion near the inversion point to eliminate completely the mass transfer effects.

However, three runs made at a volume percentage of acid phase from 30 to 33% and at stirrer speeds from 2,260 to 2,810 rev./min. gave consistent reaction rates as illustrated in Figure 6. This agreement of rates indicates that the stirrer speed had no significant effect on the reaction rates in this range of volume percentage of acid phase.

Equation (16) is empirical; however, the function

$$(X_N + 1.56X_S - 0.23X_W)^{8521/T-13.23}$$

can be considered to represent the term $(\gamma_{AN}\gamma_{OB}k_A)$ in the theoretical Equation (9). Activity coefficients must be evaluated by independent equilibrium measurements to verify this viewpoint, but only a limited amount of the necessary data is available.

Lewis and Suen (*11*) reported some vapor-liquid equilibrium measurements for nitric acid–sulfuric acid–water mixtures at 35°C. over a limited range of liquid-phase compositions. Activities of nitric acid in these mixtures were calculated according to the equation

$$A = \frac{Py}{p} \quad (17)$$

and the dashed curves in Figure 9 illustrating the activity of nitric acid as a function of acid-phase composition were drawn through the data. Equation (17) assumes that the vapor phase is an ideal gas and fixes the standard state fugacity as the fugacity of the pure component at the temperature of the mixture.

The rate of nitration of benzene is compared with the activity of nitric acid in Figure 9 where curves of constant R/X_B as calculated from Equation (16) for 35°C. and 60% acid phase are drawn as the solid lines. The rate of nitration appears to be a function of the activity of nitric acid although the relationship is not first order, as assumed in the theoretical equations. No further conclusions can be drawn from the comparison in Figure 9 because of the limitations of the equilibrium data.

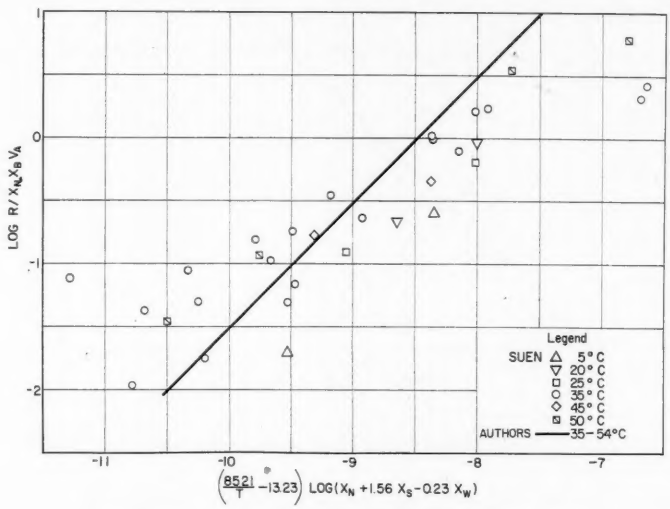

Fig. 10. Comparison of correlation with batch data of Suen.

Comparison of Correlation with Suen's Data

Reaction-rate data for the nitration of benzene with mixed acid was determined by Suen (*16*) in a series of batch experiments. A comparison of Suen's data with those of the authors is illustrated in Figure 10, where rates calculated from the conversion-time data reported by Suen are plotted with Equation (15).

Although all the data reported by Suen were not used in calculating the results plotted, Figure 10 is considered to be an objective representation of his results. A tabulation of these calculated rates is available (*1*).

Lewis and Suen (*11*) report, in addition to the batch data, the results from a study of the effect of phase ratio, or volume percentage of acid phase, in a continuous apparatus. These results indicate that there is a significant reaction rate in the organic phase relative to that in the acid phase. Values estimated from a published figure (*11*) are shown as the

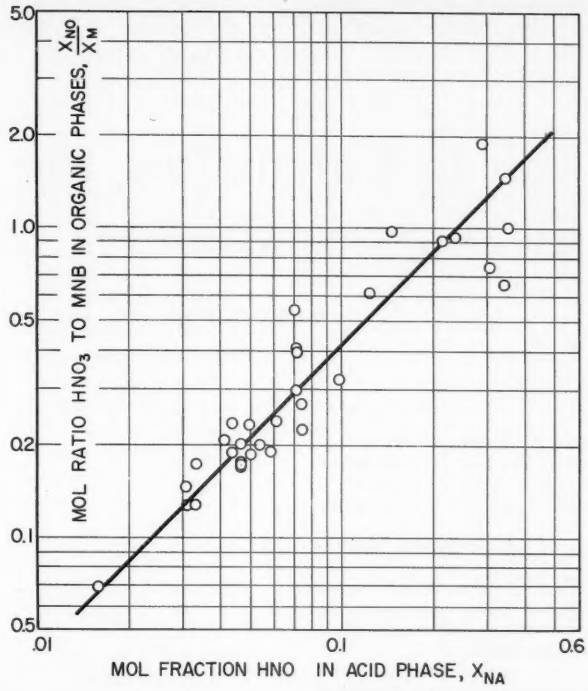

Fig. 11. Distribution of nitric acid between acid and organic phases. Equation of line: $X_{NO}/X_{MNB} = 8.4X_{NA}$.

dotted line (curve *C*) of Figure 6. No explanation of this discrepancy can be offered since neither the original data nor the equipment details were published.

Comparison with Toluene Nitration Data

The data of this investigation permit a quantitative comparison with the rate of nitration of toluene (*12*). At 35°C. the rate of nitration of toluene under comparable conditions of nitration ranges from 1.76 to 9.7 times faster than the rate of nitration of benzene in the range of acid-phase compositions studied.

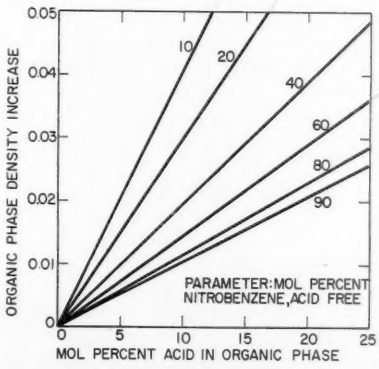

Fig. 12. Effect of dissolved acid on density of organic phase.

CONCLUSION

The rate of nitration of benzene with mixed nitric acid and sulfuric acid has been measured over ranges of phase composition, temperature, and phase ratio that are of interest in commercial nitration. Although it is not clear whether or not the effects of mass transfer have been completely eliminated for all values of the phase ratio investigated, the data do in all probability represent limiting values of the reaction rate obtainable by ordinary means of agitation. For this reason Equation (16) is recommended for use in design calculations, but it should be used with caution in view of the difficulty of obtaining the same high degree of agitation in large-scale reactors.

The distribution of nitric acid between the acid and organic phases is shown in Figure 11, and the effect of dissolved acid on the density of the organic phase is shown in Figure 12. The accuracy of the data upon which Figures 11 and 12 are based is not high, but they are useful for the purpose of estimating these effects.

NOTATION

A = constant
a_{AB} = activity of benzene in acid phase
a_{AN} = activity of nitric acid in acid phase
a_{OB} = activity of benzene in organic phase
a_{ON} = activity of nitric acid in organic phase
B = constant
e = 2.718
I = constant
K_B = mass transfer coefficient for benzene transfer, g.-moles/(hr.)(liter)
K_N = mass transfer coefficient for nitric acid transfer, g.-moles/(hr.)(liter)
k_A = reaction velocity constant for acid-phase reaction
k_O = reaction velocity constant for organic-phase reaction
P = constant
R = reaction rate, g.-moles/(hr.)(liter)
T = temperature, °K.
V_A = volume percentage of acid phase
V_O = volume percentage of organic phase
x_{AN}, x_N = mole fraction of nitric acid in acid phase
x_B = mole fraction of benzene in organic phase, acid-free basis
x_M = mole fraction of nitrobenzene in organic phase, acid-free basis
x_{OB} = mole fraction of benzene in organic phase
x_{ON} = mole fraction of nitric acid in organic phase
x_S = mole fraction of sulfuric acid in acid phase
x_W = mole fraction of water in acid phase
γ_{AN} = activity coefficient of nitric acid in acid phase
γ_{OB} = activity coefficient of benzene in organic phase

LITERATURE CITED

1. Biggs, R. D., Ph.D. thesis, Univ. Mich., Ann Arbor (1954).
2. Bost, R. W., and F. Nicholson, *Ind. Eng. Chem., Anal. Ed.*, **7**, 190 (1935).
3. Crooks, R. C., and R. R. White, *Chem. Eng. Progr.*, **46**, 249 (1950).
4. Hann, J. W., and K. A. Kobe, *Ind. Eng. Chem.*, **43**, 2355 (1951).
5. Hixson, A. W., and M. I. Smith, *Ind. Eng. Chem.*, **41**, 973 (1949).
6. Jurecek, M., *Chem. Listy*, **43**, 204 (1949).
7. Karr, A. E., and E. G. Scheibel, *Chem. Eng. Progr. Symposium Series* No. 10, **50**, 73 (1954).
8. Kobe, K. A., and J. J. Mills, *Ind. Eng. Chem.*, **45**, 287 (1953).
9. Kobe, K. A., and P. W. Pritchett, *Ind. Eng. Chem.*, **44**, 1398 (1952).
10. Kolthoff, I. M., E. B. Sandell, and B. Moskovitz, *J. Am. Chem. Soc.*, **55**, 1454 (1933).
11. Lewis, W. K., and T. J. Suen, *Ind. Eng. Chem.*, **32**, 1095 (1940).
12. McKinley, C., and R. R. White, *Trans. Am. Inst. Chem. Engrs.*, **40**, 143 (1944).
13. Mitscherlich, E., *Ann. Physik u. Chem.*, **31**, 625 (1834).
14. Othmer, D. F., J. J. Jacobs, Jr., and J. F. Levy, *Ind. Eng. Chem.*, **34**, 286 (1942).
15. Scott, W. W., "Scott's Standard Methods of Chemical Analysis," Vol. 2, 5 ed., 2212–13, 2234, D. Van Nostrand Company, Inc., New York (1939).
16. Suen, T. J., Sc.D. thesis, Mass. Inst. Tech., Cambridge (1937).

Presented at A.I.Ch.E. New York meeting

An Algebraic Approach to Calculating the Solvent Extraction of Complex Mixtures

HARRY F. HOPP, JR., and R. B. SMITH

Sinclair Research Laboratories, Inc., Harvey, Illinois

In the usual method of calculating the solvent extraction of complex mixtures it is assumed that the complex mixture behaves like a binary mixture. However, the hypothetical binary composition of the mixture is never explicitly used; rather, an additive property of the mixture is used as an indication of its composition. The calculation must be done graphically on a triangular diagram or its equivalent.

On the assumption that the complex mixture consists of only two hypothetical components, empirical equations have been arrived at relating the distribution coefficients of these two components and of the solvent to the phase compositions. These equations contain three arbitrary constants. By use of the data from a minimum of three simple laboratory batch extractions of a given complex mixture, the three constants, plus the hypothetical binary composition of the original complex mixture, can be determined.

With the equations for the distribution coefficients, the equilibrium curve and tie lines for the system can be calculated. Properties of the raffinates and extracts can be measured and related to the hypothetical binary compositions of these mixtures.

The use of the method is demonstrated by comparing calculated results with laboratory yields and properties. The calculated results show good agreement with the experimental results. Calculations can be carried out not only on the triangular diagram, but by any of the other graphical methods that have been developed for the solvent extraction of binary mixtures. Equally important, calculations can be done analytically, and therefore the use of automatic computers is feasible.

In the calculation of the solvent extraction of complex mixtures from laboratory equilibrium data, it is usually assumed that the complex mixture behaves like a binary mixture. The calculations are performed on a triangular diagram, on which the hypothetical binary composition of the complex mixture is represented by some property of the mixture, usually a property that varies linearly with composition. No attempt is made, however, to express the hypothetical binary composition of the mixture explicitly.

On the contrary, in the algebraic method which is presented here, the hypothetical binary composition of the complex mixture is explicitly derived from laboratory equilibrium data and is used in calculating the solvent extraction of the mixture just as though a true binary were being handled.

This algebraic method of approach has three advantages. First, having explicitly derived a value for the hypothetical binary composition of a complex mixture, one can use whichever of the methods of calculation developed for binary mixtures that may be convenient for the problem at hand. Second, since every relationship in this method can be expressed algebraically, the calculations can be made as precise as desired, for comparative studies. And third, the laboratory data on a system can be reduced to compact algebraic form.

THEORY

Table 1 shows the nomenclature used in considering a one-stage batch extraction of a complex mixture with a pure solvent. The complex mixture is assumed to be a mixture of hypothetical components 1 and 2, called "soluble" and "insoluble" for convenience. The solvent is component 3. The values of R, E, S, x_3, and y_3 can all be measured. The problem is to determine values for the hypothetical compositions by use of the measured data.

By writing material balances for the system, one can obtain the following equations:

$$z_1 + z_2 = 1 \tag{1}$$

$$x_1 + x_2 + x_3 = 1 \tag{2}$$

$$y_1 + y_2 + y_3 = 1 \tag{3}$$

$$z_1 = x_1R + y_1E \tag{4}$$

$$z_2 = x_2R + y_2E \tag{5}$$

and

$$S = x_3R + y_3E \tag{6}$$

Table 1. Amounts and Compositions in a One-stage Batch Extraction of a Complex Mixture

	Complex mixture		Solvent	
Component	Fraction	Amount	Fraction	Amount
Soluble	z_1	z_1		
Insoluble	z_2	z_2		
Solvent	—	—	1	S
Total	1	1	1	S

	Raffinate		Extract	
Component	Fraction	Amount	Fraction	Amount
Soluble	x_1	x_1R	y_1	y_1E
Insoluble	x_2	x_2R	y_2	y_2E
Solvent	x_3	x_3R	y_3	y_3E
Total	1	R	1	E

TABLE 2. DERIVATION OF A_3 FROM EXPERIMENTAL DATA ON THE ONE-STAGE BATCH SOLVENT EXTRACTION OF A MIDCONTINENT NEUTRAL OIL WITH NITROBENZENE AT 50°F.

S	Raffinate oil °A.P.I.	Extract oil °A.P.I.	x_3	y_3	$Y = R(1 - x_3)$	E	$\log K_3$	$A_3 = \log K_3/(y_3 - x_3)$	
	24.4								
0.7504	——	18.0	0.2757	0.6563	0.7581	0.7038	0.3766	0.989	
1.000	27.5	18.1	0.250	0.705	0.672		0.450	0.989	
1.500	28.9	18.4	0.223	0.763	0.586		0.534	0.989	$A_3 = 0.99$
2.000	29.5	18.8	0.210	0.800	0.534		0.581	0.985	
2.500	30.4	19.3	0.195	0.812	0.461		0.619	1.003	
3.000	29.9	19.8	0.205	0.842	0.429		0.614	0.964	
4.000	31.1	20.4	0.195	0.859	0.357		0.644	0.970	
5.000	31.5	21.6	0.198	0.877	0.304		0.646	0.951	
7.000	32.1	22.5	0.152	0.891	0.221		0.768	1.039	

Note: All quantities and fractions are by weight.

Written by analogy with the conventional vapor-liquid equilibrium equations, the following equations define equilibrium ratios for the system:

$$y_1 = K_1 x_1 \tag{7}$$

$$y_2 = K_2 x_2 \tag{8}$$

and

$$y_3 = K_3 x_3 \tag{9}$$

In order to relate the K's to the phase compositions, observed values of K ($= y/x$) were plotted against various functions of composition. It was found that the variation of the K's could practically all be accounted for by variation in solvent concentrations, and of course at the plait point all three K's are equal to unity. A number of empirical equations that express this behavior were examined; the following equations give the best agreement with the experimental data:

$$\log K_1 = A_1(y_3 - x_3) \tag{10}$$

$$\log K_2 = A_2(y_3 - x_3) \tag{11}$$

and

$$\log K_3 = A_3(y_3 - x_3) \tag{12}$$

These equations define three constants, A_1, A_2, and A_3, which are fundamental to this method. With values for these constants, one can calculate equilibrium phase compositions over the whole range of compositions for the system composed of components 1, 2, and 3.

The value of A_3 can easily be calculated from experimental data by use of Equations (9) and (12):

$$A_3 = \log (y_3/x_3)/(y_3 - x_3) \tag{13}$$

To find values for A_1, A_2, and z_1, Equation (7) is substituted into Equation (4) to give

$$z_1 = x_1 R + K_1 x_1 E \tag{14}$$

Solving for x_1 yields

$$x_1 = z_1/(R + K_1 E) \tag{15}$$

Similarly, Equations (5) and (8) give

$$x_2 = z_2/(R + K_2 E) \tag{16}$$

Equations (1) and (2) give

$$z_2 = 1 - z_1 \tag{17}$$

and

$$x_1 + x_2 = 1 - x_3 \tag{18}$$

Substituting Equations (15), (16), and (17) into (18) gives

$$z_1/(R + K_1 E) + (1 - z_1)/(R + K_2 E) = 1 - x_3 \tag{19}$$

Solving Equation (19) for z_1 gives

$$z_1 = \frac{1/(R + K_2 E) - (1 - x_3)}{1/(R + K_2 E) - 1/(R + K_1 E)} \tag{20}$$

Equation (20) contains K_1 and K_2, which are related to the constants A_1 and A_2 through Equations (10) and (11). Substituting data on three isothermal batch extractions of a mixture at different solvent ratios into Equation (20) gives three simultaneous equations from which values can be determined for the three unknowns.

Since A_1 and A_2 enter into Equation (20) nonlinearly, the three simultaneous equations must be solved by trial and error. This procedure can be systematized by using the Newton-Raphson method as applied to simultaneous equations (*6*). To use this method a function f is defined:

$$f = z_1 - z_1' \tag{21}$$

where

$$z_1' = \frac{1/(R + K_2 E) - (1 - x_3)}{1/(R + K_2 E) - 1/(R + K_1 E)} \tag{22}$$

Values are assumed for z_1, A_1, and A_2. Substituting these values and the data from each batch extraction into Equations (21) and (22) gives three values of f: f_a, f_b, and f_c. Unless the correct values of the unknowns have been assumed, the values of f_a, f_b, and f_c will not all be zero. Better approximations of the unknowns are then obtained by solving the following equations for h, k, and l:

$$(D_1 f_a - D_1 f_b)k + (D_2 f_a - D_2 f_b)l = f_b - f_a \tag{23}$$

$$(D_1 f_a - D_1 f_c)k + (D_2 f_a - D_2 f_c)l = f_c - f_a \tag{24}$$

and

$$h = -f_a - D_1 f_a k - D_2 f_a l \tag{25}$$

where

$$D_1 f = \frac{2.303 K_1 E(y_3 - x_3) z_1'/(R + K_1 E)^2}{1/(R + K_2 E) - 1/(R + K_1 E)} \tag{26}$$

and

$$D_2 f = \frac{2.303 K_2 E(y_3 - x_3)(1 - z_1')/(R + K_2 E)^2}{1/(R + K_2 E) - 1/(R + K_1 E)} \tag{27}$$

TABLE 3. SMOOTHED DATA FROM THE ONE-STAGE BATCH SOLVENT EXTRACTION OF A MIDCONTINENT NEUTRAL OIL WITH NITROBENZENE AT 50°F.

$A_3 = 0.99$

S	Y	x_3	y_3	R	E
0.750	0.759	0.277	0.656	1.050	0.700
1.000	0.676	0.250	0.705	0.901	1.099
1.500	0.584	0.222	0.762	0.750	1.750
2.000	0.529	0.208	0.798	0.668	2.332
2.500	0.466	0.200	0.817	0.583	2.917
3.000	0.432	0.193	0.836	0.535	3.465
4.000	0.357	0.185	0.859	0.438	4.562
5.000	0.301	0.179	0.876	0.367	5.633
7.000	0.219	0.171	0.899	0.264	7.736

The improved assumptions for the unknowns are $z_1 + h$, $A_1 + k$, and $A_2 + l$. The procedure is repeated until the values of f_a, f_b, and f_c are zero. Three to five trials are usually required.

Equilibrium phase compositions can then be calculated by use of A_1, A_2, and A_3. Starting with an assumed value of $(y_3 - x_3)$, values for K_1, K_2, and K_3 are calculated by use of Equations (10), (11), and (12). Then Equation (9) gives

$$(y_3 - x_3) = K_3 x_3 - x_3 = (K_3 - 1)x_3 \quad (28)$$

from which

$$x_3 = (y_3 - x_3)/(K_3 - 1) \quad (29)$$

Then

$$y_3 = (y_3 - x_3) + x_3 \quad (30)$$

Substituting Equations (7) and (8) into (3) gives

$$K_1 x_1 + K_2 x_2 = 1 - y_3 \quad (31)$$

Solving Equations (18) and (31) for x_1 gives

$$x_1 = \frac{(1 - y_3) - K_2(1 - x_3)}{K_1 - K_2} \quad (32)$$

Equation (7) gives y_1. The values of x_2 and y_2 are found by Equations (2) and (3).

At the plait point where $K_1 = K_2 = K_3 = 1$, Equations (29) and (32) are indeterminate. Application of L'Hôpital's rule (*1*) to these equations gives

$$x_3 = y_3 = 0.4343/A_3 \quad (33)$$

and

$$x_1 = y_1 = \frac{x_3(A_2 - A_3) - A_2}{A_1 - A_2} \quad (34)$$

at the plait point.

With values for the equilibrium phase compositions, the value of z_1 can be used to calculate R, E, and S by use of the material-balance equations (1) to (6). These equations give

$$R = (z_1 y_2 - z_2 y_1)/(x_1 y_2 - x_2 y_1) \quad (35)$$

$$E = (x_1 z_2 - x_2 z_1)/(x_1 y_2 - x_2 y_1) \quad (36)$$

and

$$S = R + E - 1 \quad (37)$$

EXPERIMENTAL DATA

In order to test the theory developed above, experimental data on the solvent extraction of a variety of complex mixtures with different solvents were required. Among the data used was a series of one-stage batch solvent extractions of a Mid-continent neutral oil carried out at a temperature of 50°F. The solvent-to-feed weight ratio was obtained, as well as the weight yields of extracts and raffinates. The oil content of each extract and raffinate was determined by distilling off the solvent from a sample of the phase in question. Table 2 summarizes these data.

In addition to these data, experimental results from similar studies found in the literature (*7* to *10*) were used.

DISCUSSION OF RESULTS

Starting with the experimental data in Table 2, the first step is to determine a value of A_3 by use of Equation (13). This calculation is summarized in Table 2. Calculated values of the empirical constant A_3 are derived for each batch extraction. Since the values of x_3 for S above 2.5 are plainly erratic, these values were omitted in arriving at the final value for A_3. Because these erratic values badly affect further calculation, the data were smoothed by use of the value of A_3 just determined. To smooth the data the experimental values of S and $Y = R(1 - x_3)$ were accepted as correct. A value of $(y_3 - x_3)$ was assumed, and x_3 and y_3 were calculated by Equations (29) and (30). Then values were calculated for R and Y by means of the material-balance equations. This procedure was repeated until the calculated value of Y matched the experimental value. The value of E was found by

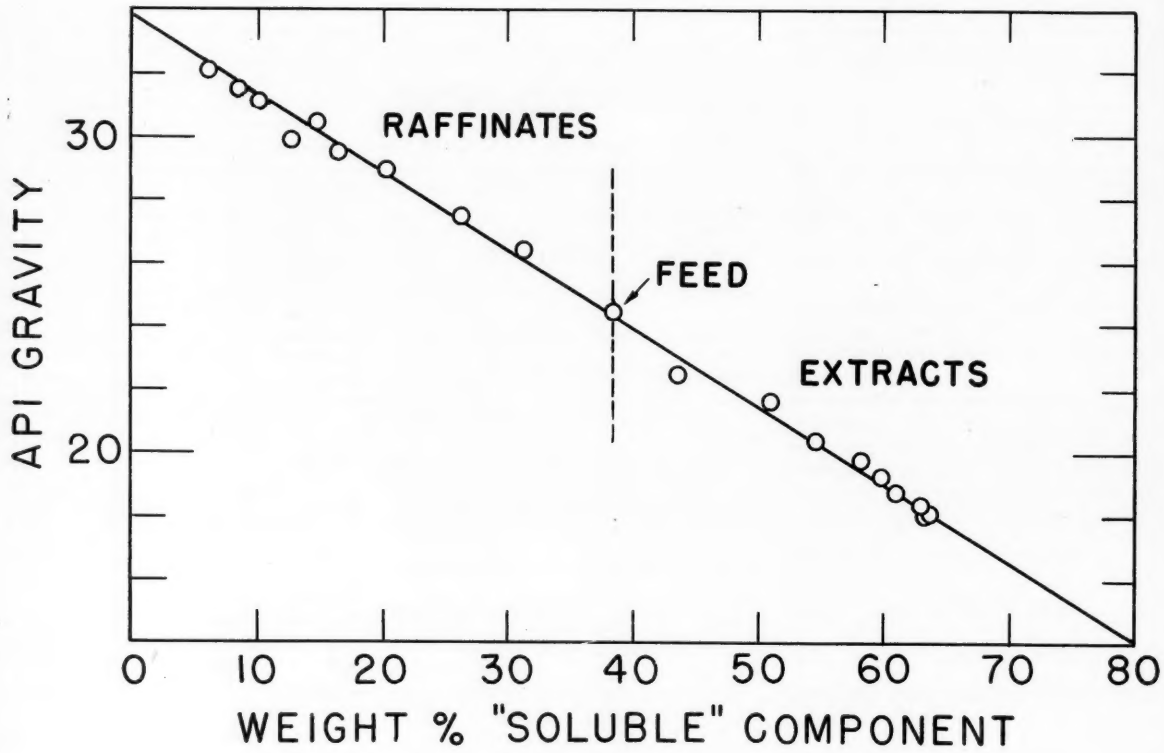

Fig. 1. Gravity vs. composition.

Table 4. Comparison of Experimental and Calculated Extractions of a Midcontinent Neutral Oil with Nitrobenzene at 50°F.

	Treat 1: Multibatch			Treat 2: Multibatch			Treat 3: Countercurrent			Treat 4: Countercurrent		
	Lab.	Calc.	H—N	Lab.	Calc.	H—N	Lab.	Calc.	H—N	Lab.	Calc.	H—N
Stages	2	2	2	4	4	4	2	2	2	4	4	4
Wt. % solvent	100	100	100	100	100	100	100	100	100	100	100	100
Wt. % yield	47.3	46.3	47.4	28.8	29.9	31.0	53.5	50.2	53.7	45.0	43.3	43.4
Raffinate gravity, °A.P.I.	30.5	30.8	30.6	32.8	33.3	32.9	29.6	29.8	29.9	31.2	32.5	32.5
Raffinate solvent, wt. %	20.5	19.1	18.8	20.2	15.9	13.5	20.8	20.7	20.5	19.7	16.9	14.4

	Treat 5: Multibatch			Treat 6: Multibatch			Treat 7: Countercurrent			Average deviation	
	Lab.	Calc.	H—N	Lab.	Calc.	H—N	Lab.	Calc.	H—N	Calc.	H—N
Stages	2	2	2	4	4	4	2	2	2		
Wt. % solvent	75	75	75	75	75	75	75	75	75		
Wt. % yield	54.0	53.0	53.7	34.5	35.5	36.9	57.8	61.6	56.9	1.8	1.1
Raffinate gravity, °A.P.I.	29.3	29.6	29.6	32.2	32.9	32.4	28.6	28.0	28.8	0.6	0.4
Raffinate solvent, wt. %	21.3	21.0	21.1	19.3	16.5	14.7	21.9	23.8	22.7	1.9	2.6

Note: The countercurrent extractions were run by the batch (pseudo) countercurrent extraction method (*5*).

Equation (37). The smoothed data are given in Table 3.

To determine the values of z_1, A_1, and A_2, the smoothed data at values of $S = 1$, 3, and 5 were chosen. Application of the procedure given above to solve Equation (20) gave these values for the unknowns:

$$z_1 = 0.382$$

$$A_1 = -0.035$$

$$A_2 = -1.570$$

$$A_3 = 0.990$$

With these values, the phase compositions were calculated for each of the extractions in Table 3. In Figure 1 the solvent-free compositions are shown plotted against the A.P.I. gravities of the oils. The resulting straight-line relation is just what one would expect from a true binary mixture—the Midcontinent neutral oil behaving as if it were a binary mixture of a 9.3°A.P.I. "soluble" component and a 33.8°A.P.I. "insoluble" component. For all systems for which data were available, this straight-line relation between hypothetical composition and a corresponding additive property was found.

Table 4 gives experimental data on four batch cocurrent multistage extractions and three batch countercurrent multistage extractions of the Midcontinent neutral. Also given are the results obtained by use of a phase diagram which was calculated from the constants A_1, A_2, A_3, and z_1. The calculated values of A.P.I. gravities were taken from Figure 1. The agreement is very good. The results calculated by the usual Hunter-Nash method (*2, 3, 4*) are shown too for comparison.

On application of the algebraic method to a variety of systems, it was found that either volume fractions or weight fractions could be used, as long as the same basis was used throughout. A straight line was given by A.P.I. gravity with weight fractions and by specific gravity with volume fractions.

Table 5 gives the derived constants for the systems studied. These results show that the hypothetical binary composition of a given mixture is not invariant under all conditions. Although the data are too few to warrant a firm conclusion, the indications are that the hypothetical composition of a given stock will be the same with closely similar solvents, but it will be quite different with a quite different type of solvent.

Table 5. Solvent-extraction Constants for Various Systems

Complex mixture	Solvent	Temp., °F.	z_1	A_1	A_2	A_3	Ref.
Midcontinent neutral oil	Nitrobenzene	50	0.382 wt.	−0.035	−1.570	0.99	
Light gas oil	Sulfur dioxide	70	0.258 vol.	−0.002	−1.794	1.042	7
Dewaxed Asiatic crude residuum	Propane	70	0.433 wt.	0.696	−1.870	1.023	8
Heavy lube oil base	Phenol	110	0.264 vol.	0.469	−1.628	1.123	9
Heavy lube oil base	Phenol + 5% H_2O	110	0.261 vol.	−0.149	−1.835	1.153	9
Heavy lube oil base	Phenol + 10% H_2O	110	0.262 vol.	−0.472	−1.988	1.172	9
Stock 2	Furfural	208	0.330 wt.	−0.090	−1.593	0.986	10
Stock 2	Nitrobenzene	32	0.268 wt.	0.817	−1.450	1.066	10
Stock 2	Nitrobenzene	50	0.457 wt.	0.144	−1.620	1.003	10
Stock 2	Aniline	149	0.436 wt.	−0.166	−1.917	0.960	10
Stock 2	Acetone	86	0.788 wt.	−0.802	−2.539	0.973	10

NOTATION

A = empirical constant
$D = \partial/\partial A$ = differential operator
E = extract amount per unit amount of feed
f = defined function
h, k, l = corrections to assumed values of unknowns
K = equilibrium ratio
R = raffinate amount per unit amount of feed
S = solvent amount per unit amount of feed
x = raffinate composition
y = extract composition
$Y = R(1 - x_3)$ = yield of refined oil
z = feed composition

Subscripts

a, b, c = each of three simultaneous equations
1 = soluble component
2 = insoluble component
3 = solvent

LITERATURE CITED

1. Eshbach, Ovid W., "Handbook of Engineering Fundamentals," 1 ed., p. 2–76, John Wiley and Sons, New York (1936).
2. Hunter, T. G., and A. W. Nash, *World Petroleum Congress Proc.*, **2**, 340 (1933).
3. ———, *Ind. Eng. Chem.*, **27**, 836 (1935).
4. Perry, John H., "Chemical Engineers' Handbook," 3 ed., p. 728, McGraw-Hill Book Company, Inc., New York (1950).
5. *Ibid.*, p. 718.
6. Scarborough, J. B., "Numerical Mathematical Analysis," pp. 187 to 189, Johns Hopkins Press, Baltimore (1930).
7. "Science of Petroleum," vol. III, p. 1841, Oxford University Press, New York (1938).
8. *Ibid.*, p. 1854.
9. *Ibid.*, p. 1857.
10. Vogel, Hans, *Oel u. Kohle*, **36**, No. 46, 547 (Dec. 8, 1940).

Presented at A.I.Ch.E. New York meeting

Prediction of Ideal-stage Requirements in Complex Liquid-liquid Extraction Systems

H. C. PETERSON and G. H. BEYER

Iowa State College, Ames, Iowa

A procedure for obtaining equilibrium data and predicting ideal-stage requirements in a complex liquid–liquid extraction system is presented. Preliminary equilibrium data are obtained from a simulated column run involving a series of batch contacts operated in such a manner as to approach steady state countercurrent conditions. The flow ratios and stage requirements for continuous operation are then estimated by trial-and-error by use of a modified McCabe-Thiele method.

The procedure lends itself particularly well to those systems with interdependent distribution of the two components. Data for the separation of hafnium from zirconium are presented to show the utility of the method.

The separation of two components by liquid-liquid extraction has not been successfully reduced to a mathematical relationship for complex systems. Bartels and Kleiman (*1*) and Klinkenberg (*3*) have developed mathematical treatments based upon the assumptions of (*a*) constant distribution coefficient, i.e., a straight equilibrium line, and (*b*) addition of zero volume in the feed stream. Scheibel (*5*) has presented a graphical treatment which requires equilibrium data over the entire range of operation. The assumptions of Bartels et al. often do not apply, and complete equilibrium data are often not available.

To facilitate the understanding of extraction calculations in complex systems, an analogy may be drawn from the McCabe-Thiele method used in distillation calculations. The following assumptions are made in this treatment of countercurrent liquid-liquid extraction: (*a*) there is no volume change in either phase flowing through the equipment and (*b*) the only solute entering the equipment enters in the feed solution.

A schematic diagram of an extraction unit is presented in Figure 1. An aqueous scrub solution passes countercurrent to organic extract in the scrub section. Aqueous feed solution is introduced into the aqueous line between the scrub and extraction sections. In the extraction section the combined aqueous phases pass countercurrent to organic solvent. Volumetric flow rates are designated by Q, solute concentrations in the aqueous phase by X, and solute concentrations in the organic phase by Y, as weight of solute per unit volume of solution. Subscripts S, F, R, E, and T identify scrub, feed, raffinate, extract, and solvent streams, respectively.

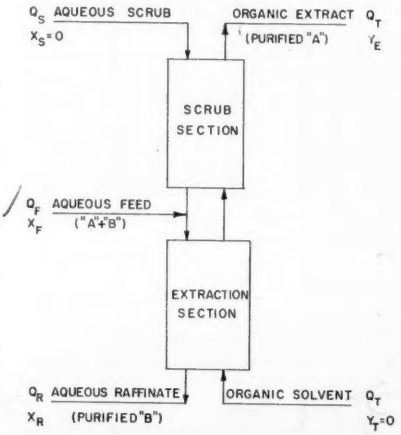

Fig. 1. Schematic diagram of extraction column.

A material balance on the solute entering and leaving the scrub section yields the equation of the operating line in the scrub section.

$$Y = (Q_S/Q_T)X + Y_E \qquad (1)$$

This equation is plotted in Figure 2 as a straight line of slope (Q_S/Q_T) and intercept Y_E.

Similarly, the equation of the operating line in the extraction section of the column is

$$Y = (Q_R/Q_T)(X - X_R) \qquad (2)$$

This equation is also plotted in Figure 2. It can be shown that the operating lines intersect at a point where $X = X_F$, although this point does not necessarily exist in the column.

The transition from one operating line to the other operating line at the feed point is illustrated in Figure 3. At the feed point the composition of the aqueous phase changes; the organic composition, however, remains constant (*see* Figure 1). Therefore, the composition of the aqueous and organic phases immediately above the feed point lie on the scrub-section operating line; the compositions of the aqueous and organic phases immediately below the feed point lie on the extraction-section operating line. Since the composition of the organic phase does not change, both operating lines have a common

H. C. Peterson is with The M. W. Kellogg Company, Jersey City, New Jersey.

ordinate at the feed point. Stages can then be stepped off as in the McCabe-Thiele method. Compere and Ryland (*2*) used a similar treatment in their work.

In multicomponent extraction each component has a separate equilibrium diagram, and if the distribution of each component is independent of the other components, a trial-and-error solution can be used to determine the relationship between stage requirements, flow ratios, and separation of the components. If the equilibrium line is straight, there is a simple mathematical relationship between the stage requirements, flow ratios, and separation. For the separation of some components, however, the equilibrium line is not straight, and the distribution of one component is dependent on the concentration of the other.

As an example, consider the separation of A and B shown in Figure 1. The feed to the extraction column contains both A and B. It is assumed that the organic solvent preferentially extracts component A, and so the organic extract will contain purified A and the aqueous raffinate will contain purified B. Since some B is transferred to the organic stream leaving the extraction section, aqueous scrub solution is introduced at the extract exit to scrub the last traces of B from the organic phase. At the raffinate exit organic solvent serves to extract the last traces of A from the raffinate phase.

A clearer concept of the problems involved in economically separating A from B can be obtained by discussing hypothetical equilibrium diagrams for each component, as shown in Figure 4. To minimize the cost of recovering A from the organic extract, it is desirable that the concentration of A in the extract be kept high and that the amount of A returned to the aqueous phase in the scrub section be small. Therefore, the operating line in the scrub section should intersect the equilibrium line for A and "pinch-in" stages. A stage is pinched in with respect to component A when the phases entering are already so close to equilibrium that very little net mass transfer of A takes place. In the extraction section of the column the operating line should assure high recovery of A by reducing its concentration in the raffinate to a low value. To ensure effective use of the available stages, the stages in the extraction section should not be pinched in for A.

The extraction of B can also be followed in Figure 4 by considering the hypothetical equilibrium diagram for component B. For B, the operating line in the extraction section should pinch in stages to ensure a high concentration of B in the raffinate. However, in the scrub section pinching in, with respect to component B, should be avoided, for it is desirable to reduce the concentration of B in the extract to a low value. Figure 4 involves a like number of equilibrium stages in each section of the column for each component, although the number of pinched-in stages cannot be clearly shown graphically. It should be noted that a stage pinched in with respect to A may accomplish considerable mass transfer of B, and vice versa.

The case will now be considered in which the distributions of A and B are assumed interdependent; i.e., the equilibrium conditions occurring in each stage depend on both the quantity and the quality of solute present. Figure 5 presents such a set of hypothetical equilibrium lines, showing the effect of composition on the distribution between phases. It should be noted that the sums of the concentrations of A and B are plotted. Following across a horizontal line, composition is seen to have a marked effect on equilibrium conditions, even though the total concentration in the organic phase remains unchanged. Similarly, a vertical line shows composition to have a marked effect even though the total concentration in the aqueous phase remains unchanged. The percentages of A and B noted in Figure 5 are the percentages of A and B in aqueous solution prior to an equilibrium contact with an equal volume of organic solvent.

Since the quality, as well as the quantity, of solute varies throughout the extractor, the equilibrium lines necessary for ideal-stage calculations are composites of the lines shown in Figure 5. Two equilibrium lines are involved: one for the extraction section, where compositions are high in B, another for the scrub section, where compositions are high in A. These composite equilibrium lines, shown dotted in Figure 5, can conveniently be obtained from a simulated column run.

A simulated column run uses a number of separatory funnels to simulate countercurrent extraction conditions. Portions of aqueous scrub, aqueous feed, and organic solvent are brought together in the flow pattern outlined by Scheibel (*6*). When the pattern has been repeated a sufficient number of times, the compositions of the aqueous and organic phases closely approach the compositions that would be obtained in a countercurrent extractor operating with the same flow ratios and the same number of ideal stages. In this way equilibrium data can be obtained for the two composite equilibrium lines.

Although the choice of flow ratios and number of stages used for a simulated column run is arbitrary, the equilibrium data obtained are generally useful in establishing the form of the composite equilibrium lines. An eight-stage simulated column run, with feed to stage four, for instance, may be assumed to yield equilibrium compositions represented by the small circles on Figure 6. These circles represent points on the composite equilibrium lines, taking into account the interaction of A and B. The upper line applies to the scrub section where solute compositions are high in A;

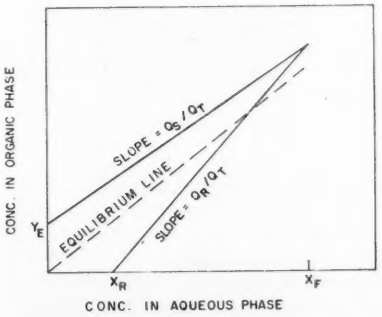

Fig. 2. Locating of operating lines.

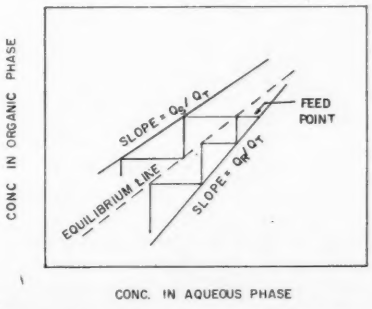

Fig. 3. Transition between operating lines at feed point.

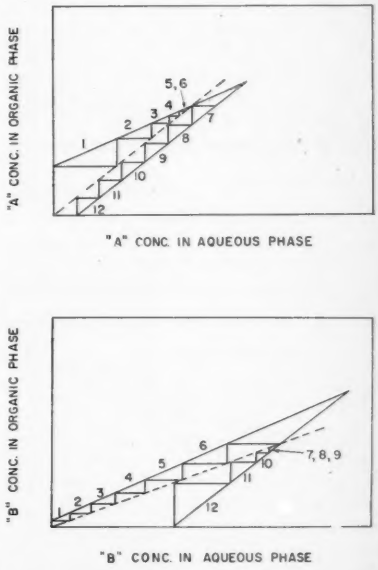

Fig. 4. Hypothetical equilibrium diagrams.

the lower line applies to the extraction section where solute compositions are high in B. Drawing horizontal and vertical lines from each point permits reconstruction of the stages and the operating lines. The quantity of solute in each phase can be conveniently shown in Figure 6; the quality of the solute—as determined by spectrographic analysis, for example—cannot be conveniently shown.

Analysis of the extract from the simulated column run indicates whether three ideal stages, operating at the flow rates chosen, are adequate to produce extract of the desired purity. It is extremely unlikely that the arbitrary choice of flow ratios and number of stages will prove entirely satisfactory. However, the knowledge gained from such a run permits trial-and-error calculations to be made by use of other flow rates and different numbers of stages. Such a trial-and-error calculation is illustrated in Figure 7. Although the composite equilibrium lines involved at other flow ratios will not be identical, the line from the simulated column run serves as a good approximation and is useful in defining the regions of operability in complex systems.

Figure 7 shows how data from a simulated column run can be used to estimate extractor performance under other operating conditions. Suppose the analysis of the extract from the eight-stage simulated column run indicated the need for an additional stage in the scrub section, to obtain A of the desired purity. What flow rates should be used if twelve ideal stages are available?

The equilibrium lines obtained from the eight-stage run are useful for the twelve-stage run because the concentrations encountered are quite similar. The trial-and-error solution involves drawing various sets of operating lines, each set intersecting at the feed concentration. The correct set of operating lines shows four ideal stages in the scrub section and eight ideal stages in the extraction section, with a common ordinate for the feed stage and the last scrub-section stage. When these conditions have been satisfied, the relative flow rates can be determined from the slopes of the operating lines. Thus in Figure 7, $Q_S/Q_T = 0.32$ and $Q_R/Q_T = 0.59$. Relative to a solvent rate of unity, $Q_S = 0.32$ and $Q_R = 0.59$. Since $Q_R = Q_S + Q_F$, $Q_F = 0.27$. Hence the flow rates of all streams can be determined relative to the solvent rate.

As an example of the utility of this method of handling complex extraction systems, data will be presented for the separation of hafnium from zirconium (4). Zirconium is found in nature with approximately 2½% hafnium as an impurity. For many specialized uses, it is desirable to separate the hafnium from zirconium. Nitrates of the two elements are readily soluble in water. Concentrations of hafnium and zirconium compounds are reported as weight of oxide per unit volume or as molarity based on oxide concentration. Use of such nomenclature eliminates assumptions regarding the exact ionic species in solution. For analysis, the hafnium and zirconium were precipitated as hydroxides, ignited to oxides, and the weight ratio of hafnium to zirconium determined spectrographically.

In the example to be cited, the feed solution was an aqueous solution of approximately 1M Zr (123 g. oxide/liter), analyzing (Hf/Zr × 100) = 2.4. Tributyl phosphate was used as the selective solvent for zirconium after dilution with n-heptane to improve the mechanical separation of the two phases. Nitric acid was found to be necessary for efficient separation of the two elements.

Figure 8 shows that the system under consideration falls into the category suggested by Figure 5. Figure 8 was experimentally determined by single-batch equilibrium contacts between solvent (acidified so that no net mass transfer of nitric acid occurred) and a 5N nitric acid solution containing the indicated ratios of hafnium and zirconium nitrates as solute. It can be seen that the distribution of the oxides is affected by their quality.

The results of an eight-stage simulated column run are shown in Table 1. Feed containing 2.4 parts by weight of hafnium /100 parts by weight of zirconium [(Hf/Zr) × 100 = 2.4] was separated into organic extract [(Hf/Zr) × 100 = 0.012] and aqueous raffinate [(Hf/Zr) × 100 = 34]. Since acidified solvent was used, there was only a small amount of acid transferred between phases; the

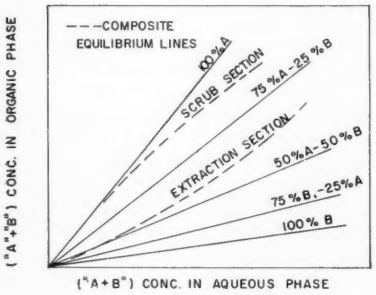

Fig. 5. Composite equilibrium lines.

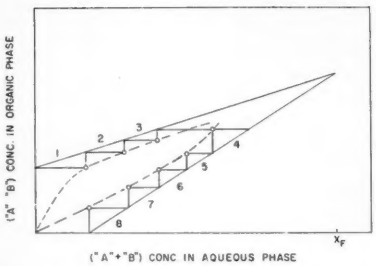

Fig. 6. Eight-stage simulated column run.

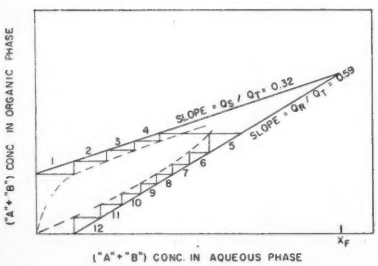

Fig. 7. Twelve-stage trial-and-error calculation.

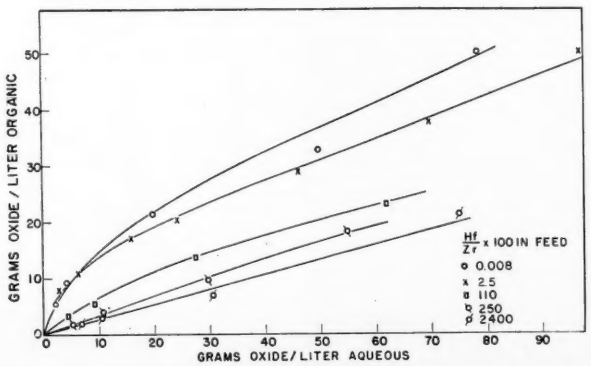

Fig. 8. Effect of hafnium on distribution of hafnium zirconium.

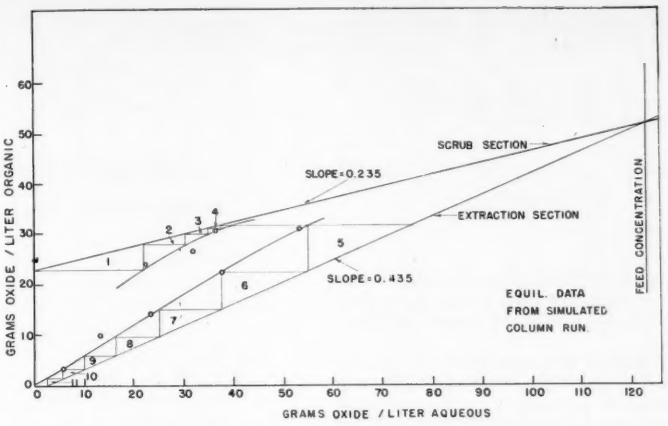

Fig. 9. Modified McCabe-Thiele diagram for stage calculation.

TABLE 1. SIMULATED COLUMN RUN

8 stages, feed to stage 4

Feed : scrub : solvent = 1.0 : 1.18 : 4.85

Feed: 1.0 *M* Zr—5.09 *N* HNO_3—0.16 *M* SO_4
Hf/Zr × 100 = 2.4

Scrub: 5.02 *N* HNO_3

Solvent: 60% TBP—40% heptane, 1.82 *N* NHO_3

Stage	Organic g. oxide/liter	Organic *N* HNO_3	Organic Hf/Zr × 100	Aqueous g. oxide/liter	Aqueous *N* HNO_3	Aqueous Hf/Zr × 100
1	24.0	1.90	0.012	22.5	5.09	<0.010
2	26.7	1.97	0.010	32.1	5.14	0.11
3	30.8	1.92	0.028	36.5	5.25	0.68
4	31.0	1.95	0.022	53.3	5.13	2.2
5	22.4	1.94	0.22	37.7	4.99	4.1
6	14.2	1.87	0.26	23.6	5.10	8.8
7	10.0	1.85	1.0	13.1	5.00	22
8	3.32	1.80	4.2	5.80	5.06	34

TABLE 2. STAGEWISE ANALYSES OF MIXER-SETTLER RUN

Stage	Organic g. oxide/liter	Organic *N* HNO_3	Organic Hf/Zr × 100	Aqueous g. oxide/liter	Aqueous *N* HNO_3	Aqueous Hf/Zr × 100
1	22.2	1.95	<0.010	17.5	5.21	<0.010
2	29.3	2.02	<0.010	27.5	5.30	<0.010
3	31.4	2.03	<0.010	33.5	5.46	<0.010
4	31.8	2.03	0.043	34.9	5.46	0.24
5	32.2	2.03	0.11	52.8	5.15	3.6
6	21.1	1.99	0.60	30.8	5.15	6.8
7	13.7	1.93	0.27	19.9	5.05	9.8
8	7.66	1.89	1.9	11.6	4.97	20
9	4.14	1.86	4.8	8.06	4.97	36
10	1.98	1.83	10	5.32	4.75	67
11	1.03	1.77	23	3.71	4.52	110
12	0.66	1.68	32	3.14	4.12	140
13	0.46	1.50	42	2.99	3.49	130
14	0.29	1.18	28	3.54	2.56	72

major components transferred were hafnium and zirconium. The equilibrium data obtained were plotted, as suggested in Figure 6, to locate the composite equilibrium lines for the scrub and extraction sections of the column.

It was desired to use these data in choosing operating conditions for a continuous run. From the simulated column run it was decided to use four stages in the scrub section, to assure zirconium product containing less than 100 p.p.m. of hafnium [(Hf/Zr) × 100 = 0.01]. The same feed concentration was used. The oxide concentration of the raffinate was arbitrarily chosen as 2.5 g./liter. Figure 9 shows the trial-and-error graphical solution, utilizing the raffinate concentration, feed concentration, and number of scrub stages already chosen. It was estimated that seven extraction stages should be used. From the slopes of the operating lines in Figure 9, $Q_S/Q_T = 0.235$ and $Q_R/Q_T = 0.435$.

The organic extract obtained from the continuous run was to be stripped of solute in another extractor, and the solvent recirculated. In the stripping of the purified zirconium from the extract, some nitric acid would also be removed. Thus the recycled solvent would contain less acid than the acidified solvent used in the simulated column run. To compensate for the use of acid-deficient solvent, three additional stages were added to the extraction section.

A continuous extraction run was then made. Fourteen mixer-settler stages were operated, with feed, scrub, and solvent flows as estimated above. After steady state had been attained, each stage was isolated and mixing continued to obtain the equilibrium data reported in Table 2.

The effect of acid-deficient solvent is evident from the [(Hf/Zr) × 100] aqueous analyses for stages 13 and 14. At the lower acidities prevailing in those stages there was some loss of raffinate quality. Taking into account the analytical difficulty of distinguishing between hafnium contents below 100 p.p.m., the run produced satisfactory product and raffinate. The equilibrium data reported in Table 2 show the equilibrium line in the continuous run to be actually somewhat higher than that obtained in the simulated column run. This shift reflects the higher nitric acid concentration in stages 1 through 7 of the continuous run.

The use of simulated column runs to obtain extraction data is recommended for complex systems where the distributions of the components are interdependent. A modified McCabe-Thiele graphical method can then be applied to determine flow-rate ratios, ideal-stage requirements, and feed-point location.

ACKNOWLEDGMENT

The authors wish to express their appreciation to the Ames Laboratory of the Atomic Energy Commission for the support of this project.

LITERATURE CITED

1. Bartels, C. R., and G. Kleiman, *Chem. Eng. Progr.*, **45**, 589 (1949).
2. Compere, E. L., and A. Ryland, *Ind. Eng. Chem.*, **43**, 239 (1951).
3. Klinkenberg, A., et al., *Chem. Eng. Sci.*, **1**, 93 (1951).
4. Peterson, H. C., Ph.D. thesis, Iowa State College, Ames, Iowa (unpublished).
5. Scheibel, E. G., *Chem. Eng. Progr.*, **44**, 771 (1948).
6. ———, *Ind. Eng. Chem.*, **44**, 2942 (1952).

Presented at A.I.Ch.E. Louisville meeting

Heat Transfer Through a Homogeneous Isotropic Turbulent Field

THOMAS J. HANRATTY

University of Illinois, Urbana, Illinois

Because of the large scale of the motion responsible for mixing in turbulent fields, turbulent transport processes differ from molecular transport processes in that the mixing depends on the previous history of the diffusing material and turbulent fields are generally nonhomogeneous.

The effect of the time dependency of the diffusion process is examined for the case of heat transfer from a hot wall to a cold wall through a turbulently flowing fluid. The fluid is assumed to have a uniform velocity and the turbulence is assumed to be homogeneous and isotropic. The calculations are carried out by assuming a distribution of heat sources along the hot wall and of heat sinks along the cold wall. G. I. Taylor's theory of turbulent diffusion for a homogeneous isotropic field is used to describe the properties of these sources and sinks. These calculations are compared with temperature profiles obtained as a solution to Fick's Law using a constant diffusion coefficient. A marked difference between the two sets of curves is obtained in the vicinity of the wall and in the beginning of the heat exchange section.

A calculated profile on the basis of an idealized model of heat transfer in channel flow is compared with actual measurements made by Page, Corcoran, Schlinger, and Sage (7) at a distance far enough downstream so that the temperature profile had reached a steady condition.

Turbulent diffusion, like molecular diffusion, occurs from the random motion of material. However, unlike molecular diffusion, the scale of the motion is of the order of magnitude of the size of the container, and two distinct differences arise:

1. Turbulent fields are generally nonhomogeneous and the diffusion rates in different positions reflect variation in the turbulence characteristics.
2. The motion of a particular set of tagged particles will depend on their previous history, i.e., their time of entry into the field. Only at very long periods of time, when the motion of the particles does not resemble the motion they had upon entry into the field, will the diffusion be time independent.

Molecular transport of heat has been described by Fick's Law:

$$\frac{\partial T}{\partial t} = \nabla\cdot(\alpha\nabla T) \qquad (1)$$

$$\alpha = \text{thermal diffusivity} = \frac{k}{\rho C_p}$$

For a homogeneous medium the thermal diffusivity α will be constant and Equation (1) becomes

$$\frac{\partial T}{\partial t} = \alpha\nabla^2 T \qquad (2)$$

Turbulent transport of heat has been described by equations of the same type as Equations (1) and (2), a turbulent exchange coefficient being used in place of the molecular thermal diffusivity. Such an approach is at best empirical, and in general the exchange coefficient will have a different value at each point in the field. As pointed out above, the variation would exist even in the case of a homogeneous, isotropic field because the turbulent-diffusion process is time dependent.

Taylor (*1*) in 1935 described this time dependency for the case of a point source or sink located in an infinite, homogeneous, isotropic field. This method of description has been substantiated by experimental investigations (*1* to *4*). However, its application to more complex systems involving a distribution of sources and sinks has not been explored. In this paper G. I. Taylor's development will be applied to the prediction of temperature profiles in a fluid flowing turbulently between parallel hot and cold walls. The turbulence will be assumed to be homogeneous and isotropic, and the velocity profile of the fluid will be assumed uniform.

The paper has been written to emphasize the empirical nature of Equations (1) and (2) when applied to turbulent transfer, to examine the magnitude of the effect of the time dependency, and to suggest what might be the basis for a different method of describing turbulent transfer.

The calculations will be carried out by assuming that the fluid in flowing between the two walls is exposed to a number of instantaneous differential plane sources of heat at the hot wall and a number of instantaneous differential plane sinks of heat of the same strength as the sources at the cold wall. The temperature profile at any position may be determined by summing the contributions of all of these sources and sinks. Therefore, the key to these calculations is the description of a single instantaneous source or sink.

SINGLE INSTANTANEOUS SOURCE

An instantaneous source consists of the instantaneous appearance of a number of particles at a given point in a field at a given time. As time proceeds, these particles diffuse into the field. The distribution of the particles in the field at any time may be described in terms of their mean square displacement in the x direction from the place at which they originated, $\overline{X^2}$. For molecular diffusion the rate of change of this distribution with time is constant. The process possesses no measurable time dependence. According to a relation derived by Einstein (*5*) for Brownian motion, this rate of change bears a definite relation to the molecular diffusivity:

$$\frac{d\overline{X^2}}{dt} = 2D \qquad (3)$$

G. I. Taylor (*1*) established an analogous relation for a turbulent field:

$$\frac{d\overline{X^2}}{dt} = 2\overline{u^2}\int_0^t R\, d\epsilon \qquad (4)$$

where $\overline{u^2}$ = root mean square velocity in the x direction

$R = \dfrac{\overline{u_t u_\epsilon}}{\overline{u^2}}$ = correlation coefficient

$u_t u_\epsilon$ = product of the velocities of a particle at times t and ϵ

$\overline{u_t u_\epsilon}$ = average for a large number of particles

G. I. Taylor (*6*) suggested that the correlation coefficient R might have an

exponential form, and recent experimental evidences (*2* and *3*) have supported his suggestion:

$$R = e^{-s/\tau} \tag{5}$$

$$\tau = \int_0^\infty R\, ds \tag{6}$$

$$s = (t - \epsilon)$$

The quantity τ is a scale factor which may be viewed as a measure of the lifetime of the oddities. If Equations (5) and (6) are substituted into Equation (4), the rate of change of $\overline{X^2}$ may be expressed in terms of two constants, $\overline{u^2}$ and τ, which characterize the turbulence:

$$1/2\,\frac{d\overline{X^2}}{dt} = \overline{u^2}\tau(1 - e^{-t/\tau}) \tag{7}$$

At long periods this equation resembles that for molecular diffusion in that the rate of change approaches a constant value. This constant value will be referred to as the eddy diffusivity.

$$E = \overline{u^2}\tau \tag{8}$$

Equation (7) describes the magnitude of the spread of diffusing material. It does not describe how the material is distributed in the field. In treating this problem Frenkiel (*4*), on the basis of experimental evidences, assumed that $\overline{X^2}$ is described by a gaussian distribution. An equivalent assumption is made in this paper to describe the behavior of a single instantaneous source of heat or mass:

$$\frac{\partial T}{\partial t} = f(t)\,\frac{\partial T}{\partial x^2} \tag{9}$$

$$\frac{\partial C}{\partial t} = f(t)\,\frac{\partial C}{\partial x^2} \tag{10}$$

The diffusion coefficient $f(t)$ is a function of time. This functionality can be related to Equation (7) through the following considerations.

A solution to Equation (10) for the case of an instantaneous source of N particles in an infinite one-dimensional field is

$$C = \frac{N}{2\sqrt{\pi}\left[\int_0^t f\, d\theta\right]^{1/2}} \cdot \exp\left\{-\frac{x^2}{4\int_0^t f\, d\theta}\right\} \tag{11}$$

By substitution, the preceding expression can be seen to satisfy Equation (10). The expression also satisfies the physical boundary conditions imposed since

$$\int_{-\infty}^{+\infty} c\, dx = N \tag{12}$$

The probability that any of the diffusing particles will have a displacement between x and $x + dx$ is

$$P(x, x + dx) = \frac{C\, dx}{N} \tag{13}$$

$$P(x, x + dx)\, dx = \frac{dx}{2\sqrt{\pi}\left[\int_0^t f\, d\theta\right]^{1/2}} \cdot \exp\left\{-\frac{x^2}{4\int_0^t f\, d\theta}\right\} \tag{14}$$

The root mean square displacement of a large number of particles becomes

$$\overline{X^2} = \int_{-\infty}^{+\infty} x^2 P(x, x + dx)\, dx = \int_{-\infty}^{+\infty} \frac{x^2\, dx}{2\sqrt{\pi}\left[\int_0^t f\, d\theta\right]^{1/2}} \cdot \exp\left\{-\frac{x^2}{4\int_0^t f\, d\theta}\right\} \tag{15}$$

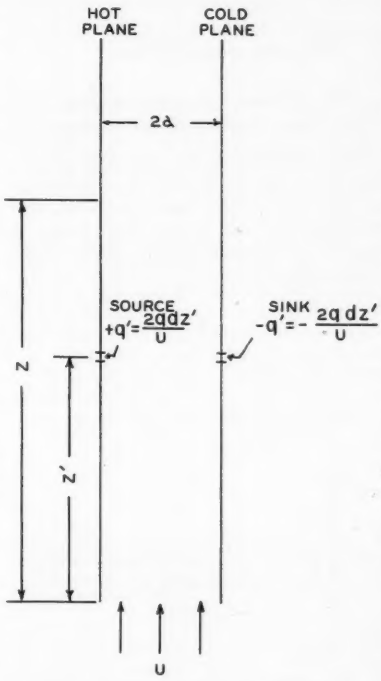

Fig. 1. Representation of the problem.

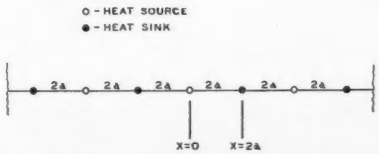

Fig. 2. Synthesis of solution for finite field from point-source solutions for infinite field.

Carrying out the preceding integration yields

$$\overline{X^2} = 2\int_0^t f\, d\theta$$

$$f = 1/2\,\frac{d\overline{X^2}}{dt} \tag{16}$$

Substituting Equation (7) gives

$$f = \overline{u^2}\tau(1 - e^{-t/\tau}) \tag{17}$$

TEMPERATURE FIELD FROM AN INSTANTANEOUS SOURCE-SINK PAIR

Equations (9) and (17) may be used to describe the behavior of an instantaneous source or sink in a homogeneous isotropic field. The problem to be solved in this paper is illustrated in Figure 1. The fluid in flowing past Z' is subject over a distance dZ' to the addition of a small amount of heat at the hot wall and to the subtraction of a small amount of heat at the cold wall. As time proceeds, or as the fluid flows down the channel, the hot fluid from the source and the cold fluid from the sink diffuse away from the walls, causing an alteration of the temperature profile.

The effect of a single source-sink pair such as this, independent of the effect of the remainder of the heat transfer surface, will first be considered. If the observer is moving with the fluid with a velocity, U, changes in the Z direction become changes with respect to the time variable. The effect of this single source-sink pair may be represented as a solution to Equation (9). The boundary conditions for which the solution will be obtained are that at zero time a fluid of zero temperature is exposed to an instantaneous heat source of strength $+ q'$ at $x = 0$ and to an instantaneous heat sink of strength $-q'$ at $x = a$. At all other times no heat transfer occurs at the walls, and the temperature gradient at the walls is zero.

In order to obtain a solution of Equation (9) which will satisfy the boundary conditions, the method of images will be employed. This consists of finding the solution for a single source or sink in an infinite field and then distributing these sources and sinks in such a way that the boundary conditions of a finite field are satisfied.

The solution for an instantaneous source in an infinite field is

$$T = +\frac{q'}{\rho C_P 2\sqrt{\pi}\,[\phi(t)]^{1/2}} \cdot \exp\left\{-\frac{x^2}{4\phi(t)}\right\} \tag{18}$$

and for an instantaneous sink in an infinite field

$$T = -\frac{q'}{\rho C_P 2\sqrt{\pi}\,[\phi(t)]^{1/2}} \cdot \exp\left\{-\frac{x^2}{4\phi(t)}\right\} \quad (19)$$

$$\phi(t) = \int_0^t f\, d\theta \quad (20)$$

Substituting Equation (17) for f

$$\phi(t) = \int_0^{\overline{X^2}} 1/2\, \frac{d\overline{X^2}}{d\theta}\, d\theta$$

$$= \int_0^t \overline{u^2}\tau(1 - e^{-\theta/\tau})\, d\theta$$

$$\phi(t) = 1/2\, \overline{X^2} = \overline{u^2}\tau t + \overline{u^2}\tau^2 e^{-t/\tau} - \overline{u^2}\tau^2$$

$$= E[t - \tau(1 - e^{-t/\tau})] \quad (21)$$

Equation (21) has been obtained by consideration of a point source. When Equation (21) is substituted into (19), an infinite temperature is obtained at the source point at zero time. To avoid this difficulty, a finite source with an initial distribution $\overline{X_0^2}$ will be assumed.* Then

$$\int_{\overline{X_0^2}}^{\overline{X^2}} 1/2\, \frac{d\overline{X^2}}{d\theta}\, d\theta = \int_0^t \overline{u^2}\tau(1 - e^{-\theta/\tau})\, d\theta$$

$$\phi(t) = E[t - \tau(1 - e^{-t/\tau})] + 1/2\, \overline{X_0^2} \quad (22)$$

A solution for an instantaneous source-sink pair in a finite field can be synthesized by placing in an infinite field, as indicated in Figure 2, an infinite number of sources and sinks the behaviors of which are described by Equations (18), (19), and (22). By examination of Equations (18) and (19), it can be seen that if such source-sink pairs had been placed only at $x = 0$ and $x = 2a$ the expression obtained would give a finite temperature gradient at the two walls. This would violate the boundary condition of no heat transfer at the walls for times greater than zero.

Using the synthesis depicted in Figure 2, one obtains an infinite-series solution to Equation (9):

$$T = \frac{2q\, dt}{2\sqrt{\pi}\,\rho C_p[\phi(t)]^{1/2}} \cdot \left\{\cdots \exp\left(-\frac{(8a + x)^2}{4\phi(t)}\right) + \exp\left(-\frac{(4a + x)^2}{4\phi(t)}\right) + \exp\left(-\frac{x^2}{4\phi(t)}\right) + \exp\left(-\frac{(4a - x)^2}{4\phi(t)}\right) + \exp\left(-\frac{(8a - x)^2}{4\phi(t)}\right) + \cdots - \exp\left(-\frac{(6a + x)^2}{4\phi(t)}\right) - \exp\left(-\frac{(2a + x)^2}{4\phi(t)}\right) - \exp\left(-\frac{(2a - x)^2}{4\phi(t)}\right) - \exp\left(-\frac{(6a - x)^2}{4\phi(t)}\right) - \exp\left(-\frac{(10a - x)^2}{4\phi(t)}\right) \cdots\right\} \quad (23)$$

The substitution

$q' = 2q\, dt$

q = rate of heat transfer per unit area

was made in the preceding equation. The numeral 2 appears because in an infinite field heat will diffuse from both sides of the differential plane source.

SYNTHESIS OF SOURCE-SINK SOLUTIONS TO DESCRIBE CHANNEL HEAT TRANSFER

The calculation of the temperature profile at any value of Z (*see* Figure 1) can be accomplished by adding the contributions of all source-sink pairs at values of Z' between zero and Z. After substitution of

$$dt = \frac{dZ'}{U} \quad (24)$$

$$t = \frac{Z - Z'}{U} \quad (25)$$

into Equation (23), this summation may be expressed by the integral

$$T = \int_0^Z \frac{2q\,\frac{dZ'}{U}}{2\sqrt{\pi}\,\rho C_p\left[\phi\left(\frac{Z - Z'}{U}\right)\right]^{1/2}} \cdot \left[\cdots + \exp\left\{-\frac{x^2}{4\phi\left(\frac{Z - Z'}{U}\right)}\right\} + \cdots - \exp\left\{-\frac{(2a - x)^2}{4\phi\left(\frac{Z - Z'}{U}\right)}\right\} \cdots\right] \quad (26)$$

In the preceding equation Z' is the variable of integration and Z is constant.

It was not apparent how this integral could be evaluated analytically. Therefore in order to indicate the behavior of the solution a graphical integration was carried out by use of values of the parameters describing point-source diffusion which seemed reasonable on the basis of the limited number of data available in the literature. These were

$$\frac{\sqrt{\overline{u^2}}}{U} = 0.04$$

$$\frac{2aU}{E} = 275 \quad (27)$$

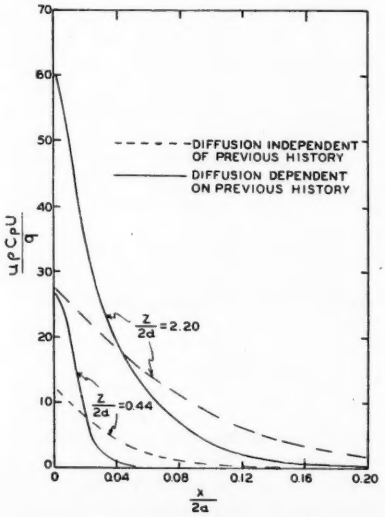

Fig. 3. Calculated temperature profiles for small Z/2a.

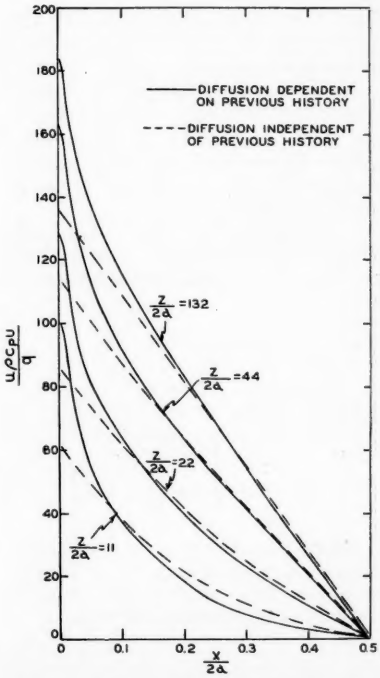

Fig. 4. Calculated temperature profiles for large Z/2a.

*Recent calculations indicate that the assumption of a finite source need not be made; however the contribution of molecular transfer must be included in the calculation of $\phi(t)$ in order that an infinite temperature not be obtained at the source location.

$$\frac{\overline{X_0^2}}{(2a)^2} = 10^{-4} \qquad (28)$$

The quantity q was assumed constant with respect to Z. The solutions obtained are presented in Figures 3 and 4. For the sake of demonstrating the time dependence of the diffusion process, solutions are also presented for the case of a constant diffusion coefficient of the magnitude presented in Equation (27).

Calculations were not carried out for $Z/2a > 132$ since very little change occurs in the temperature profile as Z is increased further. The value of $\overline{X_0^2}/2a$ chosen does not affect the shape of the curves for $x/2a > 0.01$ and $Z/2a \geq 11$. However for $Z/2a \leq 2.20$ the shape of the curves is very dependent upon $\overline{X_0^2}$ or upon the mechanism by which the fluid exchanges heat with the surface.

DISCUSSION OF RESULTS

The importance of the time dependence of the diffusion process is illustrated by the marked difference in the two calculated profiles at different values of Z. At small distances downstream of the beginning of the heat exchange section there is no resemblance between the temperature profile predicted for a homogeneous isotropic turbulent field and that calculated on the basis of a diffusion process independent of the previous history of the diffusing particles. At very large distances downstream the temperature profile in the center of the channel approximates what would exist if the diffusion coefficient were a constant. However, close to the wall there is a sharp rise in the temperature profile indicating a larger resistance to transfer in this region. Examination of Equation (7) shows that initially $\overline{X^2}$ varies with t^2 and that in the later stages of the process a linear dependence upon t is obtained. If the process were of the same type as described by Fick's Law, $\overline{X^2}$ would vary linearly with t throughout. The actual turbulent diffusion process exhibits a lower rate of transfer in its initial stages. Therefore, in regions where a large amount of the diffusing material has not been in the field for a long time a larger resistance to transfer will be in evidence. This accounts for the large temperature change in the vicinity of the wall and for the smaller penetration of heat in the beginning of the heat-exchange section for the actual turbulent transfer process as compared with one in which transfer is independent of previous history.

The magnitude of the effect of the time dependence will depend upon the parameter τ. For the particular turbulent field considered in Figures 3 and 4 the temperature profile at $Z/2a = 132$ starts to diverge from a straight line at $X/2a \backsimeq 0.15$. For a turbulent field of larger τ this divergence would begin to occur at a position closer to the center of the channel. The converse would be true for fields of smaller scale.

COMPARISON WITH EXPERIMENTAL DATA

The development in the preceding pages and the calculations presented in Figures 3 and 4 are based on the model of a homogeneous, isotropic field. Actual channel flow is neither homogeneous nor isotropic. Therefore, these calculations should be considered only as an illustration of the magnitude of

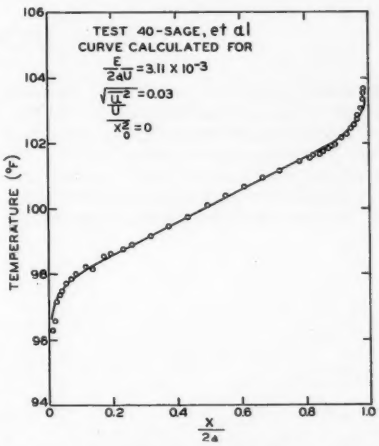

Fig. 5. Comparison of calculated curve with experimental data.

the effect of the time dependence of turbulent diffusion. They should be at best a rough approximation of actual measurements. No data are available on the development of a temperature profile for heat exchange in channel flow. Measurements have been made by Page, Corcoran, Schlinger, and Sage (7) at distances far enough downstream that the temperature profile had reached a steady condition. These exhibited a form similar to that shown in Figure 4 for large $Z/2a$. In order to obtain a more direct comparison a temperature profile was calculated for test 40 of these experimenters by use of

$$\frac{\sqrt{\overline{u^2}}}{U} = 0.03$$

$$\overline{X_0^2} = 0$$

The value assumed for the turbulence intensity seemed reasonable on the basis of measurements made with the hot-wire anemometer (8). Calculations were not made for values of $X/2a < 0.01$; therefore the assumed value for X_0^2 should not have much influence upon the calculated results. The value of the eddy diffusivity E used was obtained from the slope of the experimental temperature profile at the center of the channel.

$$\rho C_p E = \frac{q}{dt/dy}$$

The rate of heat transfer along the heated surface q was assumed constant. Under the conditions of the experiment q probably varied in an exponential manner, approaching a constant value at large Z.

The conditions of test 40 were such that if the diffusion coefficient were constant a linear temperature profile would result. The comparison of the calculated curve with the experimental data is shown in Figure 5. The fact that the calculated profile agrees with the data in the center of the channel is not surprising, as the value of E was selected so that this had to be the case. However, the agreement of the trend of the calculated curve and the data near the wall indicates that increased resistance near the boundary may not be due entirely to nonhomogeneities but may in a large part be due to the time dependence of the process.

ACKNOWLEDGMENT

This work is being continued with funds obtained from the Office of Ordnance Research. The author is grateful for this support. Future work will include physical measurements of the properties of source diffusion.

NOTATION

- a = half width of the channel
- C_P = heat capacity
- D = molecular-diffusion coefficient
- E = eddy diffusivity, value of f at infinite time
- f = diffusion coefficient
- k = thermal conductivity
- q = rate of heat transfer per unit area
- q' = instantaneous heat pulse
- R = correlation coefficient
- t = time
- T = temperature
- u = temperature difference from some base temperature (center of the channel for the case of channel flow)
- $\sqrt{\overline{u^2}}$ = root-mean-square velocity of the diffusing material
- U = average fluid velocity
- x = distance from the wall
- $\overline{X^2}$ = root-mean-square displacement of the diffusing particles
- Z = distance downstream from the beginning of the heat-exchange section
- Z' = location of a heat source or sink
- α = thermal diffusivity
- θ = time variable used in integration
- τ = time scale characterizing turbulence = $\int_0^\infty R\, d\theta$
- $\phi(t)$ = $\int_0^t f\, d\theta$

LITERATURE CITED

1. Taylor, G. I., *Proc. Roy. Soc.* (*London*), **151A**, 421 (1935).
2. Wilhelm, R. H., and T. J. Hanratty, *A.I.Ch.E. Journal* (to be published).
3. Kalinske, A. A., and E. R. Van Driest, "Fifth Intern. Congr. Appl. Mech.," John Wiley & Sons, New York (1939).
4. Frenkiel, F. N., "Advances in Appl. Mech.," Vol. III, Academic Press, Inc., New York (1953).
5. Einstein, A., *Ann. Physik*, **17**, 549 (1905); **19**, 371 (1906).
6. Taylor, G. I., *Proc. London Math. Soc.*, **24A**, 196 (1921).
7. Page, F., W. H. Corcoran, W. G. Schlinger, and B. H. Sage, *Ind. Eng. Chem.*, **44**, 419 (1952).
8. Laufer, J., *Natl. Advisory Comm. Aeronaut. Tech. Rept.* 1053 (1951).

Catalytic Hydrogenation of Carbon Monoxide and Dioxide over Steel

BUFORD D. SMITH and ROBERT R. WHITE

University of Michigan, Ann Arbor, Michigan

The hydrogenation of carbon monoxide and carbon dioxide on various steel catalysts was studied in the temperature range of 800° to 1,300°F. and at pressures from 5 to 30 atm. The feed gases (3.75 to 20 SCFH) were passed over a catalyst bed of 1/8-in. steel balls supported in a brass-lined reactor 0.81 in. in diam. The percentage of carbon oxides in the feed was 30% in the runs using a H_2—CO_2 feed and varied from 15 to 38% in the runs with a H_2—CO feed. The effects of temperature, pressure, feed composition, space velocity, and mass velocity were studied. Carbon deposition did not affect the activity of the catalyst and could be removed readily.

The catalytic hydrogenation of carbon monoxide and carbon dioxide has received intensive study since the turn of the century. In 1897 and 1902 Sabatier and Senderens (*15, 16*) reported their original work on the synthesis of methane from hydrogen–carbon monoxide and hydrogen–carbon dioxide mixtures in the presence of both reduced nickel and reduced cobalt catalysts. In 1923 Fisher and Tropsch (*8*) disclosed that iron was also an effective catalyst. Storch et al. (*18*) summarized these early discoveries and the investigations that followed.

Buford D. Smith is with Humble Refining Company, Baytown, Texas.

TABLE 1. STEEL CATALYST COMPOSITIONS (WEIGHT %)

Constituent	S. A. E. number C1013	440	302
Carbon	0.13–0.18	0.86–0.94	0.08–0.20
Chromium	—	16.5–18.0	17.0–19.0
Manganese	0.50–0.80	0.30–0.60	2.0
Silicon	—	0.60 max.	1.0 max.
Sulfur	0.05 max.	0.30 max.	0.03 max.
Phosphorus	0.04 max.	0.30 max.	0.04 max.
Molybdenum	—	0.40–0.60	
Nickel	—	—	8.0–10.0

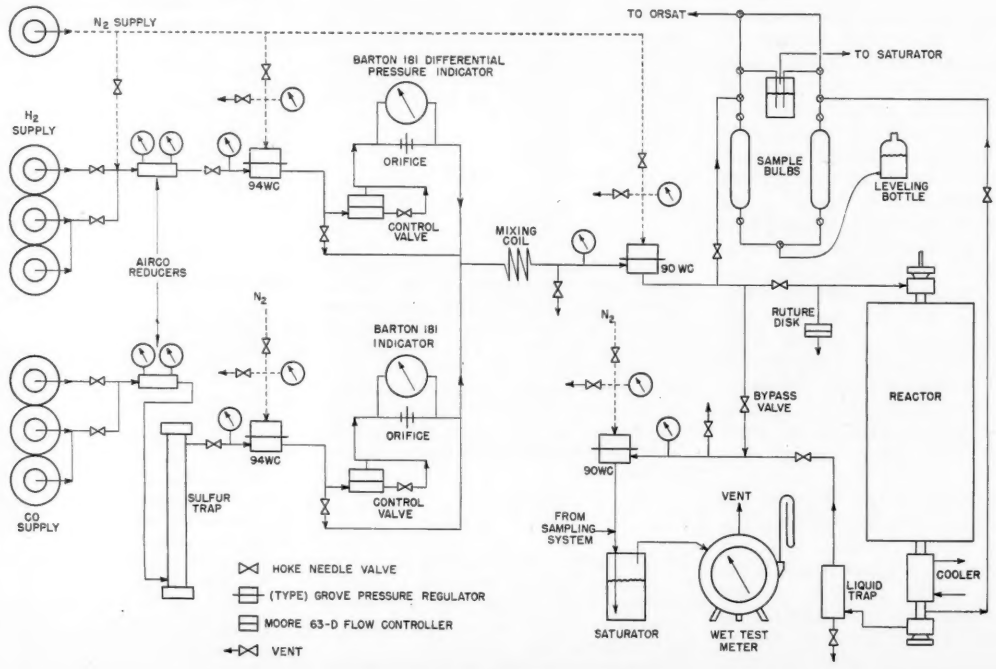

Fig. 1. Flow diagrams for the experimental unit.

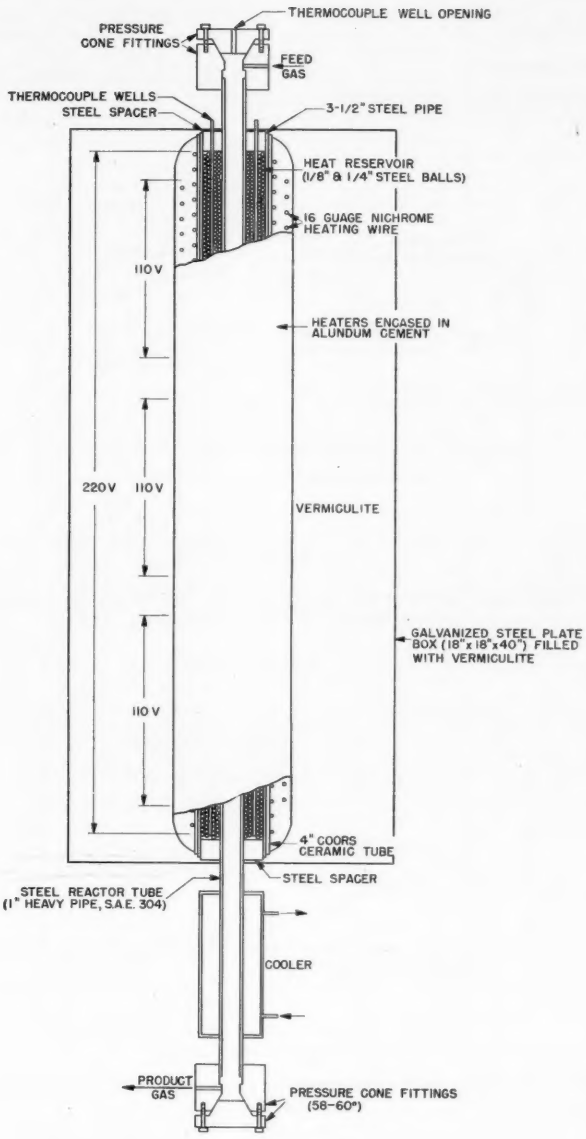

Fig. 2. Cross-sectional drawing of the reactor and cooler.

TABLE 2 CATALYST COMPARISON RUNS

(Typical Portion of Data)

Run	Catalyst age, hr.	Temperature °F.	Pressure, atm.	Feed ratio H_2/CO	Space velocity, mole/(hr.)(sq. ft.)	Feed composition, volume % CO	CO_2	H_2
Catalyst: C1013, unpolished and untreated, 194 balls (0.0661 sq. ft. of surface)								
D33	2.7	1053	30	2.3	0.20	30.6	0.2	69.2
D34	3.8	1048	30	2.3	0.20	30.6	0.2	69.2
D35	4.4	1051	30	2.3	0.20	30.6	0.2	69.2
D36	5.2	1050	30	2.3	0.20	30.6	0.2	69.2

A number of investigations have been directed toward the production of methane from carbon monoxide, carbon dioxide, and hydrogen. The results of a British project to upgrade town gas by synthesizing methane from coal gas have been periodically reported (*11, 6, 12*). Commercial processes have been outlined in the literature (*10, 5, 2*). Intensive kinetic studies of the synthesis of methane on nickel catalysts from hydrogen–carbon monoxide (*1, 14*) and hydrogen–carbon dioxide (*4, 7*) have been made recently.

Recently (*9*) stainless steel pipe was reported to be an effective methanization catalyst in the temperature range of 950° to 1,500°F. The use of finely divided stainless steel particles at lower temperatures to synthesize gasoline has been disclosed (*13*).

The high catalytic activity per unit of surface area shown by steel at 950° to 1,500°F. suggests that the greater surface area of a porous catalyst might be sacrificed to obtain the greater mechanical strength of nonporous-steel catalyst particles. Catalyst crumbling and sintering would be eliminated, making possible more severe operating and carbon-removal conditions. This work is a study of the hydrogenation reactions on such a catalyst in the form of ⅛-in. steel spheres.

EXPERIMENTAL EQUIPMENT

A flow diagram of the experimental unit appears in Figure 1. Commercial gas cylinders (size 1A) were used as the feed-gas source with activated charcoal being used to remove the sulfur from the carbon monoxide. The two feed streams were metered and controlled separately.

The feed streams were mixed before leaving the control system. A wet test meter furnished accurate measurements of the feed and product rates, and the sampling system provided samples of the feed and product streams for Orsat and infrared analyses.

The reactor (Figure 2) consisted of an electrically heated, insulated stainless steel pipe. Steel balls around the reactor pipe provided a large sensible heat reservoir and facilitated the maintenance of a constant reactor temperature. Thermocouple wells provided entry for two iron–constantan couples into the mass of steel balls. A brass liner (not shown) extended the full length of the reactor tube to mask the catalytic steel surface. The copper-covered steel thermocouple well shown in Figure 3 passed through the top pressure cone fitting and supported the catalyst support at a point about 6 in. below the middle of the insulated section of the reactor. A Brown potentiometer measured the bed temperature as indicated by an iron–constantan couple placed within this well.

MATERIALS

Aluminum tubing, steel Ermeto fittings, and Hoke needle valves with steel bodies were used in the experimental apparatus.

The feed gases were obtained commer-

cially. According to the supplier's analyses the hydrogen (electrolytic) had a purity of 99.9% with less than 0.1% oxygen; the carbon monoxide was 96.8% pure with 1% nitrogen, 0.36% carbon dioxide, 0.97% hydrogen, 0.8% hydrocarbons, and 0.3202 mg./liter of sulfur; and the carbon dioxide contained only 0.5% air as an impurity. The methane and helium had purities of 99 and 99.99% respectively.

Three S. A. E. steel alloys (C1013, 440, and 302) were used as catalysts in the form of ⅛-in. balls. Their chemical compositions are listed in Table 1.

ANALYTICAL METHODS

A conventional Orsat apparatus using a 33% sodium hydroxide solution was used for the carbon dioxide analyses. Carbon monoxide, methane, and ethane concentrations in the gas samples were determined with a Baird model B recording infrared spectrophotometer. The hydrogen in the gas streams was determined by subtracting the volume of the other gaseous constituents from the total gas volume. All analyses were on a water-free basis. The water produced in a run was calculated by making

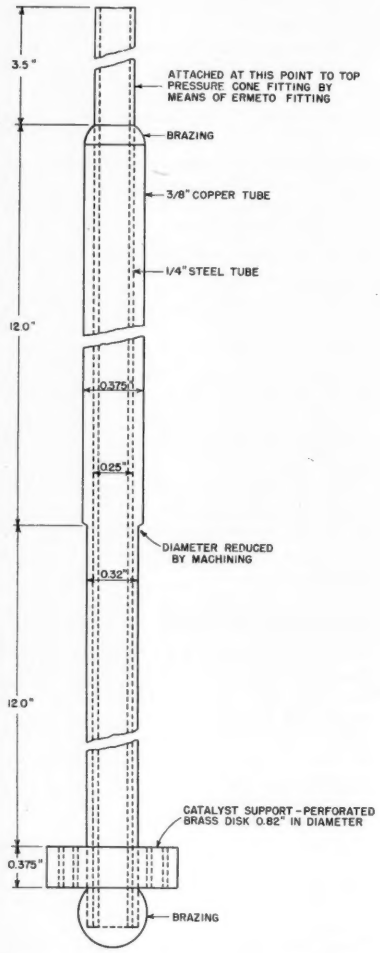

Fig. 3. Thermocouple well and catalyst support.

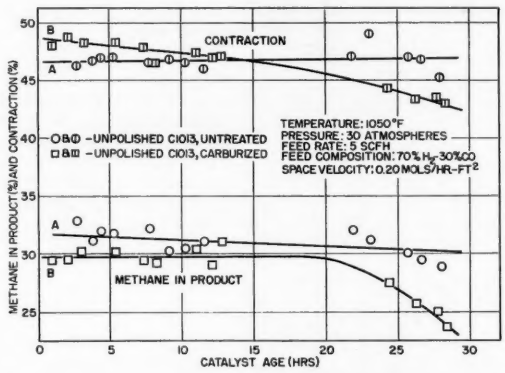

Fig. 4. Effect of carburization on the percentage of contraction and methane produced by the unpolished C1013 steel balls.

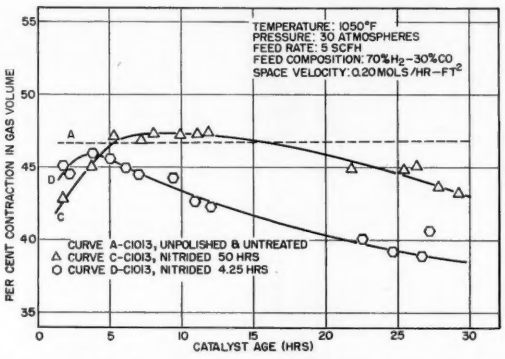
TEMPERATURE: 1050°F
PRESSURE: 30 ATMOSPHERES
FEED RATE: 5 SCFH
FEED COMPOSITION: 70% H2-30% CO
SPACE VELOCITY: 0.20 MOLS/HR-FT2
CURVE A-C1013, UNPOLISHED & UNTREATED
△ CURVE C-C1013, NITRIDED 50 HRS
○ CURVE D-C1013, NITRIDED 4.25 HRS
PER CENT CONTRACTION IN GAS VOLUME
CATALYST AGE (HRS)

Fig. 5. Effect of nitriding on the percentage of contraction obtained with the unpolished C1013 steel balls.

TABLE 3. EVALUATION OF THE UNTREATED C1013 STEEL CATALYST
(Typical Portion of Data)

Run	Catalyst age, hr.	Temperature, °F.	Pressure, atm.	Feed ratio H_2/CO	Feed ratio H_2/CO_2	Space velocity, moles/(hr.)(sq.ft.)	Feed composition, volume % CO	CO_2	H_2	CH_4	Gas flow rates, std. cu. ft./br. Feed	Product
Catalyst bed: 194 steel balls (0.0661 sq. ft. of surface)												
T2	2.3	847	30	—	2.3	0.20	—	30.4	69.6	—	5.02	5.00
T3	4.7	949	30	—	2.3	0.20	—	30.7	69.3	—	4.97	4.89
Catalyst bed: 194 steel balls (0.0661 sq. ft. of surface)												
P1	3.5	1,070	30	2.4	—	0.20	29.0	0.2	70.0	—	5.00	2.76
P4	5.1	1,070	20	2.4	—	0.20	29.0	0.2	70.0	—	5.00	2.87
Catalyst bed: 194 steel balls (0.0661 sq. ft. of surface)												
F1	2.7	1,069	30	5.5	—	0.20	15.4	0.2	84.1	—	5.05	4.36
F4	5.2	1,070	30	4.3	—	0.20	18.9	0.2	80.5	—	5.05	3.64
Catalyst bed: 388 steel balls (0.1322 sq. ft. of surface)												
A9	3.5	1,060	30	2.5	—	0.10	28.6	0.2	70.5	—	5.02	2.71
A12	6.4	1,062	30	2.4	—	0.13	29.1	0.2	69.9	—	6.63	3.65

both an oxygen and a hydrogen balance and averaging the two results.

EXPERIMENTAL METHOD

The first part of the experimental work was concerned with the selection of the best combination of steel composition and catalyst pretreatment. These pretreatments consisted of nitriding, carburizing, and deformation of the steel catalyst surfaces.

The nitriding was accomplished in a small tubular furnace at 1,000°F. with the dissociation of the ammonia maintained at approximately 30%. Precautions were taken to remove oil films from the steel by washing with benzene. Oxide films were removed from the chromium-containing steels by treatment with a 50% hydrochloric acid solution at 150°F. for 3 to 10 min.

The carburization treatment was given only to some C1013 steel balls, increasing their carbon content to 0.9%. Highly polished C1013 and 302 steel ball bearings were also obtained so as to determine the effect of surface deformation on the catalytic activity of the steel.

Samples of these various steel catalysts were tested in the reactor under identical conditions. During these comparison runs (*D* runs) the reactor was maintained at temperature and the catalyst dropped directly into the hot reactor. The reactor was flushed with hydrogen, the catalyst was charged, and the flow of synthesis gas started immediately.

In the remainder of the experimental work the catalyst was put in the reactor at room temperature and heated slowly to the desired temperature under a flow of synthesis gas. The age of the catalyst was considered as zero when the reactor first reached the run temperature.

The steel catalyst balls were always mixed with an equal number of ⅛-in. brass balls to facilitate the removal of heat. Layers of brass balls above and below the catalyst bed served to eliminate entrance and exit effects.

The important data and samples taken for each run are summarized below.

1. Run number, date, and hour.

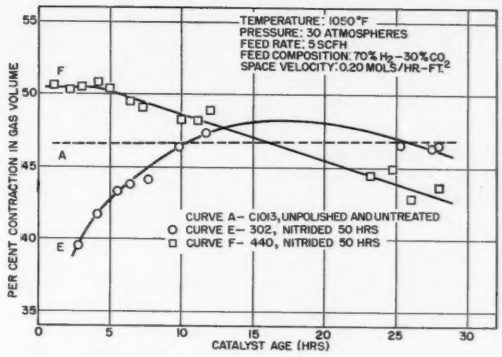
TEMPERATURE: 1050°F
PRESSURE: 30 ATMOSPHERES
FEED RATE: 5 SCFH
FEED COMPOSITION: 70% H2 – 30% CO
SPACE VELOCITY: 0.20 MOLS/HR-FT2
CURVE A – C1013, UNPOLISHED AND UNTREATED
CURVE E – 302, NITRIDED 50 HRS
CURVE F – 440, NITRIDED 50 HRS
PER CENT CONTRACTION IN GAS VOLUME
CATALYST AGE (HRS)

Fig. 6. Comparison of the nitrided 302 and 440 steel balls with the untreated C1013 balls.

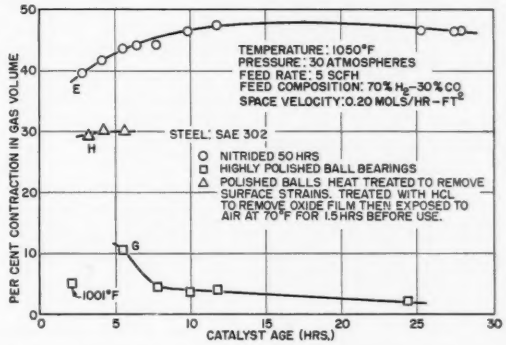
TEMPERATURE: 1050°F
PRESSURE: 30 ATMOSPHERES
FEED RATE: 5 SCFH
FEED COMPOSITION: 70% H2 – 30% CO
SPACE VELOCITY: 0.20 MOLS/HR-FT2
STEEL: SAE 302
NITRIDED 50 HRS
HIGHLY POLISHED BALL BEARINGS
POLISHED BALLS HEAT TREATED TO REMOVE SURFACE STRAINS, TREATED WITH HCL TO REMOVE OXIDE FILM THEN EXPOSED TO AIR AT 70°F FOR 1.5 HRS BEFORE USE.
1001°F
PER CENT CONTRACTION IN GAS VOLUME
CATALYST AGE (HRS.)

Fig. 7. Effect of various surface treatments on the catalytic activity of the 302 steel.

TABLE 4. MECHANISM STUDIES WITH THE UNTREATED C1013 STEEL CATALYST
(Typical Portion of Data)

Run	Catalyst age, hr.	Temperature, °F.	Pressure, atm.	Feed ratio H_2/CO	Feed ratio He/CO	Feed ratio He/CO_2	Space velocity, moles/(hr.)(sq.ft.)	Feed composition, volume % CO	CO_2	CH_4	H_2	He
	Catalyst bed: 194 balls (0.0661 sq. ft. of surface)											
M5	11.5	1,017	30	—	—	—	0.058	—	—	99.0		
M6	14.1	902	30	—	—	—	0.038	—	—	99.0		
	Catalyst bed: 194 balls (0.0661 sq. ft. of surface)											
H1	0.8	828	30	—	2.4	—	0.20	28.6	0.2	—	—	70.5
H3	3.6	950	30	—	2.4	—	0.20	29.2	0.2	—	—	69.9
H4	3.8	947	30	—	2.4	—	0.20	29.2	0.2	—	—	69.9
H5	5.7	Pressure drop through bed greater than 35 lb./sq. in.										
	Catalyst bed: 194 balls (0.0661 sq. ft. of surface)											
H6	0.1	1,042	30	—	2.4	—	0.20	29.3	0.2	—	—	69.7
	Catalyst bed: 194 balls (0.0661 sq. ft. of surface)											
H7	0.4	942	30	—	—	2.3	0.20	—	30.6	—	—	69.4
H10	4.2	1,050	30	—	—	2.3	0.20	—	30.2	—	—	69.8
	Catalyst bed: 8 balls (0.00273 sq. ft. of surface)											
G10	6.4	1,060	30	2.5	—	—	14.60	27.9	1.4	—	70.0	
G11	8.1	1,060	30	2.5	—	—	19.20	27.7	1.1	—	70.5	
G14	9.3	1,061	30	2.5	—	—	9.70	28.0	0.8	—	70.5	
G15	10.5	1,060	30	2.5	—	—	4.84	28.4	0.8	—	70.1	

2. Catalyst type, amount, and pretreatment.
3. Reactor pressure.
4. Catalyst bed temperature.
5. Wet test meter data (time per revolution for feed and product streams, gas temperature, and pressure).
6. Samples for Orsat and infrared analyses.

EXPERIMENTAL DATA

Samples of the various steel catalysts were tested in the reactor under the following conditions:

Temperature	1,050°F.
Pressure	30 atm.
Feed rate	5 std. cu. ft./hr.
Feed composition	70% H_2—30% CO
Catalyst surface	0.0661 sq. ft. (194 balls)

A typical portion of the data obtained in these comparison runs is shown in Table 2. The percentage of contraction in the feed-gas volume was the criterion of catalyst activity used. Product analyses were obtained, however, to show that no significant difference in product distribution existed between the various catalysts.

The results of the comparison runs permitted the selection of the most effective catalyst, and the next portion of the experimental work was devoted to its evaluation. Typical portions of the runs in which the effect of temperature T, pressure P, feed composition F, and space velocity A were determined appear in Table 3, in which each group of runs was made with a different batch of catalyst.

The final part of the experimental work was a study of the rate-controlling steps and the basic reaction paths in the hydrogenation of carbon monoxide and carbon dioxide. The results obtained with a pure methane feed are listed in Table 4 as the M runs. Part of the data from a study of the reactions $CO = CO_2 + C$ and $CO_2 = CO + \frac{1}{2}O_2$ in which helium was substituted for hydrogen is included as the H runs, and the G runs show the effect of mass velocity on the rates of reaction. Complete experimental data are available elsewhere (*17*).

MATERIAL BALANCES

Carbon balances were made for 175 of the experimental runs. Of these, only 23.4% had an error greater than ±5%, and 60% had an error of less than ±3%.

DISCUSSION OF RESULTS

Catalyst-comparison Studies

The results of the catalyst-comparison runs appear in Figures 4 through 7. Figure 4 shows the effect of carburization on the methane produced and the contraction in gas volume obtained with the C1013 steel. Figures 5 and 6 compare the nitrided C1013, 440, and 302 steels to the untreated C1013, represented by the dotted lines. The nitrided catalysts, with the exception of the 440 steel, exhibited an initial increase in activity. The heavily nitrided C1013 and 302 balls had almost no catalytic activity at time zero, indicating that excessive nitrogen can destroy the catalytic activity of the steel.

Tukon diamond pyramid hardnesses taken across a center plane of the nitrided steel balls before and after use in the reactor indicated a rapid loss of nitrogen during the synthesis period. Part of the hardness measurements from the nitrided

Table 5. Hardness of Nitrided C1013 Steel Balls Before and After Use in the Reactor

Distance from surface, mm.	Nitrided 4.25 hr.		Nitrided 50 hr.	
	Before	After	Before	After
0.02	289	104	—	448
0.05	288	107	—	445
0.10	270	110	500	400
0.30	214	120	175	109
0.50	175	—	150	122
0.70	168	—	127	123

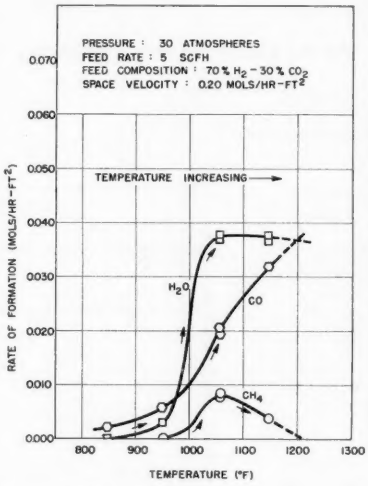

Fig. 8a. Effect of increasing temperature on the reaction rates obtained with a H_2–CO_2 feed.

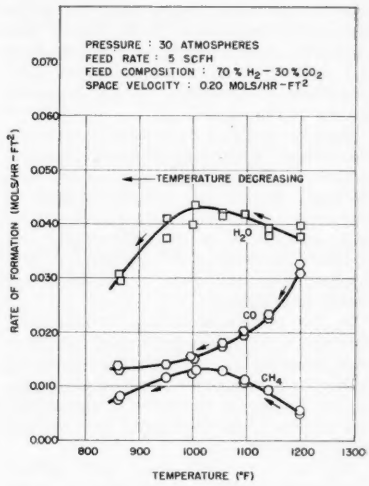

Fig. 8b. Effect of decreasing temperature on the reaction rates obtained with a H_2–CO_2 feed.

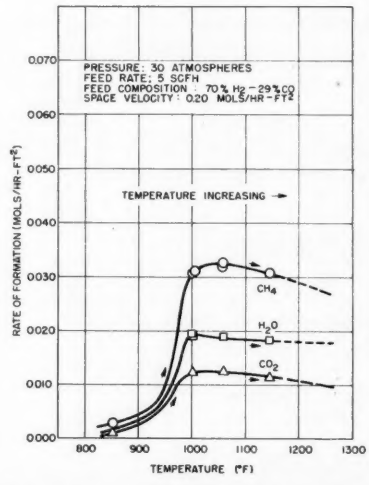

Fig. 9a. Effect of increasing temperature on the reaction rates obtained with a H_2–CO feed.

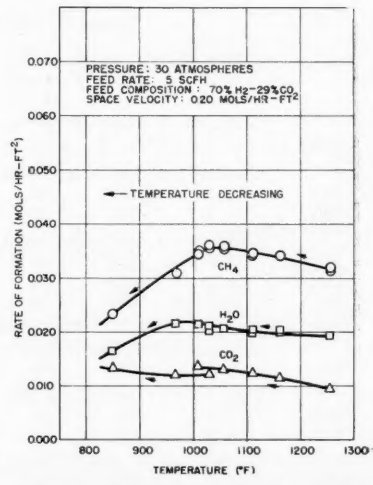

Fig. 9b. Effect of decreasing temperature on the reaction rates obtained with a H_2–CO feed.

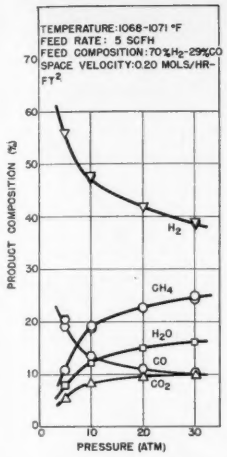

Fig. 10a. Effect of pressure on the product obtained with a H_2–CO feed.

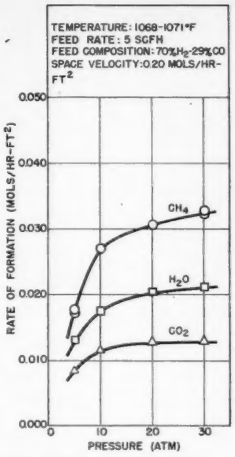

Fig. 10b. Effect of pressure on the reaction rates obtained with a H_2–CO feed.

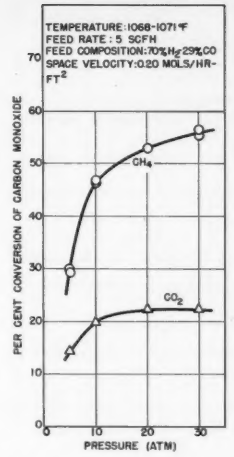

Fig. 10c. Effect of pressure on the conversions obtained with a H_2–CO feed.

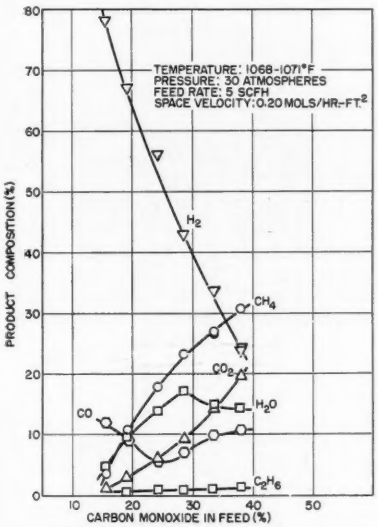

Fig. 11. Effect of varying the feed carbon monoxide concentration on the product obtained with a H_2–CO feed.

C1013 steel balls appears in Table 5. The loss of nitrogen is probably associated with the increase in activity with the maximum activity corresponding to an optimum amount of nitrogen. The behavior of the 440 steel is perhaps explained by assuming that it contained the optimum amount of nitrogen at the beginning of the test period.

Anderson et al. (*3*) in their work with a nitrided synthetic-ammonia iron catalyst reported that carbon replaced the nitrogen in the iron lattice. This is probably the reason for the serious deactivation of the nitrided catalysts in the later portion of the test period.

Figure 7 shows the effect of various surface treatments on the catalytic activity of the 302 steel. The polished balls exhibited a low activity, probably owing to the protective oxide film on stainless steel. The reactor temperature of 1,050°F. probably relieved the surface strains due to polishing, but the reduction of the chromium oxide film on stainless steel is unlikely under the reactor conditions. A heat treatment to remove surface strains followed by a treatment to remove the oxide film resulted in an increase in activity for the 302 steel, but it remained inferior to the untreated C1013 steel. Again this lower activity was attributed to the formation of a light oxide film during the 1.5 hr. of exposure to air between the hydrochloric acid treatment and the introduction of the catalyst into the reactor. Nitriding the 302 steel probably destroyed the oxide film and resulted in an activity comparable with that of the untreated C1013 steel.

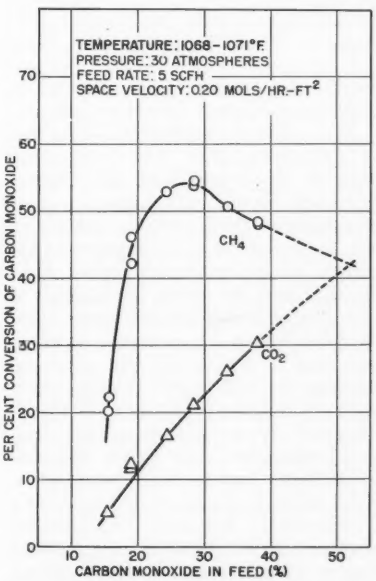

Fig. 12. Effect of varying the feed carbon monoxide concentration on the percentage of conversion of carbon monoxide to methane and carbon dioxide.

Polishing the C1013 steel had a temporary inhibiting effect on its catalytic activity. The steel exhibited almost no catalytic activity during the first 40 min. in the reactor and then suddenly became active. No conclusions could be drawn as to whether the surface distortion or an oxide film was responsible as 40 min. at the reactor conditions would be sufficient to eliminate both in this case.

The results of the catalyst comparison runs showed that ordinary carbon steel (C1013) was superior to stainless steel. Carburizing, nitriding, and surface-distortion treatments had a deleterious effect on the activity of the C1013 steel. Nitriding the 440 and 302 steels failed to produce a catalyst superior to the plain C1013 steel. The untreated, unpolished C1013 steel was therefore chosen as the most effective catalyst of those tested.

Evaluation of the Untreated C1013 Steel Catalyst

Effect of Temperature. The effect of temperature on the reaction rates obtained on the C1013 catalyst with H_2—CO_2 and H_2—CO feeds appears in Figures 8 and 9. In both cases the points were taken in the order of increasing temperature until 1,200° or 1,250°F. was reached. The reactor was allowed to operate at that temperature for 12 hr. before the decreasing-temperature curves were started. On the way down another 12-hr. period of constant temperature occurred at approximately 1,000°F. in both cases. The 12-hr. period above 1,200°F. resulted in an increase in catalyst effectiveness causing the decreasing temperature curves for methane to lie above the increasing temperature curves for that constituent. The 12-hr. period at 1,000°F. caused only minor changes in the catalyst activity. A similar independence of time is exhibited by the C1013 steel at 1050°F. in Figures 4 and 18.

Comparison of Figures 8 and 9 illustrates the difference in product distribution obtained with H_2—CO_2 and H_2—CO feeds. With a H_2—CO_2 feed the principal products in the order of their abundance were water, carbon monoxide, methane, and ethane. With a H_2—CO feed, methane became the most abundant product, followed by water, carbon dioxide, and ethane in that order. The rate of formation of methane at 1,050°F. was four times as great with a H_2—CO feed. Both feeds gave carbon deposition.

The rates of reaction experience a

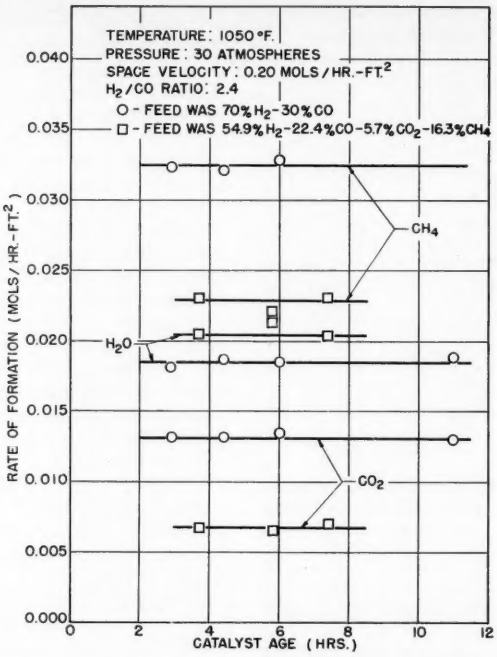

Fig. 13. Effect on the reaction rates caused by the addition of methane and carbon dioxide to a H_2–CO feed.

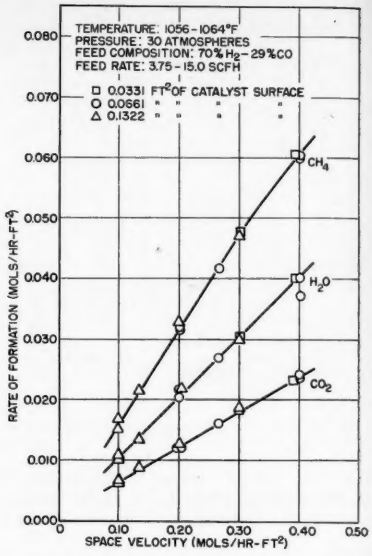

Fig. 14. Effect of varying the space velocity on the reaction rates obtained with a H_2–CO feed.

TABLE 6

Mass velocity, lb./(hr.)(sq. ft.)	Feed, % CO	CO_2	H_2	Product, CH_4, %	Order of taking
35	28.4	0.8	70.1	3.4	4
70	28.0	0.8	70.5	1.9	3
105	27.9	1.4	70.0	1.4	1
140	27.7	1.1	70.5	1.2	2

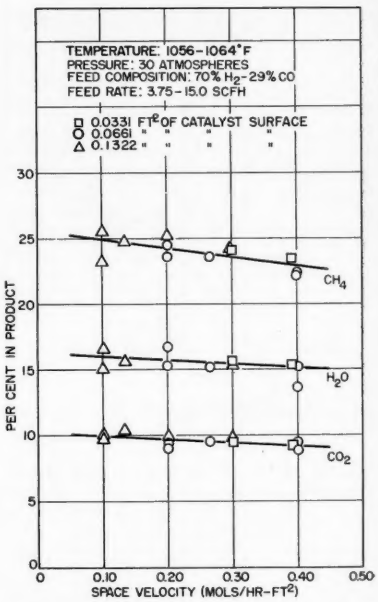

Fig. 15. Effect of varying the space velocity on the product obtained with a H_2–CO feed.

large increase as the temperature goes from 925° to 1,025°F. This threshold phenomenon occurs with both H_2—CO_2 and H_2—CO feeds.

Effect of Pressure. Increasing the pressure from 5 to 30 atm. increases the rates of reactions, with most of the increase occurring below 10 atm. The shape of the curves in Figure 10 indicates that at some pressure less than 100 atm. the rate of formation of methane would become independent of pressure, a condition already reached by the rate of formation of carbon dioxide at 20 atm.

The rate of carbon deposition below 10 atm. was much greater than at 30 atm. Six hours of synthesis at the lower pressures was sufficient to plug the catalyst bed. Operation at 30 atm. and the same feed and temperature conditions for periods of 30 hr. was accomplished in other runs without excessive carbon deposition.

The decrease in carbon deposition with increasing pressure is a stronger reason for operation at pressures above 30 atm. than is the relatively slight increase in methane production to be obtained.

Effect of Feed Composition. The effect of feed composition was investigated only in the range 0 to 38% carbon monoxide because of the heavy carbon deposition at the higher concentrations. Figure 11 shows how increasing the carbon monoxide concentration in a H_2—CO feed decreases the dilution of the product by unused reactants. However, increasing the amount of carbon monoxide in the feed is not so advantageous as this figure alone would indicate. In addition to the difficulty of increased carbon deposition, the fractional conversion of the carbon monoxide to methane begins to decrease above 27% carbon monoxide in the feed. This is illustrated in Figure 12. Extrapolation of the curves in Figure 12 indicates that the conversion to carbon dioxide would equal the conversion to methane at a H_2/CO feed ratio of approximately 1.

The effect of adding methane and carbon dioxide to a H_2—CO feed is summarized in Figure 13. The H_2/CO ratio was 2.4 for both the H_2—CO and mixed feeds. The addition of methane and carbon dioxide to the feed decreased the rates of formation of those two compounds by 29 and 48% respectively. The rate of formation of water was increased by approximately 10%. Carbon deposition was heavier with the mixed feed, indicating that the ratio $H_2/(CO + CO_2)$ is more important in predicting carbon formation than the H_2/CO ratio.

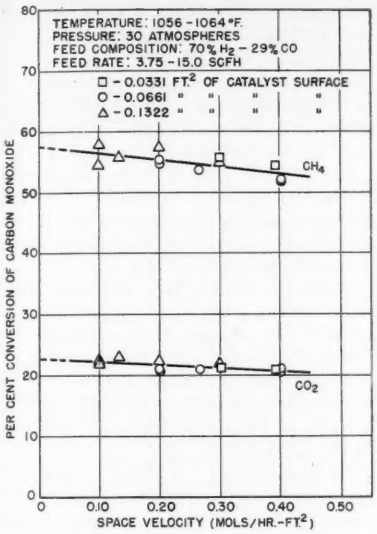
TEMPERATURE: 1056 - 1064 °F.
PRESSURE: 30 ATMOSPHERES
FEED COMPOSITION: 70% H2 - 29% CO
FEED RATE: 3.75 - 15.0 SCFH
□ - 0.0331 FT.2 OF CATALYST SURFACE
○ - 0.0661 " " " "
△ - 0.1322 " " " "
CH4
CO2
PER CENT CONVERSION OF CARBON MONOXIDE
SPACE VELOCITY (MOLS/HR.-FT.2)

Fig. 16. Effect of varying the space velocity on the conversion of the feed carbon monoxide to methane and carbon dioxide.

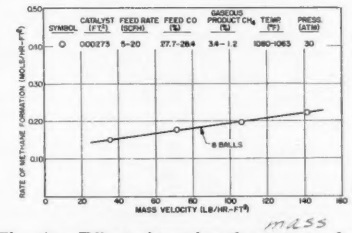

Fig. 17. Effect of varying the space velocity on the rate of methane formation.

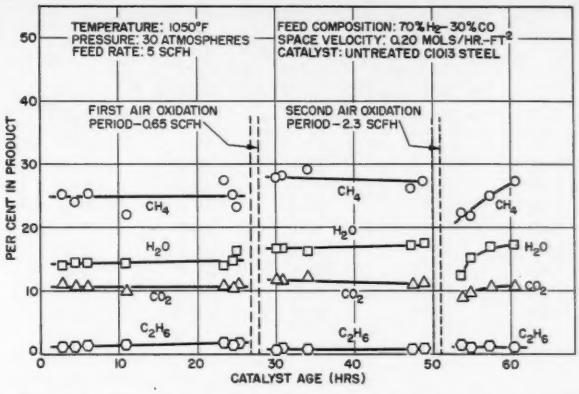

Fig. 18. Effect of regeneration by oxidation on product formation.

The large percentage decrease in the carbon dioxide formation rate caused by a relatively small amount of that constituent in the feed is encouraging. The ratio of the rate of methane formation to that of carbon dioxide was 3.4 for the mixed feed compared with 2.5 for the H_2—CO feed. An even more favorable ratio would probably have occurred if methane had not also been added with the carbon dioxide.

Effect of Space Velocity. The space velocity was defined as total moles fed/hour/square foot of catalyst surface in order to make it independent of catalyst-particle size.

The expression of average reaction rates or conversions as a function of space velocity eliminates bed depth as a variable. This was demonstrated by varying the space velocity by (1) changing the amount of gas flowing over a given number of balls and (2) holding the gas flow constant while the number of balls varied. The results are shown in Figures 14, 15, and 16. The number of balls (and the bed depths) used varied fourfold, and the flow rates ranged from 3.75 to 15.0 std. cu. ft./hr. Figure 14 shows that bed depth or mass velocity had no appreciable effect on the average reaction rates obtained at a given space velocity. Mass velocity does have an effect on the initial reaction rate, as shown later, but in these runs made with an integral reactor the effect is masked by the excessive bed depths used.

The product distribution remained essentially constant over the range of space velocity studied (Figure 15).

Extrapolation of the curves in Figure 16 to zero space velocity indicates that the maximum possible conversion of the carbon monoxide to methane and carbon dioxide is 57.5 and 22.5% respectively. Approximately 2% of the carbon monoxide would be converted to ethane, giving a total conversion of about 82%. This is considerably less than the conversion indicated by equilibrium calculations.

Effect of Mass Velocity. The rate of mass transfer of reactant and product molecules to and away from the catalyst surface is a function of the mass velocity of the gases through the catalyst bed. If mass transfer is the rate-controlling step in the over-all reaction, then the reaction rates are a function of mass velocity.

The mass velocity through a differential bed (eight balls) was varied fourfold to determine the effect on the reaction rates. A differential bed was used to give small conversions so that the composition of the reacting system was substantially independent of feed rate. Table 6 lists the feed concentrations, the methane produced, and the order of the four points shown in Figure 17. Figure 17 shows an increasing reaction rate with increasing mass velocity. If the small variation in the carbon monoxide concentration of the feed had been absent, the slope of the curve would have been greater.

The order eliminated any effect of time on the experimental results. The conversion, with the possible exception of the first run, was low enough to eliminate the effect of changing concentration potentials. Therefore, the increase in the rates of formation of methane with increasing mass velocity is probably due to the smaller resistance to mass transfer at the higher gas velocities. This indicates that mass transfer may be partially a rate-controlling step in the over-all reaction process.

At first glance, Figure 17 appears to contradict the conclusions drawn from Figure 14, namely, that the rate of formation of methane was independent of mass velocity at any given value of space velocity. No contradiction exists; the effect of mass velocity is simply masked when bed depths great enough to push the reaction close to completion are used. In that situation a change in reaction rate in the first increment of bed depth caused by a change in mass velocity is compensated for in the latter part of the bed. This was the case in the data shown in Figure 14. Figure 16 shows the almost negligible effect of quadrupling the bed size on the conversion obtained, indicating that even in the smallest bed the bottom portion of the catalyst supported only a small part of the total reaction and was always available to compensate for any change in reactivity of the top portion.

Removal of Carbon by Oxidation with Air. A series of runs was made to investigate the possibility of removing the carbon from the catalyst by oxidizing it with air. The results of these runs appear in Figure 18.

The reactor pressure was reduced to 1 atm. and the synthesis gas flushed from the reactor with nitrogen before each oxidation period. The carbon removal was incomplete during the first oxidation period (0.65 std. cu. ft./hr. of air; bed temperature = 1,015°F.) with the exit gases containing 5.9% carbon dioxide at the end of an hour. During the second oxidation period (2.3 std. cu. ft./hr.; bed temperature = 1,020° to 1,040°F.), the removal of carbon was almost complete with the exit gases containing only 0.1% carbon dioxide at the end of an hour.

The reactor was cooled and the catalyst

Table 7. Reproducibility of Results

Pressure: 30 atm.
Feed rate: 5 std. cu ft./hr.
Space velocity: 0.20 mole/(hr.)(sq. ft.)

Run	Temp., °F.	Feed composition, % CO	H_2	Percentage in product CH_4	CO_2	H_2O
O3	1050	30.0	70.0	25.4	10.5	14.2
T29	1058	28.9	69.8	25.0	9.7	14.4
A13	1060	28.6	70.5	25.6	10.2	16.5
A29	1060	29.0	70.0	24.3	9.5	16.8
A2	1063	28.8	70.3	23.7	9.1	15.3
A10	1063	28.5	70.6	23.4	9.8	15.1
F7	1069	28.3	70.8	23.4	9.4	17.0
P1	1070	29.0	70.0	24.8	9.8	16.0

removed after the second oxidation period. The usual black powder was not present in the bed. Some reddish-brown powder, presumably ferric oxide, was found. This iron oxide was not the result of oxidation of the steel but originated from the iron present in the unoxidized carbon deposit. The percentage of iron mixed with the carbon was always large enough to magnetize the powder removed from a used bed.

The catalyst was returned to the reactor after 27 days of exposure to the atmosphere at room temperature. The curves starting at approximately 53 hr. in Figure 18 show the effect of the long shutdown period on the catalyst activity.

Reproducibility of Results. Table 7 lists several runs made under approximately the same experimental conditions but with different batches of the C1013 catalyst. The results show a high degree of consistency, particularly so if allowances are made for the variations in temperature and feed concentration between the various runs.

Mechanism Studies

The identity of products obtained from H_2—CO and H_2—CO_2 feeds and the fact that both reactions exhibit the same threshold phenomenon between 925° and 1,025°F. imply that the hydrogenations follow similar paths. The conversion of a major portion of the feed carbon oxide to the other carbon oxide suggests that the reactions relating the two oxides might be basic steps in these reaction paths.

To study that part of the over-all reaction which relates the two oxides, hydrogen was eliminated from the feed. Inert helium was used in its place to permit operation at 30 atm. without changing the partial pressure of carbon oxide in the feed. The experimental conditions of the temperature traverses with H_2—CO_2 and H_2—CO feeds (Figures 8 and 9) were duplicated to permit comparisons of the conversions of the carbon oxide with and without the presence of hydrogen.

He—CO Feed. The rate of formation of carbon dioxide from a He—CO feed is compared in Table 8 with the rate obtained with a H_2—CO feed.

Table 8

Temperature °F.	Carbon dioxide formation rate, moles/(hr.)(sq. ft). H_2—CO Feed	He—CO Feed
828	0.0006	0.00099
851	0.0009	
950	0.0062	0.00875
1002	0.0121	
1042	0.0123	0.0223
1058	0.0123	

The reaction which occurred with a He—CO feed can be represented by the following stoichiometric equation:

$$2CO = CO_2 + C$$

This reaction was catalyzed by the steel balls. It underwent the same increase in activity at the threshold temperature as the over-all reaction occurring with a H_2—CO feed, indicating that the threshold phenomenon exists for the over-all hydrogenation reaction because of an increase in the rate of this reaction in that temperature range.

The rate of carbon dioxide formation at 1,042°F. with a He—CO feed was approximately twice that with a H_2—CO feed. However, the rate of carbon monoxide conversion was almost the same for both feeds, approximately 0.045 mole/(hr.)(sq. ft.). A reasonable explanation is the hydrogenation of some of the adsorbed carbon monoxide to methane. The hydrogenation occurring in this manner diverts part of the carbon from its destination of carbon dioxide and causes it to appear as hydrocarbons.

He—CO_2 Feed. The equilibrium for the reaction

$$CO_2 = CO + \tfrac{1}{2}O_2$$

is such that no appreciable conversion of the carbon dioxide to carbon monoxide could be expected in the absence of hydrogen. The ratio $(CO^{3/2}/CO_2$ at 980° and 1,160°F. is 3.3×10^{-15} and 3.7×10^{-13}, respectively, at equilibrium. Evidence exists, however, that the conversion proceeded to some extent. The steel balls when removed from the reactor possessed the blue-black color of oxidized steel surfaces. The oxidation could have been due to the 0.1% oxygen in the feed gases or to the leakage of a small amount of air into the reactor during the cooling period. It is believed, however, that the bulk of the oxidation was due to the conversion of the carbon dioxide to carbon monoxide. The ability of carbon dioxide to oxidize steel is recognized in its classification as an oxidizing atmosphere in metallurgical operations.

Methane Feed. Pure methane was passed over a fresh batch of steel balls at 1,000°F. No change in gas volume or traces of ethane in the exit gas stream could be detected. This indicated that the production of ethane was not dependent on the prior appearance of methane in the gas stream.

Hydrogen Feed. A feed stream of hydrogen was passed over a bed of used catalyst which had been operated under carbon-depositing conditions with a H_2—CO feed for several hours. The bed was thoroughly flushed with nitrogen before the hydrogen was admitted. A small amount of methane was formed initially, probably from the carbon monoxide adsorbed on the catalyst, but the hydrogen did not appear to react with the carbon deposit.

LITERATURE CITED

1. Akers, W. W., and R. R. White, *Chem. Engr. Progr.*, **44**, 553 (1948).
2. Alberts, L. W., J. S. Bardin, D. W. Beery, H. R. Jones, and E. J. Vidt, *Chem. Engr. Prog.*, **48**, 486 (1953).
3. Anderson, R. B., J. F. Schultz, B. Seligman, W. K. Hall, and H. H. Storch, *J. Am. Chem. Soc.*, **72**, 3502 (1950).
4. Binder, G. G., and R. R. White, *Chem. Engr. Prog.*, **46**, 563 (1950).
5. Breck, C. R., *Gas*, **28**, No. 5, 44 (1922).
6. Dent, J. F., and D. Hebden, *Gas J.*, **261**, 160, 167 (1949).
7. Dew, J. N., Ph.D. thesis, Univ. Mich., Ann Arbor (1953).
8. Fischer, F., and H. Tropsch, *Brennstoff-Chem.*, **4**, 276 (1923).
9. Gilkeson, M., R. R. White, and C. M. Sliepcevich, *Ind. Eng. Chem.*, **45**, 460 (1953).
10. Gross, H. W., *Erdöl u. Kohle*, **3**, 218 (1950).
11. King, J. G., *Gas Research Board (British)*, No. **GRB 67** (1952).
12. ———, *Gas World*, **122**, 196, 404 (1945).
13. Layng, E. T., U. S. Pat. 2,506,226 (May 2, 1950).
14. Pursley, J. A., R. R. White, and C. M. Sliepcevich, *Chem. Eng. Progr.*, **48**, 51 (1952).
15. Sabatier, P., and J. B. Senderens, *Compt. rend.*, **124**, 1358 (1897).
16. ———, *J. Soc. Chem. Ind.*, **21**, 504 (1902).
17. Smith, B. D., Ph.D. dissertation, Univ. Mich., Ann Arbor (1954).
18. Storch, H. H., N. Golumbric, and R. B. Anderson, "The Fischer-Tropsch and Related Syntheses," John Wiley and Sons, Inc., New York (1951).

Presented at A.I.Ch.E. New York meeting

Mechanics of Steady State Single-phase Fluid Displacement from Porous Media

D. U. VON ROSENBERG

Humble Oil and Refining Company, Houston, Texas

The physical processes are discussed by which a fluid is displaced from a porous medium during steady state viscous flow by another fluid of the same density and viscosity under conditions of complete miscibility of the two fluids. The displacement occurs on a microscopic scale as a result of combined convective and diffusional mixing. The length of the zone of mixing which comprises the displacement front is predicted to be dependent upon the rate of flow, the diffusion coefficient for the two-fluid system, the characteristics of the pore geometry, and the distance the front has traversed at the time of its observation.

Experimental data are presented for the displacement of benzene by ethyl *n*-butyrate at several rates of flow from packed sand columns. These data show that the length of the frontal mixing zone after a prescribed distance of flow is greater at the higher rates of flow. The postulated dependence of the length of the front upon the diffusion coefficient and the pore geometry has not yet been investigated.

Most of the studies carried out in the past on multifluid flow through porous media have been concerned with the behavior of immiscible fluids. Recently, however, laboratory (*1, 3, 4, 5, 7*) and field (*2*) studies of the displacement of oil from a reservoir by liquefied petroleum gas have served to call attention to the problem of miscible fluid displacement. Although these studies have yielded much valuable information, there remains a need for a fundamental study of the physical mechanism which is involved in the displacement from a porous medium of one fluid by another fluid miscible with it. It was to help fill this need that the work described in this report was undertaken. There are many parameters involved in miscible displacement. Not all were investigated in this work, which was limited to the case in which both fluids are of equal viscosity and density.

TAYLOR'S ANALYSIS OF FLOW IN A CAPILLARY

Although an analysis of miscible displacement through a porous medium is extremely complex, a study of such displacement in a capillary is feasible. The qualitative concepts gleaned from the capillary study can be extended to the more complex geometry of a porous medium. G. I. Taylor (*6*) has made such an analysis of capillary flow, and his results will be used.

For laminar flow of a single liquid in a cylindrical tube, the velocity distribution is parabolic, with the maximum velocity on the axis of the tube being exactly twice the average velocity. Thus, if one fluid is displacing another of the same density and viscosity, the invading fluid at the center of the tube moves much more rapidly than that near the edge of the tube. In the absence of radial diffusion, an ever-lengthening needle of invading fluid extends down the tube. The point of this needle traverses any length of the tube when one half of the fluid contained in that length has been displaced. Breakthrough, that is, the first appearance of invading fluid, *always* occurs after half a pore volume has been injected.

Actually, however, the penetration of the resident fluid by the invading fluid establishes a large radial concentration gradient, and the fluids interdiffuse radially, thus blunting the point of the needle. If the time required for molecular diffusion to minimize the radial concentration gradient is much shorter than the time for appreciable gradients to be established by the parabolic velocity distribution, no needle will occur. Under these conditions a diffuse front or mixing zone will be established in which there is essentially no radial variation of concentration. The length of this front can be defined as the distance through which the concentration varies from 0 to 100% invading fluid. The cross section at which the composition consists of equal amounts of the two fluids moves with an apparent velocity equal to the average stream velocity. This fact has been demonstrated by Taylor's simplified analysis and limited series of experiments. The fluid composition varies symmetrically about this cross section. The length of the front at any distance downstream from the entrance of the tube is a function of the diameter of the tube, the rate of injection, and the coefficient of diffusion between the two liquids.

In order to obtain the equation describing this displacement, one may let the maximum velocity in a capillary of radius a be V, and r be the distance in the radial direction. The dispersion of the front is then governed by

$$-D\left(\frac{\partial^2 C}{\partial r^2}+\frac{1}{r}\frac{\partial C}{\partial r}+\frac{\partial^2 C}{\partial x^2}\right)=\frac{\partial C}{\partial t}+V\left(1-\frac{r^2}{a^2}\right)\frac{\partial C}{\partial x} \quad (1)$$

where t is the time from the start of the displacement, and x is the distance downstream from the starting point of the displacement.

The equation can be put into dimensionless form by multiplying through by a^2/D to give

$$-\left(\frac{\partial^2 C}{\partial \rho^2}+\frac{1}{\rho}\frac{\partial C}{\partial \rho}+\frac{\partial^2 C}{\partial \xi^2}\right)=\frac{\partial C}{\partial \tau}+\frac{Va}{D}(1-\rho^2)\frac{\partial C}{\partial \xi} \quad (2)$$

The only parameter in the equation is $(a \cdot V/D)$. The displacement history can be described by this one parameter when the independent variables are considered in their dimensionless forms.

Taylor has obtained an approximate solution of this equation for conditions of negligible forward diffusion and very rapid lateral diffusion. This is given in a rearranged form as Equation (3).

$$C=\frac{1}{2}-\frac{1}{2}\operatorname{erf}\left[\left(x-\frac{Vt}{2}\right)\left(\frac{48D}{a^2V^2t}\right)^{1/2}\right] \quad (3)$$

where

$$\operatorname{erf} z=\frac{2}{\sqrt{\pi}}\int_0^z e^{-z^2}\,dz$$

It should be noted that the concentration for these conditions is constant across any given cross section because of the required condition of very rapid lateral diffusion.

An examination of Equation (3) will show that for negligible forward diffusion and very rapid lateral diffusion the length of the front is directly proportional to the square root of the distance traversed at any given velocity. Also, at any given distance traversed, the length of the front is directly proportional to the square root of the velocity and inversely proportional to the square root of the diffusion coefficient.

EXTENSION OF ANALYSIS TO POROUS MEDIA

These equations cannot be applied directly to flow in porous media. However, when the flow in a single flow channel or pore is examined, the same mechanism of forward convection and transverse diffusion is found to apply. Some velocity profile, certainly not parabolic, is established by the shear on the walls of the pore. Flow with this velocity profile then establishes the radial concentration gradients which give rise to the transverse diffusion.

Because of the geometry of the pore space in a porous medium, at many points two or more flow channels come together into a single channel and then separate. Observation of flow in a Lucite grid shows that the streams remain as entities as they pass through the intersections. There is no mixing of adjacent streams as a result of the flow patterns. Streams may be forced nearer together, mixing by transverse diffusion being thereby enhanced, but the mixing must take place by diffusion. The path taken by any stream is governed solely by the pressure distribution. Since the mixing occurs only as a result of diffusion, it seems likely that the parameter aV/D can be used to characterize the displacement in porous media if the average lateral distance for diffusion can be characterized by a single dimension a. The effects of the various flow variables upon the length of the front should be qualitatively the same for porous media as for displacement in a single tube.

In porous media there is variation in sizes of the pores, and this alone would tend to establish a front between the invading and resident fluids. Since the invading fluid flows faster in the larger channels than in the smaller ones, it reaches the outflow end of the medium sooner in the larger channels than in small ones. Thus, when the composition of the effluent is determined, a gradual increase in concentration of the invading fluid is found. The length of the front established by this mechanism is independent of the flow rate.

Flow in oil reservoirs is slow enough that molecular diffusion in the direction of flow is probably also important in establishing a concentration gradient between the two fluids. Since the extent of the molecular diffusion for a given system is dependent only upon the time for diffusion, the length of the front estab-

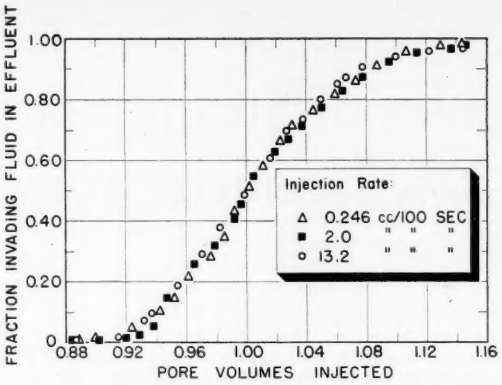

Fig. 1. Displacement curves for 1-ft. column.

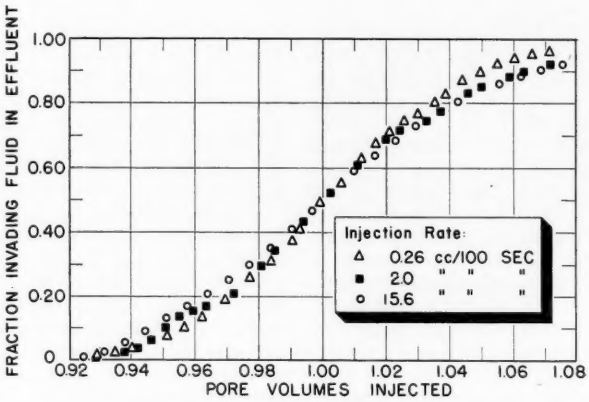

Fig. 2. Displacement curves for 2-ft. column.

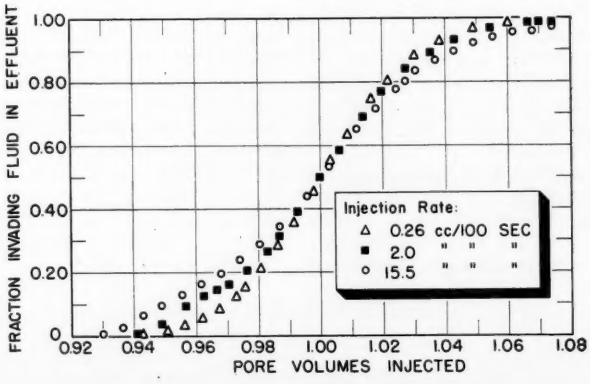

Fig. 3. Displacement curves for 4-ft. column.

lished by this mechanism should be shorter at faster rates. It should be noted that this variation is exactly opposite to that found in the longitudinal convection and subsequent transverse diffusion mechanism proposed by Taylor. Despite the obvious differences in geometry between a single capillary and a porous medium, a qualitative extension of the concepts gained from an analysis of displacement in a capillary can be made to that in a porous medium. Such an extension cannot be made for two-phase flow.

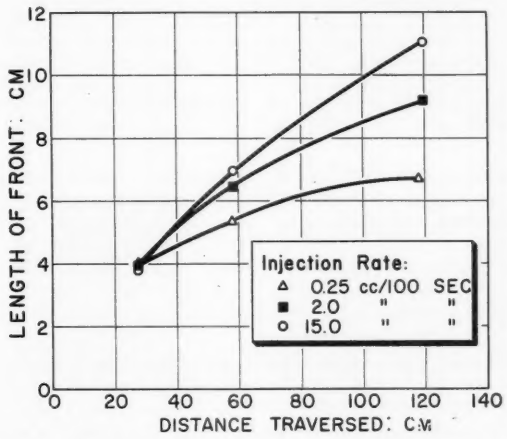

Fig. 4. Variation of length of front with distance traversed.

APPARATUS AND PROCEDURE

To investigate experimentally the applicability of the reasoning given in foregoing sections to displacement in porous media, runs were made in 1-, 2-, and 4-ft. Pyrex columns of 1½-in. I.D. The columns were packed with Ottawa sand, by use of a shaking table, to a porosity of 35 to 40%. (Although the columns were packed with the same sand, there was some variation in the permeabilities, these being 5.6, 7.5, and 6.6 darcys, respectively.)

Preliminary runs were made with sodium chloride solutions of two different concentrations. The displacement curves were found to differ according to which solution was used as the displacing fluid. When sucrose was added to the dilute solution to increase its viscosity to that of the concentrated, the displacement curves were identical, regardless of which solution was used as the displacing fluid. Furthermore, these curves very nearly approximated those obtained when the concentrated or more viscous solution displaced the less viscous one. Although salt solutions could thus be used if their viscosities were equalized, it was found more convenient to conduct later experiments with organic liquids.

A search of tables of physical properties revealed several pairs of organic liquids which would satisfy the conditions of essentially equal viscosity and equal density. The pair used was ethyl *n*-butyrate and benzene, with ethyl *n*-butyrate being used as the displacing fluid, since its viscosity is about 0.03 cp. higher than that of benzene The densities of these two liquids vary by 0.001 g./cc.

The sand column was saturated with benzene preliminary to the start of the actual run. Ethyl *n*-butyrate was then injected into the column at a constant rate by a specially constructed pump that consisted simply of a motor-driven plunger which forced the liquid from a cylinder. The rate was determined by measuring the time necessary to collect a measured volume of effluent. Samples of effluent were taken at various intervals, and refractive index measurements were made to determine their compositions and thus the displacement curve.

RESULTS AND DISCUSSION OF RESULTS

Figures 1, 2, and 3 are displacement curves (fraction displacing fluid in effluent vs. pore volumes produced) for runs in the three columns at rates of 0.25, 2, and 15 cc./100 sec. (These rates correspond to approximately 2, 16, and 120 ft./day.)

In all cases the concentration reached 0.5 very near to the time when one pore volume, as measured experimentally, had been injected. Table 1 compares the

Table 1. Calculated and Measured Pore Volumes

Rate for pore volume calculation, cc./100 sec.	Pore volume 1-ft. column, cc.	2-ft. column, cc.	4-ft. column, cc.
0.25	114	241	471
2.0	113	240	495
15	118	240	491
Measured value	115	238	

measured pore volume with that obtained by multiplying the measured rate by the time at which the concentration reached 0.5. The only wide variation is for the slow run in the 4-ft. column, and an error of 0.01 cc./100 sec. in the rate measurement would account for this deviation. In order to facilitate comparison of the curves for the various runs, the time at which the concentration reached 0.5 was taken as the time required to inject one pore volume, thus forcing all curves through one common point.

Figure 1 shows that there is little difference in the length of the front for the three rates after the liquids have flowed 1 ft. At 2 ft., as shown in Figure 2, there is a distinct effect of rate, with the front being sharper at slower rates, and at 4 ft., as shown in Figure 3, the difference in lengths of the fronts is even more pronounced. Table 2 lists the lengths of the

Table 2. Variation in Length of the Front with Distance Flowed and Velocity

Rate, cc./100 sec.	Distance flowed, cm.	Length of front, pore volumes	Length of front, cm.
0.25	27.6	0.142	3.92
0.25	57.9	0.0925	5.35
0.25	118.0	0.0570	6.73
2.0	27.6	0.143	3.94
2.0	57.9	0.112	6.45
2.0	118.0	0.078	9.20
15.0	27.6	0.137	3.78
15.0	57.9	0.120	6.95
15.0	118.0	0.0935	11.03

fronts measured between displacing-fluid concentrations of 0.10 and 0.90 in pore volumes and in centimeters. The front length here is not measured as the distance between two given concentrations at a specified time as was previously defined but is measured in terms of the volume which must be flowed to cause the concentration to decrease from 0.9 to 0.1. However, there is probably little difference between the measured and defined lengths in these experiments. Figure 4 is a plot of the lengths of the front vs. distance traversed for the three rates.

It is seen from these results that the velocity has a definite effect on the length of the front at any given distance traversed, after an initial distance in which the front is established. At the slowest rate, which is in the order of reservoir rates, the front grows very slowly. At a velocity sixty times greater, the length of the front is double that at the slowest rate in the longest column. This effect of rate on length of the front is in the direction predicted by the mechanism assumed in obtaining Equation (1).

The fact that the length of the front increases with velocity at a given distance traversed indicates that the mechanism of combined convection and radial diffusion plays at least a part in governing the behavior of the front. If the pore-size distribution were the only property which controlled the front, then the velocity should have no effect on the rate of growth of the front. On the other hand, if diffusion in the direction of flow were the controlling variable, the length of the front would decrease with increasing

velocity. In this case the time of residence in the column would directly determine the length of the front. Table 3 compares

Table 3. Length of Front for Runs with Same Residence Time

Column length, cm.	Rate, cc./100 sec.	Length of front, cm.
27.6	2.04	3.94
57.9	4.10	6.95
57.9	1.04	6.11
118.0	1.94	9.20

the length of the front for two sets of runs in which the residence time was the same although the distances traversed and flow rates were different. It can be seen that the length of the front is definitely not constant with residence time in the sand column.

CONCLUSIONS

The data obtained so far indicate that the combined convection and diffusion mechanism plays a part in controlling the growth of the front with distance downstream. Some other property, perhaps the pore-size distribution, seems to be important in establishing the front at the beginning of the displacement. Also, it is evident that the analysis of miscible displacement in a single capillary can be qualitatively extended to a similar displacement in a porous medium. Further work is needed to determine the effects of diffusion coefficient and column permeability on the displacement.

NOTATION

- a = radius of tube (lateral distance for diffusion)
- C = concentration of invading fluid
- C/C_0 = fraction invading fluid in effluent
- D = coefficient of diffusion between liquids
- Q_i = pore volumes injected
- r = radial distance variable
- t = time
- V = maximum velocity in tube
- x = transverse distance variable
- ρ = r/a
- τ = $(D/a^2)t$
- ξ = x/a

LITERATURE CITED

1. Everett, J. P., F. W. Gooch, Jr., and John C. Calhoun, *Trans. Am. Inst. Mining & Metallurgical Engrs.*, **189**, 215 (1950).
2. Griffith, V. L., and V. M. Hollrah, *Oil Gas J.*, **51**, 86 (June 30, 1952).
3. Henderson, J. H., N. B. Gove, H. J. Ledbetter, and J. D. Griffith, *Trans. Am. Inst. Mining & Metallurgical Engrs.*, **198**, 33 (1953).
4. Hendrix, V. V., and R. L. Huntington, *Petroleum Engr.*, **13** (October, 1941).
5. Offeringa, J., and C. van der Poel, *J. Petroleum Technol.*, **6**, No. 12, 37 (1954).
6. Taylor, Geoffrey, *Proc. Roy. Soc.* (*London*), **A219**, 186 (1953).
7. Whorton, L. P., and W. L. Kieschnick, *Oil Gas J.*, **48**, 78 (April, 1950).

Presented at the A.I.Ch.E. Houston meeting

Written Discussion Contributed by Paul B. Crawford and Daniel Olin Atkinson

The purpose of this discussion is to show how data of the type presented by von Rosenberg are processed and correlated in other laboratories. Figures 1, 2 and 3 show the composition curves for fluid displacement in 1-, 2-, and 4-ft.-long sand columns. The derivative of the concentration curve results in a distribution curve which indicates how the mass of fluid is distributed both ahead and behind any thin wave of injected material. If it were convenient to measure the concentration at the center of the 2-ft. column, it would be found to be the same as that shown at the end of the 1-ft. column. Similarly the composition at the center of the 4-ft. column would be the same as that at the end of the 2-ft. column. Consequently, it is possible to calculate the concentration curves at the end of the 2- or 4-ft. columns from the data obtained for the 1-ft. column. The composition at the end of the 2-ft. column may be considered to be the sum from a series of thin waves of liquid with compositions and distributions equal to those shown at the end of the 1-ft. column. The details of this procedure have been presented by Swearingen (*1*).

The data of von Rosenberg have been processed by this method, and the results are presented in Figures *A* and *B* of this discussion. Data of von Rosenberg were simplified by drawing average curves through the concentration data. Figures *A* and *B* illustrate the accuracy of the procedure which is possible when this method is applied to reliable data such as presented by von Rosenberg. It will be noted that in each instance, the calculated richness curves for the longer columns agree very closely with the data observed experimentally. It is also to be noted that although the front is lengthened in its passage through the longer columns, its length as a fraction of the dimensionless path length is shortened. (*See* Figures 4 and *A* and *B*.) This is significant in considering results for field-size models.

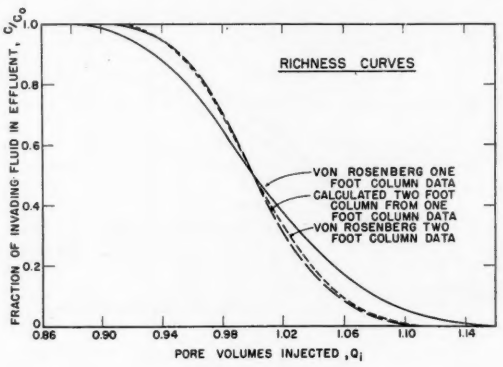

Fig. A.

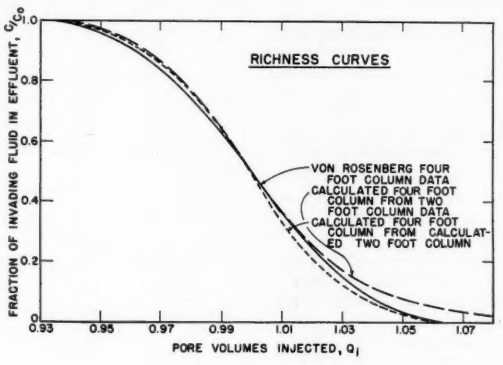

Fig. B.

LITERATURE CITED

1. Swearingen, J. S., *Oil & Gas J.*, **52**, No. 7, 283 (June 22, 1953).

Analysis of Kinetic Data for Heterogeneous Reactions

SOL WELLER

Houdry Process Corporation, Linwood, Pennsylvania

The chemical engineer frequently has to correlate kinetic data for heterogeneous reactions simply and accurately in order to make useful predictions of reaction rates over a range of conditions. The Langmuir-Hinshelwood approach, which is frequently used for this purpose, does not have the theoretical validity commonly attributed to it, and its use leads to unnecessary mathematical complexity. A simpler method of analysis is suggested which is based on power dependencies of the rate on concentrations, the powers being restricted to integral or half-integral values. The data for several reactions are shown to be adequately correlated by the suggested procedure, which is simple and convenient.

During the last decade it has become increasingly popular for chemical engineers to analyze the kinetic data for complicated solid-catalyzed gas reactions in terms of the extended Langmuir-Hinshelwood theory (*8*, *21*). This approach may be illustrated by a sample case:

The gas reaction $A + B \rightarrow C$ is catalyzed by a solid, and the reaction is not limited by mass or heat transfer. If it is assumed that a bimolecular surface reaction of A and B is rate controlling and that A, B, and C are adsorbed on the catalyst without dissociation, then the reaction rate is written

$$\text{rate} = \frac{kp_Ap_B}{(1 + K_Ap_A + K_Bp_B + K_Cp_C)^2} \quad (1)$$

the K's being (unknown) adsorption coefficients characteristic of the individual gas. Other assumed mechanisms result in different equations, and the occurrence of a better fit of the data to one equation than to another is frequently employed as a sufficient criterion of the reaction mechanism.

A large body of evidence exists which indicates that the use of these equations is unjustified, both theoretically and experimentally. Furthermore, their use has two unfortunate consequences: (1) because of the mathematical complexity of the differential rate expression, it is often very inconvenient to obtain the integral rate equation and to evaluate the numerous adjustable parameters, and (2) the unwary investigator is often led to believe that he has uniquely deduced the mechanism of the reaction.

The validity of the Langmuir adsorption isotherm has been considered in detail elsewhere, and only a few of the difficulties will be mentioned here. One of the primary assumptions underlying the theory is that no interaction occurs between adsorbed molecules, which implies that the heat of adsorption should be a constant, independent of the amount of gas adsorbed. Even for physical adsorption, this condition is satisfied in practice only in extremely rare instances (*14*); in general, the heat of adsorption is observed to be a sensitive function of the amount adsorbed. With regard to chemisorption, which presumably is involved in heterogeneous reactions, the author knows of no reported case for which the heat has been shown to be independent of the amount adsorbed.

Another serious difficulty arises in the practical application of the Langmuir isotherm to the adsorption of a mixture of gases. The Langmuir equation predicts that the addition to one gas of a second gas will always decrease the amount of the first gas adsorbed. Numerous cases of physical adsorption are known in which exactly the opposite behavior obtains, i.e., where the second gas increases the adsorption of the first gas (*3*). Very few data are available on chemisorption from gas mixtures, but recently Sastri and his coworkers have reported some excellent studies of chemisorption of hydrogen-nitrogen mixtures on iron synthetic ammonia catalysts and of hydrogen–carbon monoxide mixtures on cobalt Fischer-Tropsch catalysts (*17* and *6*). In both systems marked enhancement of adsorption of a gas from mixtures, over that of the pure gas at the same partial pressure was observed under certain conditions. Presumably this behavior arises from an attractive interaction between adsorbed molecules of the two constituents, an effect disregarded in the simple Langmuir theory. Adsorption of this sort corresponds mathematically to having a negative adsorption coefficient in the denominator of the extended Langmuir equation; for example, when the adsorption of A is increased in the presence of B, the amount of A adsorbed is given by an expression of the form

$$A_{ads} = \frac{kp_A}{1 + K_Ap_A - K_Bp_B} \quad (2)$$

In the usual application of the Langmuir-Hinshelwood approach this (experimental) result is considered to be physically impossible, and any reaction mechanism which leads to a negative adsorption coefficient is automatically discarded.

Because of difficulties of this sort, there appears to be no theoretical justification for applying the extended Langmuir equation to the kinetics of complex heterogeneous reactions. For real reactions, equations similar to (1) can be considered only as empirical relations which may or may not be useful for correlating data. Great danger exists that the form of such an empirical rate equation is accepted so literally that absolute conclusions about mechanism are deduced from what is really empirical data fitting. When one considers that the foremost investigators in the field of reaction kinetics still completely disagree on the mechanism of so simple a reaction as the ortho-parahydrogen conversion over evaporated metal films (*16* and *4*), it is naive to think that one can prove the mechanism of a complex reaction by, for example, obtaining a better fit to rate data with a square, rather than a first-power, term in the denominator of an expression such as Equation (1).

The principal utility of the Langmuir-Hinshelwood approach for real reactions is qualitative rather than quantitative. Most, if not all, gas-solid and solid-catalyzed gas reactions do involve reaction by chemisorbed gas species, and the limiting cases of the Langmuir isotherm are most helpful in furnishing a qualitative picture of the surface coverage. For a single reactant, for example, when the rate depends only on the first power of the reactant gas pressure, it is a reasonable conclusion that the reactant is only slightly adsorbed; when the rate is almost independent of reactant gas pressure, it is probable that adsorption is almost complete and that most available adsorption sites are occupied. Similarly, in the

Table 1. Oxidation of Sulfur Dioxide

Run	Eq. (4) Ref. 20 k rel.	% Dev.	Eq. (5) k rel.	% Dev.
3	25.00	24.8	0.191	37.0
4	15.46	22.8	0.250	17.5
5	16.31	18.6	0.280	7.6
6	18.30	8.7	0.304	0.3
7	16.52	17.6	0.302	0.3
8	20.61	2.8	0.347	14.5
9	24.63	22.9	0.334	10.2
10	15.83	21.0	0.285	5.9
11	19.30	3.7	0.321	5.9
12	20.68	3.2	0.270	10.9
13	23.87	19.1	0.339	11.9
14	23.95	19.5	0.417	37.6
Average	20.04	15.4	0.303	13.3

case of two reactants if the rate is directly proportional to the pressure of one and inversely proportional to the pressure of the second, the reasonable qualitative conclusion is that the second reactant is very strongly adsorbed, to the detriment of the first reactant. All these results may be deduced from the limiting forms of the isotherms (*7*).

Unfortunately, the use of the extended Langmuir-Hinshelwood expressions to obtain this sort of qualitative information is frequently a costly procedure for the chemical engineer from the standpoint of unnecessary complication. The principal job confronting the chemical engineer who has to handle kinetic data is to correlate the data in such a way that useful predictions about reaction rates may be made for a range of conditions. Incidental information which can be deduced about reaction mechanism may be useful, but it is of secondary importance. As the earlier discussion has shown, there is no real justification for using the Langmuir-Hinshelwood expressions as the correlating rate equations. It would seem reasonable, rather, for the engineer to employ the simplest possible rate equation which will adequately fit the experimental data. The following expression for rate equations is suggested as being among the simplest forms having sufficient generality:

$$\text{rate} = k(P_A)^m(P_B)^n(P_C)^o \cdots \quad (3)$$

where A and B might be reactants, C a product or a foreign gas, etc., and the exponents m, n, o are parameters having either integral or half-integral values. In practice, one or more of the exponents will frequently be found to be zero.

The exponents in Equation (3) are simply the apparent orders of the reaction with respect to the individual components. Not only does this feature furnish easy comprehension of the pressure dependencies to the nonspecialist in kinetics; it also permits the exponents to be determined by the conventional schemes for finding reaction orders (e.g., by changing the pressure of one reactant at a time). The restriction to integral or half-integral values is made for simplicity, but unless the experimental data cover an unusually wide range of conditions or are of unusual precision, this restriction does not prevent adequate correlation of the data. Furthermore, it appears that over a reasonable temperature range the values of the exponents are *independent of temperature*, and so only the temperature dependence of the specific rate constant need be considered. This is a real convenience in treating nonisothermal reactors, as it reduces the number of parameters which have to be determined as a function of temperature.

The utility of this approach is perhaps best illustrated by consideration of a few examples. The platinum-catalyzed oxidation of sulfur dioxide may be considered first. Lewis and Ries (*10*) studied this reaction in a flow system under conditions that kept the volume change during the reaction negligible. The Lewis-Ries data have been analyzed by Uyehara and Watson according to the Langmuir-Hinshelwood procedure (*20*), and the differential rate equation that they deduced is of the form

$$\text{rate} = \frac{k}{(1 + \sqrt{p_{O_2}K_{O_2}} + p_{SO_2}K_{SO_2})^2} \cdot \left(p_{SO_2}\sqrt{p_{O_2}} - \frac{p_{SO_2}}{K}\right) \quad (4)$$

The square roots arise because the limiting surface reaction is assumed to be between an adsorbed sulfur dioxide molecule and an adsorbed oxygen atom; the term p_{SO_2}/K arises from consideration of the reverse reaction, K being the equilibrium constant. The critical series of experiments carried out by Lewis and Ries (series *C*) was a group made at constant temperature, pressure, space velocity, and (approximately) oxygen pressure, but at varying inlet sulfur dioxide and sulfur trioxide concentrations. Columns 2 and 3 in Table 1 show the relative values of the rate constant, k, and of the percentage of deviation calculated by Uyehara and Watson from Equation (4) for each of the last twelve experiments in this series.

An alternate analysis has been made of the same data along the lines suggested by Equation (3). The differential rate expression used is

$$\text{rate} = k\left(\frac{p_{SO_2}}{\sqrt{p_{SO_2}}} - \frac{1}{K}\frac{\sqrt{p_{SO_2}}}{\sqrt{p_{O_2}}}\right) \quad (5)$$

The form of Equation (5) was suggested by data available in the literature; it was the first equation tested in this work, and in view of its successful application other possible equations were not investigated. The first term represents the rate of the forward reaction. It is identical with the equation found applicable to the forward reaction in the classical work of Bodenstein and Fink (*2*). The absence of oxygen pressure from this term is indicated both by Bodenstein and Fink and by Lewis and Ries. The second term, relating to the reverse reaction, was chosen as the simplest form which, in view of the choice of forward rate expression, would give the correct equilibrium relationship. [This is not the most general function which satisfies the equilibrium relation (*11*).]

In these experiments p_{O_2} was essentially constant (17.5 to 20.9%). If p_{O_2} is assumed constant, as was done also by Uyehara and Watson, Equation (5) may be integrated in a straightforward way, and a value of k for each of the experiments may be determined from the integral expression*. A value of 194 was used for the equilibrium constant at 425°C. (*9*).

Columns 4 and 5 of Table 1 contain the values of the rate constant, in arbitrary units, and of the percentage of deviation calculated in this way. It is clear that the data are fitted by Equation (5) at least as well as by Equation (4); the average deviations are 13.3 and 15.4%, respectively. On the other hand, Equation (5) is clearly simpler and more tractable than Equation (4).

As a second example, the data of Tschernitz, Bornstein, Beckmann, and Hougen (*19*) on the hydrogenation of codimer may be considered. Three series of experiments, at 200°, 275°, and 325°C., were carried out with a differential reactor. The data were fitted by an equation of the form

$$\text{rate} = \frac{k}{(1 + K_H p_H + K_U p_U + K_S p_S)^2} p_H p_U \quad (6)$$

where p_H, p_U, and p_S are the partial pressures of hydrogen, codimer, and hydrogenated codimer, respectively, and k, K_H, K_U, and K_S are temperature-dependent parameters. From the rates calculated by Tschernitz, et al., it is possible to compute the average percent-

*Uyehara and Watson treated the reactor as a differential reactor. This procedure is not valid for several of the experiments in which large fractional changes occurred in the concentrations of sulfur dioxide and sulfur trioxide.

age deviation of the specific rate constant k for each series of experiments; these values are shown in column 2 of Table 2.

Table 2. Hydrogenation of Codimer

Temp., °C.	Eq. (6), avg. % dev.	k	Eq. (9), avg. % dev.
200	20.9	0.0201	19.6
275	19.6	0.0270	32.9
325	19.4	0.0207	21.4

An alternate treatment of the same experimental data was carried out on the basis of the following equation [cf. Equation (3)]:

$$\text{rate} = kp_U{}^m p_H{}^n p_S{}^o \qquad (7)$$

A plot of rate/$p_U p_H$ (taken as a first approximation to the rate constant) vs. p_S showed that no systematic variation occurred as a function of p_S. This suggested a zero-order dependence on p_S—not a surprising conclusion in view of the known fact that hydrogen and olefins are much more strongly adsorbed by metals than are paraffins. Accordingly, Equation (7) was simplified to

$$\text{rate} = kp_U{}^m p_H{}^n \qquad (8)$$

Least-squares treatment of the data at each temperature gave the following "best values" for k, m, and n:

Temp., °C.	k	m	n
200	0.0208	0.546	0.583
275	0.0282	0.544	0.730
325	0.0230	0.510	0.772

As m and n are to be restricted to integral or half-integral values (see above), m and n were both taken as ½, independent of temperature. Equation (8) then became

$$\text{rate} = kp_U{}^{1/2} p_H{}^{1/2} \qquad (9)$$

Average values of k and the average percentage of deviation of k were computed for each temperature (columns 3 and 4 of Table 2). Although the fit of the data by Equation (9) is slightly poorer than by Equation (6), the adequacy of the former is sufficient for engineering purposes. The simplicity of Equation (9) in comparison with Equation (6) is apparent.

The maximum at 275° in the computed values of k (Table 2) is not an artifact. It occurs also in the experimental values of the rate constant of Tschernitz, et al. (their Ek = 0.580, 0.910, and 0.895 at 200°, 275°, and 325°, respectively), and it is suppressed only when the data are artificially smoothed to fit an assumed Arrhenius dependence. The occurrence of such a maximum as a function of temperature has been reported by both Rideal (*15*) and zur Strassen (*22*) for the hydrogenation of ethylene over nickel and by Maxted and Moon (*12*) for the liquid-phase hydrogenation of crotonic and maleic acids over platinum.

Akers and White (*1*) studied the kinetics of the reaction

$$CO + 3H_2 = CH_4 + H_2O$$

over a nickel-kieselguhr catalyst; their results may be considered as a third example. On the basis of the assumption that the rate-controlling step in methane formation is the surface reaction between three adsorbed hydrogen molecules and one adsorbed carbon monoxide molecule, they correlated the rate data by the equation

$$\text{rate} = \frac{p_{CO} p_{H_2}{}^3}{(A + Bp_{CO} + Dp_{CO_2} + Ep_{CH_4})^4} \qquad (10)$$

(Carbon dioxide, formed as a by-product, was assumed to be appreciably adsorbed, and carbon dioxide pressure therefore enters into the "adsorption denominator.")

Inspection of the initial reaction rates (Table 7 of Akers and White) makes it clear that, when the partial pressures of the products are zero, the rates are consistent with an expression of the form

$$\text{rate} = kp_{CO} p_{H_2}{}^{1/2} \qquad (11)$$

It further appears that this same rate expression is capable of correlating all the rate data, including those in the presence of water, methane, and carbon dioxide, with about the same accuracy as Equation (10). For example, for series 100 of Akers and White (seven values at each of the temperatures 310°, 325°, and 340°C.), the rates may be computed from Equation (11) with an average deviation of 13 to 14%, values of k of 0.299, 0.431, and 0.444 being used at 310°, 325°, and 340°C., respectively. These data cover a fivefold range in carbon monoxide pressure and a tenfold range in hydrogen pressure, with corresponding variations in the pressures of the product gases. It thus appears that in this work the rate is substantially independent of the pressures of methane, water, and carbon dioxide and that a rate expression containing four adjustable constants at each temperature may be adequately replaced by one having only a single constant.

As a final example, one may consider the formation of phosgene from carbon monoxide and chlorine over charcoal, which was studied by Potter and Baron (*13*). It was concluded in this work that the controlling mechanism was a surface reaction between adsorbed carbon monoxide and chlorine, and that the data were correlated by the rate expression

$$\text{rate} = \frac{kK_{CO} K_{Cl_2} p_{CO} p_{Cl_2}}{[1 + K_{Cl_2} p_{Cl_2} + K_{COCl_2} p_{COCl_2}]^2} \qquad (12)$$

The second column of Table 3, which contains the average percentage of deviations of the calculated rates at each of the four temperatures studied, shows the excellent fit of the data obtained by this method.

Table 3. Phosgene Synthesis from Carbon Monoxide and Chlorine

Temp., °C.	Eq. (12), avg. % dev.	k	Eq. (13), avg. % dev.
30.6	3.4	15.8	13.0
42.7	5.6	37.5	9.1
52.5	2.6	64.8	13.9
64.0	7.0	104.4	3.0

It again became clear from a preliminary inspection of the data that a reasonable fit could also be obtained at all temperatures by the following expression, of the same general form as Equation (3):

$$\text{rate} = kp_{CO} p_{Cl_2}{}^{1/2} \qquad (13)$$

Columns 3 and 4 of Table 3 show the average values and the average percentage of deviations of the rate constants computed with the use of Equation (13). Although the average percentage of deviation with Equation (13) is about double that with Equation (12), it is still within acceptable limits; moreover, this is accomplished with the use of one adjustable constant (k) at each temperature, as compared with three adjustable constants (kK_{CO}, K_{Cl_2}, and K_{COCl_2}) for Equation (13).

It is relevant to note that Potter and Baron found that the addition of nitrogen to the reaction mixture increased the apparent adsorption of chlorine and phosgene. As they also point out, this behavior is incompatible with the Langmuir assumptions. (See above.)

Additional examples can be adduced from the literature in support of rate equations of the form of Equation (3). One well-known case is that of ammonia synthesis (*5*), for which the rate can be expressed as

$$\text{rate} = k_f \frac{P_{N_2} P_{H_2}{}^{1.5}}{P_{NH_3}} - k_b \frac{P_{NH_3}}{P_{H_2}{}^{1.5}} \qquad (14)$$

It is significant that the deduction, now generally accepted, of the rate equation for this reaction by Temkin and Pyzhev (*18*) does not follow from any elementary application of the Langmuir-Hinshelwood approach.

ACKNOWLEDGMENT

R. W. Houston has pointed out to the author that the data of Wan [*Ind. Eng. Chem.*, *45*, 234 (1953)] on ethylene oxidation are much better fitted by Wan's empirical rate equation, which employs simple power dependencies, than by any formulation based on a Langmuir-Hinshelwood mechanism.

LITERATURE CITED

1. Akers, W. W., and R. R. White, *Chem. Eng. Progr.*, **44**, 553 (1948).
2. Bodenstein, M., and C. G. Fink, *Z. physik. Chem.*, **60**, 1 (1907).
3. Brunauer, S., "The Adsorption of Gases and Vapors," Vol. I, Chap. XIV, Princeton University Press, Princeton (1943).
4. Couper, A., and D. D. Eley, *Proc. Roy. Soc. (London)*, **A211**, 536, 544 (1952).
5. Emmett, P. H., and J. T. Kummer, *Ind. Eng. Chem.*, **35**, 677 (1943).
6. Ghosh, J. C., M. V. C. Sastri, and K. A. Kini, *Ind. Eng. Chem.*, **44**, 2463 (1952).
7. Hinshelwood, C. N., "Kinetics of Chemical Change," Oxford University Press, New York (1940).
8. Hougen, O. A., and K. M. Watson, *Ind. Eng. Chem.*, **35**, 529 (1943).
9. Kapustinskii, A. F., *Compt. rend. acad. sci. U.R.S.S.*, **53**, 719 (1946).
10. Lewis, W. K., and E. D. Ries, *Ind. Eng. Chem.*, **19**, 830 (1927).
11. Manes, M., L. J. E. Hofer, and S. Weller, *J. Chem. Phys.*, **18**, 1355 (1950).
12. Maxted, E. B., and C. H. Moon, *J. Chem. Soc.*, p. 1190 (1935).
13. Potter, C., and S. Baron, *Chem. Eng. Progr.*, **47**, 473 (1951).
14. Rhodin, T. N., *J. Am. Chem. Soc.*, **72**, 5691 (1950).
15. Rideal, E. K., *J. Chem. Soc.*, 309 (1922).
16. ———, and B. M. W. Trapnell, *Discussions Faraday Soc.*, No. 8, 114 (1950).
17. Sastri, M. V. C., and H. Srikant, *Current Sci. (India)*, **20**, 15 (1951).
18. Temkin, M. I., and V. Pyzhev, *Acta Physicochim. (U.R.S.S.)*, **12**, 327 (1940).
19. Tschernitz, J. L., S. Bornstein, R. B. Beckmann, and O. A. Hougen, *Trans. Am. Inst. Chem. Engrs.*, **42**, 883 (1946).
20. Uyehara, O. A., and K. M. Watson, *Ind. Eng. Chem.*, **35**, 541 (1943).
21. Yang, K. H., and O. A. Hougen, *Chem. Eng. Progr.*, **46**, 146 (1950).
22. zur Strassen, H., *Z. physik. Chem.*, **A169**, 81 (1934).

Kinetics on Ideal and Real Surfaces

MICHEL BOUDART

Princeton University, Princeton, New Jersey

The wide applicability of the Langmuir-Hinshelwood classical kinetics to surfaces which are known to depart strongly from ideal Langmuir behavior is a well-known paradox of surface catalysis. The applicability and limitations of the classical method are illustrated by means of a simple reaction. The generality of the method is demonstrated by its applicability to ammonia synthesis with and without water vapor. The limitations are often more than compensated for by the added insight into reaction mechanism which it can provide without undue complexity. A three-step approach to surface kinetics is suggested and discussed.

PARADOX OF HETEROGENEOUS KINETICS

As recalled in the preceding paper (*17*) in this issue, use is frequently made in catalytic studies of the model of an ideal surface with constant heat of adsorption for each chemisorbed species. Although real surfaces invariably depart from this ideal model, a systematic application of it to kinetic problems has deepened understanding of surface reactions and in practice yields rate laws which are valid over a certain useful range of the kinetic variables. This successful application of an inadequate model constitutes a well-known paradox of heterogeneous kinetics.

This paradox was first considered and resolved for a special case by Constable (*5*) in 1925, the same year that Taylor set forth his concept of active centers to describe the behavior of real surfaces. Constable showed that a surface with a broad distribution of active centers would act in a given reaction as if only one kind of center were operating under given conditions. In other words a real surface may be considered as a statistical collection of ideal surfaces, and for a given catalytic reaction only a limited number of members of the ensemble play an active part, forming a quasiideal surface.

Thus, in spite of the known complex behavior of real surfaces, the ideal model was used extensively in subsequent years by Hinshelwood, Schwab, Hougen, Jungers, and many others to describe in considerable detail the kinetics of surface reactions. These investigators were well aware of the limitations of their model and in particular have pointed out repeatedly that the kinetic constants obtained from such rate laws did not usually agree with adsorption constants obtained in separate experiments. The nature of the problem can be illustrated by a simple example.

ANALYSIS OF A TYPICAL CASE (*1*)

The decomposition of stibine, SbH_3, on the walls of a vessel covered with a film of antimony is one of the first catalytic reactions studied from the kinetic standpoint. The reaction velocity was measured at 0°, 25°, 50°, and 75°C. by Stock and coworkers (*13*) and more recently by Tamaru (*15*). Stock found that the rate r could be expressed by a relation of the type

$$r = kp^n \qquad (1)$$

with $n = 0.6$. In this expression p is the partial pressure of SbH_3 and $r = -dp/dt$. The results of Tamaru are similar to those of Stock, and only the latter will be discussed. It was verified by Stock that the reaction goes to completion, solid antimony and gaseous hydrogen being the sole products, and that hydrogen had no effect on the velocity of decomposition. Stock and Bodenstein (*14*) proposed the following interpretation of these findings: the hydride is adsorbed on the surface and decomposes there monomolecularly. Thus the rate is proportional to the concentration of adsorbed species, i.e., to the fraction of surface θ covered with hydride molecules:

$$r = k_1\theta \qquad (2)$$

The relationship between θ and p known at the time was the empirical Freundlich adsorption isotherm:

$$\theta = k_2p^n \qquad (3)$$

with $0 < n < 1$. If adsorption equilibrium be granted, substitution of (3) into (2) immediately gives the observed rate law (1).

Subsequently the suggestion was made to replace the empirical isotherm of Freundlich by the Langmuir isotherm:

$$\theta = \frac{bp}{1 + bp} \qquad (4)$$

where $b = b_0 \exp(q/RT)$, q being the heat of adsorption assumed to be constant over the surface. The mechanism of Stock and Bodenstein then gives by substitution of (4) into (2)

$$r = \frac{k_1 bp}{1 + bp} \qquad (5)$$

an alternative rate law that must be compared with that originally proposed. This comparison (*1*) shows that rate laws (1) and (5) are equally satisfactory and that there is no way of deciding which one best represents the kinetic data. More recently the Freundlich isotherm has been interpreted as being due to an exponential distribution of heats of adsorption (*6*). The comparison between both rate laws thus indicates that the assumption of a Freundlich isotherm corresponding to a real surface is not superior from the kinetic standpoint to the assumption of a Langmuir isotherm corresponding to an ideal surface.

It would be erroneous to conclude that the good fit of expression (5) shows that the surface of the antimony film is an ideal one. Indeed, the adsorption constants b can be examined more closely. At the four temperatures investigated they have approximately the same value. However the Langmuir constant b must decrease exponentially with temperature. Since in this case b remains practically constant within the temperature interval considered, the heat of adsorption q must be very small and practically zero. This result has no physical meaning, as a heat of adsorption at least equal to the heat of liquefaction of antimony hydride, viz., 5,700 cal./g. mole, would be anticipated. In a similar way a comparison of b_0, the preexponential factor of Langmuir's constant, with possible values for b_0 which depend on the entropy of adsorption, leads to the conclusion that experimental b_0 values are considerably larger than permissible theoretically.

Thus from the viewpoints of both apparent energy and entropy, the kinetic constants b strongly suggest that the surface cannot be ideal in spite of the good behavior of the rate law following Langmuir. If however the surface presents a distribution of heats of adsorption, the situation can be understood qualitatively by means of the following simple argument. As the temperature of the catalytic experiment is increased, the surface coverage decreases and sites with a higher adsorption energy become operative. In the first approximation it may be assumed that

$$q = q_0 + aT$$

to describe this temperature dependence of the heat of adsorption. Then

$$b = b_0 \exp(q/RT) = b_0 e^a e^{q_0/RT}$$

The constant q_0 can be small even if the true heat of adsorption q is larger and the apparent preexponential factor $b_0 e^a$ will be larger than the true one b_0.

When the heat of adsorption varies sufficiently rapidly with coverage, relatively small variations of pressure (by one order of magnitude) as normally encountered in kinetic experiments do not change the surface coverage appreciably. As a result, the surface appears ideal kinetically at a given temperature. Variations of temperature which change the surface coverage in a more striking way, reveal the nonideality of the surface.

A practical consequence of this analysis is the well-known fact that an expression of the type $p^n (0 < n < 1)$ may always be substituted for the more cumbersome hyperbolic function $bp/(1 + bp)$, the value of the fraction n being approximately constant at a given temperature for a restricted range of pressure. Thus, practically, kinetic data that can be fitted by means of Langmuir expressions can also be fitted by means of power expressions and vice versa. This simple situation was pointed out in the preceding paper (*17*) and illustrated by a number of examples.

THE CASE OF THE AMMONIA SYNTHESIS (*2*)

It is common belief that there are a few cases where a kinetic expression fitting the data cannot be derived on the assumption of an ideal surface. The most celebrated case is that of the ammonia synthesis for which Temkin and Pyzhev (*16*) proposed the following rate expression:

$$r = k_s P_1 \left(\frac{P_3^3}{P_2^2}\right)^m - k_d \left(\frac{P_2^2}{P_3^3}\right)^n \qquad (6)$$

where r is the over-all rate of synthesis of ammonia (partial pressure P_2) from nitrogen (P_1) and hydrogen (P_3); k_s and k_d are rate constants for synthesis and decomposition respectively; m and n are fractions which for ease of integration are often put equal to 0.5 although other values have been reported.

The Temkin-Pyzhev rate expression was originally derived on the assumption of a uniform distribution of sites corresponding to a heat of adsorption of nitrogen decreasing linearly with coverage. Although there is abundant evidence for such a departure of surface behavior from ideality, it would appear surprising, in view of the general validity of the paradox of heterogeneous kinetics, that such an assumption be essential to the derivation of the rate expression. Indeed, De Bruyne (*4*) has shown that the postulation of a particular analytical distribution function was superfluous. The same rate expression can be obtained on the basis of an exponential adsorption heat curve (*11*). In particular, it can be obtained quite simply on the basis of ideal-surface kinetics.

Independent evidence suggests that the slow step on a large variety of catalysts is the adsorption of nitrogen

$$N_{2(g)} \rightarrow 2N_{(a)}$$

for ammonia synthesis and its desorption

$$2N_{(a)} \rightarrow N_{2(g)}$$

for ammonia decomposition. Adsorption equilibrium is maintained by means of the over-all fast process

$$NH_{3(g)} \rightleftarrows N_{(a)} + \tfrac{3}{2}H_{2(g)}$$

which determines the fraction of surface θ covered with adsorbed nitrogen atoms $N_{(a)}$. The surface coverage is determined directly by a Langmuir type of argument which gives the following Langmuir type of adsorption isotherm:

$$\theta = \frac{b(P_2/P_3^{1.5})}{1 + b(P_2/P_3^{1.5})} \qquad (7)$$

The rate of synthesis r_s is that of nitrogen adsorption:

$$r_s = k_1 P_1 (1 - \theta)^2 \qquad (8)$$

The rate of decomposition is that of nitrogen desorption:

$$r_d = k_2 \theta^2 \qquad (9)$$

Substitution of (7) into (8) and (9) gives a rate expression in the Langmuir form:

$$r = r_s - r_d = k_1 P_1 \left[\frac{1}{1 + b(P_2/P_3^{1.5})}\right]^2 - k_2 \left[\frac{b(P_2/P_3^{1.5})}{1 + b(P_2/P_3^{1.5})}\right]^2 \qquad (10)$$

Although this rate expression has not been tested, the remarks of the preceding paper and of the section above leave little doubt that it would satisfactorily represent the kinetic data. Indeed, because of the good approximation of power functions to represent Langmuir expressions in a limited pressure range and vice versa, Equation (10) can be written more simply:

$$r = k_s P_1 \left(\frac{P_3^{1.5}}{P_2}\right)^{2m} - k_d \left(\frac{P_2}{P_3^{1.5}}\right)^{2n} \qquad (11)$$

with $0 < m < 1$ and $0 < n < 1$. But (11) is identical with the Temkin-Pyzhev rate law (6), as was expected. When synthesis or decomposition is carried out in conditions removed from equilibrium, their rates can be described by Equation (8) or (9) respectively, the limiting cases of which are obvious.

Thus, if the surface coverage by nitrogen is small during synthesis conditions, $\theta \approx 0$, and (8) becomes simply

$$r_s = k_1 P_1$$

a case which has been found experimentally (*9*).

If during decomposition the surface is nearly saturated with nitrogen, $\theta \approx 1$, and (9) gives

$$r_d = k_2$$

a zero-order decomposition which has been reported also (*7*).

Langmuir expressions or simplifications thereof have been shown to give correct rate expressions for ammonia synthesis in general and limiting conditions, in spite of the fact that ammonia catalysts are known to be highly nonideal (*2*). The practical advantage of such reasoning is even more apparent in more complex situations.

For example, a rate expression for ammonia synthesis in the presence of water vapor (partial pressure P_4) can be derived readily by taking into account the additional adsorption equilibrium:

$$H_2O_{(g)} \rightleftarrows O_{(a)} + H_{2(g)}$$

Taking into account both adsorption equilibria, a straightforward Langmuir type of reasoning gives for the fraction of surface θ covered with nitrogen atoms:

$$\theta = \frac{b(P_2/P_3^{1.5})}{1 + b(P_2/P_3^{1.5}) + b'(P_4/P_3)} \quad (12)$$

and for the fraction of surface θ' covered with oxygen atoms:

$$\theta' = \frac{b'(P_4/P_3)}{1 + b(P_2/P_3^{1.5}) + b'(P_4/P_3)} \quad (13)$$

The rate of ammonia synthesis becomes

$$r_s = k_1 P_1 (1 - \theta - \theta')^2 \quad (14)$$

The rate of decomposition is given by

$$r_d = k_2 \theta^2 \quad (15)$$

Substitution of (12) and (13) into (14) and (15) would give a rate expression of the Langmuir type that would be quite cumbersome. Again simplifications are indicated; thus

$$1 - \theta - \theta' = \frac{1}{1 + b(P_2/P_3^{1.5}) + b'(P_4/P_3)}$$

$$\approx \frac{1}{b(P_2/P_3^{1.5})} \cdot \frac{1}{b'(P_4/P_3)}$$

$$\approx k\left(\frac{P_3^{1.5}}{P_2}\right)^m \left(\frac{P_3}{P_4}\right)^n$$

$$\theta \approx k'\left(\frac{P_2}{P_3^{1.5}}\right)^{1-m} \left(\frac{P_3}{P_4}\right)^n$$

where m and n are fractions. Then the rate expression becomes

$$r = k_s P_1 \left(\frac{P_3^{1.5}}{P_2}\right)^{2m} \left(\frac{P_3}{P_4}\right)^{2n} - k_d \left(\frac{P_2}{P_3^{1.5}}\right)^{2-2m} \left(\frac{P_3}{P_4}\right)^{2n}$$

Following the suggestion of the preceding paper (*17*) to limit the choice of exponents to integers or half integers, it may be assumed that $m = n = \frac{1}{2}$, as was done above for the case of pure ammonia; such a choice facilitates integrations. Then, finally,

$$r = k_s P_1 \frac{P_3^{2.5}}{P_2 \cdot P_4} - k_d \frac{P_2}{P_3^{0.5} \cdot P_4} \quad (16)$$

The rate law (16) has been used recently by Kiperman (*10*) to correlate the data of Brunauer and Emmett (*3*) as well as those of Larson and Tour (*12*) on ammonia synthesis at atmospheric and elevated pressures in the presence of water vapor. The fit of the data is very satisfactory. However, to derive (16), Kiperman used the statistical Temkin-Pyzhev approach. The latter may be more satisfactory from the theoretical viewpoint but is again shown to be superfluous if the main objective is to find an adequate rate law representing the kinetic data.

SUGGESTED PROCEDURE IN KINETIC STUDIES

In the case of the ammonia synthesis, the reaction mechanism was suggested by independent experiments, and from this mechanism it was possible to obtain rate laws following the procedure of ideal kinetics. Generally, if the mechanism of a reaction is not known, the following procedure is suggested:

The first step is to write down a kinetic expression of the type

$$r = kP_A{}^a P_B{}^b P_C{}^c \cdots$$

where A, B, C, etc., are reactants and products, and to find the values of the exponents a, b, and c. Depending on the accuracy of the data and the ambition of the investigator, these exponents may or may not be restricted to integral or half-integral values.

The second step is to find a possible mechanism which gives, after suitable simplifications of the type indicated above, the rate law found empirically in the first step. In view of the paradox of surface kinetics, this part of the search may be conducted on the assumption of classical ideal kinetics, following the systematic approach to be found in text books. Depending on the nature of the problem, kinetic adsorption constants may or may not be determined at this stage.

The third step is to confirm the assumed mechanism by a rigid analysis of the kinetic constants previously determined. The nonideality of the surface process, including heterogeneity and interactions, must then be taken into account either by postulating a surface distribution of energy sites or by introducing real adsorption isotherms determined separately.

While the third step, which must ultimately lead to an absolute rate calculation, is hardly feasible in the vast majority of cases, there are a number of reasons for going beyond the first step whenever possible.

First of all, by virtue of the paradox of surface kinetics, there is no theoretical reason against the use of classical ideal kinetics provided its limitations are kept in mind.

Second, an assumed reaction mechanism, even without adequate and independent substantiation, may and often does lead to some understanding and control of reaction conditions and catalyst behavior. It may in particular suggest novel experiments, as any theoretical framework should do. *It would appear regrettable if investigators confined themselves to the first step of the procedure, because they believed that any higher approximation, short of considering in detail all the complexities of real surface kinetics, is illegitimate and objectionable.*

Third, a set of kinetic adsorption constants determined according to the rules of classical kinetics for a variety of reactants on a given catalyst or a given reactant on a series of catalysts, may lead to useful predictions as to the behavior of new systems. The usefulness of such a systematic approach is clearly demonstrated by the work of Jungers and his collaborators (*8*). Such a systematization is impossible with empirical rate laws as used in the first step. Adsorption kinetic constants may lead to practical correlations and as such are of interest to the practical worker in the field of applied catalysis, whatever may be the ultimate theoretical interpretation.

LITERATURE CITED

1. Boudart, M., in "Structure and Properties of Solid Surfaces," edited by Robert Gomer and C. S. Smith, p. 400, Chicago University Press, Chicago (1953).
2. ———, *Ind. Chim. belge*, **19**, 489 (1953).
3. Brunauer, S., and P. H. Emmett, *J. Am. Chem. Soc.*, **52**, 2682 (1930).
4. Bruyne de, J., *Discussions Faraday Soc.*, No. 8, 69 (1950).
5. Constable, F. H., *Proc. Roy. Soc. (London)*, **A108**, 355 (1925).
6. Cremer, E., and S. Flügge, *Z. physik. Chem.*, **B41**, 453 (1938).
7. Hinshelwood, C. N., and R. E. Burk, *J. Chem. Soc.*, **127**, 1105 (1925).
8. Jungers, J. C., and co-workers, *Bull. soc. chim. Belges*, **54**, 303 (1945); **55**, 160 (1946); **57**, 555, 618 (1948); **58**, 210, 331 (1949); **59**, 295, 97, 604 (1950).
9. Kiperman, S. L., and V. S. Granovskaya, *Zhur. Fiz. Khim.*, **26**, 1415 (1952).
10. ———, *loc. cit.*, **28**, 389 (1954).
11. Kwan, T., private communication.
12. Larson, A. T., and R. S. Tour, *Chem. Met. Eng.*, **26**, 647 (1922).
13. Stock, A., et al., *Ber. deut. chem. Ges.*, **40**, 532 (1907); **41**, 1309 (1908).
14. ———, and M. Bodenstein, *loc. cit.*, **40**, 510 (1907).
15. Tamaru, K., to be published.
16. Temkin, M. I., and V. Pyzhev, *Acta Physicochim. U.R.S.S.*, **12**, 327 (1940).
17. Weller, Sol, *A.I.Ch.E. Journal*, **2**, No. 1, 59 (1956).

Adsorption Phase Equilibrium Correlations

Light-hydrocarbon Vapors on Activated Charcoal

LEWIS D. ETHERINGTON, ROY E. D. HANEY, WALTER A. HERBST, and HAROLD W. SCHEELINE

Esso Research and Engineering Company, Linden, New Jersey

Data correlations are presented for equilibrium adsorption of pure hydrocarbon vapors and their mixtures. The systems represented are C_1 to C_4 hydrocarbons (olefins and paraffins) on gas-adsorbent grades of activated charcoal. The mixture data are limited to binary and ternary gas systems. The adsorption conditions represented among the correlated data cover ranges of 77° to 175°F. temperature and 0 to 100 lb./sq. in. gauge. With the use of empirical adsorption constants, a common correlation of specific adsorption capacity for the various hydrocarbons is presented; it applies for either pure components or their mixtures. A correlation is given also for adsorption relative volatilities. Approximate adsorption heats, a limited amount of high-temperature steam adsorption data, and sample calculations on application of the correlations are included. The prediction methods are recommended for adsorption conditions up to 250°F. and 250 lb/sq. in. gauge for the particular systems studied.

A companion paper (*11*) describes a new development for continuous adsorptive separation of gas mixtures called the Fluid Char Adsorption (FCA) Process. The development required considerable laboratory study to evaluate alternate adsorbents and to obtain vapor-adsorption data for FCA process designs and interpretation of pilot plant results. This paper includes such data* on light-hydrocarbon–activated-charcoal systems, methods developed for correlating the phase equilibrium relations, and application of the correlations to adsorption-tower design.

Adsorption can be a valuable supplement to conventional techniques for some of the more difficult gas separations encountered in industry. The general category of adsorption applications includes separation of difficult-to-condense gas mixtures and removal of materials such as water and solvent vapors (present in low concentrations) from various process-gas streams. It is a necessary requirement, of course, that the adsorbent used exhibit good selectivity among the key mixture components or fractions to be separated. The fractionation of materials such as methane and ethylene with activated charcoal fits into this category, and intensive study has been given to use of the FCA process for separation of refinery light hydrocarbons. The data and correlations presented here are specific to this application.

Some of the methods and concepts used in the design of a continuous adsorption system differ from those applied for the older fixed-bed unit. In the FCA design, for example, finely divided activated char is handled as a fluidized solid in a multistage bubble-plate column. The gas to be separated is contacted with char in a continuous countercurrent tower operation closely analogous to that of a rectified (reboiled) oil absorber. Thus design of FCA columns requires stepwise plate calculations involving material and heat balances, phase equilibrium relations, and plate efficiencies—quite similar to calculations for design of fractionators handling vapor-liquid systems. This similarity and the indicated design methods served as guides to the mixture adsorption variables correlated: specific adsorption capacities, adsorption relative volatilities, and adsorption heats. The method of applying the vapor-mixture adsorption correlations is illustrated by sample calculations which parallel those for vapor-liquid equilibria.

GAS-ADSORPTION PHASE EQUILIBRIUM DATA AND CORRELATIONS

The first step in the light-hydrocarbon–adsorption study was the evaluation of adsorbents. Preliminary isotherm and attrition data indicated activated coconut chars to be the best available adsorbents for separating light hydrocarbons according to molecular weight. A special petroleum-derived char was subsequently developed which possessed adsorption-desorption-attrition properties substantially identical to those of the familiar Columbia *G* activated coconut charcoal. The data presented in this paper all pertain to light hydrocarbons and steam on either Columbia *G* or the special char used for pilot plant studies (*11*).

A substantial quantity of mixture ad-

*Adsorption isotherms and vapor-adsorbate data obtained by Esso Research and Engineering Company are given in tabular form in Appendix Tables A and B. Derivation of the basic correlating equation for the mixture data is available in Appendix A. These appendices are obtainable from the American Documentation Institute, Photoduplication Service, Library of Congress, Washington 25, D. C., as document 4785 for $1.75 for microfilm or $2.50 for photoprints.

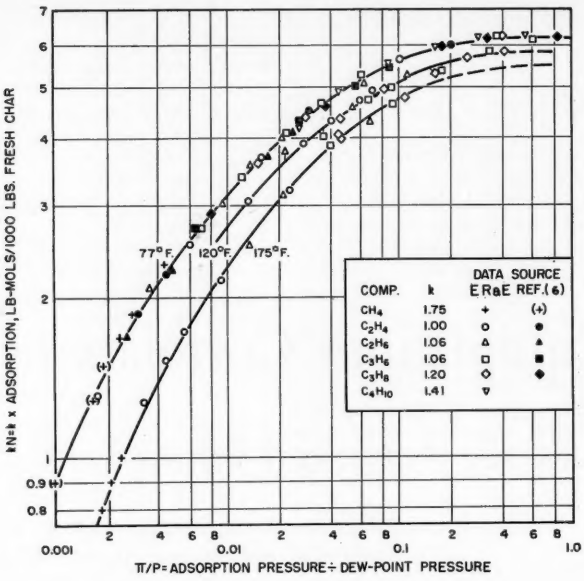

Fig. 1. Adsorption isotherm correlation: pure hydrocarbons on activated charcoal.

sorption data was obtained for design studies and for evaluation of pilot plant results on adsorptive separation of refinery residue gas. This gas contains H_2, N_2, CO, CO_2, H_2S, CH_4, C_2's, C_3's, and small amounts of C_4^+. Gas compositions vary appreciably in a multistage adsorber for separating a gas of this complexity. Thus a correlation of mixture adsorption was undertaken at an early stage of preliminary design studies. It was felt that the best approach to predicting mixture behavior would be through a correlation of pure-component adsorption data, and the correlations presented below for light-hydrocarbon adsorption on activated chars were developed with this line of approach.

Pure-component Absorption

A number of investigators have presented theories and correlations pertaining to pure-component adsorption. Among the most important contributions are works published by Langmuir (*5*), Brunnauer, Emmett, and Teller (*1*), Polanyi (*9*), and London (*7*). A convenient starting point for the authors' correlations was provided by the "adsorption-potential" concept derived by Polanyi and London. The combined derivations of these two workers gave a method for predicting adsorption of various pure components at different temperatures and pressures from a single pure-component isotherm, all pertaining to the same homopolar adsorbent such as charcoal. The adsorption-potential prediction method was modified by Dubinin et al. (*3*) to provide the more conveniently applicable form:

$$\left(\frac{T}{V}\log\frac{P}{\pi}\right)_v = \text{constant} \qquad (1)$$

On applying their data, Dubinin et al. found this relation to hold for various pure adsorbates on a single char at varying adsorption conditions.

Equation (1) is obviously not applicable when supercritical temperatures are involved. Most of the components in refinery residue gas, for example, would be above their critical temperatures at practical adsorption conditions. It was theorized, however, that the molecular packing of an adsorbed gas (above and below its critical temperature) should

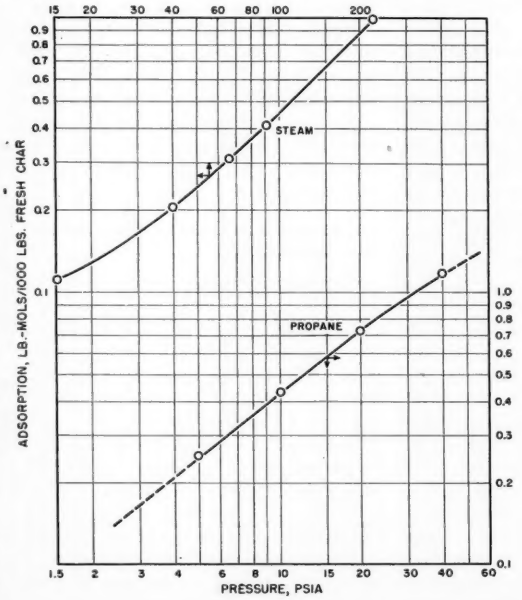

Fig. 2. Steam and propane adsorption on activated char at 500°F.

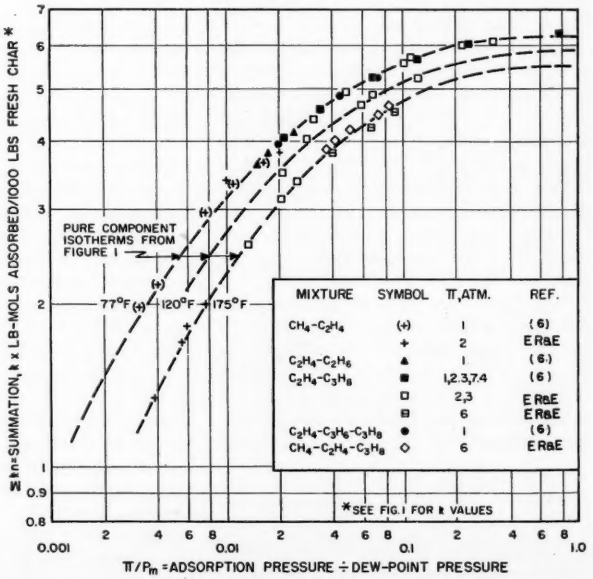
Σkn=SUMMATION, k x LB-MOLS ADSORBED/1000 LBS FRESH CHAR *
PURE COMPONENT ISOTHERMS FROM FIGURE 1
77°F (+) 120°F 175°F
MIXTURE SYMBOL π,ATM. REF.
CH4-C2H4 (+) 1 (6)
+ 2 E R&E
C2H4-C2H6 ▲ 1 (6)
C2H4-C3H8 ■ 1,2,3,7.4 (6)
□ 2,3 E R&E
⊟ 6 E R&E
C2H4-C3H6-C3H8 ● 1 (6)
CH4-C2H4-C3H8 ◇ 6 E R&E
*SEE FIG. 1 FOR k VALUES
π/Pm=ADSORPTION PRESSURE ÷ DEW-POINT PRESSURE

Fig. 3. Adsorption isotherm correlation: hydrocarbon mixtures on activated charcoal.

approach that of normal liquid, owing to the strong adsorption forces. Also, it was observed that the molal saturated-liquid volumes of light hydrocarbons are not too far apart and that the ratios of these volumes change very little with temperature. It was further presumed that extrapolated pressures at supercritical temperatures, obtained from a Clapeyron P-T plot, would satisfy the adsorption-potential relation derived by Polanyi. These considerations and subsequent testing of the data led to the following modification of Equation (1) as a basis for correlating pure light-hydrocarbon adsorption on the same char at temperatures above and below critical values:

$$(kN)_t = \phi(\pi/P) = N_\gamma' \qquad (2)$$

The correlation constant k (different for each component) and the constant-temperature restriction were provided to correct for imperfections in the theories and assumptions discussed above.

Pure-component adsorption data on C_1-C_4 hydrocarbons are correlated with Equation (2) in Figure 1. kN (constant times moles adsorbed on a constant weight of adsorbent) is plotted vs. "relative pressure" (π/P) at constant temperature. The data cover ranges of 77° to 175°F. temperature and 0 to 100 lb./sq. in. abs. pressure. The laboratory equipment and techniques used to obtain the data were substantially the same as described by Lewis et al. (*6*). These coworkers obtained similar data on Columbia G char at 77°F., which are included in Figure 1 for comparison.

Extrapolated vapor pressures, as previously described, are used in Figure 1 for supercritical temperatures. The dimensionless correlation constant k is defined as adsorption of the arbitrary reference component, ethylene, relative to that for the component in question at the same temperature and relative pressure; k for ethylene is always unity, by definition. The k values listed in Figure 1 were determined empirically from the 77°F. data. The various components all approach the average 77°F. correlation curve very closely with individual k values constant over the whole range of relative pressure. The same k values were used also for the 120° and 175°F. correlation isotherms. A minimum of data were obtained at the latter temperatures, and overlapping of the various components with respect to relative pressure is somewhat limited. As shown below, however, these correlations were found to be quite satisfactory when applied to prediction of mixture behavior.

Isotherm data on C_3 and steam are presented in Figure 2 for adsorption at 500°F., a representative temperature for desorption with steam. C_3's are substantially the only hydrocarbons present in significant amounts in the desorption zone of an adsorber for refinery C_1-C_2-C_3 separations. At the highly superheated conditions used for desorption in the pilot unit (*11*) (relative pressure in the range of 0.1), steam and light hydrocarbons were observed to adsorb substantially independently of each other at their respective partial pressures. The adsorption behavior of steam-hydrocarbon vapor near the dew point, however, is quite complex. Conditions of low superheat for such mixtures could be encountered in an adsorber refluxed with wet desorbate or in a low-temperature desorber steaming zone.

At total pressures in the range of 0 to 100 lb./sq. in. abs., it was found that adsorption of hydrogen, nitrogen, and carbon monoxide from refinery gas is negligible relative to hydrocarbon adsorption.

Gas-mixture Adsorption

A substantial amount of two- and three-component-mixture adsorption data on C_1, C_2, and C_3 hydrocarbons were obtained at 77°F. and 0 to 100 lb./sq. in. abs. Similar spot measurements were made at 120° and 175°F. These and similar data of Lewis et al. (*6*) are correlated in Figure 3 with a relation analogous to Equation (2) (Figure 1) for single components:

$$(\sum kn)_t = \phi(\pi/P_m) = N_\gamma' \qquad (3a)$$

or

$$\sum n/N_\gamma = 1 \qquad (3b)$$

The curves of Figure 1, representing the pure-component correlation iso-

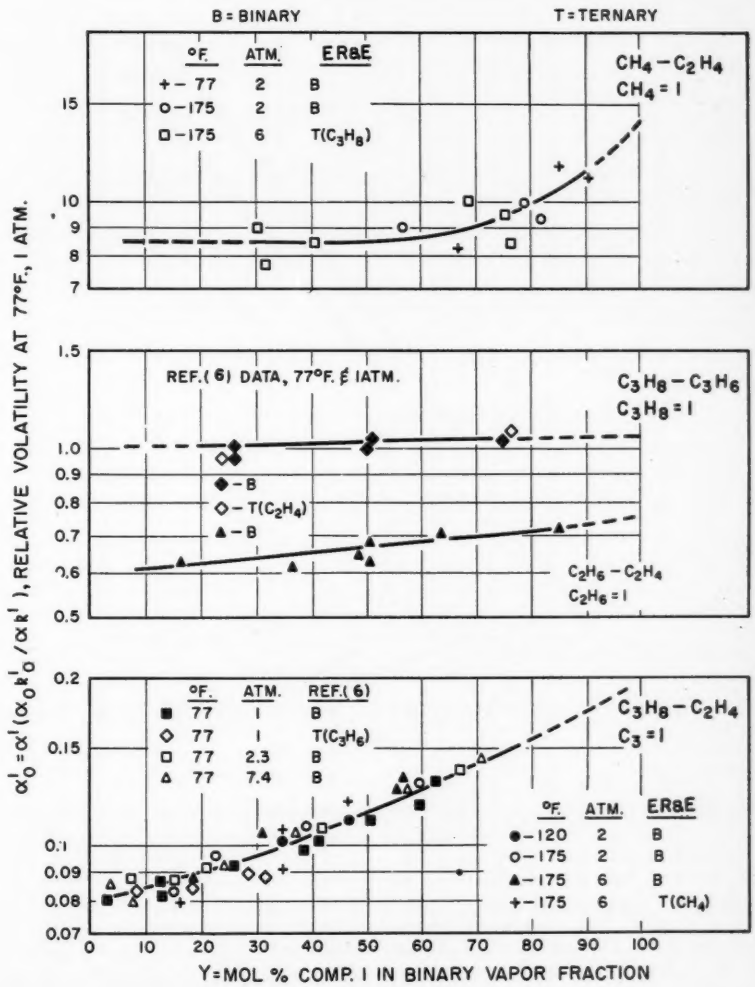

Fig. 4. Adsorption relative-volatility correlations: hydrocarbon mixtures on activated charcoal.

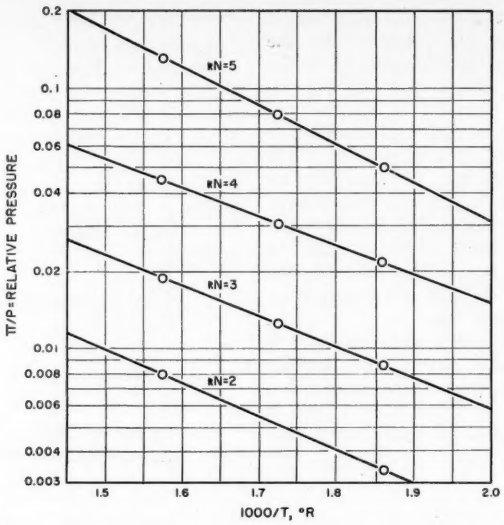

Fig. 5. Light-hydrocarbon adsorption on activated char: extension of correlation isotherms.

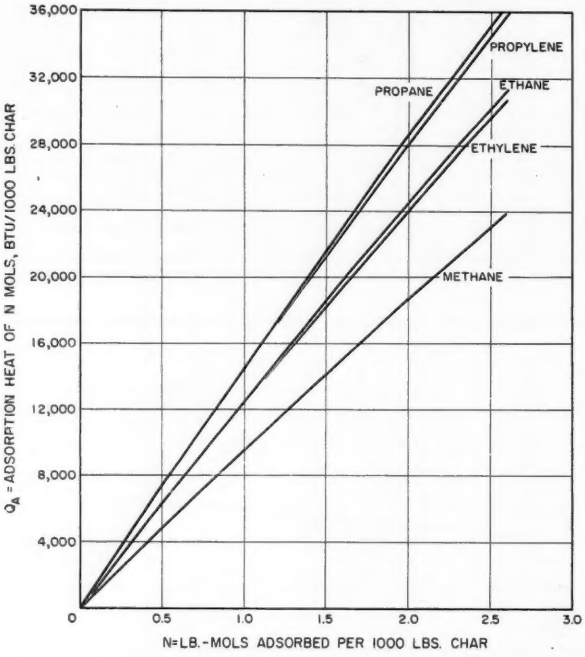

Fig. 6. Approximate isothermal adsorption heats: light hydrocarbons on activated charcoal.

therms, are superimposed on the mixture data in Figure 3. Thus the gas-mixture adsorption is indicated to be correlated satisfactorily by the pure-component isotherms of Figure 1. The same k constants derived from single-component data may be used for mixtures, $\Sigma\, kn$ being substituted for kN in Figure 1, and π/P_m for π/P.

The Figure 3 correlation obviously is not sufficient for a complete resolution of mixture adsorption. The adsorption relative-volatility concept (α') was introduced as the necessary supplement. The mixture adsorption relation observed by Lewis et al. (*6*) was very helpful in deriving a correlation basis for relative volatility:

$$\sum n/N_\pi = 1 \qquad (4)$$

[It is interesting to note the similarity of this relation and Equation (3b).] In order to develop a more fundamental correlation of relative volatility, mathematical expressions were sought for the adsorption isotherm correlation function ϕ for substitution in Equation (3a). A Freundlich type of relation (*4*) was substituted, Equations (3a) and (4) were combined, and the following α' correlation equation was developed:*

$$\alpha_0' = \alpha'\left(\frac{\alpha_0 k_0'}{\alpha k'}\right) = f\left(\frac{y}{y'}\right) \qquad (5)$$

This expression relates adsorption relative volatility to pure-component adsorption, vapor composition, and liquid relative volatility. Actually the Raoult-law value of the latter was indicated by the derivation. but the fugacity value was found to give a better correlation. Lewis and coworkers (*6*) correlated α' as a function of n/n' and pure-component adsorption.

Adsorption relative-volatility data on light-hydrocarbon mixtures are correlated in Figure 4, based on Equation (5). (The same data are represented in Figure 3.) α' values vary as much as threefold over the whole range of binary composition. The combined effects of temperature and pressure over the range covered produce the same order of variation. However, the data deviate by a maximum of about 15% from the averaged correlation curves. This deviation is not very significant in terms of estimated adsorber-char rates and separation stages.

The derivation of Equation (5) was based on binary-mixture adsorption. It was observed, however, that α' for two components is primarily a function of composition ratio (y'/y or n/n'), temperature and total pressure, and substantially independent of mixture complexity. This observation is in agreement with that of Lewis et al. (*6*). Thus Figure 4 may be applied for a given binary fraction of a complex mixture; e.g., k' and α' for each constituent relative to the same reference component are evaluated at the same π, t, and y/y' as for the complete mixture. The equilibrium adsorption of each constituent (n) from a multicomponent gas mixture can then be estimated with Figure 3†, Equation (5), and the following relation:

$$n' = \sum kn / \sum (ky/\alpha' y') \qquad (6)$$

Extension of Correlation Isotherms; Adsorption Heats

Clapeyron plots provide a means of interpolating or extrapolating the correlation isotherms. With reference to

*On substitution of a Langmuir type of relation for the ϕ function, a very simple relative volatility expression is obtained: $\alpha' = k\alpha$. This relation applies quite well for close-boiling pairs, as borne out by the data in Figure 4. (Relative pressure for close-boiling pairs at constant π and t varies very little over the whole range of composition.)

†Figure 7, discussed below, is equivalent to Figures 1 and 3.

Figure 5, log relative pressure is noted to vary linearly with reciprocal absolute temperature at constant mass adsorption. As approximations of isothermal adsorption heats H_A for light hydrocarbons, slopes of the curves in Figure 5 were taken equal to $(H_L - H_A)/2{,}300R$ for all the hydrocarbons at the same value of kN. H_L is necessarily a calculated quantity estimated with the Clapeyron relation and may not be real or representative of the true liquefaction heat.

The estimated differential adsorption heat H_A decreases with increasing N. Integral adsorption heats were estimated as

$$Q_A = \int_0^N H_A \, dN \qquad (7)$$

Estimated integral adsorption heats for light hydrocarbons on Columbia G char are plotted in Figure 6 as a function of N. These values at $N = 1$ are roughly twice the corresponding heats of liquefaction. Heats of adsorption for steam, which were estimated similarly in the range of 0.3 to 1 relative pressure, are close to liquefaction heats, indicative of capillary condensation. For estimation of adsorption heats of mixtures, it has been assumed that adsorption heat for each component is the same as for the pure component at $N = n$ and that adsorption heats are additive.

Figures 1 and 5 are combined in the form of an alignment chart, Figure 7, to permit more convenient estimates of kN or Σkn at various temperatures and relative pressures.

Limitations to the Adsorption Correlations

Quite extensive data on pure components and mixtures were obtained for the 77°F. correlation isotherms. At the higher temperatures (referring to Figure 1) the various pure components overlap to a somewhat limited extent with respect to relative pressure. The isotherm correlations were found to be adequate for mixture predictions, however, as borne out by spot data covering the range of adsorption and rectification conditions for the pilot plant (Figure 3).*

Cadogan (*2*) applied his thesis data to evaluate the authors' correlations. He found the constant k values listed in Figure 1 to be satisfactory for correlating light hydrocarbons on Columbia G char at constant temperature and over a wide range of relative pressure. His data on an activated carbon derived from coal, however, indicated a variation in k with temperature. On applying the Figure 1 correlation to the extensive adsorption data of Ray and Box (*10*), the authors observed a drift in hydrocarbon k values with both temperature and relative pressure. In view of these considerations, the reader is warned against applying Figures 4, 6 and 7 for conditions far outside the data range, other than for rough approximations, limited to 250°F. and 250 lb./sq. in. In a wide range of adsorption conditions the Figure 7 correlation no doubt should allow for variations in k values with temperature and relative pressure. These variations could be handled conveniently with alignment charts. Furthermore, as suggested by the derivations made in developing Equation (5), a varying k may be more satisfactory than k' for correlating adsorption relative volatility.

It is interesting to note that adsorption relative pressure is equal to Σx, estimated by Raoult's Law. This term may be considered as the total mole fraction of gases dissolved in a nonvolatile liquid at the same equilibrium gas composition, temperature, and total pressure as for the adsorption system considered. These considerations and the original "adsorption potential" or work concept of Polanyi (*9*) suggest the use of Σx estimated by the fugacity method, rather than relative pressure, for isotherm correlations. The fugacity method was tested and found to give correlation as good as but no better than relative pressure for both pure components and mixtures. As mentioned previously, however, fugacity α was substituted for the Raoult's Law value in Equation (5) in order to improve the Figure 4 correlation. The fugacity α value would have appeared in the derivation if fugacity Σx had been used for the isotherm correlations. Equilibrium liquid mole fractions might provide a satisfactory basis for a more general correlation of gas adsorption, by use of actual vapor-liquid data or Σx estimates based on fugacities and allowance for nonideal liquids.

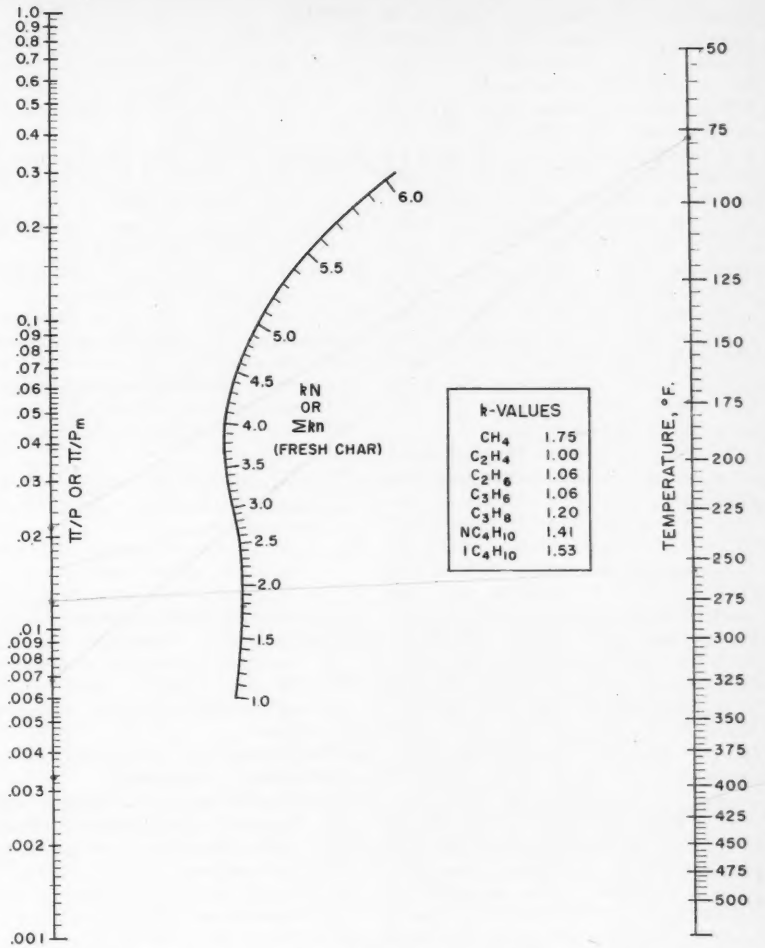

Fig. 7. Light-hydrocarbon adsorption on activated charcoal (Figures 1 and 5 combined).

Sample Calculations

Data and calculated results on equilibrium adsorption from a hypothetical gas mixture are summarized in Table 1. The first column in the table gives the equilibrium gas composition. The adsorption conditions are 6.5 atm. abs. pressure and 160°F. The following sample calculations

*The correlation methods should apply for other adsorbents, possibly even polar solids, as the correlation term k could allow for variation in adsorbate polarity. A new set of k values would have to be determined for each adsorbent.

demonstrate the suggested method of applying the correlations: $\Sigma y/P = 0.0071$ (Table 1); $\pi/P_m = 6.5(0.0071) = 0.0461$; $\Sigma kn = 4.13$ (Figure 7). Sample calculations of values in Table 1, with CH_4 used as an example: $P = 485$ atm. (Ref. 8); $\pi/P = 0.0134$; $N_\pi = 1.56$ (Figure 7). Similarly, $N_\pi' = 4.15$ (pure ethylene adsorption at 6.5 atm. and 160°F.); $k' = 4.15/1.56 = 2.66$. Similarly, $k_0' = 3.25$; $\alpha/\alpha_0 = 0.72$ (Ref. 8); $\alpha'/\alpha_0' = 0.59$ [Equation (5)]*; $y/(y + y') = 0.8$; $\alpha_0' = 10$ (Figure 4); $\alpha' = 0.59\ (10) = 5.9$; $n/n' = 0.4/(0.1 \times 5.9) = 0.68$ [α' definition]; $k = 1.75$ (Figure 7); $kn/n' = 1.18$; $\Sigma kn/n' = 11.25$ (Table 1); $n' = \Sigma kn/\Sigma(kn/n') = 0.37$ [Equation (6)]; $n = 0.37\ (0.68) = 0.25$ lb.-mole CH_4 adsorbed/1,000 lb. fresh char.

Similarly, n is calculated for each of the other mixture constituents to obtain the equilibrium adsorption of each component on the fresh char represented by Figure 7 (right-hand column of Table 1). Note that the adsorption of inert gas (H_2, N_2, CO) is negligible and was assumed to be zero in the sample calculations. Adsorption relative volatilities for deactivated chars were found to vary insignificantly over an activity range of 75 to 100%. Thus n values for fresh char multiplied by char activity give satisfactory estimates of mixture adsorption on deactivated chars. Pure-component adsorption at atmospheric conditions, relative to that on fresh char, provides a satisfactory index of adsorbent activity. The method of estimating adsorption heats is described in the discussion of Figure 6.

Table 1. Sample Data and Calculation Results on Mixture Adsorption

Comp.	y	P	$100\ y/P$	N_π	α/α_0	α_0'	α'	n/n'	k	kn/n'	n
H_2, N_2, CO	0.25	—	0	—	—	—	—	—	—	—	0
CH_4	0.40	485	0.083	1.56	0.72	10.0	5.90	0.68	1.75	1.18	0.25
C_2H_4	0.10	137	0.073	4.15	1.00	1.00	1.00	1.00	1.00	1.00	0.37
C_2H_6	0.15	89	0.169	4.30	1.10	0.68	0.80	1.88	1.06	1.99	0.70
C_3H_8	0.10	26	0.385	4.77	1.63	0.11	0.17	5.90	1.20	7.08	2.18
Totals	1.00		0.710							11.25	3.50

ACKNOWLEDGMENT

The authors wish to express their appreciation to the Esso Engineering and Research Company for permission to publish this paper. Sincere thanks are extended to W. K. Lewis and coworkers (6), who at an early stage of their investigations made their preliminary adsorption data and the Equation (4) relation available to the authors. Acknowledgment is made to the Carbide and Carbon Chemicals Company for helpful information on their Columbia activated carbons.

*Before adsorber-design calculations, it is convenient to prepare constant-pressure working plots of α'/α_0' vs. temperature by application of Equation (5). This procedure minimizes calculations on N_π, k', α/α_0, etc.

NOTATION

f = function of y/y' or Y, Equation (5)
H_A = differential isothermal adsorption heat at N, obtained from slope of log π vs. $1/T$ at constant N, B.t.u./lb.-mole
H_L = isothermal heat of liquefaction obtained from slope of log P vs. $1/T$, B.t.u./lb.-mole
k = adsorption isotherm correlation constant, defined as N_r'/N_r
k' = N_π'/N_π. The term N_π represents component 1 in Figure 4.
N = equilibrium adsorption from pure vapor at π and t, lb.-moles/1,000 lb. adsorbent
N_r = N at same relative pressure (and temperature) as for an equilibrium vapor mixture or a reference component
N_r' = N_r for arbitrary reference component (ethylene) = Σkn or kN at r and t
N_π = N at the same pressure (and temperature) as for a mixture
N_π' = N_π for reference adsorption relative-volatility component
n = equilibrium adsorption of one component from a vapor mixture, lb.-moles/1,000 lb. adsorbent (n represents component 1 in Figure 4).
n' = n for reference adsorption relative-volatility component
P = equilibrium vapor pressure of pure liquid at t, atm.; values at supercritical temperatures obtained by extrapolation, log P vs. $1/T$; values used for correlations obtained from Maxwell (8)
P_m = dew-point pressure of equilibrium-adsorption vapor mixture at t, based on Raoult's Law; $P_m = 1/\Sigma(y/P)$, atm.
Q_A = integral isothermal adsorption heat of N [Equation (7)], B.t.u./1,000 lb. adsorbent
r = relative pressure, π/P or π/P_m
R = perfect-gas law constant = 1.99 B.t.u./(lb.-mole)(°R.)
t, T = temperature of equilibrium adsorption system, °F. and °R., respectively
v = equilibrium adsorption of pure vapor, expressed as saturated liquid volume at t, cc./g. adsorbent
V = molal saturated liquid volume of pure component at t, cc./g.-mole
x = equilibrium liquid mole fraction at y, π, and t = component 1 in Figure 4
x' = x for reference relative volatility component
y = mole fraction of one component in adsorption vapor mixture = component 1 in Figure 4
y' = y for reference relative-volatility component
Y = mole fraction in a binary fraction of a vapor mixture = $y/(y + y')$
α = liquid relative volatility = $yx'/y'x$ at π, t; fugacity values obtained from Maxwell (8) used in Figure 4
α' = adsorption relative volatility at Y, π, and t, defined as $yn'/y'n$
π = total absolute pressure of equilibrium adsorption system, atm.
Σ = summation of all mixture quantities
ϕ = adsorption-isotherm correlation function of relative pressure at constant t; same for Equations (2) and (3a)

Subscripts

m = a mixture quantity
0 = arbitrary standard conditions of $\pi = 1$ atm. and $t = 77$°F.
r = a pure-component adsorption value at the same relative pressure and temperature as for a mixture or another pure component
v = constant v
t = constant t
π = a pure-component adsorption value at the same total pressure and temperature as for a mixture

LITERATURE CITED

1. Brunauer, S., P. H. Emmett, and E. Teller, *J. Am. Chem. Soc.*, **60**, 309 (1938).
2. Cadogan, W. P., Sc.D. thesis, p. 132, Mass. Inst. Technol. (1948).
3. Dubinin, M. M., and D. P. Timofeyev, *Compt. rend. acad. sci. U.R.S.S.*, **54**, No. 8, 701 (1946); **55**, No. 2, 137 (1947).
4. Freundlich, H., "Colloid and Capillary Chemistry," translated from 3d German edition by H. S. Hatfield, Methuen and Co., London (1926).
5. Langmuir, I., *J. Am. Chem. Soc.*, **40**, 1361 (1918).
6. Lewis, W. K., E. R. Gilliland, B. Chertow, and W. P. Cadogan, *Ind. Eng. Chem.*, **42**, 1319 (1950).
7. London, F., *Z. physik. Chem.*, **11**, 222 (1931).
8. Maxwell, J. B., "Data Book on Hydrocarbons," D. Van Nostrand Company, Inc., New York (1950).
9. Polanyi, M., *Verhandl. deut. physik. Ges.*, **16**, 1012 (1914); **18**, 55 (1916); *Z. Elektrochem.*, **26**, 370 (1920); *Trans. Faraday Soc.*, **28**, 316 (1932).
10. Ray, G. C., and E. O. Box, Jr., *Ind. Eng. Chem.*, **42**, 1315 (1950).
11. Etherington, L. D., et al., paper presented at the New York meeting of Am. Inst. Chem. Engrs. (December, 1954).

Presented at A.I.Ch.E. New York meeting

Regeneration of Fluidized Cracking Catalysts

WILLIAM F. PANSING

Standard Oil Company (Indiana), Whiting, Indiana

An equation for correlating regeneration process variables in fluid-catalytic cracking has been developed from pilot plant data. This equation takes into account not only the chemical-reaction rate for burning coke deposited on the catalyst but also the diffusional resistance to oxygen transfer. The resistance presumably occurs between the bubbles within the fluidized bed and the void spaces in the relatively denser mass of particles. The coefficient of mass transfer was found to be inversely proportional to the 1.5 power of the average particle diameter and directly proportional to the square of the gas mass velocity. The specific reaction-velocity constant was found to be a function of temperature and catalyst activity as well as the nature of the feed from which the coke was deposited. Comparison of pilot plant data with commercial data suggests that nonuniform gas distribution in larger beds makes some of the catalyst ineffective.

Regeneration of coked or spent catalyst by burning the coke with air is an essential part of the catalytic-cracking process; indeed, the capacity of the regenerator for burning the formed coke often limits the rate at which a unit can crack feed. To understand the performance of the regenerator, the process variables involved in regeneration must be recognized and a knowledge of the relations among them obtained.

The kinetics of regeneration have been established from fixed-bed studies (*2, 14*). Other studies have shown how the mechanics of fluidization might influence the reaction rate in a fluidized bed (*3, 4*). Combination of these two types of information should lead to a useful relationship between the important variables. Such a correlation has been developed from theoretical considerations. Pilot plant studies have been used to evaluate the constants.

THEORY

During burning of coke, oxygen must be transferred from the air stream to the surface of the catalyst. Burning rate may as well be limited by diffusion from the air stream to the surface as by reaction on the surface. In a fixed bed, the resistance to diffusion occurs in a stagnant film surrounding the individual catalyst particles. In a fluidized bed, however, much of the gas passes through the catalyst in the form of pseudobubbles or pockets and relatively little flows through the interstices between the more densely packed particles (*3*). Much of the catalyst can receive oxygen only by diffusion or mass transfer of gas from the bubbles. Resistance to mass transfer can be combined with reaction kinetics to develop an equation for the over-all rate of reaction. A material balance can be combined with this equation to give an equation interrelating the process variables (*7*), provided certain assumptions are made.

The concentration of carbon on the catalyst can be considered uniform throughout a fluidized bed, because the rate of catalyst mixing is rapid (*3*). The gas flow can be assumed unidirectional, because by-passing or short-circuiting of gas in a fluidized bed is far more pronounced than back mixing (*3, 4*). Gas by-passing causes the oxygen concentration to vary across the horizontal cross section of the regenerator, but an average oxygen concentration can be assumed to exist at a given vertical level. Although coke contains 5 to 15% hydrogen, the carbon on the catalyst can be taken as a measure of the coke.

Resistance to mass transfer can be combined with reaction kinetics in a manner similar to that proposed by Hurt (*8*). The rate of reaction of carbon is known to be first order with respect to the concentration of carbon on the catalyst (*14*) and the partial pressure of oxygen (*2*). However, carbon and oxygen must react in some stoichiometric ratio. Hence the rate of reaction of oxygen r_r in moles/hr./lb. of catalyst can be expressed as

$$r_r = k_r C_r p_i \qquad (1)$$

where the proportionality constant relating the rates of carbon and oxygen reactions is contained in k_r, the specific reaction-velocity constant in moles/hr./atm./lb. The term C_r is the fraction of carbon on regenerated catalyst, and p_i is the partial pressure of oxygen in interstices of catalyst in atm. The rate of oxygen transfer depends upon the pressure gradient of the oxygen from the interior of the bubbles to the interstices of the catalyst. Thus r_d, the rate of oxygen diffusion from bubbles to catalyst

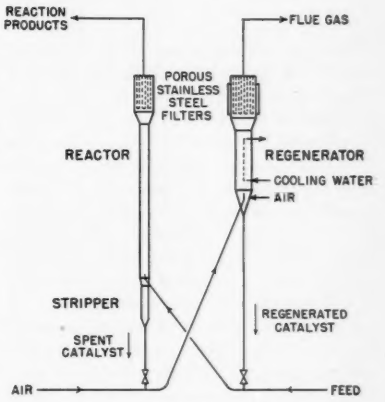

Fig. 1. Pilot plant.

in moles/hr./lb. of catalyst, can be expressed as

$$r_d = k_d(p - p_i) \qquad (2)$$

where k_d is the coefficient of mass transfer in moles/hr./atm./lb. and p is the partial pressure of oxygen in bubbles in atm. At steady state conditions, the over-all rate of reaction must equal the rate of oxygen transfer or rate of surface reaction. Thus, after equating Equations (1) and (2), solving for p_i, and substituting this expression in Equation (1) one can express the over-all rate of reaction r, in moles/hr./lb. of catalyst, as

$$r = \frac{p}{\frac{1}{k_d} + \frac{1}{k_r C_r}} \qquad (3)$$

A material balance on oxygen across a differential length of regenerator may be written

$$F\,dN = -r\,dW \qquad (4)$$

where F is the feed rate of gas in lb./hr., N is the oxygen concentration in the gas in lb. moles/lb. feed, and W is the weight of catalyst in lb. If Equation (3) is substituted in Equation (4) and the total moles of reactants and products is considered constant, the resulting equation may be integrated from the inlet to the outlet oxygen concentration to give

$$-\frac{W}{F} = \frac{N_t}{P}\left(\frac{1}{k_d} + \frac{1}{k_r C_r}\right) \ln \frac{N}{N_0} \qquad (5)$$

where N_t is the total moles gas/lb. of feed to the regenerator, P is the total pressure in atm., and N_0 is the inlet oxygen contration in lb. moles/lb. feed. The quantity FN_t/W is defined as the space velocity S and equals the moles of gas fed to the regenerator/hr./lb. of catalyst. The quantity N/N_0 is the fraction of inlet oxygen unconverted in the regenerator and is defined as f. If these terms are introduced in Equation (5), it may be rearranged to give

$$-\frac{PC_r}{S \ln f} = \frac{C_r}{k_d} + \frac{1}{k_r} \qquad (6)$$

Significant variables are thus related in terms of a specific reaction-velocity constant and coefficient of mass transfer.

Equation (6) could be used to evaluate the specific reaction-velocity constant k_r from regeneration data if values of k_d were available. Although some data on mass transfer in fluidized beds exist (*11*), there are no data on particles in the 0- to 100-μ range. Hence the coefficient of mass transfer can be assumed to be a function of some powers of the mass velocity of the gas and the average particle diameter. Higher gas velocities or finer catalysts will increase the distance between particles and so the resistance to diffusion will be less. Thus the coefficient of mass transfer k_d may be expressed as

$$k_d = \frac{1}{\alpha} \frac{G^m}{D_p^n} \qquad (7)$$

where α is a proportionality constant, m and n are unknown exponents, G is the gas mass velocity in the regenerator in lb./hr./sq. ft., and D_p is the average particle diameter in μ. Equation (7) can be substituted in Equation (6) to give

$$-\frac{PC_r}{S \ln f} = \alpha \frac{CD_p^n}{G^m} + \frac{1}{k_r} \qquad (8)$$

which represents a straight line of slope α and intercept $1/k_r$ when $-PC_r/(S \ln f)$ is plotted against $C_r D_p^n/G^m$. Both k_r and α can be evaluated from regeneration data if suitable values of m and n can be obtained.

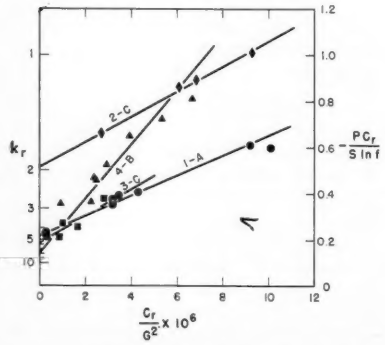

Fig. 2. Determination of correlation constants. Curves identified by catalyst number and feed letter.

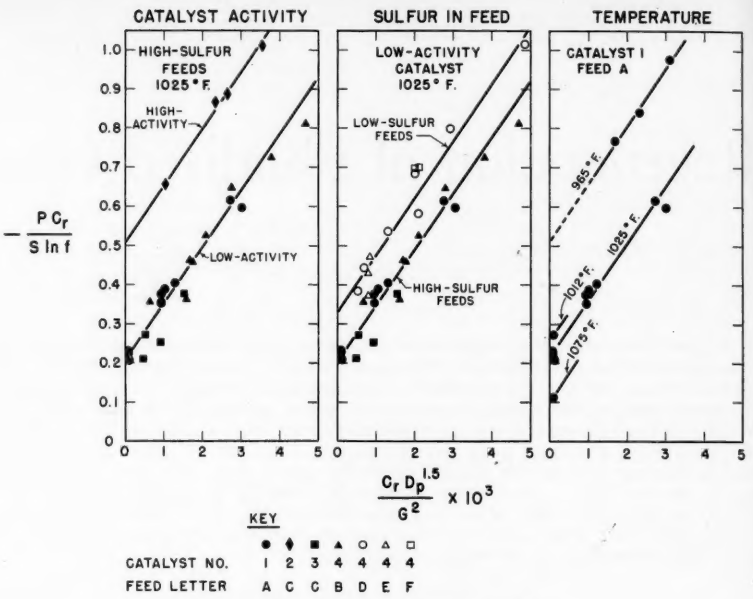

Fig. 3. Correlation of regeneration variables.

EVALUATION OF CONSTANTS

Forty-two pilot plant tests were made to evaluate the constants α, m, and n in Equation (8) and to determine k_r for catalysts of different activities and with carbon deposited by various feeds.* For each catalyst and feed, a series of tests was made at a constant temperature but with differing superficial gas velocities, carbon-on-catalyst levels, pressures, catalyst inventories, and oxygen conversions.

The capacity of the pilot plant was 2 bbl./day. A simplified diagram of the unit is shown in Figure 1. The regenerator, excluding the filter section, was constructed of 10-in. extraheavy steel pipe 5 ft. long.

*Data on these tests have been filed as document 4792 with the American Documentation Institute, Photoduplication Service, Library of Congress, Washington 25, D. C., and may be obtained for $1.25 for photoprints or 35-mm. microfilm.

Synthetic silica-alumina catalysts were used. Three of them were removed from commercial units to obtain samples with representative equilibrium activities. The fourth was a fresh catalyst which was deactivated in the pilot plant. Table 1 gives the properties. Activity was measured by the Indiana relative activity method (*13*) and particle-size distribution was determined by a modified Roller analysis (*9, 12*). The average particle diameter was defined as that diameter representing the specific surface of the catalyst (*5, 6*).

Properties of the gas-oil feeds are shown in Table 2. Feeds *A*, *B*, and *C* were derived from high-sulfur West Texas crude; *E* and *F* from low-sulfur Midcontinent crude; feed *D* was a West Texas gas oil that had been extracted to remove sulfur and aromatic compounds. Concentration of oxygen in the flue gas was

Table 1. Properties of Catalysts

Catalyst	Roller analysis, μ 0–10	10–20	20–40	40–80	80+	Average particle diam. μ	Indiana relative activity
1	1.5	4.4	16.4	34.1	43.6	44.5	35
2	4.0	3.0	6.7	21.2	65.1	52.7	90
3	0.0	0.1	16.3	35.3	48.3	67.1	32
4	0.0	0.0	3.2	40.1	56.7	79.0	20

Table 2. Properties of Feeds

Feed No.	Gravity, °A.P.I.	A.S.T.M. distillation Initial	50%	90%	Max.	Sulfur, wt. %	Aniline Point, °F.
A	26.7	378	640	764	—	1.62	158
B	26.7	420	650	744	750	1.61	157
C	28.2	268	619	741	—	1.65	150
D	30.0	408	658	768	—	0.64	172
E	31.1	496	640	752	—	0.40	177
F	31.6	410	612	738	744	0.36	175

continuously measured by a Beckman analyzer (*10*).

The carbon on the catalyst was determined by igniting a catalyst sample in a boat placed in a furnace with a stream of oxygen. The carbon dioxide and traces of sulfur dioxide formed were absorbed in soda lime and weighed. No correction was made for the sulfur dioxide. The hydrogen in the coke was estimated from the difference between the oxygen actually consumed in the regenerator and that required to burn the carbon.

A trial-and-error procedure was used to determine the value of m, exponent of mass velocity. Data obtained at a constant temperature, with a given catalyst, and with superficial velocities of 0.1 to 0.6 ft./sec. were plotted as $-PC_r/(S \ln f)$ vs. C_r/G^m. The value of m was adjusted to produce the best straight line. A value of $m = 2$ provided the best correlation, as shown in Figure 2.

According to Equation (8), the slopes of the straight lines in Figure 2 for catalysts of different particle sizes should equal αD_p^n. Thus a plot of the log of the slope against the log of the average particle size should give a straight line of slope n. Such a plot gave the value of n as 1.5.

Finally plots of $-PC_r/(S \ln f)$ vs. $C_r D_p^{1.5}/G^2$, as shown in Figure 3, established the slope α as 146. The final equation relating the fundamental process variables to the specific reaction-velocity constant of the catalyst is

$$-\frac{PC_r}{S \ln f} = 146 \frac{C_r D_p^{1.5}}{G^2} + \frac{1}{k_r} \quad (9)$$

DISCUSSION

The effects of catalyst activity, type of feed, and temperature of regeneration are shown in Figure 3. The low-activity catalysts show a higher reaction-velocity constant than does the high-activity catalyst. This effect was observed in laboratory fixed-bed and commercial fluidized-bed units in which fresh or high-activity catalysts regenerated more slowly than low-activity or used catalysts. Metals deposited from the feed lower the catalyst activity for cracking but apparently act as catalysts to promote burning of carbon.

At a constant temperature and catalyst activity, the reaction-velocity constant for carbon deposited from high-sulfur feeds is higher than from low-sulfur feeds. It is not known whether a fundamental difference exists in the nature of the coke or whether sulfur or some other compound promotes the burning of coke.

The effect of temperature on the reaction-velocity constant is pronounced. A plot of the constants from Figure 3, according to the Arrhenius equation, is shown in Figure 4. The slope of the plot gives an activation energy of 63,000 B.t.u./lb. mole (35 kcal./g. mole). Fixed-bed data have given a value of 36 kcal./g. mole (*14*). These values agree only because mass transfer resistances have been separated from the reaction-velocity constants; otherwise the activation energy in the fluidized bed would have been much lower.

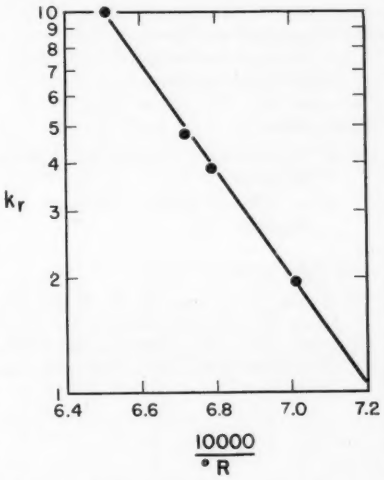

Fig. 4. Arrhenius plot for catalyst 1, feed A.

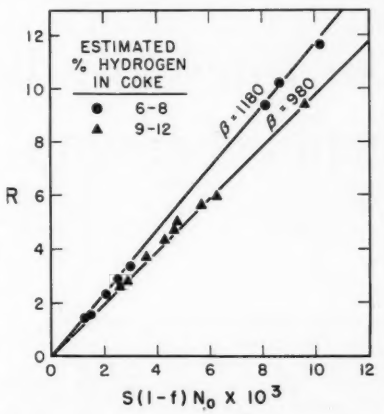

Fig. 5. Relation between rate of carbon burning and oxygen consumption.

APPLICATION OF CORRELATION

To aid in the application of Equation (9) for predicting regenerator performance, an auxiliary equation relating the total coke-burning capacity of the unit to the regeneration variables may be developed. Thus, from the stoichiometry of the regeneration process, the weight of carbon burned must be proportional to the moles of oxygen consumed. R, the lb. of carbon burned/hr./100 lb. of catalyst, can be expressed as

$$R = \beta N_0 (1 - f) S \quad (10)$$

where β is a proportionality constant. By definition

$$R = (C_s - C_r) \frac{U}{W} \quad (11)$$

where C_s is the fraction of carbon on spent catalyst and U is the catalyst-circulation rate in lb./hr.

A plot of Equation (10) with data for seventeen tests is shown in Figure 5. The slope of the line β is a function of the percentage of hydrogen in coke, because R was calculated in terms of carbon and neglects the hydrogen in the coke.

The application of Equations (9), (10), and (11) for analyzing pilot plant regenerator performance may be shown by an example. A regenerator may be required to burn a certain quantity of coke with a given catalyst inventory and air rate. From Equation (10), the value of f may then be calculated. If catalyst-circulation rate and concentration of carbon on spent catalyst are also fixed by reactor conditions, the concentration of carbon on regenerated catalyst may be calculated from Equation (11). If the regenerator operates at constant pressure, the reaction-velocity constant may be calculated from Equation (9). The regeneration temperature may then be estimated from Figure 4.

The correlation has proved less useful when applied to commercial units, where such interfering factors as afterburning and partial combustion in large transfer lines are more difficult to control. Equation (9) usually gives lower reaction-velocity constants than are observed in the pilot plant. Reaction-velocity constants developed from pilot plant data contain a factor that represents the extent of participation of the catalyst in the reaction. In commercial units, where the regenerator may be 30 ft. in diam., part of the catalyst may be ineffective because of nonuniform gas distribution in the fluidized bed. The observed better regenerator performance with finer catalysts (*1*) may be the result of more uniform fluidization and greater participation of the catalyst. Higher superficial velocities would also be expected to increase the effectiveness of the catalyst.

Two additional types of investigations might increase the usefulness of the correlation for commercial units. Pilot plant studies at the higher velocities used in commercial units might lead to constants more applicable in the correlation. A study of the effect of superficial velocity in a commercial unit should increase understanding of the differences in fluidization in small and large regenerators.

NOTATION

C_r = fraction of carbon on regenerated catalyst
C_s = fraction of carbon on spent catalyst
D_p = average particle diameter representing specific surface of catalyst, μ
f = fraction of inlet oxygen unconverted in regenerator (N/N_0)
F = rate of gas feed to regenerator, lb./hr.
G = gas mass velocity in regenerator, lb./(hr.)(sq. ft.)
k_d = coefficient of mass transfer, lb. mole/(hr.)(atm.)(lb.)
k_r = specific reaction velocity constant, lb. mole/(hr.)(atm.)(lb.)
m = exponent on G
n = exponent on D_p
N = oxygen concentration in gas, lb. mole/lb. feed
N_0 = inlet oxygen concentration in gas, lb. mole/lb. feed
N_T = total moles gas/lb. feed to regenerator
p = partial pressure of oxygen in bubbles, atm.
p_i = partial pressure of oxygen in interstices of catalyst, atm.
P = total pressure, atm.
r = over-all rate of reaction of oxygen, lb. mole/(hr.)(lb.)
r_d = rate of diffusion of oxygen from bubbles to catalyst, lb. mole/(hr.)(lb.)
r_r = rate of reaction of oxygen at surface of catalyst, lb. mole/(hr.)(lb.)
R = carbon burning rate, lb./(hr.)(100 lb. catalyst)
S = space velocity, moles/(hr.)(lb.)
T = catalyst temperature, °F.
U = catalyst circulation rate, lb./hr.
W = catalyst inventory, lb.

Greek Letters

α = a proportionality constant, slope of Equation (8)
β = a proportionality constant in Equation (10)

LITERATURE CITED

1. Brown, C. O., and R. B. Wainright, *Chem. Eng.*, **59**, 148 (1952).
2. Dart, J. C., R. T. Savage, and C. G. Kirkbride, *Chem. Eng. Progr.*, **45**, 102 (1949).
3. Gilliland, E. R., paper presented before New Jersey Section of A.I.Ch.E. (May 5, 1953).
4. ———, E. A. Mason, and R. C. Oliver, *Ind. Eng. Chem.*, **45**, 1177 (1953).
5. Hatch, T., *J. Franklin Inst.*, **215**, 27 (1933).
6. ———, and S. P. Choate, *loc. cit.*, **207**, 369 (1929).
7. Hougen, O. A., and K. M. Watson, "Chemical Process Principles—Part III," John Wiley and Sons, Inc., New York (1947).
8. Hurt, D. M., *Ind. Eng. Chem.*, **35**, 522 (1943).
9. Matheson, G. L., *Proc. Am. Petroleum Inst.*, **27** [III], 18 (1947).
10. Pauling, L., R. E. Wood, and J. H. Sturdivant, *J. Am. Chem. Soc.*, **68**, 795 (1946).
11. Resnick, W., and R. R. White, *Chem. Eng. Progr.*, **45**, 377 (1949).
12. Roller, P. S., *Proc. Am. Soc. Testing Materials*, **32**, 607 (1932).
13. Shankland, R. V., and G. E. Schmitkons, *Proc. Am. Petroleum Inst.*, **27** [III], 57 (1947).
14. Webb, G. M., and M. J. Den Herder, paper presented before the Am. Inst. Chem. Engrs., Kansas City (May, 1951).

Presented at A.I.Ch.E. New York meeting

Performance of an Internally Baffled Multistage Extraction Column

EDWARD G. SCHEIBEL

Hoffmann La Roche, Inc., Nutley, New Jersey

Internally agitated extraction columns generally require increasing heights for a theoretical stage for the larger column diameters. The present work describes a design developed to minimize this objection and presents the performance data on a system considered easy to extract and on systems considered difficult to extract. H.E.T.S. values as low as 3 in. on the first system and 4 in. on the second type of system were obtained in an 11½ in. I.D. glass column. The stage efficiencies were correlated as a function of power input per unit volume of solvent throughput and the ratio of the flow rate of the dispersed phase to that of the continuous phases. The supplementary effect of packing was studied and found to be most beneficial in the system which has a low interfacial tension and is considered easy to extract. By the use of this particular arrangement of internal baffles, it is believed possible, in the larger diameter columns, to reduce the height to a ratio of H.E.T.S. to diameter below the value of ¼ obtained in the present column.

The performance studies on mechanically agitated liquid-liquid extraction columns generally indicate that the height required for a theoretical stage increases as the diameter of the column becomes greater although not necessarily in a direct proportionality. In the design of extraction columns consisting of alternate mixing sections and packed calming sections, it was found that the optimum packing height which gives the minimum H.E.T.S. values was approximately proportional to the square root of the column diameter for the 1- and 12-in. sizes. Early studies on the use of vertical baffles in the mixing sections of such a column indicated that although these baffles eliminated the rotational motion of the fluids and probably improved the mixing, they transformed this motion into vertical motion and required an even greater

Present address: York Process Equipment Corp., est Orange, New Jersey.

amount of packed height to isolate the flow patterns of the individual mixing sections. It then became obvious that horizontal baffles were essential for the best performance of an internally agitated extractor. Oldshue and Rushton (*4*), using a flat-bladed turbine to promote the mixing, studied the performance of a column with annular horizontal baffles.

Reman (*5* and *6*) presented performance data on a similar column with a rotating disk used in place of the turbine for the agitating means. On an easy extraction system such as methyl isobutyl ketone–water–acetic acid, an 8-in.-diam. column gave a theoretical stage in as little as 5 in. of height. This was in substantial agreement with the performance of the Oldshue and Rushton column on the same system. On a difficult extraction system such as water–kerosene–butylamine, a 16-in.-diam. extractor required more than 2 ft. for a theoretical stage. A 4-in.-diam. column of the same design gave substantially the same stage height and on this basis Reman and Olney (*6*) postulated that there is no loss of efficiency in scaling up this type of column.

In general, however, in internally agitated extractors the height required for a theoretical stage increases with diameter because of the tendency of the flow pattern in the mixing section to follow a geometrically similar shape when scale-up is made on the basis of dimensional similitude. The present work describes an arrangement of internal baffling in a mixing section whereby the relationships of dimensional similitude need not be followed in a scale-up design. Figure 1*a* illustrates a normal vertical-flow pattern in a fully baffled tank. Figure 1*b* shows the geometric scale-up of this flow in a tank four times the diameter. In order to retain the same mixing height at the larger diameter, it will be necessary to direct the flow across the entire diameter by means of the stationary horizontal baffles shown in Figure 1*c*. These baffles can be so spaced as to give any desired flow pattern across the diameter of the column without regard to dimensional similarity. Scale-up based on dimensional similitude and a constant linear velocity through the column will increase the residence time in the mixing section proportional to the scale-up factor. This will tend toward better mass transfer and will allow some decrease in the spacing of the baffles for the same efficiency.

On the other hand, if the spacing is decreased so that residence time in the mixing section is maintained constant, the corresponding linear velocities between the baffles, which will maintain the same number of recycles of the liquid over the flow pattern in passing through the mixing section, will be increased in proportion to the scale factor. This will increase the contacting and resulting mass transfer between the phases but will also increase the difficulty of phase separation between the mixing stages. Obviously a compromise is necessary and desirable. Increasing the height of the mixing section based on the square root of the scale-up factor represents a compromise halfway between the two previous extremes. In the present work only one column diameter was tested and so this conclusion could not be tested. However in the previous design with unbaffled mixing sections separated by packing, the data on the easy extraction system, acetic acid–methyl isobutyl ketone–water, gave a minimum observed H.E.T.S. of 2¼ in. in a 1-in. column (*7*) and 9.2 in. in a 12-in.-diam. column (*8*). In the latter column no runs were made at the optimum packing height, which was intermediate between the two heights investigated, and it was estimated that

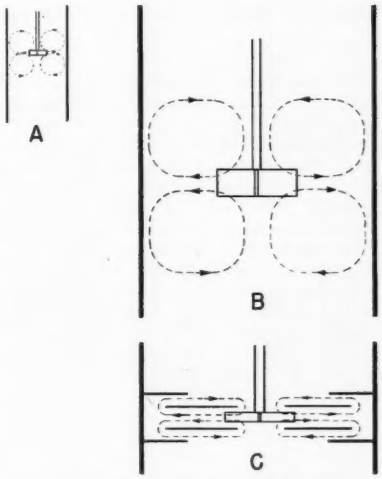

Fig. 1. Schematic design of vertical flow components in agitated column. A, original pattern; B, dimensional-similitude scale-up by factor of 4; C, modified pattern for scale-up factor of 4 with original height.

for the best design the H.E.T.S. would be reduced by about 10%. On a difficult extraction system such as *o*-xylene-water the 1-in. column gave a minimum observed H.E.T.S. of 4.2 in. (*7*) and the 12-in. column gave a minimum value of 15 in. (*8*). In the latter case one of the packing heights investigated was close to the optimum, and so the value represents very nearly the lowest value obtainable. From these data it is readily established that the H.E.T.S. on this type of column varies as the square root of the diameter, and this has been successfully extrapolated to the design of larger columns. In the new design described in this work it is expected that the control of the mixing height will give an even smaller variation of H.E.T.S. with diameter, and square root factor can be conservatively used until more data are available.

When packing was used to separate the mixing stages without baffles, the normal flow pattern carried the fluids up into the packing, where all the rotational motion was removed before the fluids returned to the agitator. Thus there was no accumulation of rotational energy, as in an unbaffled tank. In this new design with no appreciable flow expected through the packing, the rotational energy might accumulate excessively and interfere with the desired net flow through the column. To eliminate this possibility, vertical baffles can be installed around the column wall or between the two inner annular baffles at the discharge of the impeller. In the present study two layers of knitted-wire mesh were inserted between these inner annular plates and held in place against the vertical support rods by threading them on a circular ring of ⅛-in. stainless steel rod. This served to promote the contacting of the two phases by pumping them through the fine openings in the mesh, and it also served to remove most of the rotational energy. Preliminary tests on a single stage at low agitator speeds indicated that a double thickness of mesh was adequate, but in the subsequent tests on the column one of the liquid systems required such large agitator speeds that this thickness of mesh removed only a fraction of rotational motion and more layers would be necessary to achieve a fully baffled appearance. In spite of the appearance, however, the measured power consumption of the agitator at these conditions was in perfect agreement with the correlation for a fully baffled tank.

EQUIPMENT AND OPERATIONS

Figure 2 shows the details of the column assembly. Three different arrangements were investigated. The first consisted of nine mixing sections 2 in. high with 2 in. of packing between the mixing sections and at the ends. In the second arrangement the packing bundles were removed and the mixing sections were separated by the void chambers. In the third arrangement baffles and agitators were installed in all the intermediate void sections to give a total of seventeen mixers and the two end sections were left void to ensure complete phase separation at the top and bottom of the column.

The flow sheet for the tests was identical with that previously described for the study of the performance of a multistage semicommercial extraction column (*8*). Much of the same equipment was used, including the original column shell, consisting of two 12 in. O.D. glass cylinders 24 in. high.

The solvent systems used in this work were methyl isobutyl ketone–water–acetic acid, *o*-xylene–water–acetic acid, and *o*-xylene–water–phenol. The first system is considered easy to extract and employs approximately equal solvent ratios. The other systems are considered difficult to extract, the second one requiring solvent ratios of about 20 to 1 and the third requiring about

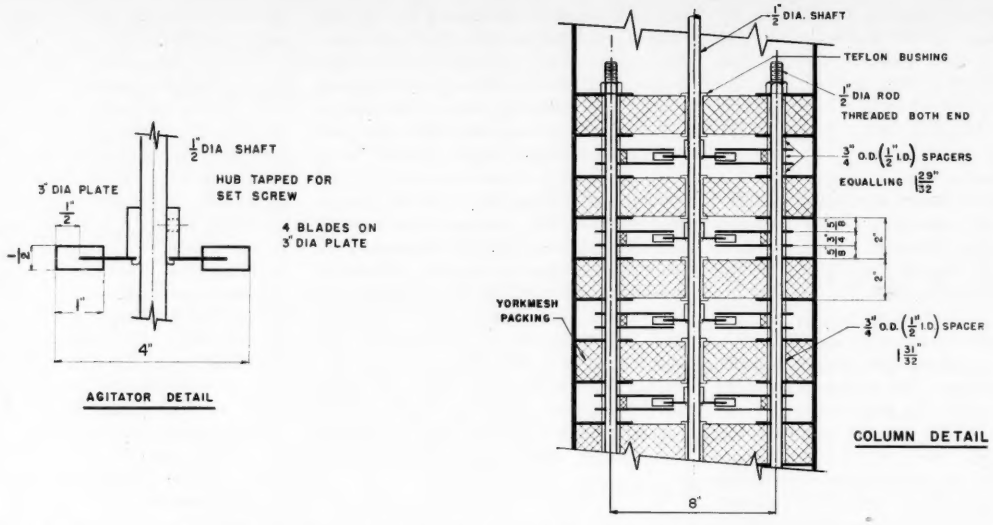

Fig. 2. Construction details of experimental extraction column.

equal solvent ratios for comparison with the first system.

All solvents were the commercially available materials and were used as received. In the test runs the large number of stages gave a close approach to equilibrium at one of the ends of the column even though an effort was made to maintain the operating line parallel to the equilibrium curve. This was difficult to achieve because of the curvature of the equilibrium curve. In all runs where the approach to the equilibrium curve was so close that an error of 1 or 2% would appreciably change the number of theoretical stages, the samples of two liquid streams at this end of the column were mixed and brought to equilibrium. This equilibrium was used in the graphical calculations, and it soon became evident that a slight difference in equilibrium data was present over the previously used data.

In the acetic acid systems, concentrations up to 20% in the water were used, corresponding to concentrations up to 20% in the methyl isobutyl ketone and 1.5% in *o*-xylene. Phenol solute concentrations ranged up to 0.25% in each of the phases.

The same operating technique used in the previous work (*8*) was employed in which the solute was transferred alternately from one solvent to the other so that errors in the equilibrium data would produce a twofold discrepancy among the observed stage efficiencies. The agreement between consecutive runs made at the same conditions was taken as a check of the equilibrium data, and toward the end of the series successive runs were made at different conditions to accelerate the investigation of the different variables. Direction of diffusion has been found to affect the performance of the mixing section and small differences could be attributed to this effect. Because of the large number of stages involved in this work a relatively small error in the equilibrium curve would produce a significant discrepancy in the number of theoretical stages. Thus the present data could not be used to evaluate the small effect for the direction of diffusion, but rather the close agreement verified the equilibrium data.

Previous work described on this same unit indicated that changing the total holdup in the column two to three times was adequate for attaining steady state conditions (*8*), and in all these runs the holdup was turned over three to five times before the products were collected. The collecting period was also sufficient to change the total holdup two to four times, and in the first few runs spot samples were taken before and after the collecting period and confirmed that steady state had been reached. Material balances checked generally within 5%, and in the methyl isobutyl ketone–water–acetic acid system the material-balance point on the ternary diagram determined from the acid concentrations of all four streams coincided with the point located according to the measured product-stream quantities.

Stage efficiencies were calculated by stepping off the theoretical stages on a graph of the solute ratio in the light phase against the solute ratio in the heavy phase as previously described (*8*), because this method of plotting gives a straight operating line when changes in the mutual solubility are small over the range of solute concentrations. The application of the method to the *o*-xylene–water system is obvious, and the rigorous method of Varteressian and Fenske (*9*) in the other solvent system gave a straight operating line within the limits of accuracy of the scale of construction used.

MEASUREMENT OF POWER INPUT

The first runs on the column using methyl isobutyl ketone–water–acetic acid showed that at low agitator speeds the stage efficiency was greater at the low throughput and at high agitator speeds the efficiency was greater at the high throughput. This indicated that there was an optimum power input per unit volume of solvents flowing through the column, and for the second series of runs using the *o*-xylene–water–acetic acid system a torque indicator was constructed and installed on the agitator shaft as an integral part of the drive pulley.

The power was transmitted through a coil spring to the column shaft from the drive pulley fixed to the outer housing, which rotated along a spiral path on small bearings. This rotation converted the rotational distortion of the spring into a vertical displacement, which was measured by a depth gauge resting on the top of the outer housing at its center of rotation. The torque indicator was calibrated in position by measuring the vertical displacement produced by suspending different weights from a cord wrapped around the outer housing and passing downward over a pulley rotating in a plane tangent to the outer housing. After the initial small preloading of the spring was relieved, the calibration curve of torque against depth reading was linear.

The power input to the agitator shaft was calculated from the speed and torque, and it was found to vary as the cube of the speed, as has been observed for fully baffled tanks at high Reynolds numbers.

In the columns without packing, both for the nine- and the seventeen-stage arrangements the observed power consumption per agitator was in exact agreement with that calculated from the correlation of Mack (*3*) for fully baffled tanks at turbulent flow. The packing bundles used in this work contained Teflon bushings at the center, which had been bored $\frac{1}{16}$ in. greater than the shaft diameter, but there was apparently some friction in these bushings because the observed power input per stage was 15% greater when they were installed than was calculated from the previously mentioned correlation. Thus for all the runs on the column, including those with the packing, the calculated power input per agitator was used for the correlation of the data.

For the type of agitator used in this

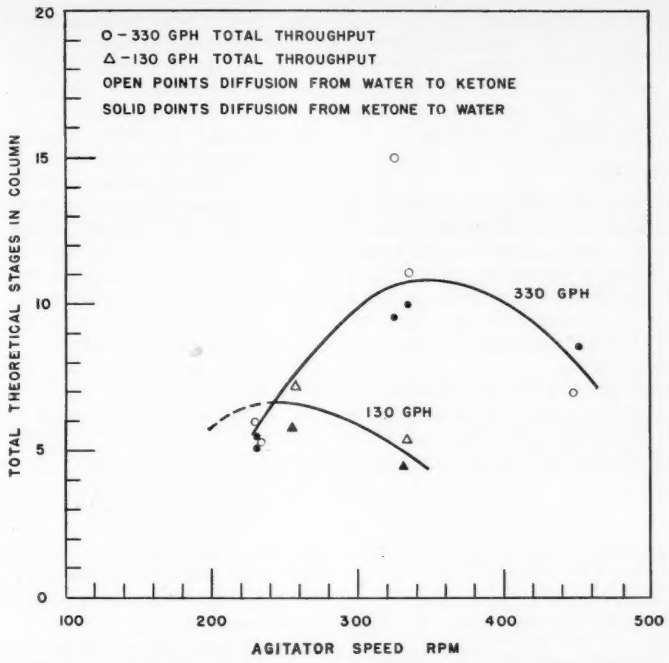

Fig. 3. Effect of agitation speed at different throughputs on acetic acid–methyl isobutyl ketone–water system in nine-stage column.

work, the general correlation for the power consumption gives

$$P = 1.85 \frac{D^5 \rho N^3}{g}$$

and, with an average density in the mixing section based on about one-third holdup of dispersed phase, the following equations were used to calculate the power consumed per stage:

$P = 0.0132N^3$ for water dispersed in *o*-xylene
$P = 0.0140N^3$ for *o*-xylene dispersed in water
$P = 0.0128N^3$ for water dispersed in MIBK
$P = 0.0136N^3$ for MIBK dispersed in water

INTERPRETATION OF DATA*

The first series of runs on the acetic acid–methyl isobutyl ketone–water system indicated a maximum efficiency with agitator speed at a given throughput. As shown in Figure 3, the maximum occurs at lower agitator speeds at the lower throughput. Excessive agitator speeds produce finer dispersions which do not coalesce in the calming section and also cause some overlapping of the flow patterns in successive mixing section. Both effects contribute to lowering of the stage efficiency. At speeds below 230 rev./min. the appearance of the column did not indicate good efficiency and so no runs were made. However, the transfer of material between the phases in this system is so easy that fairly good performances have been obtained on unagitated columns either packed or void. It is therefore not the best system with which to study the performance of an agitated column. The additive effects provide abnormally high efficiencies of more than one theoretical stage per actual stage. In this case the high efficiencies are very sensitive to the operating and equilibrium data. Also the curves were drawn between the points determined for the different directions of diffusion although, as acknowledged previously, the performance curves probably differ.

Systems with hydrocarbon and water as solvents are generally classified as difficult extraction systems because they exhibit very poor efficiencies in the unagitated columns. The *o*-xylene–water system gave the same general shape of curves in the agitated column, but the maxima occurred at lower values because of the lack of extraction in the packed separating section. Also the absolute value of the function in this system was much different when the acetic acid and the phenol were used as solutes. This was attributed to the difference in the solvent ratio in the column, and it was observed that considerably more power was required to give the best efficiency with the acetic acid solute when the small amount of water had to be uniformly dispersed in the *o*-xylene phase. It was assumed that the power necessary to produce a satisfactory dispersion of one volume of solvent in ten volumes of another was ten times as great as when five and one half volumes of one solvent was dispersed in an equal volume of the other solvent.

The additional extraction obtained by the countercurrent flow through the packing masked the effect in the mixing section in the first arrangement. In the second and third arrangements, in which the packing was omitted, the stage efficiencies of the nine- and seventeen-stage columns are shown in Figure 4 plotted against the function $[P/(L_C+L_D)]$ L_D/L_C. No consistent difference can be noted between the efficiency of the nine- and seventeen-stage columns, and it was concluded that the void intermediate calming section could be eliminated to save half the height of the column without affecting the individual stage efficiency. This will then double the number of theoretical stages per foot of height.

The data show appreciable scattering; however, all the points significantly below the curve were obtained at the highest power input of the given series of runs and represent a close approach to flooding conditions. Flooding is not adequately covered in this correlation. The amount of power that can be put into a particular system without producing an emulsion or a flooding condition is a function of fluid properties. However, the maximum power input also differs, depending upon which phase is dispersed. For example, the series of points for the phenol–*o*-xylene–water system at the opposite ends of the curve represent the same solvent and solute system; the points at the left correspond to a dispersion of the light phase, and at the right the points correspond to a dispersion of the heavy phase. These data could obviously not be correlated on the basis of static fluid properties. Qualitatively it is recognized that in a mixing section the tendency of the mass of liquid to rotate will force the lighter liquid to the middle. When the problem is one of dispersing the light phase, this effect facilitates the mixing, and when it is desired to disperse the heavy phase, this effect opposes the mixing. This had been noted in a previous work (*2*). Nevertheless, it does not seem reasonable to attribute the three-hundredfold increase in the permissible power input in the latter situation to this rotational effect alone, and differences in the dynamic interfacial conditions for the two types of dispersion may also contribute to the discrepancy. At any rate, it appears to be much more difficult to disperse water in the *o*-xylene than in the inverse arrangement and the physical reasons for this are not fully understood.

The data on the column with packing between the mixing sections (shown in

*Performance data have been filed as document 4784 with the American Documentation Institute, Photoduplication Service, Library of Congress, Washington 25, D. C., and may be obtained for $1.25 for photoprints or 35-mm. microfilm.

Figure 5) are consistently above the curve for the column without packing. Also in this case the different throughputs and properties of the system affect the deviation. The curve for a total throughput of 330 gal./hr. on the methyl isobutyl ketone–water–acetic acid system is much higher than the curve for 130 gal./hr. on the same system and also much higher than the curve for 270 gal./hr. of total throughput on the *o*-xylene–water–acetic acid system. The usefulness of the packing in providing additional transfer of material is thus an inverse function of the interfacial tension, or, more specifically, it is probably a function of the Weber number.

It is significant that the maximum efficiencies in all cases are obtained in the region of values of 100 to 150 lb./sq. ft. for the function $[P/(L_C + L_D)]$ L_D/L_C. It was also noted that greater power inputs per unit volume of solvents were possible with the packing than without, but this was not the most economical method of operation.

CONCLUSIONS

A new type of baffling arrangement has been devised for an internally agitated extraction column which provides uniform mixing of the phases in a smaller height than previously possible, and this will allow the design of large-diameter columns without requiring a proportional increase in height.

A correlation of the efficiency of the mixing section is proposed based on the power input per unit volume of fluids flowing and the ratio of the dispersed to continuous phase. Packing between the stages was found to increase the over-all efficiency and to decrease somewhat the solvent-flow capacity of the column. The minimum H.E.T.S. in an 11½-in. I.D. column was 5 in. when no packing was used between the stages. When packing was used, the minimum H.E.T.S. was 6 in. on the *o*-xylene–water system and 3 in. on the methyl isobutyl ketone–water system at the higher throughput. Thus it appears that in a difficult extraction system where the interfacial tension is high insufficient benefit is derived from the packing to justify its use. On the other hand, in a system which has a low interfacial tension and is easy to extract, the greater amount of mass transfer obtained in the packing gives it an economic advantage over the use of additional mixing sections.

By use of this baffling arrangement in larger diameter columns, it should be possible to decrease the ratio of H.E.T.S. to column diameter considerably below the value of one quarter reported in the present work.

Patent application has been filed on the extraction-columns described, and an exclusive license to fabricate and furnish them has been granted to the York Process Equipment Corporation.

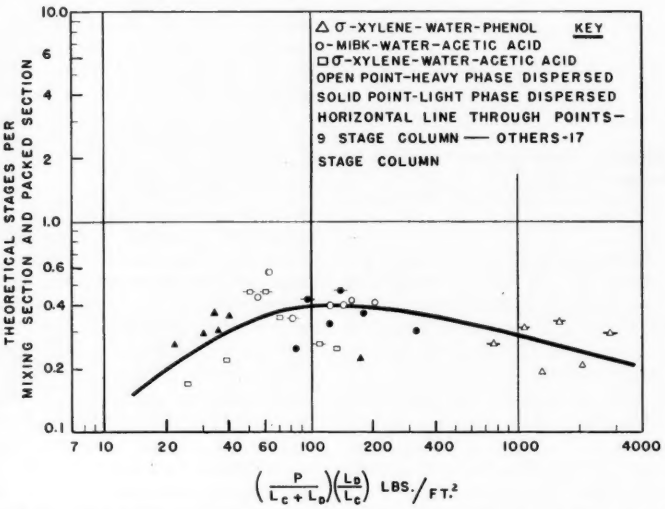

Fig. 4. Correlation of mixing efficiency with power throughput and solvent ratios.

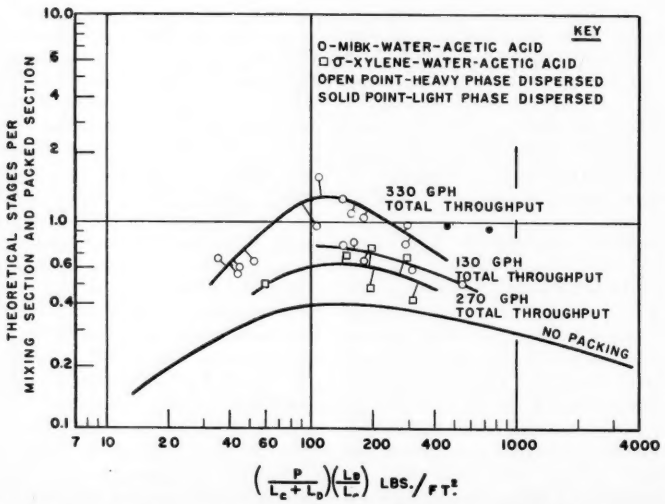

Fig. 5. Effect of packing on stage efficiency for different throughputs and different extraction systems.

ACKNOWLEDGMENT

The author wishes to thank Hoffmann La Roche, Inc., for permission to publish this work and particularly to thank Albert J. Frey for his interest and encouragement during this investigation.

NOTATION

D = outside diameter of the agitator, ft.
g = gravitational constant, 32.2 ft./sec.²
L = solvent flow rates, cu. ft./sec.
N = agitator speed, rev./sec.
P = power input, ft.-lb./sec.
ρ = fluid density, lb./cu. ft.

Subscripts

D = dispersed phase
C = continuous phase

LITERATURE CITED

1. Flynn, A. W., and R. E. Treybal, *A. I. Ch. E. Journal*, **1**, 324 (1955).
2. Karr, A. E., and E. G. Scheibel, *Chem. Eng. Progr. Symposium Series* No. 10, **50**, 73 (1954).
3. Mack, D. E., *Chem. Eng.*, **58**, No. 3, 109 (March, 1951).
4. Oldshue, J. Y., and J. H. Rushton, *Chem. Eng. Progr.*, **48**, 297 (1952).
5. Reman, G. H., U. S. Patent 2,601,674 (June 24, 1952).
6. ——— and R. B. Olney, *Chem. Eng. Progr.*, **51**, 141 (1955).
7. Scheibel, E. G., *Chem. Eng. Progr.*, **44**, 681 (1948).
8. ——— and A. E. Karr, *Ind. Eng. Chem.*, **42**, 1048 (1950).
9. Varteressian, K. A., and M. R. Fenske, *Ind. Eng. Chem.*, **28**, 928 (1936).

Pressure Drop Through Porous Media

L. E. BROWNELL, D. C. GAMI, R. A. MILLER, W. F. NEKARVIS

Part V

Fluid flow data are presented for beds of uniformly sized spheres consolidated with resin over a porosity range from 36.4 to 12.3%. The data are analyzed in terms of an effective pore volume and equations are given for predicting pressure drop by use of a friction-factor–Reynolds-number plot.

In Part IV of this study (*4*) data on beds having porosity ranging from 40 to 90% were reported. This article presents data on porous beds of consolidated spheres with a porosity range of from 36.4 to 12.3%.

A bed of randomly packed uniformly sized spheres normally has a porosity of about 40%. Beds of lesser porosity can be obtained by several methods: by stacking uniformly sized spheres in a geometrical pattern (*6*), by compressing beds of uniformly sized spheres by vibration (*9*), by using mixed sizes (*5*), and by filling the interstices between the particles. The last method was used in this work.

APPARATUS AND PROCEDURE

The laboratory apparatus used in obtaining the data for consolidated beds was the same as that pictured in Figure 1 of Part IV of this series (*4*). Bakelite resin BR 940 0 was selected as a suitable consolidating agent which would not shrink appreciably on drying. The bed, composed of 0.208-in.-diam. glass spheres, was filled with resin by slowly displacing air upward and taking precautions, such as tapping, to ensure that no air remained trapped in the bed. After a short interval the resin was allowed to drain out of the bed and air was forced downward through the bed at a pressure of 20 lb./sq. in. gauge. The air stream displaced the liquid resin in the open pores but left it (residual saturation) in the interstices. Final drying of the resin was accelerated by using warm air and heating the bed to 200°F.

The resin that was left in the bed after the first consolidation reduced the porosity of the bed to 36.4%. The resin coated the spheres with a thin layer and formed a thicker layer at the interstices where the spheres touched. Therefore most of the reduction in porosity was obtained by filling the smaller interstices, which contribute less to flow. With this consolidated bed, a range of flow data from completely laminar to highly turbulent flow was obtained by use of water and Karo-syrup solutions of various viscosities. The porosity of the bed was measured before and after the experimental runs to check any possible compaction as a result of pressure drop. This procedure was repeated with additional coatings of resin to obtain flow data on beds of porosity of 34.2, 27.0, 22.0, 19.6, and 12.3%. Before each additional coating of resin was applied, the bed was inverted to minimize any porosity gradient along the axis of the bed. The data obtained in this manner are plotted in Figure 1 as a modified Reynolds number vs. modified friction factor. The solid line in Figure 1 was previously reported (*4*) and is for spheres of the same size without consolidation.

THEORETICAL ANALYSIS

In a consolidated bed the length of the flow path is greater than the length of the bed, the pore diameter is less than the diameter of the particle, and the linear velocity of the fluid flowing through the consolidated bed is greater than the superficial velocity based on total cross-sectional area. In Part II it has been shown that all the pore volume is not effective in contributing to flow (*2*). It is proposed for the purposes of the analysis that the total pore volume be considered as consisting of two parts: one part, termed the "noneffective" pore volume, consists of the blind channels, dead voids, and fine interstices which do not contribute materially to flow; the other part,

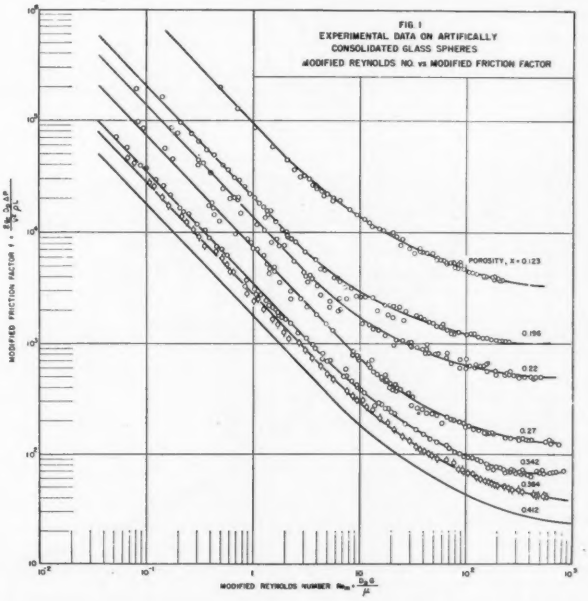

Parts I through IV of this article appeared in the *Transactions of the American Institute of Chemical Engineers* and *Chemical Engineering Progress* (*1* to *4*).

L. E. Brownell is at the University of Michigan, Ann Arbor, Michigan; D. C. Gami at the Institute of Gas Technology, Chicago, Illinois; R. A. Miller with Wyandotte Chemicals, Wyandotte, Michigan; and W. F. Nekarvis with Dow Chemical Company, Midland, Michigan.

termed the "effective" pore volume, consists of the more open channels which conduct fluid in flow. The distinction between the effective and noneffective pore volumes can be shown by analysis of experimental flow data. Certain assumptions are necessary in order to arrive at the analysis. First it is assumed that the length of the fluid path is proportional to the length of the bed and that changing the porosity by consolidation has no effect on the length of the fluid path, or

$$L = K_1 L_b \tag{1}$$

where

L = length of flow path, ft.
K_1 = proportionality constant
L_b = length of bed, ft.

The linear velocity in the bed is directly proportional to the superficial velocity based on total cross-sectional area and inversely proportional to the ratio of flow area to total area. By definition the available area for flow is proportional to the effective pore volume.

$$V_i = K_2 V_s / X_e \tag{2}$$

where

V_i = linear velocity of fluid, ft./sec.
V_s = superficial velocity of fluid based on total cross-sectional area, ft./sec.
K_2 = proportionality constant
X_e = effective porosity, cu. ft. effective voids/cu. ft. total bed

The pore diameter for an unconsolidated bed of uniformly sized, randomly packed particles (such as the experimental bed prior to consolidation) cannot be larger than the particle diameter or the bed would collapse. Also, the pore diameter will not be much smaller than the particle diameter except in the case of selective packing arrangement or consolidation. Consolidation involves decreasing the pore volume. The term pore *diameter* involves the consideration of an equivalent cylindrical path in the effective pore volume. For a cylinder the diameter is proportional to the square root of the cross-sectional area. Therefore, it is assumed that the pore diameter is a linear function of particle diameter and is proportional to the square root of the area available for flow. Other definitions might be used based on the concept of hydraulic radius, but insufficient data exist at present to indicate the need to include this concept.

$$D_i = K_3 D_p (X_e)^{1/2} \tag{3}$$

where

D_i = pore diameter, ft.
K_3 = proportionality constant
D_p = particle diameter, ft.

By use of the foregoing relationships the Reynolds number and friction factor are defined as follows:

$$Re = \frac{D \cdot V \cdot \rho}{\mu}$$

$$= (K_3 D_p X_e^{1/2}) \cdot \frac{(K_2 V_s)}{X_e} \frac{\rho}{\mu}$$

$$= \frac{K_2 K_3 D_p V_s \rho}{\mu X_e^{1/2}} \tag{4}$$

$$f = \frac{2 g_\rho D \Delta p}{L \cdot \rho \cdot V^2} = \frac{2 g_c (K_3 D_p X_e^{1/2})(\Delta p)}{(K_1 L_b) \cdot \rho \cdot \left(\frac{K_2 V_s}{X_e}\right)^2}$$

$$= \frac{2 g_c K_3}{K_1 K_2^2} \cdot \frac{D_p (\Delta p) \cdot X_e^{5/2}}{L_b \cdot \rho \cdot V_s^2} \tag{5}$$

Comparing Equations (4) and (5) with corresponding functions in Part IV shows that the Reynolds number function F_{Re} and friction factor function F_f can be defined as follows:

$$F_{Re} = \frac{K_2 K_3}{X_e^{1/2}} = K_4 X_e^{-1/2} \tag{6}$$

$$F_f = \frac{K_1 K_2}{K_3 X_e^{5/2}} = K_5 X_e^{-5/2} \tag{7}$$

In the foregoing relationship the constants K_4, K_5, and the effective porosity X_e are unknown for a particular system. However by consolidating the bed the effective porosity X_e can be changed while the constants K_4, K_5 remain unchanged. Determination of the functions F_{Re} and F_f for consolidated beds and comparison of these functions with the corresponding functions of the unconsolidated bed will eliminate the constants K_4, K_5:

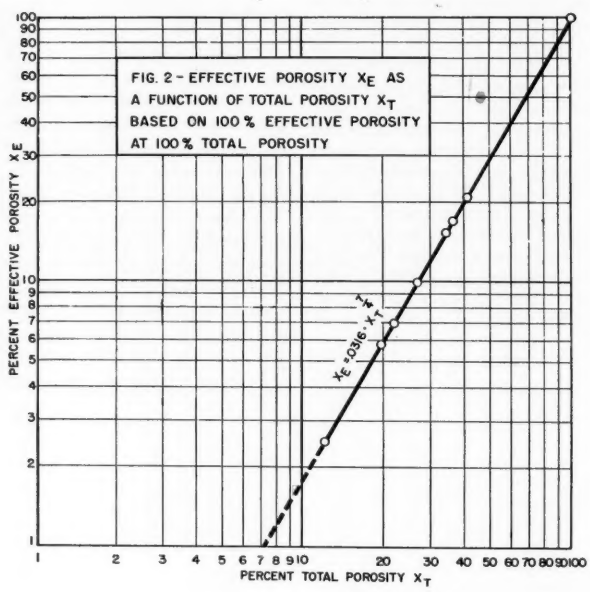
FIG. 2 - EFFECTIVE POROSITY X_E AS A FUNCTION OF TOTAL POROSITY X_T BASED ON 100% EFFECTIVE POROSITY AT 100% TOTAL POROSITY
PERCENT EFFECTIVE POROSITY X_E
PERCENT TOTAL POROSITY X_T
$X_E = .0316 \cdot X_T^{3.4}$

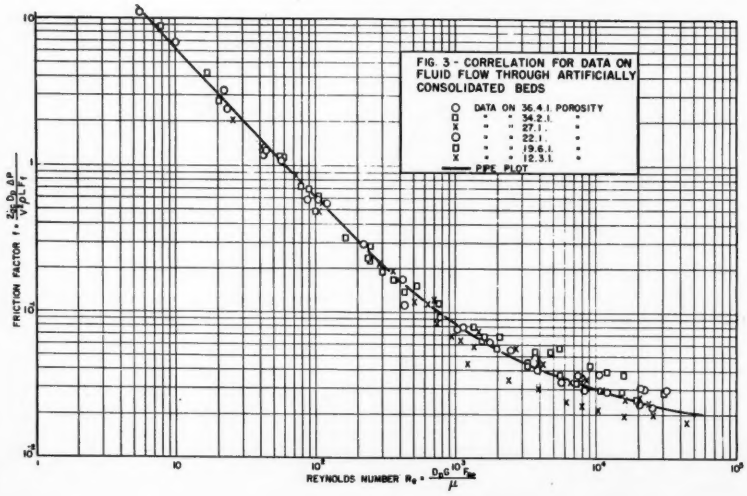

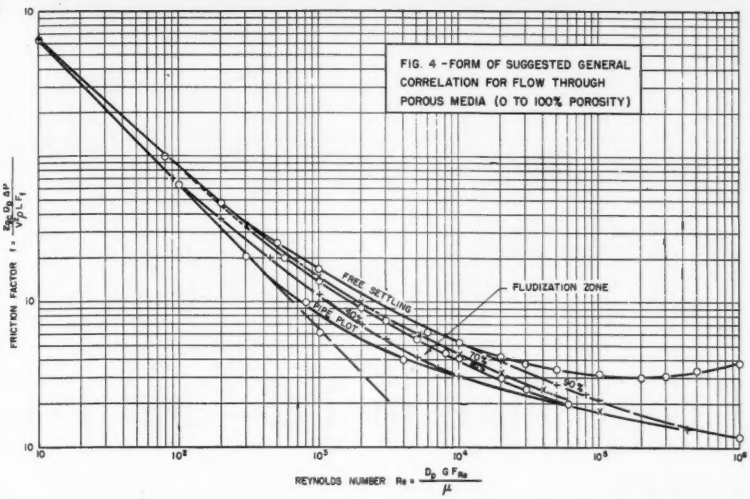

$$\frac{F_{Re}\ \text{Uncons.}}{F_{Re}\ \text{Cons.}} = \frac{K_4\ \text{Uncons.}\ X_e^{1/2}\ \text{Cons.}}{K_4\ \text{Cons.}\ X_e^{1/2}\ \text{Uncons.}} = \frac{X_e^{1/2}\ \text{Cons.}}{X_e^{1/2}\ \text{Uncons.}}$$

$$\frac{F_f\ \text{Uncons.}}{F_f\ \text{Cons.}} = \frac{K_5\ \text{Uncons.}\ X_e^{5/2}\ \text{Cons.}}{K_5\ \text{Cons.}\ X_e^{5/2}\ \text{Uncons.}} = \frac{X_e^{5/2}\ \text{Cons.}}{X_e^{5/2}\ \text{Uncons.}}$$

For any value of effective porosity for the unconsolidated bed the corresponding value of effective porosity for the consolidated bed can be calculated from either F_{Re} or F_f. Obviously a variety of solutions can be obtained depending upon the value of effective porosity for the unconsolidated bed. When effective porosity calculated by this procedure was plotted against total porosity for the different consolidated beds, a straight line was obtained on logarithmic paper with a slope of 1.75 in each case but with an intercept which depended upon the values of X_e for the unconsolidated bed. Such plots can be extrapolated to the region of high porosity such as exist in fluidized beds and to a limit of 100% porosity representing free settling of a single particle in an infinite volume of fluid. It was assumed that the value of X_e must be such that at 100% total porosity the effective porosity must also be 100%. This reasoning makes possible the use of a single line for the relation between the effective and total porosity as shown in Figure 2. The equation of this line is

$$X_e\% = 0.0316(X_T\%)^{1.75} \qquad (8)$$

Use of Equation (8) permits the evaluation of the constants K_{Re} and K_f of Equations (6) and (7).

$$F_{Re} = 182(X_e)^{-1/2} \qquad (9)$$

$$F_f = 2.2 \times 10^6 (X_e)^{-5/2} \qquad (10)$$

By use of Equations (8), (9), and (10) the friction factors and Reynolds numbers were calculated from random points of the data and are plotted in Figure 3. This figure indicates the spread of the data based on the correlations. Average deviation ranged from 6.1% for the bed of 12.3% porosity to 24.6% for the bed of 27% porosity.

DISCUSSION

Equations (8), (9), and (10) provide a means of predicting pressure drop in beds of consolidated uniformly sized spheres. It is not expected that these relationships will necessarily hold for particles of other shapes or for beds compacted by methods other than consolidation. However additional data on particles of other shapes may make it possible to handle the other cases by the use of an effective porosity. For example data on particles of different shapes might give a family of curves as in Figure 2 with a parameter of shape (sphericity).

The concept of the effective porosity has the intriguing possibility of leading to a relationship which might be general for consolidated beds, unconsolidated beds, fluidized beds, and free settling. Figure 4 shows how such a relationship might look on a friction-factor–Reynolds-number plot. The lower curve represents flow through consolidated beds, unconsolidated beds, and smooth pipes (conduits). The upper curve represents free settling of a single particle. These two curves are expected to have a different shape in the turbulent region because of the increased turbulence resulting from the spin or flutter of the particle in free settling. The lines between the two curves represent fluidized beds and hindered settling. As fluidization of the bed increases, the friction factor would be expected to rise from the friction factor of a fixed bed to the friction factor of free settling. Although Figure 4 was prepared from experimental data, it represents only a suggestion as to how the general relationship might be developed, as there are insufficient data at present to determine the relationship of effective porosity for such a variety of conditions.

Although the specific relationships derived from the limited data will in all probability require revision when new data become available, the concept of effective porosity should be retained because it must be recognized that pore volume has "quality." Earlier correlations (*2*) for two-phase flow through porous media were based upon an attempt to define empirically the "quality" of the pore volume for the wetting fluid and for the nonwetting fluid. A broad definition of effective pore volume based on a great variety of data should greatly improve the methods of predicting two-phase flow through porous media.

ACKNOWLEDGMENT

The authors wish to acknowledge support from the funds for faculty research of the Horace H. Rackham School for Graduate Studies, University of Michigan, which made this study possible.

NOTATION

D_i = pipe I. D. or pore diameter, ft.
D_p = mean particle diameter, ft.
g_c = gravitational const.
$K_{1,2,3,4,5}$ = proportionality constants, dimensionless
L = length of flow, ft.
L_b = length of bed, ft.
Δp = pressure drop due to flow, lb./sq. ft.
V_i = actual fluid linear velocity, ft./sec.
V_s = superficial fluid velocity, cu. ft. fluid/(sq. ft. bed area) (sec.)
X_e = effective porosity
X_T = total measured porosity
μ = viscosity of fluid, lb./(ft.)(sec.)
ρ = fluid density, ft./cu. ft.

LITERATURE CITED

1. Brownell, L. E., and D. L. Katz, *Trans. Am. Inst. Chem. Engrs.*, **43**, No. 10, 527 (1947).
2. ———, *Chem. Eng. Progr.*, **43**, No. 11, 601 (1947).
3. *Loc. cit.*, **46**, No. 8, 415 (1950).
4. Brownell, L. E., C. A. Dickey, and H. S. Dombrowski, *Chem. Eng. Progr.*, **46**, No. 8, 415 (1950).
5. Burke, S. P., and W. D. Plumer, *Ind. Eng. Chem.*, **20**, 1196 (1928).
6. Martin, J. J., *Chem. Eng. Progr.*, **47**, No. 2, 91 (1951).
7. Wilhelm, R. H., and Mooson Kwauk, *Chem. Eng. Progr.*, **44**, No. 3, 216 (1948).
8. Fancher, George H., and James A. Lewis, *Ind. Eng. Chem.*, **25**, No. 10, 1139 (1933).
9. Oman, A. O., and K. M. Watson, *Natl. Petroleum News*, **36**, No. 44, R 795 (November, 1944).
10. Symposium on Fluidization, *Ind. Eng. Chem.*, **41**, 1099 (1949).

Presented at A.I.Ch.E. San Francisco meeting

Distribution of Temperature in 1-2– and 1-4–pass Heat Exchangers

Vertical Units in Which the Shell-side Pure Fluid Changes Phase and Temperature

HERBERT T. BATES

University of Nebraska, Lincoln, Nebraska

Because of practical construction advantages, heat exchangers with two or more tube passes are often used as condensers. In such cases if the exchanger is overdesigned or underloaded or if the vapor supplied is superheated, the unit may serve as both a condenser and a cooler. It is customary to ignore the temperature change of the condensing fluid when the mean temperature is calculated, provided that the cooling load is a small part of the total heat transfer load. However, when the cooling load is appreciable, this simplified approach is inaccurate.

A heat exchanger mounted vertically with the vapor entering the shell side at the top and flowing downward will be considered. If the vapor is superheated, its temperature must be reduced to the saturation value. When the vapor is desuperheated by heat transfer alone, the tube-wall temperature would have to be above the saturation temperature of the steam in order to have a dry tube wall. This might be so for the hot tube pass, but the cold tube pass would probably be wet. With water vapor the latent heat is so large compared with the sensible heat of desuperheating that revaporization of condensate would quickly remove the superheat. However, many organic vapors have latent heats low enough so that desuperheating would be accomplished primarily by heat transfer with the superheated vapor. At some cross section the vapor in the shell would become saturated and the remaining heat transfer would result in condensation. Owing to the vertical arrangement the condensate would drain to the bottom of the exchanger.

A similar case results when saturated vapor enters the top of the shell of a vertical exchanger at a rate so low that condensation does not require all the heat transfer surface. If there is very little noncondensable gas, the vacuum produced by condensation holds up the liquid in the bottom of the condenser shell and it becomes subcooled before emerging.

In either case the condensation and the cooling occur in separate sections of the exchanger. Each section has its own over-all coefficient of heat transfer, and ordinarily they are not the same because condensation of pure vapors occurs at a higher film coefficient than does cooling of either vapor or liquid.

The division between the sections should be fairly sharp in order to comply with the assumption made in the derivation to be given. This is true if the shell-side fluid is reasonably pure or if it is a constant-boiling mixture and if there is a reasonably high pressure drop through the shell.

The location of the division between the sections usually cannot be determined by test, nor does it remain fixed when the load changes. The areas required for each of the sections can be calculated, and from them the location of the division between the sections can be obtained.

In the carrying out of the derivations the following assumptions were made.

1. The shell-side fluid is a single pure substance or a constant-boiling mixture.
2. The shell-side fluid is completely mixed at each cross section but not in the direction of the tubes.
3. The two over-all coefficients are constant throughout their respective sections of the exchanger.
4. The mass rates of flow and the heat capacities of each fluid are constant.
5. Each tube pass contains the same transfer area.
6. Heat losses are negligible.

The first two of these assumptions are necessary in order that there will be a sharp separation between the two sections of the exchanger. If a considerable amount of another substance is present in the shell-side fluid stream, the saturation temperature varies and the two sections of the exchanger become almost indistinguishable.

The equation for use with a 1-2–pass heat exchanger involving no change of phase was derived by Underwood (*2*) many years ago. Kern (*1*) made use of the same equation for situations involving change of both temperature and phase when the heating or cooling section is next to the tube return header. In these cases one of the internal tube-side

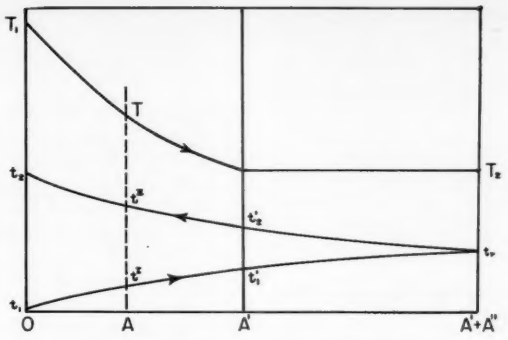

Fig. 1. Desuperheater condenser.

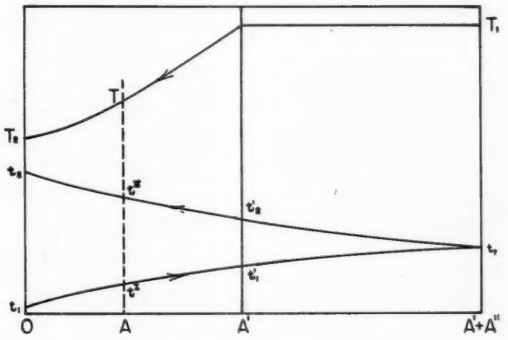

Fig. 2. Condenser subcooler.

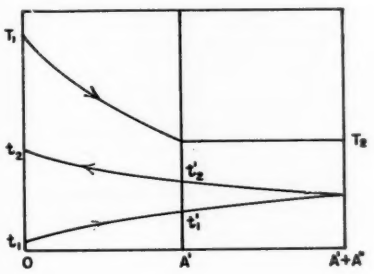

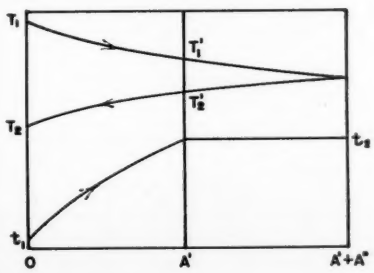

Fig. 3. Desuperheater-condenser heater boiler.

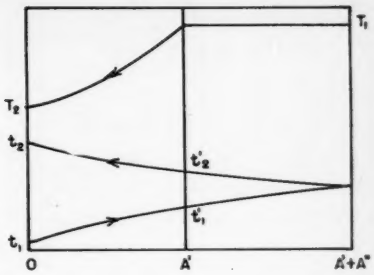

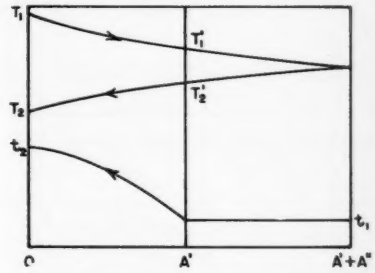

Fig. 4. Condenser-subcooler boiler superheater.

temperatures must be determined by solving a quadratic equation. The other internal temperature can be obtained by a heat balance over either section.

If the heating or cooling section is next to the channel end, i.e., the end where the tube-side fluid enters and leaves, new equations must be derived. When this is done, a new parameter M must be included which represents the ratio of the condensing load to the total heat transfer load of the exchanger.

DERIVATION OF THE EQUATIONS FOR THE 1-2-PASS DESUPERHEATER CONDENSER OF FIGURE 1

Heat Balances

Differential

$$-WC\,dT = wc\,dt^{\mathrm{I}} - wc\,dt^{\mathrm{II}} \quad (1)$$

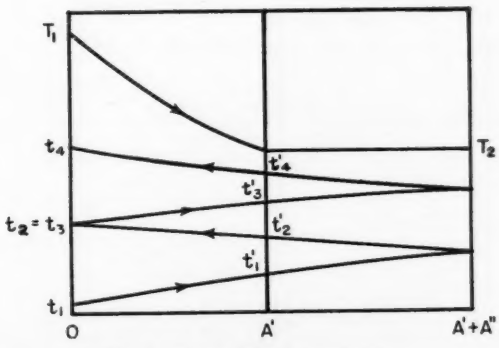

Fig. 5. Desuperheater condenser.

Condensing section

$$W\lambda = wc(t_2' - t_1') \quad (2)$$

Over-all

$$WC(T_1 - T_2) + W\lambda = wc(t_2 - t_1) \quad (3)$$

Around the right end

$$WC(T - T_2) + W\lambda = wc(t^{II} - t^{I}) \quad (4)$$

Rate Equations

Pass I

$$wc\, dt^{I} = U'\, dA/2\,(T - t^{I}) \quad (5)$$

Pass II

$$-wc\, dt^{II} = U'\, dA/2\,(T - t^{II}) \quad (6)$$

Solving (10) by standard methods gives

$$T = T_2 - W\lambda/WC + G_1 \exp m_1 A + G_2 \exp m_2 A \quad (11)$$

where

$$m_1 = -\frac{U'}{2wc}(R + \sqrt{R^2 + 1}) \quad (12)$$

$$m_2 = -\frac{U'}{2wc}(R - \sqrt{R^2 + 1}) \quad (13)$$

Evaluate (11) at the left end where $A = 0$, $T = T_1$

$$T_1 - T_2 + W\lambda/WC = G_1 + G_2 \quad (14)$$

Evaluate (11) at the center where $A = A'$, $T = T_2$

Let

$$R = wc/WC \quad (17)$$

Substitute (12), (13), and (17) into (16)

$$R(2T_1 - t_1 - t_2) = G_1(R + \sqrt{R^2 + 1}) + G_2(R - \sqrt{R^2 + 1}) \quad (18)$$

Combine (3) and (17)

$$T_1 - T_2 + W\lambda/WC = R(t_2 - t_1) \quad (19)$$

Combine (14) and (19)

$$R(t_2 - t_1) = G_1 + G_2 \quad (20)$$

---

and eliminate G_1 between (18) and (20)

$$G_2 = \frac{R(t_2 - t_1)(R + \sqrt{R^2 + 1}) - R(2T_1 - t_1 - t_2)}{2\sqrt{R^2 + 1}} \quad (21)$$

Combine (20) and (21)

$$G_1 = -\frac{R(t_2 - t_1)(R - \sqrt{R^2 + 1}) - R(2T_1 - t_1 - t_2)}{2\sqrt{R^2 + 1}} \quad (22)$$

Combine (21) and (22) with (15)

$$\frac{W\lambda}{WC} = -\frac{R(t_2 - t_1)(R - \sqrt{R^2 + 1}) - R(2T_1 - t_1 - t_2)}{2\sqrt{R^2 + 1}} \exp m_1 A' + \frac{R(t_2 - t_1)(R + \sqrt{R^2 + 1}) - R(2T_1 - t_1 - t_2)}{2\sqrt{R^2 + 1}} \exp m_2 A' \quad (23)$$

Multiply by $2\sqrt{R^2 + 1} \exp -m_2 A'$ and solve for $\exp (m_1 - m_2)A'$

$$\exp (m_1 - m_2)A' = \frac{R(t_2 - t_1)(R + \sqrt{R^2 + 1}) - R(2T_1 - t_1 - t_2) - 2\sqrt{R^2 + 1}\,(W\lambda/WC) \exp - m_2 A'}{R(t_2 - t_1)(R - \sqrt{R^2 + 1}) - R(2T_1 - t_1 - t_2)} \quad (24)$$

Substitute (5) and (6) into (1) and rearrange

$$\frac{dT}{dA} = -\frac{U'}{2WC}(2T - t^{I} - t^{II}) \quad (7)$$

Subtract (6) from (5) and rearrange

$$\frac{dt^{I}}{dA} + \frac{dt^{II}}{dA} = \frac{U'}{2wc}(t^{II} - t^{I}) \quad (8)$$

Rearrange (4)

$$t^{II} - t^{I} = (WC/wc)(T - T_2) + (W\lambda/wc) \quad (9)$$

Differentiate (7) with respect to A and substitute in (8) and (9).

$$\frac{d^2T}{dA^2} + \left(\frac{U'}{WC}\right)\frac{dT}{dA} - \left(\frac{U'}{2wc}\right)^2 \cdot \left(T - T_2 + \frac{W\lambda}{wc}\right) = 0 \quad (10)$$

$$\frac{W\lambda}{WC} = G_1 \exp m_1 A' + G_2 \exp m_2 A' \quad (15)$$

Differentiate (11) with respect to A, equate to (7), and evaluate this at the left end where $A = 0$, $T = T_1$, $t^{I} = t_1$, $t^{II} = t_2$

$$-\frac{U'}{2WC}(2T_1 - t_1 - t_2) = G_1 m_1 + G_2 m_2 \quad (16)$$

Let

$$S = \frac{t_2 - t_1}{T_1 - t_1} \quad (25)$$

$$M = \frac{W\lambda}{wc(t_2 - t_1)} \quad (26)$$

Divide numerator and denominator of (24) by $R(t_2 - t_1)$ and substitute (17), (25), and (26) into (24):

$$\exp (m_1 - m_2)A' = \frac{R + \sqrt{R^2 + 1} - (2/S - 1) - 2M\sqrt{R^2 + 1} \exp - m_2 A'}{R - \sqrt{R^2 + 1} - (2/S - 1)} \quad (27)$$

Combine (12) and (13):

$$(m_1 - m_2)A' = -U'A'/wc\sqrt{R^2 + 1} \quad (28)$$

Multiply numerator and denominator of (27) by S, take logarithms, and substitute (28):

$$\frac{U'A'}{wc} = \frac{1}{\sqrt{R^2 + 1}} \ln \frac{2 - S(R + 1 - \sqrt{R^2 + 1})}{2 - S(R + 1 + \sqrt{R^2 + 1} - 2M\sqrt{R^2 + 1} \exp - m_2 A'} \quad (29)$$

Equation (13) is rewritten as

$$m_2A' = \frac{U'A'}{wc}\left(\frac{\sqrt{R^2+1}-R}{2}\right) \quad (30)$$

Equation (29) requires a trial-and-error solution, which can best be accomplished by letting $\exp -m_2A' = 1$ for the first trial. Then when a value of $U'A'/wc$ becomes available from (29) it can be inserted into (30) and correction made if necessary. Since R is usually quite a large number, (30) becomes very small and it is rarely necessary to make a second trial with Equation (29); for example if R is 10 and $U'A'/wc$ is 0.1 then $\exp -m_2A'$ is 0.9975.

It is worth noting that if there is no condensation $M = 0$ and (29) reduces to Underwood's (2) equation.

DETERMINATION OF INTERMEDIATE TEMPERATURES

In order to analyze the condensation section it becomes necessary to find t_1' and t_2'.

Rewrite (5) and equate this to (11):

$$\frac{2wc}{U'}\frac{dt^1}{dA} + t^1 = T_2 - \frac{W\lambda}{WC} + G_1 \exp m_1A + G_2 \exp m_2A \quad (31)$$

This differential equation (31) may be solved with the aid of the integrating factor $\exp(U'A/2wc)$ to yield the solution

$$T_2 - t^1 = \frac{G_1}{R-1+\sqrt{R^2+1}} \cdot \left[\exp m_1A - \exp\left(-\frac{U'A}{2wc}\right)\right] + \frac{G_2}{R-1-\sqrt{R^2+1}} \cdot \left[\exp m_2A - \exp\left(-\frac{U'A}{2wc}\right)\right] + \frac{W\lambda}{WC}\left[1 - \exp\left(-\frac{U'A}{2wc}\right)\right] + (T_2 - t_1)\exp\left(-\frac{U'A}{2wc}\right) \quad (32)$$

Evaluate (32) at the middle where $A = A'$, $t^1 = t_1'$; also substitute (21) and (22) and put in dimensionless form with the aid of (17) and (25).

$$\frac{T_1 - t_1'}{t_2 - t_1} = \left(\frac{R}{S}\right)\frac{2 - S(R+1-\sqrt{R^2+1})}{2\sqrt{R^2+1}\,(R-1+\sqrt{R^2+1})}\left[\exp m_1A' - \exp\left(-\frac{U'A'}{2wc}\right)\right] - \left(\frac{R}{S}\right)\frac{2 - S(R+1+\sqrt{R^2+1})}{2\sqrt{R^2+1}\,(R-1-\sqrt{R^2+1})}\left[\exp m_2A' - \exp\left(-\frac{U'A'}{2wc}\right)\right] + \left(\frac{1}{S} - R\right)\exp\left(-\frac{U'A'}{2wc}\right) + R \quad (33)$$

Equation (12) is rewritten as

$$m_1A' = -\frac{U'A'}{wc}\left(\frac{\sqrt{R^2+1}+R}{2}\right) \quad (34)$$

m_2A' is given by (30), and (33) gives the value of t_1'. In order to find t_2' rewrite (2).

$$t_2' - t_1' = \frac{W\lambda}{wc} \quad (35)$$

The logarithmic mean formula applies to the condensing section on the right side of Figure 1.

$$\frac{U''A''}{wc} = \ln\left(\frac{T_2 - t_1'}{T_2 - t_2'}\right) \quad (36)$$

The unknown in most practical problems is either U or A. Equations (29) and (36) give the dimensionless ratios UA/wc for their respective sections of the exchanger. The U's or the A's may be calculated directly from these ratios. If one wishes to calculate the true mean driving force for purposes of comparison, the over-all average rate expression may be set up and rearranged:

$$\Delta t = \frac{t_2 - t_1}{\left(\frac{UA}{wc}\right)} \quad (37)$$

In a later section it will be desirable to have the temperature t_r at the tube return-bend header. Setting up logarithmic mean formulas for both passes and equating the two yields

$$T_2 - t_r = \sqrt{(T_2 - t_1')(T_2 - t_2')} \quad (38)$$

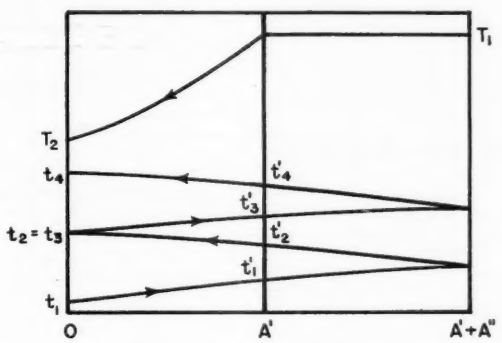

Fig. 6. Condenser subcooler.

OTHER ARRANGEMENTS OF 1-2-PASS EXCHANGERS

Figure 2 shows a condenser subcooler. If the derivation is repeated in an analogous manner, the pertinent equations are

$$\frac{U'A'}{wc} = \frac{1}{\sqrt{R^2+1}}\ln\frac{2 - S(R+1-\sqrt{R^2+1}-2RM+2M\sqrt{R^2+1}\exp - m_2A')}{2 - S(R+1+\sqrt{R^2+1}-2RM)} \quad (39)$$

$$\frac{T_1 - t_1'}{t_2 - t_1} = -\left(\frac{R}{S}\right)\frac{2 - S(R+1+\sqrt{R^2+1}-2RM)}{2\sqrt{R^2+1}\,(R+1+\sqrt{R^2+1})}\left[\exp m_1A' - \exp\left(-\frac{U'A'}{2wc}\right)\right] + \left(\frac{R}{S}\right)\frac{2 - S(R+1-\sqrt{R^2+1}-2RM)}{2\sqrt{R^2+1}\,(R+1-\sqrt{R^2+1})}\left[\exp m_2A' - \exp\left(-\frac{U'A'}{2wc}\right)\right] + \left(\frac{1}{S} + RM\right)\exp\left(-\frac{U'A'}{2wc}\right) - RM \quad (40)$$

$$\frac{U''A''}{wc} = \ln\left(\frac{T_1 - t_1'}{T_1 - t_2'}\right) \quad (41)$$

where

$$m_1A' = \frac{U'A'}{wc}\left(\frac{\sqrt{R^2+1}+R}{2}\right) \quad (42)$$

$$m_2A' = -\frac{U'A'}{wc}\left(\frac{\sqrt{R^2+1}-R}{2}\right) \quad (43)$$

$$T_1 - t_r = \sqrt{(T_1 - t_1')(T_1 - t_2')} \quad (44)$$

t_2' is given by Equation (35) and the other symbols are the same as before. In these equations the RM terms arise because the shell-side fluid and the tube-side fluid enter at opposite ends of the exchanger.

The heater-boiler arrangement shown in Figure 3 is solved with the same equations as the desuperheater condenser of Figure 1 if the following symbols are interchanged: w and W, c and C, t_1 and T_1, t_2 and T_2, t_1' and T_1', t_2' and T_2' and the sign of λ is changed. The temperature-distribution diagram is inverted from Figure 1 to Figure 3.

The boiler-superheater arrangement shown in Figure 4 is solved with the same equations as is the condenser-subcooler arrangement of Figure 2 by interchanging the symbols as above.

EQUATIONS FOR USE WITH 1-4-PASS EXCHANGERS

Equations* for use with 1-4-pass exchangers have been derived because it is sometimes necessary to increase the tube-side fluid velocity when this becomes the limiting factor in design. The procedure is somewhat more complicated than for 1-2-pass exchangers.

Figure 5 shows the temperature distribution in a desuperheater condenser analogous to that of Figure 1. Any of the diagrams of Figures 5, 6, 7, or 8 may be inverted and the equations apply when the following symbols are interchanged: w and W, c and C, t_1 and T_1, t_2 and T_2, t_3 and T_3, t_4 and T_4, t_1' and T_1', t_2' and T_2', t_3' and T_3', t_4' and T_4', and the sign of λ is changed.

1-2- AND 1-4-PASS EXCHANGERS COMPARED

Comparison of the area requirements of 1-2- and 1-4-pass-exchanger arrangements has been made in two practical cases, a steam condenser subcooler with cooling water in the tubes and an ether desuperheater condenser using cooling water in the tubes. If the two over-all coefficients of heat transfer U' and U'' were equal, the area required would be the same for 1-2- or 1-4-pass exchangers, and the shell-side–nozzle orientation would not make any difference. In view of the fact that the over-all coefficient of heat transfer for the cooling section is likely to be lower than that for the condensing section, the area requirements of the cooling section become of primary importance. In both problems investigated the same order of preference prevailed.

For the ether desuperheater condenser the 1-2-pass exchanger of Figure 1 required the least area for desuperheating followed in order by the 1-4-pass exchanger of Figure 5, the 1-4-pass exchanger of Figure 7, and the 1-2-pass exchanger analyzed by Kern (*1*). The steam con-

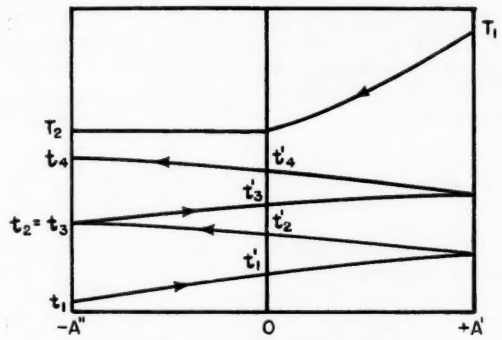

Fig. 7. Desuperheater condenser.

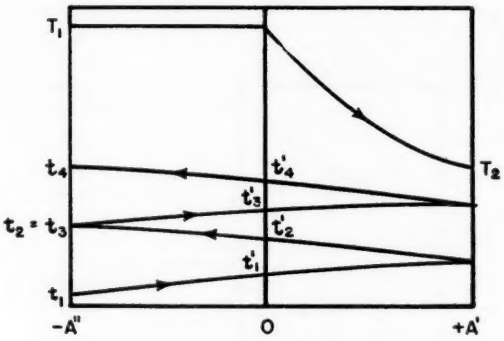

Fig. 8. Condenser subcooler.

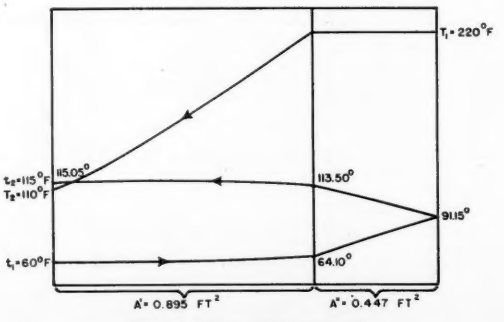

Fig. 9. Numerical example.

*These equations, numbered (45) through (83), have been filed as document 4796 with the American Documentation Institute, Photoduplication Service, Library of Congress, Washington 25, D. C., and may be obtained for $1.25 for photoprints or $1.25 for 35-mm. microfilm.

TABLE 1. COMPARISON OF HEAT EXCHANGER ARRANGEMENTS

Figure	Number of passes	Cooling section, $U'A'/wc$	Condensing section, $U''A''/wc$	Total, $U'A'/wc + U''A''/wc$
		Ethyl ether desuperheater condenser		
1	1–2	0.0842	1.234	1.3182
5	1–4	0.0896	1.221	1.3106
7	1–4	0.0936	1.218	1.3116
Kern	1–2	0.0981	1.214	1.3121
		Steam condenser subcooler		
2	1–2	0.0905	0.3837	0.4742
6	1–4	0.0927	0.3818	0.4745
8	1–4	0.0931	0.3818	0.4749
Kern	1–2	0.0967	0.3778	0.4745

denser subcooler required the least area for subcooling for the 1-2–pass exchanger of Figure 2 followed in order by the 1-4–pass exchanger of Figure 6, the 1-4–pass exchanger of Figure 8, and the 1-2–pass exchanger analyzed by Kern (*1*). Probably 1-6–pass and higher exchangers would lie between the two 1-4–pass exchanger arrangements.

Table 1 shows the results of the calculations. The differences between the various arrangements are only about 9% in the extreme cases, and so other considerations such as ease of piping or standardization of heat exchangers may be of greater importance.

In working with these equations it is necessary to have a consistent set of data to satisfy the assumption of negligible heat losses. In design work this requirement can be met. When exchangers are tested experimentally, there is usually some heat loss. However, if the heat balance be altered in such a way that there is a minimum of change in the temperatures, the results will be satisfactory.

A NUMERICAL EXAMPLE

Examination of Figures 2, 4, and 6 shows that the exit temperatures can cross. This is an undesirable condition because heat transfer surface is wasted. However, if a condenser operates temporarily at low load and the exit temperatures do cross, the equations are still applicable, as this example shows.

A vertical 1-2–pass heat exchanger condensing saturated steam at 220°F. and cooling the condensate to 110°F. may be considered. Steam flow amounts to 30 lb./hr. Cooling water passes through the tube side at the rate of 586 lb./hr., entering at 60° and leaving at 115°F. This is a 5° cross of the outlet temperatures. Table 2 summarizes the calculation of pertinent data, and Figure 9 shows the distribution of temperatures.

Estimations of the over-all coefficients for the cooling section U' and for the condensing section U'' were made by the usual empirical methods.

If the change in shell-side temperature had been neglected and a logarithmic mean temperature driving force used which involved the saturation temperature of the steam and the entering and leaving cooling-water temperatures, the result would have been $U'A' + U''A'' = 246.7$ B.t.u./(hr.)(°F.), an error of 11%.

SUMMARY

Equations have been presented for determining the temperature distribution and the ratios UA/wc for both cooling and condensing or heating and boiling sections of 1-2– and 1-4–pass heat exchangers. Systematic procedures for using these equations have also been worked out. Comparison of two practical designs showed that the vertical 1-2–pass exchanger with cooling section next to the channel end requires the least area, followed in decreasing order of preference by the 1-4–pass exchanger with cooling next to the channel end, the 1-4–pass exchanger with condensing next to the channel end, and the 1-2–pass exchanger with condensing next to the channel end. It may be presumed that 1-6– and higher pass exchangers lie between the 1-4–pass arrangements.

TABLE 2

$w = 586$ lb./hr.
$c = 1$ B.t.u./(lb.)(°F.)
$R = 19.52$ [Eq. (17)]
$\sqrt{R^2 + 1} = 19.54$
$S = 0.344$ [Eq. (25)]
$U'A'/wc = 0.0917$ [Eq. (39)]
$U'A' = 53.7$ B.t.u./(hr.)(°F.)
$t_1' = 64.10$ °F. [Eq. (40)]
$t_2' = 113.50$ °F. (Eq. (35)]
$t_r = 91.15$ °F. [Eq. (44)]
$U''A'' = 223.4$ B.t.u./(hr.)(°F.) [Eq. (41)]
$U'A' + U''A'' = 277.1$ B.t.u./(hr.)(°F.)
$U' = 60$ B.t.u./(hr.)(sq. ft.)(°F.)
$A' = 0.895$ sq. ft.
$A' + A'' = 1.342$ sq. ft.

$W = 30$ lb./hr.
$C = 1$ B.t.u./(lb.)(°F.)
$\lambda = 965$ B.t.u./lb.
$M = 0.898$ [Eq. (26)]

$m_2A' = -0.00115$ [Eq. (43)]
$\exp -m^2A' = 1.0011$
$m_1A' = 1.791$ [Eq. (42)]
$\exp m_1A' = 5.993$

$U'' = 500$ B.t.u./(hr.)(sq. ft.)(°F.)
$A'' = 0.447$ sq. ft.

ACKNOWLEDGMENT

Grateful acknowledgment is due the Nebraska Engineering Experiment Station for funds to support that portion of the work involving 1-4–pass exchangers.

NOTATION

Capital letters refer to the hot fluid, lower case letters to the cold fluid. Subscript 1 refers to the inlet, subscript 2 to the outlet.

- A = exposed tube area, sq. ft.
- A' = tube area exposed in the temperature-change section of the exchanger, sq. ft.
- A'' = tube area exposed in the phase-change section of the exchanger, sq. ft.
- c, C = fluid heat capacity, B.t.u./(lb.)(°F.)
- d = differential
- exp = exponential
- g, G = integration constants
- λ = latent heat of vaporization, B.t.u./lb.
- ln = natural logarithm
- m = roots defined by Equations (30), (34), (42), (43), (54), (55), (62), (63), (71), (72), (81), and (82)
- M = latent heat load/total heat load of the exchanger
- Q = parameter defined by Equation (46)
- R = wc/WC
- S = parameter defined by Equation (25) or (45)
- $t^{\text{I}}, t^{\text{II}}$, etc. = cold-fluid temperature in the tube passes I, II, etc., °F.
- t_1', t_2', etc. = cold-fluid temperatures in the tube passes at the boundary between the sections, °F.
- t_r = cold-fluid temperature at the tube return header, °F.
- Δt = true-mean-temperature-difference driving force, °F.
- T = hot-fluid temperature, °F.
- U' = over-all heat transfer coefficient for the cooling or heating section of the exchanger, B.t.u./(hr.)(sq. ft.)(°F.)
- U'' = over-all heat transfer coefficient for the condensing or boiling section of the exchanger, B.t.u./(hr.)(sq. ft.)(°F.)
- w, W = rate of fluid flow, lb./hr.

LITERATURE CITED

1. Kern, D. Q., "Process Heat Transfer," p. 283, McGraw-Hill Book Company, Inc., New York (1950).
2. Underwood, A. J. V., *J. Inst. Petroleum Tech.*, **20**, 145 (1934).

Prediction of Specific Heat of Organic Liquids

BYRON C. SAKIADIS and JESSE COATES

Louisiana State University, Baton Rouge, Louisiana

A theoretical equation is presented for predicting the specific heat at constant volume and constant pressure of organic liquids as a function of temperature from data on the velocity of sound, infrared and Raman spectra. By use of this equation, the average deviation of the calculated from the experimental values of specific heat for 100 organic liquids at 68°F. is ±1.5%.

An alternate correlation for hydrocarbon liquids based on a modified statement of the theory of corresponding states is also presented. Based on it, the average deviation of the calculated from the experimental values for 100 points representing the entire temperature range is ±0.9%.

Heat transfer calculations require, in addition to other physical properties, specific heat data. Reliable experimental data (*9*) are scanty, particularly for organic liquids other than hydrocarbons, and the data for hydrocarbon liquids are mostly for temperatures below 86°F. Although considerable progress has been made toward an understanding of the liquid state, it is still difficult to derive results of any practical value.

The specific heat of a liquid at its boiling point has been related to that of its vapor by thermodynamic expressions. This method is tedious and its practical value limited.

Chow and Bright (*2*) have related the specific heat of a liquid with its parachor and molar refraction. The method has little theoretical foundation and is applicable only to homologous series of liquids.

The problem of predicting the specific heat of a liquid is solved here by consideration of a simplified model of liquid state and use of data on the velocity of sound, infrared and Raman spectra. The resulting equation is applicable over large intervals of temperature. An alternate method of correlation based on a modified statement of the theory of corresponding states has been applied to hydrocarbon liquids.

PART I

The prediction of the specific heat of a liquid is somewhat complicated in view of the fact that the liquid state is not so well understood as are the gaseous and solid states. Attempts have been made to predict liquid properties by use of models approximating the liquid to a highly compressed gas or a quasicrystalline solid.

Owing to the large intermolecular forces existing in the liquid state, only a small fraction of the total energy is transferred by individual molecules over relatively long distances. Rather, the greatest part of the energy transfer takes place by the action of neighboring molecules, much in the same way that mechanical motion is transferred from point to point along a vibrating network of spheres connected by springs. The success obtained by using such a model for the prediction of thermal conductivity of liquids (*7*) suggests that the translational motion of a molecule in the liquid state may be considered as a harmonic oscillation about a mean position. In this way the liquid behaves as a quasicrystalline solid.

The different types of motion of a molecule may be classified into an *acoustical branch* and several *optical branches*. The acoustical branch consists of all vibrations in which the molecule moves essentially as a whole. The optical branches consist of the motion of atoms, or groups of atoms, with respect to each other.

The internal energy of a molecule is present in kinetic and potential forms that result from the motion and attractive forces of the molecules, atoms, and component groups (*5*).

A nonlinear molecule consisting of n number of atoms possesses $3n$ degrees of freedom, or independent modes of motion.

CONTRIBUTION TO SPECIFIC HEAT OF ACOUSTICAL BRANCH

Translational Motion

A nonlinear molecule possesses three degrees of freedom for translation. The contribution to the specific heat of these degrees of freedom will be evaluated by assuming that the translational motion is actually a harmonic oscillation about a mean position.

The vibration of the molecules will have a broad distribution of frequencies which are determined by the velocity of sound in the medium. The contribution to heat capacity at constant volume can be evaluated by means of a Debye function (*5*).

$$C_{v_t} = 9R\left(\frac{kT}{h\nu_m}\right)^3 \cdot \int_0^{h\nu_m/kT} \frac{U^4 e^u\, du}{(e^u - 1)^2} = 3Rf_D \quad (1)$$

where $\nu_m = U_s(3N_0\rho/4\pi M)^{1/3}$. The Debye function f_D has been evaluated (*5*) as a function of $h\nu_m/kT$. As compared with the solid, however, there can be no transverse waves in the liquid and U_s is simply the velocity of sound in the liquid.

For liquids at temperatures of 300°K. and higher $f_D \sim 1$ and $C_{v_t} \sim 3R$, or R for each degree of freedom.

External Rotation

In the liquid state, with the exception of molecules of very small moments of inertia, the frequency of rotation characteristic of the isolated molecule is less than the frequency of collision with other molecules. Free rotation is so restricted that infrared and Raman spectra do not show bands corresponding to external rotational motion. As a result the rotation may be considered as a torsional motion and its contribution to the heat capacity evaluated by treating it as a harmonic oscillation having a certain fundamental frequency.

The fundamental frequency of the torsional oscillation cannot be observed as such, but, being of the same order of magnitude as the frequencies of translational motion, it can be evaluated from the velocity of sound in the liquid. For this reason this contribution was included in the acoustical branch of energy transfer.

The contribution to the heat capacity at constant volume should be evaluated by means of an Einstein function (*5*).

$$C_{v_r} = 3R\,\frac{u^2 e^u}{(e^u - 1)^2} = 3Rf_E \quad (2)$$

where $u = h\nu/kT$. The Einstein function f_E has been evaluated (*5*) as a function of u.

On the basis of the considered model of liquid state, calculation of u would require use of velocity of sound and X-ray diffraction data.

The Einstein and Debye functions, however, yield the same result to a close approximation, and, to avoid use of X-ray diffraction data, the Debye function will be used to evaluate the contribution to the heat capacity due to the external rotation also. Hence

$$C_{v_r} = 3Rf_D \qquad (4)$$

The total contribution to heat capacity at constant volume of the acoustical branch is

$$C_{v(t+r)} = (6R)f_D \qquad (5)$$

CONTRIBUTION TO SPECIFIC HEAT OF OPTICAL BRANCHES

It is well known that the internal motions of polyatomic molecules take place in the liquid and solid state without appreciable change. The observed characteristic vibrations are substantially independent of temperature and of the molecule in which they occur.

The constancy of group frequencies in different molecules was at first established by observation and later explained theoretically on the basis of the constancy of bond force constants. The observation of the characteristic frequencies has led to the concept that for every bond in a molecule there exist a vibration in which the bond is stretched and another one of much smaller frequency in which it is bent.

Hence, to a good approximation, generalized average values of the stretching and bending frequencies may be assigned to a given bond. The contribution to the specific heat of the internal rotating, stretching, and bending vibrations can be evaluated by treating the motions as harmonic oscillations having the assigned fundamental frequencies.

This general procedure for organic vapors was developed by Bennewitz and Rossner (*1*), modified by Dobratz (*3*), and extended by Stull and Mayfield (*8*). In Table 1 are given the two characteristic fundamental frequencies of various bonds expressed in wave numbers as given by Herzberg. Additional frequencies were obtained from the values of Stull and Mayfield (*8*). Most values were checked with experimental data and slight changes made. As was previously mentioned, the values of the frequencies are also applicable to liquids.

Internal Rotation

The internal rotation contributions to the specific heat in large molecules are difficult to evaluate. These contributions result from the rotation of groups of atoms about single bonds. As the complexity of the molecule increases, the contributions change. Internal rotation about a multiple bond is highly restrained and the rotation is treated as a harmonic oscillator.

The large intermolecular forces in liquids possibly restrict internal rotation to a greater extent. As an approximation all internal rotations will be treated as harmonic oscillations and their contributions evaluated by Debye functions.

TABLE 1

Bond	Stretching, ω_v, cm.$^{-1}$	Bending, ω_δ, cm.$^{-1}$
>C—H	2,960	
		1,450
		1,000
		1,450
>C—H	3,020	
		1,100
≡C—H	3,300	700
C—C	900	370
C=C	1,650	
C≡C	2,050	
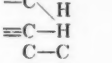		600
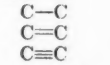		300
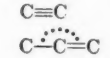		350
C—O	1,030	205
C=O	1,700	390
C—N	900	370
C=N	1,620	845
—C≡N	2,250	
C—S	650	330
C=S	1,550	530
>C—F	1,100	530
>C—Cl	650	330
>C—Br	560	280
>C—I	500	260
O—H	3,400	1,150
>N—H	3,350	1,320
N—O	1,030	205
N=O	1,700	390
N—N	990	390
S—H	2,570	1,050
S—S	500	260

$$C_{v_{r'}} = n_{r'}Rf_D \qquad (6)$$

where

$n_{r'}$ = number of single bonds about which internal rotation of groups can take place, e.g., C—C.

Stretching and Bending Vibrations

These vibrations are essentially harmonic oscillations and their contribution is evaluated by Einstein functions using the fundamental bond frequencies assigned from spectroscopic data. For a given bond two characteristic fundamental frequencies, one stretching and one bending, are used, each representing one degree of freedom. The total contribution due to stretching and bending vibrations is obtained by summing up the atomic contributions.

$$C_{v(v+\delta)} = \sum_i q_i f_{Ei_v} + \sum_i q_i f_{E\delta_i} \qquad (7)$$

where

f_{Ev_i} = contribution to the heat capacity from the stretching vibrations of bond i

$f_{E\delta_i}$ = contribution to the heat capacity from the bending vibrations of bond i

$\sum q_i$ = total number of bonds in the molecule

In addition to the considered contributions there are

$$3n - 6 - n_{r'} - 2\sum q_i$$

degrees of freedom to be accounted for. Assuming that the remaining degrees of freedom make the same contribution to the heat capacity that the known bending vibrations do, their contribution is added to that of the bending vibrations as follows

$$\left[\frac{3n - 6 - n_{r'} - \sum q_i}{\sum q_i}\right] \sum_i q_i f_{E\delta_i}$$

The contribution to heat capacity at constant volume of the optical branches is

$$C_{v(r'+v+\delta)} = n_{r'}Rf_D + \sum_i q_i f_{Ev_i} + \left[\frac{3n - 6 - n_{r'} - \sum q_i}{\sum q_i}\right] \cdot \sum_i q_i f_{E\delta_i} \qquad (8)$$

The complete expression for the heat capacity of a liquid at constant volume becomes

$$C_v = (6 + n_{r'})Rf_D + \sum_i q_i f_{Ev_i} + \left[\frac{3n - 6 - n_{r'} - \sum q_i}{\sum q_i}\right] \cdot \sum_i q_i f_{E\delta_i} \qquad (9)$$

PREDICTION OF SPECIFIC HEAT OF LIQUIDS

Equation (9) was used to predict the specific heat at constant volume of a number of liquids. Since very few values of the specific heat at constant volume for liquids are available, and further since the specific heat at constant pressure is more useful, the ratio of the specific heats at constant pressure and constant volume was used as a check of Equation (9).

The velocity of sound in a liquid can be expressed in terms of the adiabatic and isothermal compressibility

$$K_{ad} = \frac{1}{U_s^2 \rho} \qquad (10)$$

$$K_{is} = \frac{C_p/C_v}{U_s^2 \rho} \qquad (11)$$

Given the coefficient of thermal expansion, β, of a liquid the following thermodynamic relation may be used:

$$C_p - C_v = \frac{T\beta^2}{K_{is}\rho} \qquad (12)$$

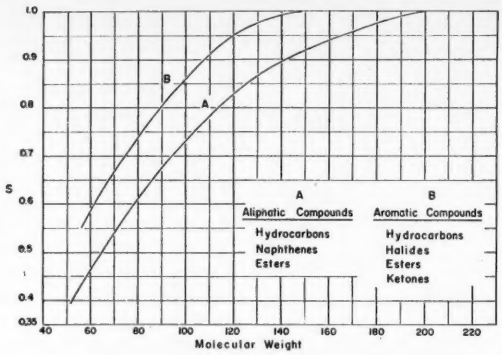

Fig. 1. Correction factor, S, vs. molecular weight.

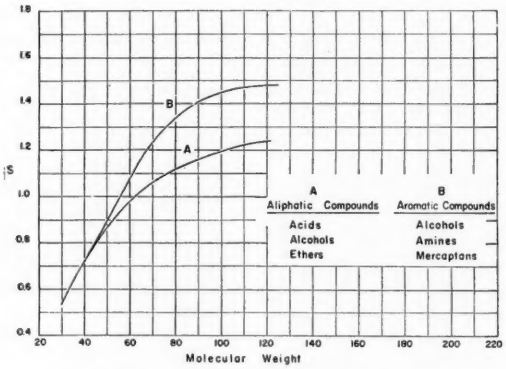

Fig. 2. Correction factor, S, vs. molecular weight.

TABLE 2. COMPARISON OF SOME EXPERIMENTAL VALUES OF SPECIFIC HEAT WITH VALUES CALCULATED BY THEORETICAL EQUATION AT 68°F.

Liquid	$C_{p_{exp.}}$, B.t.u./(lb.)(°F.)	S	$C_{p_{obs.}}$,	% Dev. B.t.u./(lb.)(°F.)
n-Hexane	0.534	0.655	0.534	0
n-Dodecane	0.521	0.957	0.521	0
Pentene-1	0.524	0.524	0.523	−0.2
2-Methyl pentane	0.533	0.655	0.523	−1.9
2,2,3—Trimethyl butane	0.497	0.732	0.510	+2.6
2-Methyl butadiene	0.530	0.652	0.533	+0.6
Ethyl cyclohexane	0.446	0.795	0.452	+1.3
1, 2, 4-Trimethyl benzene	0.420	0.952	0.418	−0.5
n-Propyl acetate	0.459	0.742	0.451	−1.7
Ethyl *n*-butyrate	0.457	0.807	0.456	−0.2
Ethyl benzoate	0.387	1.000	0.389	+0.5
Acetone	0.517	0.568	0.513	−0.8
o-Methyl cyclohexanone	0.439	0.920	0.445	+1.4
n-Propyl alcohol	0.563	0.985	0.566	+0.5
Benzyl alcohol	0.481	1.470	0.469	−2.5
Caproic acid	0.533	1.235	0.530	−0.6
Aniline	0.496	1.430	0.487	−1.8
Phenetole	0.446	1.240	0.453	+1.6
Chlorobenzene	0.318	0.925	0.319	+0.3
Iodobenzene	0.186	1.000	0.183	−1.6

Substituting Equation (11) in (12) and dividing by C_v results in

$$C_p/C_v = 1 + \frac{T\beta^2 U_s^2}{C_p} \qquad (13)$$

Hence the ratio of the specific heats can be calculated independently from the velocity of sound and used to check that calculated from Equation (9). The procedure was as follows

1. C_v was calculated from Equation (9) and, given C_p, the ratio C_p/C_v was determined.
2. Given C_p, β, and U_s, the ratio C_p/C_v was calculated from Equation (13).
3. Next the ratio **R** of the C_p/C_v values calculated from Equations (9) and (13) was taken.

If Equation (9) is correct, the ratio **R** would be unity. The results showed that the ratio varied a maximum of ±25% from unity.

This deviation probably results from the fact that (1) in the calculation of the contribution to the heat capacity of the remaining degrees of freedom, the arbitrary assumption was made that their contribution is the same as that of the bending vibrations and evaluated by the ratio

$$\frac{3n - 6 - n_{r'} - \sum q_i}{\sum q_i}$$

or (2) that all internal rotations are possible and contribute to the same extent to the specific heat.

Next the calculated C_v from Equation (9) was adjusted in such a way as to make **R** equal to unity. The adjustment was made by multiplying the term by an appropriate factor S. This factor will correct the contribution to the specific heat of the remaining degrees of freedom. Further, as a good approximation, the Debye factor f_D was taken as 1.0 in these calculations.

As expected, it was found that this correction factor was a simple function of molecular weight, or actually molecular mass. Plots of S as a function of molecular weight are given in Figures 1 and 2.

Procedure for Calculating the Specific Heat of a Liquid

The final equation for calculating the specific heat at constant volume of a liquid is

$$C_v = (6 + n_{r'})R + \sum_i q_i f_{Ev_i} + \left[\frac{3n - 6 - n_{r'} - \sum q_i}{\sum q_i}\right] S \cdot \sum_i q_i f_{Es_i} \qquad (14)$$

The specific heat at constant pressure of a liquid may be evaluated as follows:

1. Calculate the specific heat at constant volume, C_v, from Equation (14).

2. Calculate the ratio C_p/C_v as a function of C_p from Equation (13).
3. Substitute C_v from Equation (14) in Equation (13) and solve for C_p.

An example follows.

Calculation of Specific Heat at Constant Volume and Constant Pressure for Ethyl Butyrate at 68°F.

Mol. wt. = 116.16

$\beta = 6.57 \times 10^{-4}$ 1/°F.

$U_s = 3874$ ft./sec.*

$T = 528$°R.

Formula:

$CH_3 \cdot CH_2 \cdot CH_2 \cdot CO_2 \cdot C_2H_5$.

Bond	$q_{i\nu}$	$q_{i\delta}$	ω_ν†	ω_δ†	$f_{E\nu}$‡	$f_{E\delta}$‡	$q_i f_{E\nu i}$	$q_i f_{E\delta i}$
≥C—H	12		2960		0.0002		0	
		6		1450		0.0829		0.498
		6		1000		0.3610		2.167
C—C	4	4	900	370	0.482	1.522	1.928	6.088
C—O	2	2	1030	205	0.329	1.829	0.658	3.658
C=O	1	1	1700	390	0.033	1.476	0.033	1.476
							2.619	13.887

*The velocity of sound in the liquid may be obtained from reference 6 or estimated by the method given in reference 7.

†Frequencies were read from Table 1.

‡The contributions to the heat capacity of the stretching and bending vibrations are calculated as follows: $u = 2.585\,\omega/T$ for C—C bending

$u = 2.585 \times 370/528 = 1.816$

Read $f_{E\delta}$ from Figure 3.

$f_{E\delta}/R = 0.7652$ at $u = 1.816$

$f_{E\delta} = 1.987 \times 0.7652 = 1.522$ B.t.u./(lb. mole)(°F.)

Number of atoms in molecule, $n = 20$

Number of bonds about which internal rotation is possible, $n_r' = 4$ (C—C).

Total number of bonds in molecule, $\Sigma q_i = 19$

$$\left[\frac{3n - 6 - n_r' - \sum q_i}{\sum q_i}\right] = \left[\frac{(3)(20) - 6 - 4 - 19}{19}\right] = 1.630$$

Read S factor from Figure 1.

$S = 0.807$ at $M = 116.16$

$$C_v = (6 + 4)\,1.9872 + 2.62 + 1.630 \times 0.807 \times 13.89 \qquad (14)$$

$C_v = 40.782$ B.t.u./(lb. mole)(°F.)

$C_v = 0.351$ B.t.u./(lb.)(°F.)

Use Equation (13).

$$C_p/C_v = 1 + \frac{T\beta^2 U_s^2}{32.174 \times 778.16 \times C_p}$$

$$C_p/C_v = 1 + \frac{528 \times (6.57 \times 10^{-4})^2 \times (3874)^2}{32.174 \times 778.16 \times C_p}$$

$$C_p/C_v = 1 + \frac{0.1368}{C_p}$$

$$C_p = 0.351 + \frac{0.0480}{C_p}$$

Solve for C_p.

Answer $C_v = 0.351$ (B.t.u./(lb.)(°F.)

$C_p = 0.456$ (B.t.u./(lb.)(°F.)

The observed value of the specific heat at constant pressure is 0.457 B.t.u./(lb.)(°F.)

The curves of Figures 1 and 2 cover a large range of molecular weights and chemical types of organic compounds. This method of calculation was used to predict the specific heat at constant pressure at 68°F. for 100 liquids. A sample of the results is given in Table 2. The average deviation of the calculated from the observed values of the specific heat for the 100 liquids was found to be ±1.5%. The maximum deviation was ±4.0%. *It must be emphasized that this method must not be used with the first one or two members of the series, or small molecules, since the generalized frequencies apply mainly to the higher members.*

Variations of Specific Heat with Temperature

The specific heat of a liquid at a temperature other than 68°F. may be calculated also by use of Equations (13) and (14). The method of calculation is the same. Results for seven liquids for which reliable values of the specific heat are available (*9*) are given in Table 3.

It will be noted that the agreement between the calculated and observed values is good. The agreement is better at the higher temperatures than at the lower. In these calculations the factor S was taken to be the same as at 68°F.

Table 3. Variation of Specific Heat with Temperature

T, °F.	$C_{p_{obs.}}$, B.t.u./(lb.)(°F.)	$C_{p_{calc.}}$, B.t.u./(lb.)(°F.)	% Dev.
Low Temperatures			
n-Heptane			
−94	0.481	0.460	−4.3
14	0.504	0.505	+0.2
50	0.518	0.520	−0.4
1,2-Dimethyl transcyclohexane			
−94	0.365	0.359	−1.6
14	0.411	0.418	+1.7
50	0.430	0.435	+1.2
Ethyl acetate			
−94	0.435	0.402	−7.6
14	0.445	0.434	−2.5
50	0.454	0.443	−2.4
2,2-Dimethyl pentane			
−94	0.430	0.459	+6.7
14	0.485	0.502	+3.5
50	0.507	0.514	+1.4
High Temperatures			
p-Xylene			
68	0.406	0.406	0
194	0.460	0.463	+0.7
266	0.495	0.489	−1.2
Benzene			
68	0.412	0.399	−3.1
122	0.433	0.419	−3.2
149	0.446	0.428	−4.0
Iodobenzene			
68	0.1857	0.1830	−1.45
86	0.1866	0.1851	−0.81
113	0.1884	0.1898	+0.74

Table 4. Comparison of Some Experimental Values of Specific Heat with Values Calculated by Correlation Based on Theory of Corresponding States

T_r	$C_{p_{exp.}}$, B.t.u./(lb.)(°F.)	$C_{p_{calc.}}$, B.t.u./(lb.)(°F.)	% Dev.
n-Pentane			
0.345	0.468	0.465	−0.6
0.456	0.485	0.485	0
0.605	0.536	0.536	0
n-Nonane			
0.384	0.489	0.488	−0.2
0.500	0.523	0.525	+0.4
2,3-Dimethyl butane			
0.375	0.428	0.432	+0.9
0.599	0.525	0.527	+0.4
2,2,4-Trimethyl pentane			
0.364	0.403	0.394	−2.2
0.469	0.452	0.454	+0.4
0.542	0.489	0.496	+1.4
Benzene			
0.511	0.409	0.407	−0.5
0.569	0.431	0.431	0
0.600	0.444	0.445	+0.2
Ethyl benzene			
0.294	0.354	0.354	0
0.495	0.424	0.414	−2.3
Pentene-1			
0.350	0.443	0.446	+0.7
0.461	0.464	0.464	0
0.626	0.526	0.525	−0.2
2 Methyl butene-2			
0.350	0.451	0.446	−1.1
0.498	0.474	0.476	+0.4
0.638	0.522	0.531	+1.7

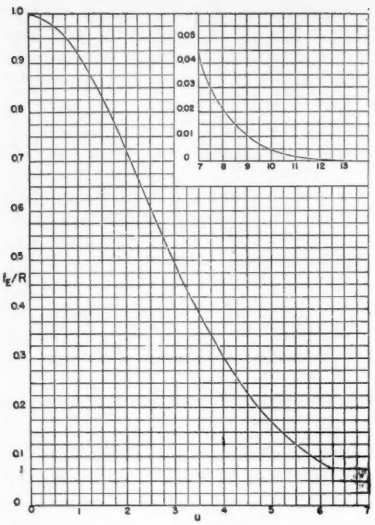

Fig. 3. Einstein function vs. u.

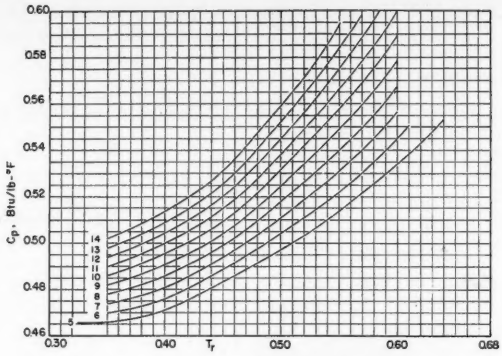

Fig. 4. Branch contribution to C_p vs. T_r.

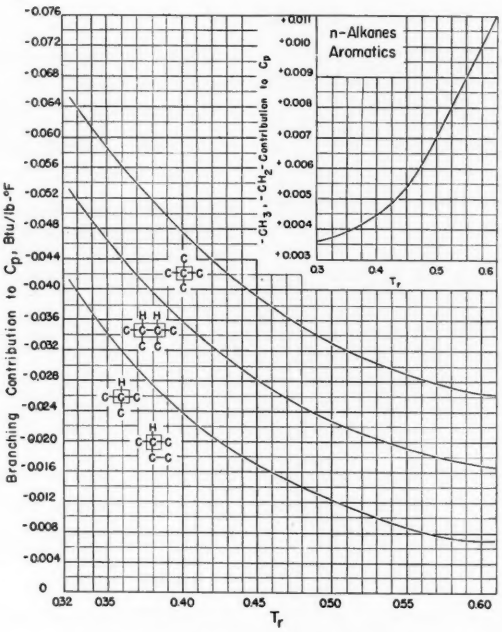

Fig. 5. Branch contribution to C_p vs. T_r.

The results show that the correction factor S is independent of temperature.

SUMMARY

An equation for predicting the specific heat of liquids at constant volume and pressure from molecular structure is proposed. The different types of motion of a molecule were classified into an acoustical branch and several optical branches. The contribution to the specific heat of the optical branches is evaluated by means of generalized frequencies assigned from spectroscopic data. The contribution to the specific heat of the acoustical branches is evaluated on the basis of a simplified model of liquid state and data on the velocity of sound in liquids. The total specific heat is evaluated by summing all contributions.

The equation has been tested on 100 organic liquids of all chemical types at 68°F. The average deviation of the calculated from the observed values of specific heat at constant pressure is ±1.5%. The equation has also been tested on seven liquids over wide temperature ranges.

PART II

An alternate correlation of specific-heat data for liquids based on a modified statement of the theory of corresponding states is possible. This method of correlation was applied successfully to thermal conductivity data (7). Essentially, at the same reduced temperature T_r, it involves consideration of corresponding behavior between the same members of two different series to the same other members of their respective series. The reduced pressure is omitted from the correlation since at 1 atm. the effect of differences in P_r on specific heat is very small.

DEVELOPMENT OF CORRELATION

The correlation was limited to hydrocarbons, as reliable data of specific heat as a function of temperature over a large temperature range, for other types of compounds, are not available. The specific-heat data on hydrocarbons were obtained from reference 9.

As a first step the specific heat of normal aliphatic hydrocarbons was plotted as a function of reduced temperature with the number of carbon atoms as a parameter. Smooth curves were drawn through the points and it was noted that a family of parallel curves was obtained. This set of curves is shown in Figure 4. The difference in specific heat between one curve and another at a given reduced temperature represents the contribution of a —CH_2— group. This difference was found to be independent of chain length, and its variation with reduced temperature is shown in the insert of Figure 5.

Next the effect of branching in the chain was determined by taking the difference in specific heat between a branched alkane and the normal alkane with the same number of carbon atoms at the same reduced temperature. This contribution was found to be independent of chain length, and its variation with reduced temperature for three main types

of branching is shown in Figure 5. The contribution for two types of branching in the same molecule may be taken as the sum of the component contributions.

For the olefinic compounds the procedure for determining the effect of the double bond was the same as that for the effect of branching. It was found that the contribution of one or two double bonds in the molecule is −0.020 B.t.u. (lb.)(°F.) at all temperatures. The few

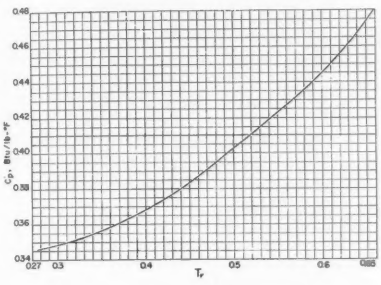

Fig. 6. C_p vs. T_r for benzene.

available data show that the effect of one branched group

in an olefinic hydrocarbon is negligible.

The aromatic hydrocarbons were treated the same way as the normal aliphatic hydrocarbons, and their behavior was found to be similar. In Figure 6 is shown the specific heat of benzene as a function of reduced temperature. The curve has been extrapolated by use of the data of *p*-xylene. The effect of adding one or more $—CH_2$ or $—CH_3—$ groups to the benzene ring is shown in the insert of Figure 5, which applies also to the aliphatic hydrocarbons.

Procedure for Calculating Specific Heat

1. Normal saturated aliphatic hydrocarbons: Figure 4.
2. Branched saturated aliphatic hydrocarbons: Figures 4 and 5.
3. Normal and branched olefinic hydrocarbons: Figure 4, also

Contribution to C_p

One or two double bonds −0.020 B.t.u./(lb.)(°F.) at all T_r

O

4. Aromatic hydrocarbons: Figures 5 (insert) and 6.

The method of calculation will be illustrated by a few examples.

a. Estimate the specific heat of *n*-decane at 75°F.

T_c = 1,100.4°R.

T_r = 535/1,110.4 = 0.482

Estimated C_p = 0.523 B.t.u./(lb.)(°F.): Figure 4

Observed C_p = 0.523 B.t.u./(lb.)(°F.)

b. Estimate the specific heat of 3-ethyl pentane at 70°F.

T_c = 973.4°R.

T_r = 530/973.4 = 0.544

Number of carbon atoms in molecule = 7

C_p, *n*-heptane at T_r = 0.544, = 0.528 B.t.u./(lb.)(°F.): Figure 4

Type of branching *A*,

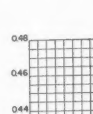

Effect of branching, at T_r = 0.544, = −0.010 B.t.u./(lb.)(°F.): Figure 5

Estimated C_p = 0.428 − 0.010 = 0.518 B.t.u./(lb.)(°F.)

Observed C_p = 0.519 B.t.u./(lb.)(°F.)

c. Estimate the specific heat of transpentene-2 at −163.0°F.

T_c = 848.5°R.

T_r = 297/848.5 = 0.350

C_p, *n*-pentane at T_r = 0.350, = 0.466 B.t.u./(lb.)(°F.): Figure 4

Effect of double bond = −0.20 B.t.u./(lb.)(°F.)

Estimated C_p = 0.466 − 0.020 = 0.446 B.t.u./(lb.)(°F.)

Observed C_p = 0.444 B.t.u./(lb.)(°F.)

d. Estimate the specific heat of *p*-xylene at 257°F.

T_c = 1,108.8°R.

T_r = 707/1,108.8 = 0.638

Number of $—CH_3$ groups on ring = 2

Contribution of each $—CH_3$ group, at T_r = 0.638 = 0.0125 B.t.u./(lb.)(°F.) (Insert Figure 5)

C_p, benzene at T_r = 0.638, = 0.466 B.t.u./(lb.)(°F.): Figure 6

Estimated C_p = 0.466 + 2 × 0.0125 = 0.491 B.t.u./(lb.)(°F.)

Observed C_p = 0.486 B.t.u./(lb.)(°F.)

Figures 4 to 6 were constructed from 400 individual points picked at random from a total of over 1,000 points. The accuracy of the correlation was tested on 32 liquids, or a total of 100 points selected in such a way as to cover the entire range of temperatures. A sample of the results is shown in Table 4.

The average deviation of the calculated from the observed values of specific heat at constant pressure for the 100 points was found to be ±0.9%. The maximum deviation was ±2.7%. Propane and butane show somewhat higher deviations. There are no data on ethane.

SUMMARY

A correlation, based on a semiempirical application of the theory of corresponding states, for predicting the specific heat of hydrocarbons at constant pressure as a function of temperature has been developed. Contributions to the specific heat of chain length, different types of branching, and unsaturation were evaluated. The correlation was tested on a total of 100 points selected to cover the entire range of temperatures. The average deviation of the calculated from the observed values of specific heat was found to be ±0.9%. The method of calculation is simple and rapid.

NOTATION

C_p = specific heat at constant pressure
C_v = specific heat a constant volume
f_D = Debye function
f_E = Einstein function
h = Planck's constant
K_{ad} = adiabatic compressibility
K_{is} = isothermal compressibility
k = Boltzmann's constant
M = molecular weight
n = number, number of atoms in molecule
N_0 = Avogadro's number
P = pressure
q = bond
R = gas constant
$\mathbf{R}$ = ratio
S = factor
T = absolute temperature
U_s = velocity of sound in liquid
u = $h\nu/kT$

Greek Symbols

β = coefficient of thermal expansion
δ = bending
ν = stretching
ν = frequency
ρ = density
ω = wave number

Subscripts

c = critical
m = maximum
r = external rotation
r = reduced
r' = internal rotation

LITERATURE CITED

1. Bennewitz, K., and W. Rossner, *Z. Physik. Chem.*, **39B**, 126 (1938).
2. Chow, W. M., and J. A. Bright, Jr., *Chem. Eng. Progr.*, **49**, 175 (1953).
3. Dobratz, C. J., *Ind. Eng. Chem.*, **33**, 759 (1941).
4. Herzberg, G., "Infrared and Raman Spectra," D. Van Nostrand Company, Inc., New York (1945).
5. Pitzer, K. S., "Quantum Chemistry," Prentice-Hall, Inc., New York (1953).
6. Sakiadis, B. C., and Jesse Coates, *Eng. Exp. Sta. Bul.* **46**, Louisiana State University, Baton Rouge.
7. ———, *A.I.Ch.E. Journal*, **1**, 275 (1955).
8. Stull, D. R., and F. D. Mayfield, *Ind. Eng. Chem.*, **35**, 639, 1303 (1943).
9. Timmermans, J., "Physico - Chemical Constants," Elsevier Publishing Company, Inc., New York (1950).

Determination of Relative Permeability Under Simulated Reservoir Conditions

J. W. WILSON

Union Oil Company of California, Brea, California

An apparatus for the determination of relative permeability under simulated reservoir conditions has been designed, constructed, and operated successfully. Complete water-oil relative-permeability data, with kerosene and simulated reservoir brine have been taken on four natural-sandstone cores at fluid pressures to 5,000 lb./sq. in. and overburden pressures to 10,000 lb./sq. in. One run was made at low pressure at a temperature of 160°F. for comparison with the results at low temperature. The apparatus is now being expanded so that gas-oil relative-permeability data may be taken, and crude oil containing gas in solution may be employed as the oil phase.

The results indicate that essentially the same water-oil relative-permeability data are obtained at fluid pressures of 5,000 lb./sq. in. as at 30 lb./sq. in. gauge. The application of overburden pressure causes a reduction in both water and oil effective permeability in about the same proportion as it affects the single-phase permeability. Consequently the calculated relative permeabilities are affected to only a moderate extent. The results of the one run at 160°F. were in good agreement with the values obtained at room temperature.

Laboratory determinations of relative permeability of oil-field cores are usually made at low pressure and room temperature by use of relatively pure fluids and solvent-extracted cores. There is general concern among both those who make the measurements and those who apply the data as to whether information obtained under such idealized conditions is truly representative.

The influence on relative permeability of two of the more obvious effects of high pressure and temperature—changes in viscosity and interfacial tension—was investigated and reported by Wykoff and Botset (*1*) in the first published paper to present permeability vs. saturation curves for two-phase flow in porous media. They found little effect on the relative-permeability behavior of a carbon dioxide–water system when sugar was added to the water to increase the viscosity of the water from 0.9 to 3.4 cp. or when amyl alcohol was substituted for water to decrease the surface tension from 72 to 27 dynes/cm. Leverett (*2*) made a systematic investigation of the effects of liquid viscosity and interfacial tension on the water-oil system. He found no significant variation in relative permeability to either oil or water for the system studied when the viscosity ratio was varied from 0.057 to 90.0. Reduction of interfacial tension from about 30 to 5 dynes/cm. by substituting amyl alcohol for the oil caused a moderate increase in relative permeabilities. Subsequent investigations (*3, 4*) of the effect of viscosity have been contradictory, and the problem appears to be still unsolved. If the effects of viscosity or interfacial tension were the only significant ones, it would be possible to take account of them by employing fluids having appropriate viscosities and interfacial tension in the laboratory tests. However, the multiphase flow behavior is so complex and little understood that there may well be other important factors. For example, change in wettability of the rock with pressure, such as was observed by Hough, Rzasa, and Wood (*5*) for stainless steel in a methane-water system, would drastically affect the relative-permeability behavior.

Therefore, it seemed that a direct approach to the problem by actual measurements of relative permeability at reservoir pressures and temperatures would be highly desirable. An apparatus was designed and constructed for this

purpose, and the results of the first phase of the work, which involved a comparison of the relative permeability to kerosene and brine of several natural cores at ordinary pressures and at fluid pressures of 5,000 lb./sq. in., are reported in this paper.

APPARATUS

The apparatus employed in this work was designed to permit the determination of relative permeabilities at fluid pressures up to 5,000 lb./sq. in., core overburden pressures to 10,000 lb./sq. in., and temperatures to 300°F. In addition to the usual problems involved in high-pressure work, the following requirements had to be met: (1) the establishment and maintenance of constant fluid-flow rates as low as 0.1 and as high as 100 ml./hr., (2) the measurement of differential pressures of the order of 2 to 5 lb./sq. in. at total pressures of 5,000 lb./sq. in. by some instrument requiring only minute amounts of fluid for its operation, and (3) the determination of the amount of oil (or water) in the core being examined with an accuracy of about 0.05 ml.

The apparatus is shown in simplified form in Figure 1. Because of the rather large volumes of fluid involved, small temperature fluctuations could greatly affect the flow rates, and therefore nearly the entire equipment was installed in a constant-temperature air bath.

In normal operation P2 (Figure 1) pumps hydraulic oil from C2 to C1, moving brine through the core at the set rate. Similarly, P1 pumps hydraulic oil from C6 to C5, establishing a constant oil flow rate through the core. The oil to be flowed through the core is separated from the hydraulic oil by a water seal into which a cylindrical baffle extends from the top of the vessel. The oil-brine mixture from the core is separated in C4, from which the oil passes to C5 and the brine to C2. The level of the oil-brine interface in C4 changes as the saturation of the core and the lines from the core to C4 vary. C4 is made just large enough to accommodate this change.

Pressure is maintained on the fluids in the core by compressed nitrogen in vessel C3. The nitrogen is separated from the hydraulic oil by a mercury seal into which a cylindrical baffle extends. Closing valve V4 with the probe in C8 just out of contact gives warning of any leak in the system when mercury contacts the probe.

Pumps

Each of pumps P1 and P2 consists of two opposed cylinders 16 in. long fitted with polished piston rods ¾-in. in diam. The seals at the ends of the cylinders were made removable so that the ¾-in. rods might be replaced by ⅜-in. rods for the lowest flow rates, if necessary. The rods are joined by a 16-in.-long screw, which is caused to move in either direction by a rotating nut, to which is attached a worm gear. The cylinders are attached to the opposite ends of a section of 4-in.-diam. tubing 34 in. long with the worm and nut housed midway between the cylinders. Thus the force needed to move the pistons is dependent on the differential pressure between the cylinders rather than on the total pressure, and there is no bending torque such as exists when the cylinders are mounted on a flat plate.

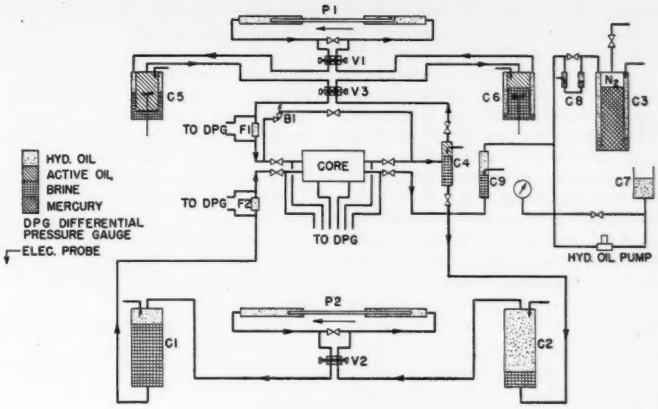

Fig. 1. Simplified flow diagram.

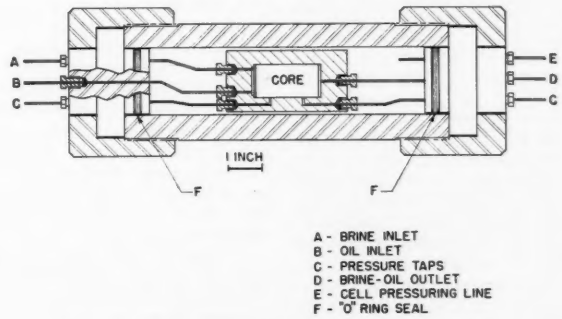

Fig. 2. Mounted core in overburden pressure cell.

The oil pump is driven through a lathe "quick-change" unit combined with a specially built two-speed reducer. Ninety flow rates, increasing in steps of about 10%, are available covering the range from 0.152 to 152.3 ml./hr. The brine pump is driven by a simple unit having low- and high-speed shafts, on which speed is varied by means of change gears. By use of six pairs of gears, twenty-two flow rates increasing in steps of about 40% and covering the range from 0.0766 to 120.5 ml./hr. are available.

With the ¾-in. pistons, the pumps deliver 80 ml./stroke, and this quantity is nearly always sufficient to obtain one point on the relative permeability curve. Flow may be continued from C1 through the core to C2 by reversing P2 and the four-way valve V2 simultaneously. The volume of C1 is about 1 liter, which is adequate for several relative-permeability runs.

Because it was desirable to minimize the volume of radioactive oil in the system, a four-way valve was installed in the active oil lines, so that by reversing V3 at the same time that P1 was reversed, oil could be flowed through the core in the normal direction either from C5 to C6 or C6 to C5. The total volume of active oil in the system was about 150 ml. Because large volumes of oil must be flowed at relatively high rates to desaturate the core at the end of each run, the shifting of P1 and V3 at the end of each pump stroke was made automatic. Also, a by-pass relief valve B1, which could be set for any differential pressure up to about 40 lb./sq. in., was installed so that desaturation might be carried out at constant pressure.

Saturation Determination

The oil saturation of the cores was determined by a radioactivity method described previously (*6*). Iodine 131 in the form of iodobenzene was employed as the oil-phase tracer. Generally 75 mcurie. was used, and this quantity was sufficient for about 4 weeks' work. Vessels C5 and C6 were provided with motor-driven stirrers to facilitate mixing of the radioactive iodobenzene at the beginning of a run. Ten or more passes through the core were required to ensure thorough mixing; this operation was performed overnight automatically. The activity of the core was read at two positions: two ¼-in.-diam. holes ¾ in. deep and 1 in. apart were drilled into the 1-in.-thick wall of the overburden pressure cell, and additional lead shielding ½ in. thick was provided so that the activity reaching the counter through each opening was predomi-

nantly from that part of the core between one pressure tap and the middle of the core. Thus some indication of nonuniform saturation might be had; however, the data were generally employed only to determine the average saturation of the core. Continuous standardization of the counting equipment was achieved by counting a section of the oil inlet line before each traverse of the core. The counting apparatus was the same as that described previously (*6*). Auxiliary equipment was constructed to permit completely automatic scanning of the core and recording of the counting times.

Core Mounting

Cores *A* and *B* were mounted in Lucite with water-wet diaphragms and one pair of side taps in the manner described previously for low-pressure cores (*6*), except that the side-tap connections were drilled in from the ends. The mounting for cores *C* and *D* was simplified by omitting the water-wet membranes, and desaturation was accomplished by dynamic flow. The mounted core was placed in an overburden pressure cell with walls 1 in. thick, and connection made as shown in Figure 2.

Pressure Measurements

Two differential-pressure gauges (Wianckо type 3PDF20) capable of operating at absolute pressures to 5,000 lb./sq. in. were used in this apparatus. One was connected throughout each run to the core side taps; the other could be switched by means of a manifold to any of the pressure connections shown in Figure 1, including the core side taps. Both gauges were of the 0 to 20 lb./sq. in. range, and each gauge could be adjusted through a range and balance circuit to give full-scale deflection on a Foxboro Dynalog multipoint recorder for selected differential pressure ranges from 0 to 2 to 0 to 20 lb./sq. in. The differential pressure could be read with an accuracy of better than 1% in any of these ranges.

Filters, F1 and F2, were installed in the water- and oil-flow lines just ahead of the core. In addition to ensuring that no plugging material could reach the core, these were of value in checking the change in viscosity of the fluids when the fluid pressure was increased. The filters were cylinders of diatomaceous earth mounted in Lucite and sealed in stainless steel vessels.

Most of the valves were standard high-pressure needle valves; however, several sliding valves, such as V1, were built for special purposes. Such a valve can replace four ordinary valves and is easily adapted to automatic changing. The details of the valve are shown in Figure 3.

The design of an electrical probe that gave excellent service and could be installed in cramped quarters is shown in Figure 4. All the probes were connected in parallel to a sensitive relay with a toggle switch in each line.

The simple but highly successful seals employed on the stirring shafts in C5 and C6 are illustrated in Figure 5. Similar seals were used to connect ⅛-in. tubing to the various vessels.

EXPERIMENTAL PROCEDURE AND RESULTS*

The procedure employed on each core was generally as follows.

1. Two or more relative-permeability runs were made at 30 lb./sq. in. gauge fluid pressure, zero overburden pressure.
2. Two or more runs were made at 30 lb./sq. in. gauge fluid pressure, 5,000 lb./sq. in. gauge overburden pressure to determine the effect of overburden pressure.
3. Two or more runs were made at 5,000 lb./sq. in. gauge fluid pressure, 10,000 lb./sq. in. gauge overburden pressure to determine the effect of fluid pressure (same net overburden pressure).
4. Two or more runs were made at 30 lb./sq. in. gauge fluid pressure, 5,000 lb./sq. in. gauge overburden pressure to determine whether there had been any permanent change in the core.

The results for cores *A* and *B* were calculated for each run relative to the brine permeability determined under the same overburden pressure conditions. To do this it was necessary to measure the brine permeability both with and without overburden pressure before making the first relative-permeability run and to allow several weeks for the cores to recover their original permeabilities. It was noted on these cores and on other cores run in this laboratory (*7*) that the effect of overburden pressure on the oil permeability at interstitial water was very nearly in proportion to that upon the 100% brine permeability; and therefore on cores subsequently run the relative-permeability results were based on the respective oil permeabilities at interstitial-water saturation. The procedure employed on core *A* will be described in detail.

The core was mounted in Lucite with a Snow Floss diaphragm incorporated to permit desaturation by capillary pressure. The dimensions of the core are given in Table 1. The air permeability after mounting was 32 md., and the brine permeability was 16.8 md. without overburden pressure and 11.1 md. with 5,000 lb./sq. in. overburden pressure. The brine permeability had recovered to 13.9 md. within 24 hr., when capillary desaturation with kerosene was started.

When desaturation was complete, the core was placed in the apparatus, and 30 lb./sq. in. air pressure applied to C3. Kerosene containing about 50 mcurie. of radioactive iodobenzene was charged to vessel C5; the total volume of kerosene charged (about 150 ml.) was sufficient to give about 100 ml. below the probe in C5, when the probes in C4 and C6 were just in contact. After three

*Data have been filed as document 4795 with the American Documentation Institute, Photoduplication Service, Library of Congress, Washington 25, D. C., and may be obtained for $1.25 for photoprints or 35-mm. microfilm.

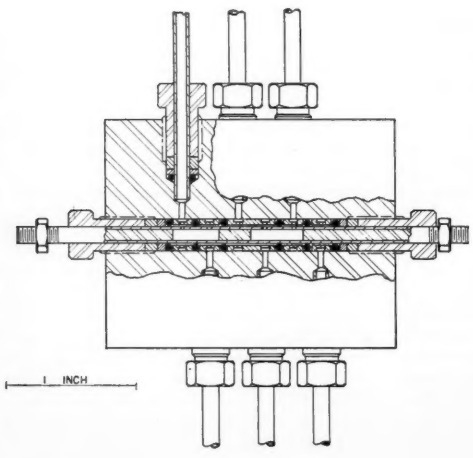

←Fig. 3. Sliding 0 ring valve.

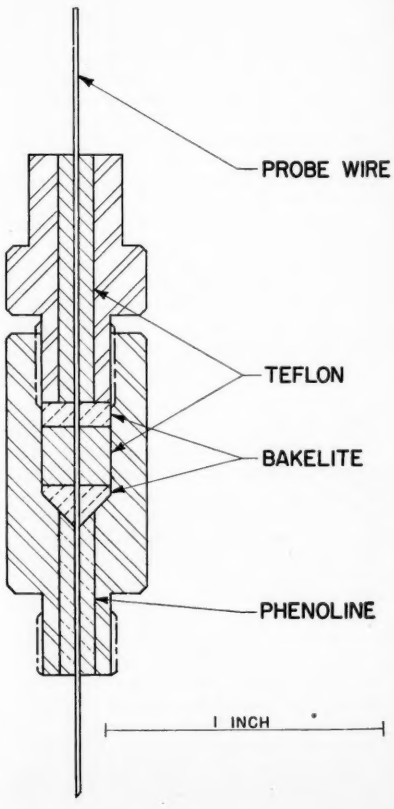

Fig. 4. Electrical probe.→

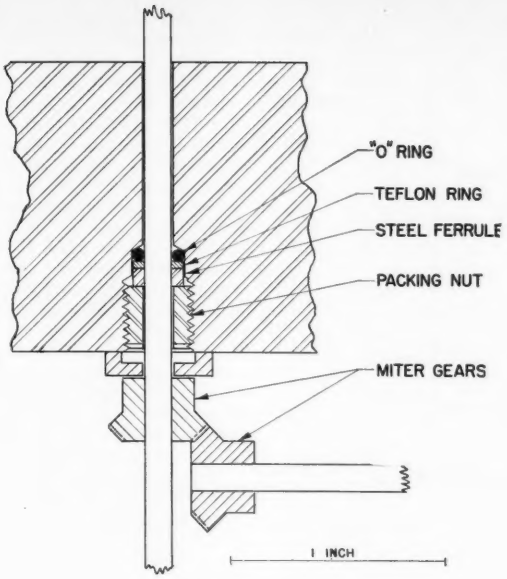

Fig. 5. Stirrer seal.

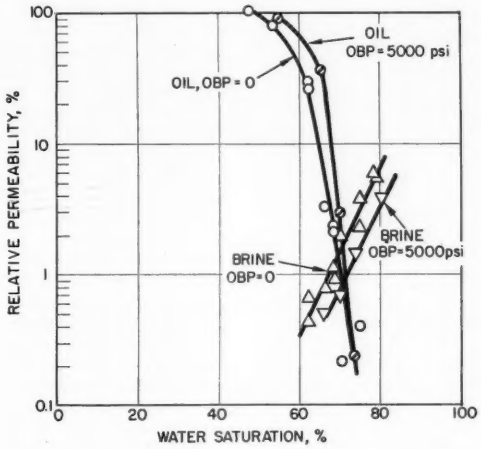

Fig. 6. Effect of overburden pressure on relative permeability of core *A*.

Table 1. Properties of Cores Tested

Core	*A*	*B*	*C*	*D*
Length, in.	2.186	2.12	2.32	2.579
Diameter, in.	1.018	0.95	0.873	0.945
Pore vol., ml.	6.54	6.53	5.53	6.09
Porosity, %	23.2	26.3	24.2	20.5
I.W., %	47.4	35.0	44.3	39.5
K_{air}, md.	30.1	142	81.1	31
K_w, md.	16.8	99	41.1	15.0
K_w at 5,000 lb./sq. in., md.	11.1	50		
K_{eo} at I.W., md.	17.4	104	39	20.1
K_{eo} at I.W., at 5,000 lb./sq. in., md.	9.7	49	22.1	14.7

passes through the core from C5 to C6, stirring before each pass, the radioactive oil appeared to be thoroughly mixed with the inactive oil in the core and lines. (This run was made before the reversing valve V1 was installed, and it was necessary to return the oil from C6 to C5 through the core by-pass valve between each pass. It was later found that three passes are not fully adequate.) While the oil was being mixed, the oil permeability was measured and found to be 17.4 md.

The next point on the relative permeability curve was obtained by reducing the oil rate to 4.68 ml./hr. and commencing to flow water at 0.254 ml./hr. The radioactivity measurements and the differential pressure reading between side taps on the core indicated that equilibrium was reached in about 11 hr. at a brine saturation of 62.5%. After 16 hr. of flow at these rates the oil rate was reduced to 0.950 ml./hr. and the brine rate increased to 0.915 ml./hr. to obtain the next point. About 9 hr. was required to reach equilibrium (68.7% brine). The rates were next changed to 0.158 ml./hr. oil and 2.032 ml./hr. brine. The brine saturation rose to 75.0% within a few hours. The oil flow was then stopped, and brine flow continued at 2.032 ml./hr. The pressure drop leveled off in about 12 hr., and no measurable additional oil was produced in an additional 12 hr. flowing at 2.032 and 16 hr. at 4.063 ml./hr. The results of the run are shown in Figure 6.

The core was desaturated by dynamic flow prior to the second run. As shown in Figure 6, the minimum brine saturation attained by dynamic flow was 53.3%, as compared with 47.4% obtained by capillary pressure desaturation, and the effective permeability to oil was 13.8 md. as compared with 17.4, but the relative-permeability curves were not altered significantly. (It is felt that the two lowest points on the oil curve are not accurate because the oil rates employed were below the value of 0.25 ml./hr., now thought to be the minimum practicable rate for the pump when ¾-in.-diam. pistons are used.)

The core was again desaturated by dynamic flow, and 5,000 lb./sq. in. overburden pressure was applied. The effective permeability was found to be 9.7 md., as compared with 13.8 md. without overburden pressure. This value represented a reduction of 30%. The relative permeability based on the original brine permeability without overburden pressure was 58%; however, it was equal to 87% based on the brine permeability with 5,000 lb./sq. in. overburden pressure. The pore volume of the core was decreased approximately 5% when the overburden pressure was applied, and, because the core was at interstitial water saturation at the time, only oil was squeezed out of the core, and the water saturation, expressed as percentage of pore volume, was increased from 52.2 to 54.8%. [The total change in pore volume of the core plus Snow Floss diaphragms, as measured by radioactivity readings taken before and after the application of overburden pressure, was 10%. The assumption, based on considerable overburden-pressure data (7) taken in this laboratory, was made that the change in pore volume of the core alone was 5%.] Because of this change in percentage of water saturation, the relative permeability is actually a little higher than the value obtained at the

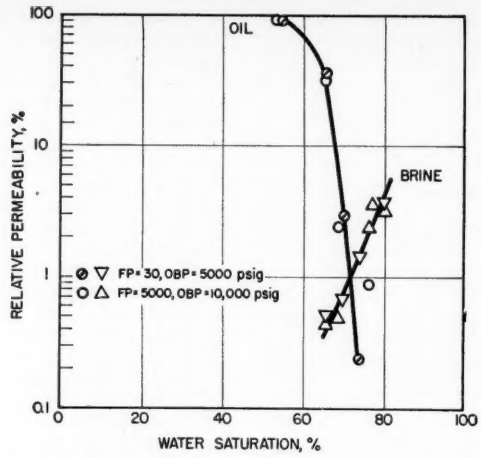

Fig. 7. Effect of high fluid pressure on relative permeability of core *A*.

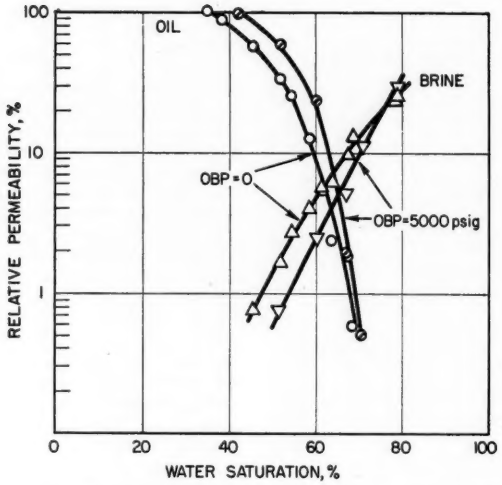

Fig. 8. Effect of overburden pressure on relative permeability of core *B*.

same water saturation, in percentage of pore volume, without overburden pressure. The complete relative permeability curves were then taken, approximately the same rates being used as were employed in the previous runs. The results are given in Figure 6. The oil relative-permeability curve is higher, and the water curve lower than the curves obtained without overburden pressure.

The overburden pressure was then slowly increased to 10,000 lb./sq. in. gauge. At the same time, pressure was applied to the fluids in the core, the difference between the overburden pressure and the fluid pressure being kept at approximately 5,000 lb./sq. in. during the process. *PVT* studies in this laboratory (*8*) on samples of kerosene similar to the oil employed in this work have shown that the effect of an increase in pressure from 30 to 5,000 lb./sq. in. gauge is to increase the viscosity by 58% and to increase the density by 3%. Measurements of the effective permeability of the core and of the filter F1 and of the radioactivity of the inlet cell before and after application of the fluid pressure agreed within experimental error with these values. Accordingly, they were employed in the saturation and permeability calculations. The effect of this pressure change on the viscosity of water is an increase of only 1% (International Critical Tables).

A relative-permeability run was then made at the elevated pressures, with somewhat lower oil-flow rates. A comparison of the results at high and low fluid pressure is given in Figure 7. Although the experimental errors are evidently larger in this apparatus than in conventional low-pressure equipment, it is nevertheless clear that the application of high fluid pressure had no significant effect on the relative-permeability behavior.

Core *B* was subjected to a similar study. This core was mounted with Aloxite distribution plates at each end and at the side pressure taps, and a Snow Floss diaphragm was built around the circumference of the core near one end for capillary desaturation only. Pertinent data on the core are given in Table 1. The effect of 5,000 lb./sq. in. gauge overburden pressure on the relative-permeability values is shown in Figure 8. The effect is approximately the same as observed with core *A*, except that relative permeabilities to brine at residual oil (calculated relative to the 100% brine permeabilities at corresponding overburden pressure) were little affected by the application of overburden pressure.

As the fluid and overburden pressures were being raised in preparation for the next phase of the study, the inlet oil line to the core ruptured, allowing the net overburden pressure on the core to rise abruptly to a value approaching 9,000 lb./sq. in. The overburden pressure was then dropped back to 5,000 lb./sq. in., and it was found that the permeability of the core had suffered a sharp decline. The effective permeability to oil at interstitial water saturation was now 19.3 md., as compared with 49 md. before. It seemed, however, to be very stable in this new condition, and two relative permeability runs at 30 lb./sq. in. gauge fluid pressure and 5,000 lb./sq. in. overburden pressure gave results in good agreement. The fluid pressure was then increased to 5,000 lb./sq. in., the overburden pressure to 10,000 lb./sq. in., and two runs were made at these pressures. The pressures were then dropped back to a fluid pressure of 30 lb./sq. in. gauge and an overburden pressure of 5,000 lb./sq. in., and a single run was made. All five runs were in good agreement (*see* Figure 9), and there was evidently no appreciable effect of high fluid pressure on the relative permeabilities. The core apparently suffered permanent mechanical change when the excessive overburden pressure was suddenly applied. This damage not only greatly reduced the effective permeabilities to oil and water, but changed the relative-permeability relationships (*compare* Figures 8 and 9).

Similar data are given in Figures 10, 11, and 12 for core *C*. Figure 10 shows an effect of overburden pressure quite similar to that observed on cores *A* and *B*. As with core *B*, some permanent change in the core took place when the fluid pressure and overburden pressure were first raised to 5,000 and 10,000 lb./sq. in. gauge, respectively, although this time there was no obvious cause (such as the breaking of a line, which occurred on core *B*). Relative-permeability curves taken before and after the first application of high fluid pressure are shown in Figure 11. The fluid pressure and overburden pressure were then dropped simultaneously to 30 and 5,000 lb./sq. in. gauge, and the relative permeabilities determined again. As shown in Figure 12, the results taken before and after the removal of the high fluid pressure agreed within experimental error.

The results for core *D* are given in Figures 13 and 14. The effect of overburden pressure was small, but in the same direction as on the other cores. The results at low and high fluid pressures agreed within experimental error.

Cores *C* and *D* were mounted without semipermeable pads and were desaturated initially, as well as between runs, by dy-

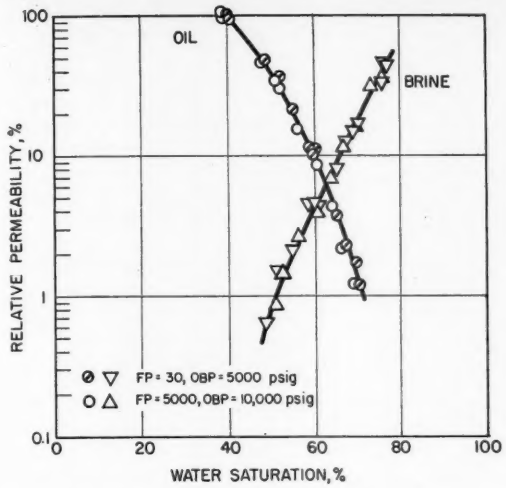

Fig. 9. Effect of high fluid pressure on relative permeability of core *B*.

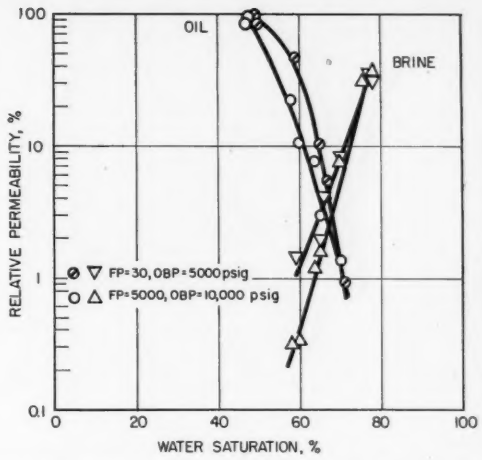

Fig. 11. Effect of first application of high fluid pressure on relative permeability of core *C*.

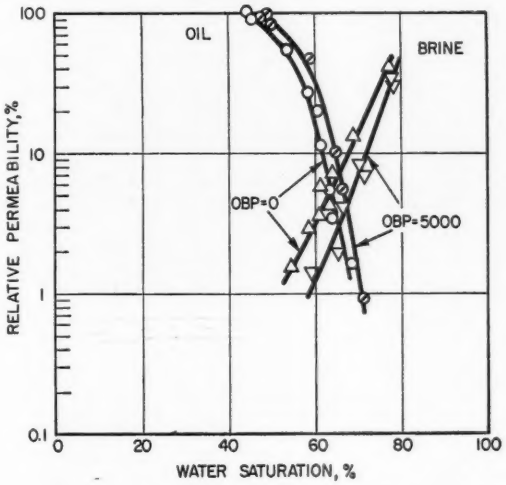

Fig. 10. Effect of overburden pressure on relative permeability of core *C*.

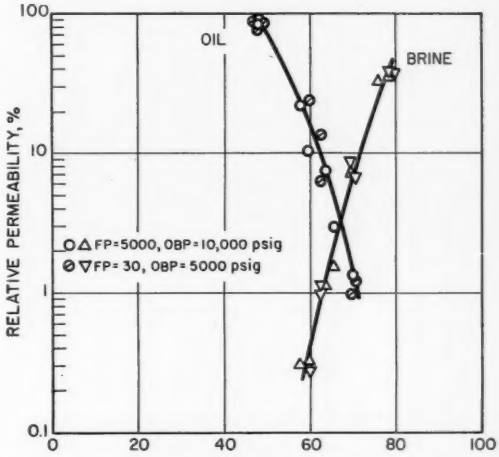

Fig. 12. Effect of removal of high fluid pressure on relative permeability of core *C*.

namic flow. The absence of compressible pads made it possible to determine the change in porosity by radioactivity measurements before and after the application of overburden pressure. The change for both cores was found to be 5% of the pore volume.

One run was made in this apparatus at elevated temperatures. Figure 15 shows a comparison of results of runs at low pressure on core *A* at 90° and 160°F. Although one point on the oil curve is out of line, this is probably the result of experimental error, and there is actually no significant effect of high temperature.

DISCUSSION OF RESULTS

The precision of these data is definitely less than can be obtained in conventional low-pressure equipment, but it is nevertheless clear that for the four cores studied here there was no significant effect of high fluid pressure as such on the relative permeabilities to oil and water. Although there is no real basis in the literature for predicting any appreciable effect, the mechanism of multiphase flow in porous media is so complex and little understood that actual experimental data are needed. It is possible that the drastic changes in cores *B* and *C* observed when the fluid pressure was first increased were a direct result of fluid pressure as such (for example, a change in wettability such as referred to above). However, the fact that the cores did not revert when the fluid pressure was removed would seem to indicate otherwise. The apparatus is now being modified so that gas may also be flowed, and a closer approximation to reservoir condition made.

Other work in this laboratory has shown some effect of a change in oil viscosity on effective permeability to water (*3*). However, these unpublished data indicate that the magnitude of the viscosity change caused by the application of 5,000 lb./sq. in. pressure to the oil employed in this study (from approximately 1.7 to 2.7 cp.) would change the relative permeability by an amount less than the experimental error. (It would shift the curve less than 1% on the saturation scale.) The effect of increasing the temperature to 160°F. on core *A* was to reduce the oil viscosity by 48% and the

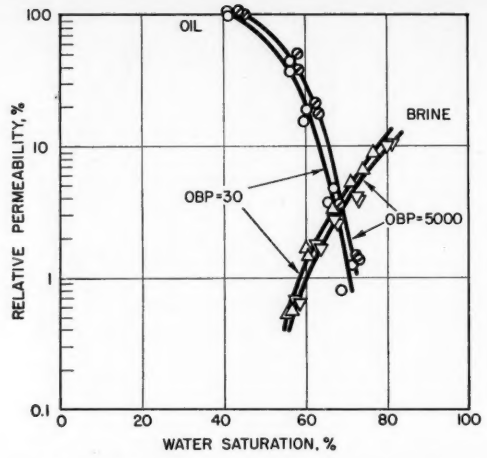

Fig. 13. Effect of overburden pressure on relative permeability of core *D*.

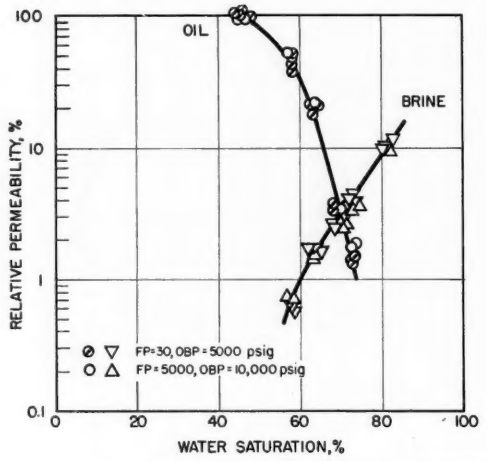

Fig. 14. Effect of high fluid pressure on relative permeability of core *D*.

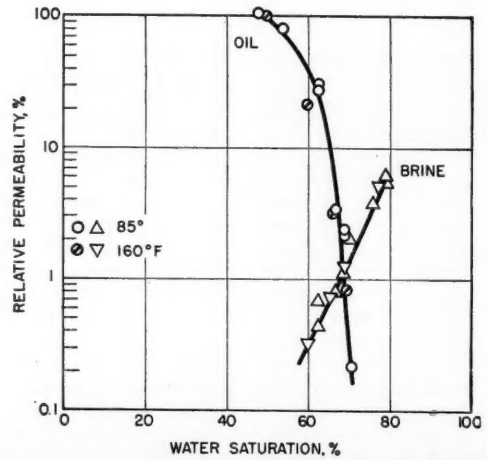

Fig. 15. Effect of temperature on relative permeability of core *A*.

brine viscosity by 50%, so that there was little change in viscosity ratio.

The application of overburden pressure reduced the effective permeabilities to oil and water to about the same extent as it did the single-phase permeability, and consequently the relative permeabilities were changed only moderately. The effect was, however, detectable in all cases. This is in contrast to the work of Fatt (*9*), who found no effect of 3,000 lb./sq. in. overburden pressure on relative permeability to gas in a gas-oil system. It might be expected that any distortion of a core sufficient to reduce the porosity by 5% would change the pore-size distribution significantly and thereby affect the relative-permeability relationships, but whether the expected change would be greater than the experimental error cannot be predicted in the absence of data. Some experiments to determine the change in pore-size distribution by capillary pressure measurements made with and without overburden pressure on the core are underway in this laboratory. Preliminary indications are that the effect is very slight.

It has been pointed out by Fatt (*10*) that the stress conditions in a Lucite-mounted core pressured by hydraulic oil may be different from those existing in a reservoir. The horizontal component of stress in reservoirs is probably less than the vertical component. This difference could influence in some degree the measurements of the effect of overburden pressure but should have no bearing on the conclusions regarding the effect of high fluid pressure.

ACKNOWLEDGMENT

The writer is indebted to E. R. Schmidt for careful execution of much of the experimental work and for many improvements in the apparatus conceived and installed by him, to J. E. Sherborne and Dr. R. S. Crog for many helpful discussions, and to the management of the Union Oil Company of California for permission to publish this report.

LITERATURE CITED

1. Wykoff, R. D., and H. G. Botset, *Physics*, **7**, 325 (1936).
2. Leverett, M. C., *Trans. Am. Inst. Mining Met. Engrs.*, **132**, 149 (1939).
3. Sandiford, B. B., private communication.
4. Odeh, A. S., and S. T. Yuster, Annual Meeting, Am. Inst. Mining Met. Engrs., Los Angeles (February, 1953).
5. Hough, E. W., M. J. Rzasa, and B. B. Wood, *Trans. Am. Inst. Mining Met. Engrs.*, **192**, 57 (1951).
6. Josendal, V. A., B. B. Sandiford, and J. W. Wilson, *loc. cit.*, **195**, 65 (1952).
7. Showalter, W. E., private communication.
8. Wilson, J. F., private communication.
9. Fatt, I., *J. Petroleum Technol.*, **5**, No. 10, 15 (1953).
10. ———, private communication.

Presented at A.I.Ch.E. Houston Meeting

Mass Transfer in a Wetted-wall Column: Turbulent Flow

W. H. SCHWARZ and H. E. HOELSCHER

The Johns Hopkins University, Baltimore, Maryland

The object of this study has been the measurement of concentration profiles of water vapor in a wetted-wall column with fully developed turbulent pipe flow of air for several positions downstream of the inlet. The air Reynolds number was 25,000. The mathematical formulation of this problem involves the Navier-Stokes equations and the mass transfer equation with a boundary condition of constant concentration at the wall. No attempt has been made toward an analytical solution of this problem, as the exact solution of the turbulence problem has not been developed. Instead, values of the mass and momentum transfer correlation, $\overline{u,h}$ and $\overline{u,u_z}$, have been computed as a function of the radius. The eddy diffusivity for momentum and mass and the local mass transfer rates are shown for engineering purposes.

In the past, investigators of the wetted-wall column have been interested only in the measurement of over-all mass transfer coefficients of a liquid evaporating into the air or in its analogous problem, a chemical contaminent being absorbed into the liquid. These over-all mass transfer coefficients were correlated by the use of dimensionless groups (*17*). Considerable discrepancy has been found in the experimental results.

Obviously the measurement of the gross properties of a system does not give an insight into the mechanisms of the transport of mass into a turbulent gas stream. More meaningful information can be obtained by the measurement of mean concentration profiles, especially when coupled with the detailed statistical information of Laufer (*10*) on the turbulent flow of air in a round duct.

From measurements of the mean velocity and concentration profiles, distributions of momentum and mass transport coefficients are directly calculable. However, it has been found that the mean profile is relatively insensitive to phenomenological assumptions on the transfer coefficient, and so direct experimental determination of the local transfer rates would be desirable and could presumably be obtained by the use of the hot-wire anemometer, giving direct measurement of statistical correlation such as $\overline{u,h}$ ~ the concentration diffusion, concentration fluctuation level h/H, the spectrum of concentration scale, and microscale. Having these statistical properties will allow partial solution of other types of shear flows where the properties of the flow field are known. Although theory has been developed for the hot-wire anemometer for the purpose of these measurements (*1*), it has apparently never been applied to mass transfer problems. It is logical, therefore, that the next step would be the development of the hot wire for this purpose and its application to the turbulent mass transfer problem.

There are few experimental data in the literature pertaining to wetted-wall columns where conditions have been defined satisfactorily and the properties measured to ensure reproducibility of results. Most of the difficulty stems from the lack of the fully developed state of the flow, the poor choice of measurement techniques, and failure to consider the effect of the development of the concentration profile.

Probably the most reliable wetted-wall data for evaporation of liquids into a turbulent air stream is the work of Gilliland and Sherwood (*5*). However, only over-all measurements of the mean outlet and inlet concentrations and temperatures were made. No rippling effects were noted.

Linton and Sherwood (*11*) noted the effect of the length of tube-to-diameter ratio on the mass transfer coefficient. An excellent review of the methods of correlation and a listing of other references are found in an article by Sherwood and Pigford (*17*). Mixing-length theories are discussed in several articles (*6, 13, 15*).

The information gained from this problem is fundamental in many applications to reactors, absorption towers, and numerous other unit operations involving the transfer of material. They are all concerned with the basic mass transfer differential equation. From the concentration profiles, transport coefficients may be measured which, combined with the mixing-length theory, offer engineering solutions to other problems where the flow conditions are similar.

DESCRIPTION OF EQUIPMENT

Operational Equipment

The wetted-wall column was constructed from a standard Pyrex-glass tube (3.33 in. I.D.) 4 ft. in length. The top edge was ground flat so that the liquid flowing over the edge would be distributed uniformly around the periphery, and the bottom edge was flared into a 30° angle (about 2 in. long) so that the liquid might be removed from the column. The liquid was fed into the upper calming section of the column from a 5-gal. constant-head tank. This tank was connected into a recycling system. A constant liquid-supply temperature was maintained by regulating the current on a heater in the constant-head tank. The water fed into the calming section was metered by a calibrated Fischer and Porter rotameter. This liquid was introduced into the calming section through a length of $\frac{3}{8}$-in. copper tubing. Holes of varying size and spacing were drilled in the tubing in order to achieve a uniform distribution in the upper section. A schematic diagram of the apparatus is shown in Figure 1.

The liquid was drawn from the column at the flared end of the tube into a removal section, where it was returned to the recycling system. A swing arm was built into the return line in order to maintain a constant level of liquid in the removal section.

The air was supplied by a 1-hp. centrifugal fan the speed of which was controlled by a rheostat. The fan had a 10- by 10-in. outlet leading into a tunnel which had 16-mesh screens properly spaced to reduce velocity fluctuations from the blower. It was necessary, owing to insufficient head room, to

have the blower and tunnel on a horizontal plane and, therefore, to provide a right angle in the system. In order to minimize deleterious velocity perturbations and vortexes created by a right angle, a vane cascade was built. The vanes were constructed from sheet metal and were built in the shape of a single quadrant of a circle with two tangential pieces in the manner suggested by Pankhurst (*14*). The gap to chord ratio was 0.25; the chord was 3.17 in. radius 2.24 in.; the ratio of the radius to trailing edge was 6.32; and fifteen vanes were used in the cascade.

After the right-angled bend the air passed through a screen into a contraction which had a twofold purpose; it acted both as a contraction and as a section going from a square to a circular cross section. The contraction was made from plaster-of-Paris–impregnated gauze, reinforcing wire, and plaster of Paris. It was cast on a form constructed from sheet metal and a block of wood which was turned down on a lathe into the wide-bottomed-bell contraction shape. The inside of the contraction was sanded smooth and lacquered. The contraction area ratio was 10 to 1.

The contraction was coupled to a brass pipe, approximately 8 ft. in length, in which fine sand was glued to a 7-in. length of the walls at the entrance section to hasten transition from laminar to turbulent flow and to increase the rate of growth of the boundary layer. The brass pipe was beveled on the outer surface of the top to a 60° angle, in order to ensure a smooth fit with the tapered glass section.

The whole system was carefully aligned in the vertical direction by means of a carpenter's level and plumb bob. This was very important in obtaining smooth flow of liquid down the walls of the tube.

Measuring Equipment

The air flowing up through the column was sampled in ten places simultaneously over the cross section by means of multiple probe. This probe was constructed of a 4-ft. length of ⅜-in. brass tubing through which were inserted ten sections of 18/8-16 gauge stainless steel hypodermic tubing. At the outlet end of the brass tube each piece of hypodermic tubing was bent through two right angles so as to orient each sampling tube along the axis of the support tube but displaced from it by a predetermined amount. In cross section the probe assembly resembled a pitchfork, but the prongs, being the hypodermic sampling tubes, were located in two dimensions instead of one and were spaced over the cross section of the column so that relatively more samples were taken near the wall than in the center.

The ⅜-in. brass tube containing the hypodermic sampling tubes was mounted in a traversing gear movable in three directions. The sampling probe was carefully aligned in the column by use of the two horizontal adjustments on the traversing gear and was thence raised or lowered vertically by means of the third adjustment to any desired measurement point.

Each of the sampling tubes was connected through a separate capillary flow meter to a drying tube containing commercial Drierite. A vacuum pump and a control needle valve permitted the sampling rate to be adjusted so that the velocity through the sampling tube equaled the air velocity at the corresponding sampling point in the column. A by-pass connection around each drying tube permitted adjustment of the flows prior to actual measurement.

A by-pass T was located in each sampling line near the probe inlet and was connected to a Meriam micromanometer. This manometer could be read to approximately 0.0001 in. of water. In this manner the velocity distribution in the column was obtained from the total head reading.

Each of the ten capillary flow meters was calibrated by means of a wet-test meter whose calibration was checked by a water-displacement method.

The temperatures of the inlet and outlet water and air streams were measured by copper–constantan thermocouples and a Rubicon potentiometer accurate to ±2 μv. The temperatures were correct to ±0.2°F.

The drying tubes were weighed on a Becker chainomatic balance which read to 0.1 mg. To compensate for external addition or subtraction of weight by surface moisture, the U tubes were counterbalanced by a similar U tube during the weighing operation.

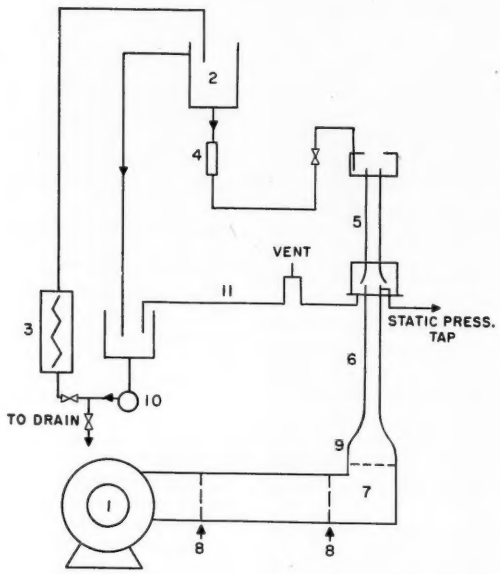

Fig. 1. Apparatus: 1, blower; 2, constant-head tank; 3, heater; 4, rotameter; 5, wetted-wall column glass section; 6, calming section (copper tube); 7, vanes; 8, screens, 9, contraction section; 10, recycle pump; 11, swing arm.

Table 1. Velicity Distribution

Run 1		Run 2	Short tube	
y/a	U/U_{max}	U/U_{max}	y/a	U/U_{max}
1	1	1	1	1
0.8619	0.9894	0.9930	0.887	0.9973
0.7022	0.9763	0.951	0.768	0.9834
0.6027	0.9409	0.954	0.649	0.9504
0.5063	0.9022	0.9229	0.530	0.9166
0.375	0.8484	0.8576	0.411	0.8609
0.2724	0.8149	0.8032	0.292	0.8200
0.1989	0.7539	0.7764	0.1732	0.7599
0.1235	0.7171	0.6973	0.0541	0.6448
0.0603	0.6371	0.6526		

EXPERIMENTAL PROCEDURE

Water was added to the circulating system and brought to temperature. To this was added sufficient detergent (commercial Alconox) to make a 0.3% (weight) solution. The blower was turned on and adjusted to provide a flow of air equivalent to a Reynolds number of 25,000. All U tubes were weighed and mounted in place. The velocity head in the center of the tube was determined by the micromanometer and, from this U_{max} was calculated. From Figure 2, the velocity at the positions of the various sampling tubes was calculated. This velocity coupled with the area of the hypodermic tubing and specific volume of air per pound of dry air gave the flow rate in pounds per second to be drawn through each sampling tube. The capillary-flow-meter calibration charts gave the proper sampling flow rate at each point. All the needle valves were ad-

justed and the flow was switched from the by-pass to the U tubes. The air-flow rate was maintained at the desired level during the run. After a run of 2 hr. the tubes were reweighed to determine the moisture pickup.

EXPERIMENTAL MEASUREMENTS AND CORRECTIONS

In mass transfer operations a careful knowledge of the transfer surface is necessary. One of the inherent problems of the wetted-wall column is the difficulty of obtaining a smooth film. Rippling is always present, causing uncertainty in the measurement of the interfacial area. By the addition of small amounts of detergent to the water, rippling is eliminated. The water film was virtually undetectable upon visual observation. It was found that the optimum concentration of wetting agent (commercial Alconox) was 0.3% for the best smoothness at the operating range used. This result agrees closely with the work of Emmert and Pigford (*3*).

The air Reynolds number was fixed at 25,000 in order that the velocity be sufficiently high to give measurable total head readings, but low enough to have negligible effect upon the liquid surface. The liquid flow rate was set to obtain the smoothest film. Too low a liquid flow rate produced low-frequency and high-amplitude waves; whereas high flow rates gave high-frequency, low-amplitude waves.

The presence of the wetting agent on the evaporation of the liquid suggested that an equilibrium interfacial condition might not exist. Emmert and Pigford (*3*) determined that the wetting agent has little effect upon the assumed boundary condition at the interface, that of equilibrium with the film. Also, from the calculations of Schrage (*16*) using the data of Gilliland, it is shown that the interfacial resistance for this operation is negligible. Therefore, in a study of evaporation from a wetted-wall column of this type, the boundary condition of saturated water vapor at the wall seems justifiable.

The total head readings were all corrected for the velocity gradient by use of the method of Young and Maas (*19*). The empirical formula $E = 0.131e_1 + 0.082e_2$ was used to find the displacement of the probe to obtain its relative position in the tube. It was found on computation of the Reynolds number, based on the diameter of the probe, that the correction for viscous effects on the total head reading was negligible (*7, 12*).

The velocity traverse was taken by the probe used in sampling the air. The static pressure was measured by a small tap in the brass pipe slightly below the glass section. The static pressure at the probe was calculated from the linearity of the pressure drop with distance down the column. From these readings the velocity head was determined.

The velocity distribution measured with liquid flowing down the walls was not different from the distribution determined with a dry column within the limits of experimental error. In order to determine the effect of the joint between the brass pipe and glass tube, a small glass section 5 in. long was made and assembled into place. A velocity traverse across the open end was not discernibly different from that further downstream. The velocity profile across the open end of the brass pipe was also measured. Again the results were the same. Rotation of the probe gave a velocity traverse which was the same within experimental error. Thus the existence of fully developed turbulent flow was assured. It also showed that, although the interface velocity was not zero (*see below*), it was small enough to have negligible effect on the gas-flow field.

The velocity profile plotted as U/U_{max} vs. r/a is shown in Figure 2 and compared with the data of Laufer (*10*) for a Reynolds number of 50,000.

When the concentration profile was measured, no correction was used to determine a relative position of the probe, as was used to map the velocity field, since there is a reversal of signs of the velocity gradient (dU/dr) and concentration gradient (dH/dr). Thus the portion of the probe receiving the higher velocity was receiving a lower concentration and the part of the probe receiving a lower velocity was receiving a higher concentration of water vapor. The two effects will tend to cancel each other and the relative position probably matched the actual position very closely.

The velocity of the sample being sucked through the tubing was adjusted to the velocity of the air at the point of location. Corrsin (*2*), by an approximate analysis, has shown the error to be as high as 8% by letting only the head pressure of the air do the work in obtaining a sample and applying no suction.

An estimate of the liquid velocity was experimentally determined by spreading a powder on the liquid film and timing its movement over a measured distance. The maximum speed at the interface from many runs for the system used was 0.963 ft./sec. This allowed calculation of the liquid film thickness, which was 0.0050 in. It was assumed that the air velocity did not appreciably affect the film thickness, and a parabolic velocity distribution existed. With these assumptions, the ratio of average velocity to surface velocity is two thirds. A calculation of the film thickness, by the formula shown in Fallah, Hunter, and Nash (*4*), gave the same result. The Reynolds number of the liquid film showed the film to be in the laminar state ($Re_L = 167$). The critical Reynolds number is about 1,200 for this system.

To show that the U drying tubes picked up all the moisture possible, air was drawn

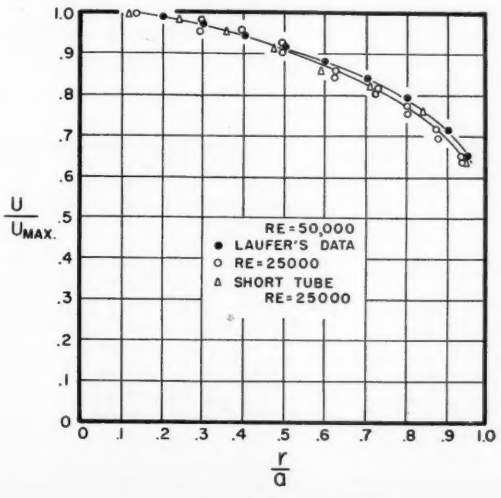

Fig. 2. Mean-velocity distribution.

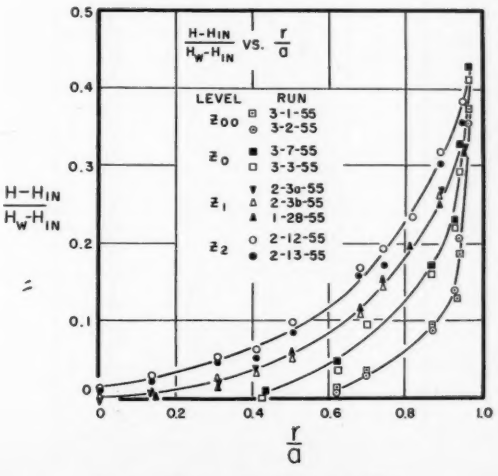

Fig. 3. Mean-concentration profiles.

TABLE 6

r/a	$\overline{u_r u_z}$	ϵ_m	$-\dfrac{\overline{u_r h} \times 10^{-3}}{H_w - H_{in}}$	$\epsilon \times 10^{-3}$	σ
0.05	0.04245	0.0209	0.7650	2.35	8.89
0.10	0.0846	0.01442	1.6446	2.915	4.946
0.15	0.1265	0.01078	2.725	3.351	3.217
0.20	0.1690	0.00973	4.2010	4.007	2.428
0.25	0.2105	0.00957	6.013	5.089	1.881
0.30	0.2525	0.00956	8.0971	6.398	1.494
0.35	0.2945	0.00982	10.39	7.605	1.291
0.40	0.3367	0.01004	12.574	8.368	1.199
0.45	0.3793	0.01032	14.498	8.717	1.183
0.50	0.4194	0.01053	16.30	8.467	1.243
0.55	0.4635	0.01072	18.237	8.062	1.329
0.60	0.5059	0.01085	20.251	7.843	1.384
0.65	0.5483	0.01092	22.29	7.324	1.490
0.70	0.5903	0.01097	24.379	6.577	1.667
0.75	0.6323	0.01062	26.448	5.88	1.806
0.80	0.6737	0.00966	28.425	5.088	1.898
0.85	0.008005	0.008005	30.699	4.566	1.753
0.90	0.00627	0.00627	32.998	4.183	1.4989
0.95	0.004192	0.004192	30.736	1.633	2.567
1.00					

through two U tubes in series at an airflow rate corresponding to the maximum air-sampling rate used. There was no measurable weight increase of the second U tube.

RESULTS

The velocity distribution in the column as determined by the total head tube, which is shown in Figure 2, is compared with the results of Laufer (*10*). The data are tabulated in Table 1. The results have been put in the dimensionless form U/U_{max} vs. r/a.

The concentration profiles are plotted as $(H - H_{in})/(H_w - H_{in})$ vs. r/a and shown in Figure 3 and tabulated in Tables 2, 3, 4, and 5.* The curve shows the growth of the concentration profile down the tube. From these curves and the velocity profile, the correlation $\overline{u_r h}/(H_w - H_{in})$ was calculated as a function of the radius and is tabulated in Table 6. Equation (3) was used for this calculation. A plot of ϵ (eddy diffusivity for mass) vs. r/a is shown in Figure 4. The values of $\overline{u_r h}/(H_w - H_{in})$ and ϵ were calculated for level Z_2. [ϵ was calculated from Equation (4).] The method of calculation is shown in the Appendix. All values were computed by graphical methods.

From the velocity distribution in the tube, values of $\overline{u_r u_z}$ and ϵ_m were calculated, then tabulated and plotted in Table 6 and Figure 5, respectively. The ratio ϵ_m/ϵ is shown as a function of the radius in Figure 6. Equations (5) and (7) were used.

The rise in diffusivity along the center line is dictated by the fact that the diffusivity must tend toward infinity at the center line. In fact, the values of eddy diffusivity for mass and momentum have no meaning at the center-line region of the pipe because of the manner in which the diffusivities are defined. At the center line the terms $\partial H/\partial r$ and $\partial U/\partial r$ equal zero and the eddy diffusivities have no meaning. This explains the dashed portion of the curve on Figures 4 and 5. Also in Figure 6 the large rise of the curve of σ vs. r/a has little significance.

The results may be compared with the analogous heat transfer problem of a fluid flowing in a pipe with stepwise wall temperature. Isakoff and Drew (*8*) present data for the eddy diffusivity of heat calculated from temperature profiles in heating mercury flowing through a tube. These values are of the same order of magnitude as the values of ϵ calculated for mass transfer in the wetted-wall column. Johnson (*9*) has computed values of the turbulent Prandtl number for the boundary layer of a heated flat plate where the conditions are similar to the flow field in the column. In the portion of the flow of interest, he has found values between 0.8 and 1.1 as compared with values of σ between 1 and 2.

The local mass transfer was computed at the four levels by Equations (10) and (12). (*See* Appendix.) These values are tabulated in Table 7. The value of w_0 from Equation (12) is found by differentiation with respect to z of the curve on Figure 7. From this curve it may be seen that the local mass transfer rate is approximately constant over the range

*Tables 2 through 5 have been deposited as document 4793 with the American Documentation Institute, Photoduplication Service, Library of Congress, Washington 25, D. C., and may be obtained for $1.25 for photoprints or 35-mm. microfilm.

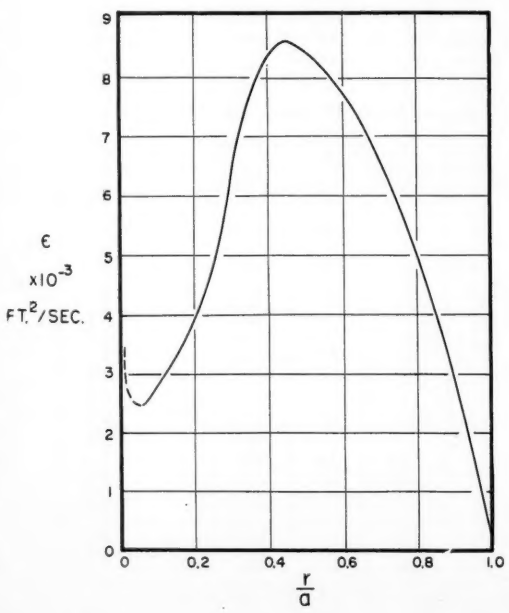

Fig. 4. Eddy diffusivity for mass vs. r/a. ←

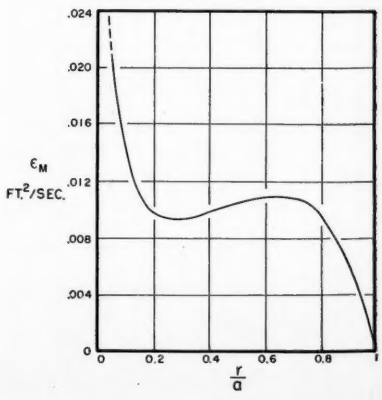

Fig. 5. Eddy diffusivity for momentum vs. r/a. →

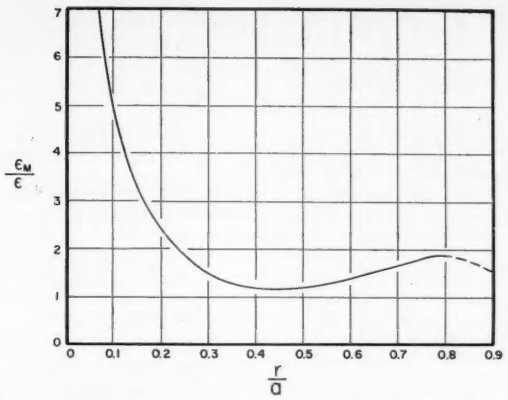

Fig. 6. Ratio of eddy diffusivity of momentum to mass vs. r/a.

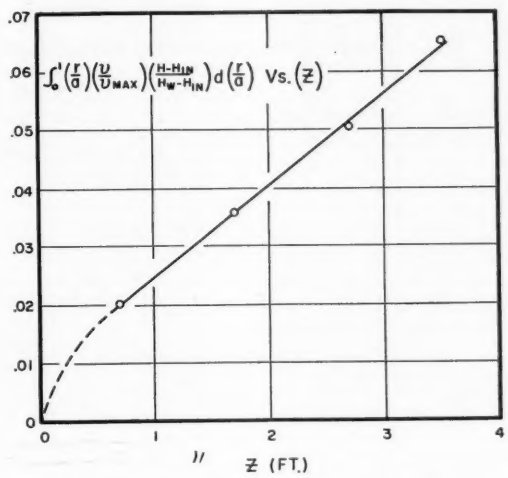

Fig. 7. Local mass transfer vs. column height.

measured. It can readily be seen that the rate becomes much higher near the inlet of the tube, where the concentration gradients are very much steeper.

CONCLUSIONS

A wetted-wall column has been constructed which produces a falling film essentially free from rippling. Special care has been taken to produce a fully developed turbulent profile of the air, which was measured and compared with the data of Laufer (*10*). The concentration profiles were measured at various distances downstream of the inlet. From these data the correlations $\overline{u_r u_z}$, $\overline{u_r h}$, and the eddy diffusivity for mass and momentum and their ratio were calculated. The local mass transfer was calculated at the various levels.

From the concentration profiles it is readily seen that many of the discrepancies in the literature concerning mass transfer data result from failure to consider entrance effects. Previous data have been correlated by the evaluation of the coefficients and exponents of a dimensionless equation, in which an over-all coefficient is expressed. Since the length of the column enters as a parameter of the problem, each system will have its own specific constants in the dimensionless equation, depending on the dimensions of the column. From the curve in Figure 7, it can be seen that the mass transfer rate does not become constant until the downstream distance has reached about six diameters.

Table 7. Local Mass Transfer Rate Computed from Equation (10)

$$w_{Z_{00}} = (0.002562)(H_w - H_{in})$$
$$w_{Z_0} = (0.002450)(H_w - H_{in})$$
$$w_{Z_1} = (0.002733)(H_w - H_{in})$$
$$w_{Z_2} = (0.002609)(H_w - H_{in})$$

From the slope of the curve (shown in Figure 13), the local mass transfer rate may be computed by Equation (12).

$$w = (0.002587)(H_w - H_{in})$$

NOTATION

a = radius of tube (measured to interface) (0.1383 ft.)
e_1 = outside diameter of probe (0.0655 in.)
e_2 = inside diameter of probe (0.0451 in.)
E = displacement of probe toward region of higher velocity
h = humidity fluctuation—defined by the equation $H' = H + h$; *Note:* $\bar{h}$(mean value of h) = 0
H = mean humidity, lb. H_2O/lb. dry air

Subscripts

in = inlet humidity of air
w = humidity of air at the wall in equilibrium with the water on the wall

H' = instantaneous humidity
P = pressure, lb./sq. ft.
dP/dZ = pressure drop along axis of tube [mean value 0.02898 lb./(sq. ft.)(ft.)]
r = distance from center line, ft.
Re = Reynolds number = $2U_{max}\, a/\nu$
Re_L = Reynolds number = $4\Gamma/\mu$
t = time, sec.
T = temperature, °K.
u = velocity fluctuation—defined by the equation $U' = U + u$; *Note:* $\bar{u}$(= mean value of u) = 0 (Reynolds restriction)
U = mean velocity, ft./sec.

Subscripts

θ = azimuthal direction
Z = along center line of tube
r = in radial direction
max = maximum velocity—corresponds to center-line velocity (mean value 15.6 ft./sec.)

L = liquid velocity
U' = instantaneous velocity
w = local mass transfer rate, lb. H_2O/(sq. ft.)(sec.)
W = mass flow rate, lb. dry air/sec.
Z = distance along axis of tube from inlet of wetted section

Subscripts

00 = 8.56 in. from inlet (5.6 diam.)
0 = 20.56 in. from inlet (12.39 diam.)
1 = 32.56 in. from inlet (19.62 diam.)
2 = 42.31 in. from inlet (25.50 diam.)

D = molecular diffusivity = sq. ft./sec. (1.626×10^{-4} sq. ft./sec.)
ϵ = eddy diffusivity of mass, defined by Equation (4)
ϵ_m = eddy diffusivity of momentum, defined by Equation (5)
θ = azimuthal coordinate
μ = viscosity of fluid, lb./(ft.)(sec.) for air, mean value 1.226×10^{-5}
ν = kinematic viscosity of the air, sq. ft./sec. (1.626×10^{-4} sq. ft./sec.)
Γ = flow rate of liquid = lb./(sec.)(ft.) of wetted perimeter
ρ = density of air, lb. dry air/cu. ft. of air
σ = defined as ϵ_m/ϵ

LITERATURE CITED

1. Corrsin, S., *Natl. Advisory Comm. Aeronaut., Tech. Note* 1864 (April, 1949).
2. ———, The Effect of Fluctuations in Chemical Concentration as Determined by a Sampling Probe, Course in Experimental Fluid Mechanics, The Johns Hopkins University, Baltimore, Md.
3. Emmert, R. E., and R. L. Pigford, *Chem. Eng. Progr.*, **50**, 87 (1954).
4. Fallah, J., T. G. Hunter, and A. W. Nash, *J. Soc. Chem. Ind. (London)*, **53**, 368 (1934).
5. Gilliland, E. R., and T. K. Sherwood, *Ind. Eng. Chem.*, **26**, 516 (1934).
6. Goldstein, S., "Modern Developments in Fluid Dynamics," Oxford University Press, New York (1938).
7. Hurd, C. W., K. P. Chesky, and A. H. Shapiro, *J. Appl. Mechanics*, **20**, 253 (1953).
8. Isakoff, S. E., and T. B. Drew, *Proc. General Discussion on Heat Transfer*, Institution of Mechanical Engineers, London (1951).
9. Johnson, D. S., Ph.D. dissertation, Johns Hopkins Univ., Baltimore, Md. (1955).
10. Laufer, John, *Natl. Advisory Comm. Aeronaut. Tech. Note* 2954 (June, 1953).
11. Linton, W. H., and T. K. Sherwood, *Chem. Eng. Progr.*, **46**, 258 (1950).
12. Macmillan, F. A., *J. Royal Aeronaut. Soc.*, **58**, 570 (1954).
13. Martinelli, R. C., *Trans. Am. Soc. Mech. Engrs.*, **69**, 947 (1947).
14. Pankhurst, R. C., and D. W. Holder, "Wind Tunnel Technique," Sir Isaac Pitnam and Sons, Ltd., London (1952).
15. Schlinger, W. G., and B. H. Sage, *Ind. Eng. Chem.*, **45**, 657 (1953).
16. Schrage, R. W., "A Theoretical Study of Interphase Mass Transfer," Columbia University Press, New York (1953).
17. Sherwood, T. K., and R. L. Pigford, "Absorption and Extraction," 2nd ed., McGraw-Hill Book Company, Inc., New York (1952).
18. Whitwell, J. C., *Ind. Eng. Chem.*, **30**, 1157 (1938).
19. Young, A. D., and J. N. Maas, *Rept. & Memo.* 1770, Great Britain Aeronautical Research Council (September, 1936).

APPENDIX

The general mass transfer equation for axisymmetric flow, based on Reynolds restrictions, the assumption of steady state, and constant physical properties, is given in reference *6* as

$$U_z\frac{\partial H}{\partial z} = \frac{1}{r}\frac{\partial}{\partial r}r\left[(-\overline{u_r h}) + D\frac{\partial H}{\partial r}\right] \quad (1)$$

Integrating this equation with respect to r and using the boundary conditions that

$$\overline{u_r h} = 0 \quad \text{and} \quad \frac{\partial H}{\partial r} = 0$$

at $r = 0$, one obtains

$$\overline{u_r h} = D\frac{\partial H}{\partial r} - \frac{1}{r}\int_0^r rU_z\frac{\partial H}{\partial z}dr \quad (2)$$

where

$$\int_0^r rU_z\frac{\partial H}{\partial z}\,dr = [H_w - H_{in}]U_{max}a^2 \cdot\int_0^{r/a}\left(\frac{r}{a}\right)\frac{U}{U_{max}}\frac{\partial}{\partial z}\left(\frac{H-H_{in}}{H_w-H_{in}}\right)d\left(\frac{r}{a}\right)$$

and

$$\frac{\partial H}{\partial r} = \frac{(H_w - H_{in})}{a}\frac{\partial}{\partial(r/a)}\left(\frac{H-H_{in}}{H_w-H_{in}}\right)$$

Equation (2) thus may be written

$$\frac{\overline{u_r h}}{[H_w - H_{in}]} = \left\{\frac{D}{a}\frac{\partial}{\partial(r/a)}\left(\frac{H-H_{in}}{H_w-H_{in}}\right) - \frac{U_{max}}{(r/a)}a \cdot\int_0^{r/a}\frac{r}{a}\left(\frac{U}{U_{max}}\right)\frac{\partial}{\partial z}\left(\frac{H-H_{in}}{H_w-H_{in}}\right)d\left(\frac{r}{a}\right)\right\} \quad (3)$$

A "transport coefficient" ϵ may be defined by $\epsilon(\partial H/\partial r) \equiv -\overline{u_r h}$. Thus

$$\epsilon = \frac{-\overline{u_r h}}{\dfrac{\partial H}{\partial r}} = -\frac{-\overline{u_r h}}{\dfrac{(H_w - H_{in})}{a}\dfrac{\partial}{\partial(r/a)}\left(\dfrac{H-H_{in}}{H_w-H_{in}}\right)} \quad (4)$$

A "momentum transport coefficient" ϵ_m may be defined as

$$-\overline{u_r u_z} \equiv \epsilon_m\frac{\partial U}{\partial r}$$

Thus

$$\epsilon_m = \frac{-\overline{u_r u_z}}{\dfrac{\partial U}{\partial r}} = \frac{-\overline{u_r u_z}a}{\left\{\dfrac{\partial}{\partial(r/a)}\left(\dfrac{U}{U_{max}}\right)\right\}U_{max}} \quad (5)$$

Finally, by definition, $\sigma = \epsilon_m/\epsilon$ = a "turbulent Schmidt number."

From the Navier-Stokes equation one may obtain

$$\int_0^r\frac{r}{\rho}\frac{dP}{dz}\,dr = r\left[-\overline{u_r u_z} + \nu\frac{\partial U_z}{\partial r}\right] + \text{constant} \quad (6)$$

When the boundary conditions

$$\frac{\partial U_z}{\partial r} = 0 \quad \text{and} \quad \overline{u_r u_z} = 0$$

at $r = 0$ are utilized, the constant is seen to be zero.

Thus

$$\overline{u_r u_z} = \frac{-a}{2\rho}\frac{\partial P}{\partial z}\left(\frac{r}{a}\right) + \frac{\nu}{a}U_{max}\frac{\partial}{\partial(r/a)}\left(\frac{U}{U_{max}}\right) \quad (7)$$

The local mass transfer rate may be written as follows:

$$w = \frac{\rho}{a}\int_0^a rU_z\frac{\partial H}{\partial z}\,dr \quad (8)$$

This has been shown equal to $\rho[D(\partial H/\partial r) - \overline{u_r h}]$ and values of N_0 may be found by graphical integration. In terms of dimensionless ratios,

$$\frac{U}{U_{max}}, \quad \frac{r}{a}, \quad \text{and} \quad \frac{H-H_{in}}{H_w-H_{in}},$$

Equation (8) becomes

$$w = \rho[H_w - H_{in}]U_{max}a \cdot\int_0^1\left(\frac{r}{a}\right)\left(\frac{U}{U_{max}}\right)\frac{\partial}{\partial z}\left(\frac{H-H_{in}}{H_w-H_{in}}\right)d\left(\frac{r}{a}\right) \quad (9)$$

N_0 may also be calculated from Equation (1) written in the form

$$\int_0^a\frac{d}{dz}(rU_z H)\,dr = \int_0^a\frac{\partial}{\partial r}r\left[(-\overline{u_r h}) + D\frac{\partial H}{\partial r}\right]dr \quad (10)$$

By Leibnitz rule, with $\overline{u_r h} = 0$ taken at the wall,

$$\rho\frac{d}{dz}\int_0^a rU_z H\,dr = aw$$

Thus

$$w = \frac{1}{a}\frac{d}{dz}\int_0^a \rho rU_z H\,dr \quad (11)$$

And at the wall

$$w = D\frac{\partial H}{\partial r}\cdot\rho$$

Letting

$$r = \frac{r}{a}\cdot a,$$

$$H = \left(\frac{H-H_{in}}{H_w-H_{in}}\right)(H_w - H_{in}) + H_{in}$$

$$dr = ad\left(\frac{r}{a}\right) \qquad U_z = \frac{U_z}{U_{max}}\cdot U_{max}$$

and simplifying, one may write Equation (11) as

$$w = aU_{max}(H_w - H_{in})\rho\frac{d}{dz} \cdot\int_0^1\left(\frac{r}{a}\right)\left(\frac{U}{U_{max}}\right)\left(\frac{H-H_{in}}{H_w-H_{in}}\right)d\left(\frac{r}{a}\right) \quad (12)$$

This equation permits the calculation of w by, first, a graphical integration, which is a smoothing effect, then a differentiation.

Crystal-size Distribution in Mixed Suspensions

W. C. SAEMAN

Olin Mathieson Chemical Corporation, New Haven, Connecticut

Although vacuum crystallizers are used widely, crystal-size–control methods have not been adequately analyzed. This paper supplies in part the deficiency of technical information on this problem. Industrial crystallizers may have inherent nucleation rates in excess of or below the seed-crystal requirement for the desired product-crystal size. This paper deals specifically with means of crystal-size control by removal of excess nuclei from mixed circulating suspensions as encountered in vacuum crystallizers. It is shown that under certain conditions the cumulative size distribution in the suspension varies as the fourth power of the size. Therefore, it may also be shown that the key to effective size-control procedures is the segregation time of nuclei in the fines-removal system. Procedures based mainly on crystal-size classification by hydraulic elutriation can hardly be effective unless they are also designed to meet the segregation-time requirements.

Effective correlation of the various factors which affect the performance of industrial crystallizers has been hampered by the multitude of factors involved and the obscure interrelations between them. It is for this reason that crystallization is often referred to as being more of an art than a science. The important basic relations governing crystal growth have, however, been disclosed. If these are systematically consolidated to yield derived relationships between the crystallizer operating conditions, the number of independent crystallizer variables may be reduced to simplify the correlation of the remaining factors.

The methods discussed are intended particularly for analysis of the performance of continuous vacuum crystallizers operating with mixed or semiclassified suspensions. Crystallizers of these types have been described (*5*). A typical single-body evaporator crystallizer, illustrated in Figure 1, is widely used, but little, if any, information has been published on crystal-size control for this type of unit. Although descriptions of the single-body types generally fail to include or depict any specific means for size control by removal of excess nuclei, segregation of fines by hydraulic elutriation in separate vessels is adaptable to this type.

The design which most strongly emphasizes means for size control by the segregation and removal of excess fines is the Oslo-Krystal type (*9*). Modified arrangements which have been demonstrated and described by the T.V.A. (*7*) are illustrated in Figure 2. The design of the two-body Oslo-Krystal type permits rather wide flexibility in the choice of crystallization conditions with a nearly completely classified suspension on one extreme and a fully mixed suspension on the other. An analysis of crystal-size distribution for classified suspensions was reported earlier by Miller and Saeman (*4*). More interference from salt deposits may, however, result from the relatively larger wall area in contact with solutions of appreciable supersaturation.

The use of mixed suspensions in crystallizers permits operation at higher rates than with classified suspensions though at an intermediate crystal size (*7*). Where the primary emphasis shifts to crystals of large size with lesser emphasis on production rate, operation with a semiclassified suspension is highly advantageous, as shown by Miller and Saeman (*4*). The reasons for this variation in crystallizer performance with respect to crystal size and production rate will be clarified when the principles governing size distribution are analyzed.

DERIVATION OF RELATIONS FOR CRYSTAL-SIZE DISTRIBUTION

Crystallization operations may be characterized by the fact that the inherent nucleation is either greater or smaller than the seed rate required for crystals of the specified size. This analysis deals only with cases where the nucleation rate is excessive. This situation is illustrated diagrammatically in Figure 3, where it is presumed that product crystals are removed only after they have attained full size.

The basic assumptions illustrated in Figure 3 and underlying the derivation of a relation for crystal-size distribution are

1. The suspension is completely mixed.
2. The system is operating at steady state conditions.
3. The number of crystals withdrawn as product and fines per unit time is equal to the nucleation rate.
4. The weight of crystals withdrawn as product and fines per unit time is equal to the crystallization rate.
5. Product crystals are withdrawn at full size only.

Although crystal size is usually measured as length or screen mesh, the average size and size distribution must satisfy assumptions 3 and 4 above, so that the number of crystals per unit weight is equal to the nucleation or seed rate divided by the crystallization rate.

Although the linear crystal size depends on crystal geometry, the shape coefficient is as a rule constant and so the linear size may be presumed to vary as the cube root of the volumetric size, or

$$l = k_1 v^{1/3} \tag{1}$$

where

k_1 = shape coefficient.

For crystals growing in turbulent solution, as in a dense suspension, the rate of crystal growth is proportional to the supersaturation (*1*). Although the relative velocity of the solution with respect to crystals influences the crystallization rate as shown by McCabe and Stevens (*3*), this effect can be disregarded in this instance owing to the relatively small change in growth rate over the velocity range (0.05 to 0.15 ft./sec.) of interest for larger crystals (*4*). Furthermore, it is presumed that the large and small crystals are intimately mixed under conditions of hindered settling and so the differential effects of solution velocity on the growth rate of large and small crystals will be appreciably less than for suspensions of crystals segregated by size. These conditions together with the finding that each crystal axis is characterized by a unique rate of growth coefficient lead to the derivation of the principle of geometric-shape similarity for the various stages of growth experienced by crystals and to McCabe's ΔL law (*2*). Both large and small crystals are exposed to solution of the same supersaturation in mixed suspensions; therefore no variation in growth rate is attributable to this source. Under these conditions the linear rate of growth is constant in time and is proportional to the average supersaturation

$$\frac{dl}{dt} = k_2 s \tag{2}$$

where

k_2 = coefficient relating supersaturation to rate of growth.

If the seed size is presumed negligible relative to the product, Equation (2) integrates to give

$$l = k_2 s t \tag{3}$$

as the relation between the crystal size l and age t.

The number of crystals in suspension smaller than l is equal to the seed rate times the age t [Equation (3)] of crystal size l, or

$$N = St = \frac{Sl}{k_2 s} \qquad (4)$$

where N = cumulative number of crystals smaller than l.

Since Equation (4) relates the cumulative number of crystals in suspension to the size l, it may be transformed to show a similar relation between the cumulative crystal weight and the size l. The increment in crystal weight dW, associated with an increment in size dl, is equal to the product of crystal density, crystal volume, and the number of crystals dN in increment dl, or

$$dW = \frac{Dl^3\, dN}{k_1} \qquad (5)$$

Using the derivative dN from Equation (4) in Equation (5) gives

$$dW = \frac{Dl^3 S\, dl}{k_1 k_2 s} \qquad (6)$$

which on integration ($l = 0$ being assumed for lower limit) yields

$$W = \frac{DSl^4}{4k_1 k_2 s} \qquad (7)$$

Under steady state conditions all the factors on the right-hand side of Equation (7) are presumed to remain constant except the size l of crystals in suspension. The cumulative weight, therefore, varies as the fourth power of the crystal size. For example, crystals up to one-half product size constitute only $(\frac{1}{2})^4$, or one sixteenth, of the total weight of crystals in suspension.

The actual residence time of crystals in suspension is dependent on the weight of crystals in suspension and the production rate. For convenience, the crystal age may be expressed as a function of the draw-down time T, which is defined as the ratio of the weight of suspension W divided by the production rate P, or

$$T = \frac{W}{P} \qquad (8)$$

Since $P = DSl_i^3/k_1$,

$$T = \frac{W}{P} = \frac{DSl^4/4k_1 k_2 s}{DSl^3/k_1} = \frac{l}{4k_2 s} \qquad (9)$$

Substituting Equation (3) ($l = k_2 st$) in (9) yields

$$T = \frac{k_2 st}{4k_2 s} = \frac{t}{4} \qquad (10)$$

Thus it is shown that the age of product crystals for classified-product removal is four times the draw-down time. Equation (7) for crystal-size distribution is further simplified by replacing absolute size l by relative size l/L, where $L = k_2 sT$.

Thus

$$W = \frac{DSl^4}{4k_1 k_2 s} = \frac{DSTL^4}{4k_1 k_2 sT}\left(\frac{l}{L}\right)^4 = \frac{DSTL^3}{4k_1}\left(\frac{l}{L}\right)^4 \qquad (11)$$

Equation (11) is written in this form to facilitate subsequent comparisons of suspensions for classified- and mixed-product removal. The variable term $(l/L)^4$ of Equation (11) is plotted graphically in Figure 5. Since the product crystal size for classified-product removal is $4L$, the total weight of suspension is

$$W = \frac{DSTL^3}{4k_1}\left(\frac{4L}{L}\right)^4 = \frac{64DSTL^3}{k_1} \qquad (12)$$

DERIVATION OF RELATIONS FOR CRYSTAL-SIZE DISTRIBUTION FOR MIXED PRODUCT

Withdrawal of product direct from the suspension distorts the simple seed-to-product relationship pictured in Figure 3 and necessitates the use of additional relations to derive the weight-vs.-size relationship. The new relations are depicted in Figure 4. Here it is presumed that the probability that seed crystals and crystals of intermediate size are withdrawn as product is proportional to the population density of each crystal size in the system. Since the population density of the smaller crystals is greater than that of the larger sizes, the cumulative weight-vs.-size relation will be biased so that smaller crystals account for more of the total bulk than that which corresponds to the simple fourth-power relation.

To analyze this situation one may assume that the size range is subdivided into equal size intervals where n is the population density of crystals within the interval. If no crystals were lost as product, the number of crystals entering and leaving each size interval would be the same, as it is presumed that the rate of crystal growth is independent of size. Crystals withdrawn from each interval as product will, however, change the population density, and, since the number of crystals withdrawn per unit time is proportional to the population density and the withdrawal rate,

$$\frac{dn}{dt} = -\frac{n}{T} \qquad (13)$$

where $T = V/Q = W/P$.
Integration of Equation (13) between the limits n_0 and n gives

$$n = n_0 e^{-t/T} \qquad (14)$$

where n_0 corresponds to the initial population density of seed crystals. The value of n_0 is equal to the seed rate divided by the rate of growth, or

$$n_0 = \frac{S}{k_2 s} \qquad (15)$$

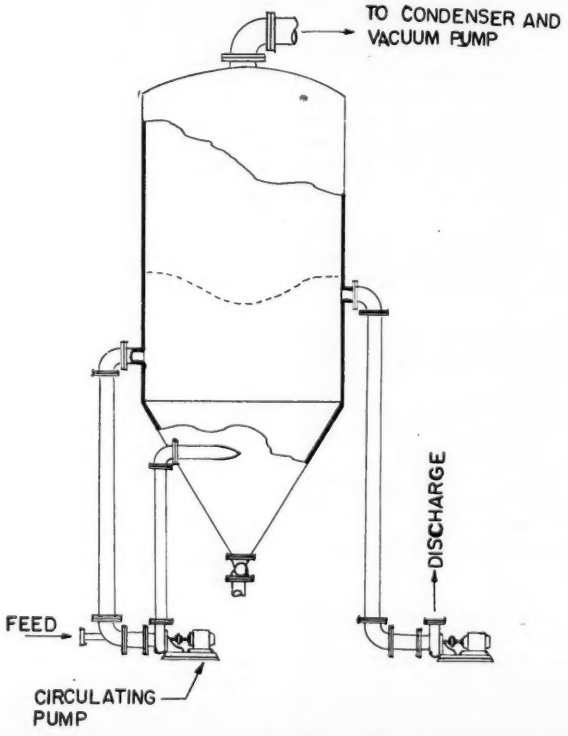

Fig. 1. Continuous vacuum crystallizer with pump circulation (8).

By substituting $t = l/k_2 s$ and $L = k_2 sT$, Equation (14) can be rewritten as

$$n = \frac{ST}{L} e^{-l/L} \qquad (16)$$

As shown in Equation (5), the weight of crystals in any size interval is

$$dW = \frac{Dl^3\, dN}{k_1}$$

In this case $dN = n\, dl$, and so

$$dW = \left(\frac{DST}{k_1 L}\right) l^3 e^{-l/L}\, dl \qquad (17)$$

The integral solution for (17) is

$$W = C - \left(\frac{DSTL^3}{k_1}\right) e^{-l/L} \cdot \left[6 + 6\left(\frac{l}{L}\right) + 3\left(\frac{l}{L}\right)^2 + \left(\frac{l}{L}\right)^3\right] \qquad (18)$$

Since $W = 0$ when $l = 0$ the constant of integration C is $6DSTL^3/k_1$ and so

$$W = \left(\frac{DSTL^3}{k_1}\right)\left(6 - e^{-l/L} \cdot \left[6 + 6\left(\frac{l}{L}\right) + 3\left(\frac{l}{L}\right)^2 + \left(\frac{l}{L}\right)^3\right]\right) \qquad (19)$$

For convenience, the variable term in Equation (19) is represented as a function of the size ratio l/L,

$$f\left(\frac{l}{L}\right) = 6 - e^{-l/L} \cdot \left[6 + 6\left(\frac{l}{L}\right) + 3\left(\frac{l}{L}\right)^2 + \left(\frac{l}{L}\right)^3\right] \qquad (20)$$

and is plotted for reference in Figure 5. The weight of suspension up to size l is therefore

$$W = \frac{DSTL^3}{k_1} f\left(\frac{l}{L}\right) \qquad (21)$$

Approximate coincidence has been observed between the distribution function derived here and numerous samples of crystals taken from crystallizers operating with mixed-product removal from suspension. Owing to the relatively long crystal retention time, deviations may readily occur because of variation in nucleation and seed rates which induce nonequilibrium conditions in the suspension.

Equation (13) also represents the crystal-size distribution for crystals withdrawn as product. The contribution of each size interval to total production is given by

$$\frac{dP}{dl} = \frac{Dl^3}{k_1}\frac{dn}{dt} = \frac{-Dl^3 n}{k_1 T} \qquad (22)$$

Substitution of (16) in (22) converts the relation to a function of l only, and so

$$dP = \left(\frac{DS}{k_1 L}\right) l^3 e^{-l/L}\, dl \qquad (23)$$

Since Equations (23) and (17) agree in functional form, the function $f(l/L)$ plotted in Figure 5 is applicable and the cumulative product rate up to size l is

$$P = \frac{DSL^3}{k_1} f\left(\frac{l}{L}\right) \qquad (24)$$

Comparison of Equations (24) for P and (21) for W shows that $W = TP$ in agreement with the definition [Equation (8)].

The derivative curve of $f(l/L)$ (also shown in Figure 5) shows that the mixed product has a dominant size fraction for $l/L = 3$ compared to the size $l/L = 4$ for classified product. Also, half the product is greater than $3.7L$, as $f(l/L) = 3$ at $l/L = 3.7$. [$f(l/L) = 6$ corresponds to 100% of product.]

COMPARISON OF CONDITIONS FOR CLASSIFIED- AND MIXED-PRODUCT REMOVAL

Comparable operating conditions are presumed to exist in crystallizers producing classified and mixed products when the rates of crystal growth in the two systems are equal. The rate of growth is selected as a criterion since the quality of crystal structure tends to deteriorate as the rate of growth increases; so for purposes of comparison the crystals from the two systems should be of comparable quality.

The weight of the suspension carried in the system is a further criterion for comparative operating conditions since the suspension capacity of the system is fixed. The same weight of suspension will, therefore, be assumed in both cases. Since the production rates, suspensions, and rate of crystal growth are presumed equal for both systems, the draw-down time T and crystal reference size L are also the same. The two cases can therefore be equated only by an adjustment in seed rate to satisfy the equations

$$W_c = \frac{64DS_cTL^3}{k_1} = W_m = \frac{6DS_mTL^3}{k_1} \qquad (25)$$

and

$$P_c = \frac{64DS_cL^3}{k_1} = P_m = \frac{6DS_mL^3}{k_1} \qquad (26)$$

where the subscripts c and m refer to classified and mixed products, respectively.

In either case it is found that

$$S_c = 0.094 S_m \qquad (27)$$

For operation under comparable conditions for mixed and classified product, the required seed rate for mixed product is therefore about eleven times the number required for classified product. This difference is hardly significant on a weight basis since the extra seed crystals for mixed product are confined to sizes smaller than $2.34L$. This value is derived from Equation (16), where the factor $e^{-l/L}$ for mixed product was made equal to 0.094 to calculate the seed size for which both suspensions had equal population densities. Mixed product has 77% of its weight in crystals larger than $2.34L$. Thus 77% of the mixed product will contain the same number of crystals as is found in 100% of the classified product. The remainder of the mixed product will consist of smaller sizes.

If comparisons are to be made between equal weight percentages of mixed and classified product, it is found that the 71% fraction of the largest crystals in the mixed product contains the same number of crystals as those in 71% of the classified product. The mixed-product

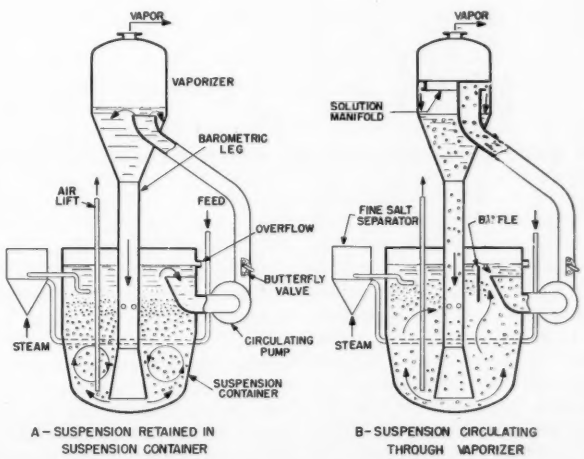

Fig. 2. Two methods of operation for vacuum crystallizers for ammonium nitrate (7).

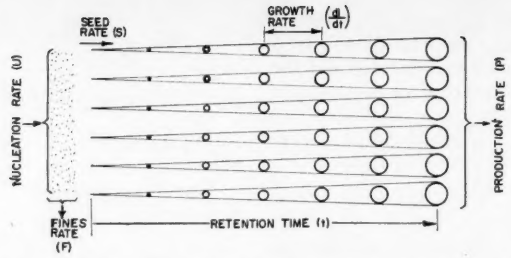

Fig. 3. Idealized crystal-size distribution for withdrawal of crystals at full size.

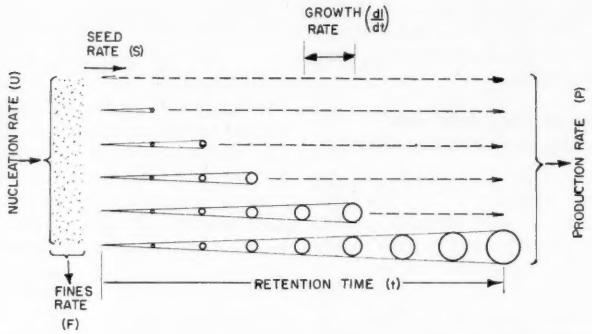

Fig. 4. Idealized crystal-size distribution for withdrawal of crystals from mixed suspensions.

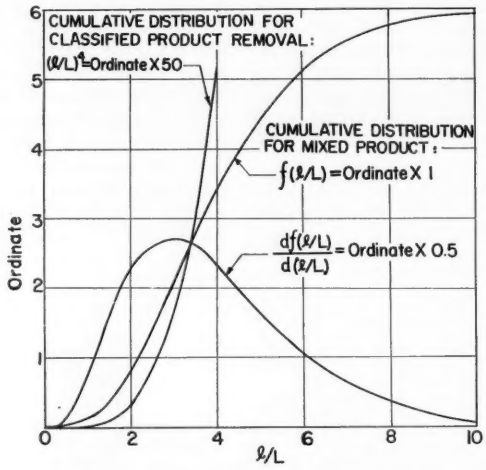

Fig. 5. Relative-distribution curves for classified- and mixed-product removal.

fraction in this case consists of crystals larger than $2.7L$. On the large-size end of the crystal spectrum it is, therefore, apparent that classified and mixed product may be regarded as equivalent for practical purposes. On the small-size end comparisons must be limited to size distribution of crystals in suspension where it was shown that the population density for mixed product must start out about eleven times greater than the density required for classified-product removal. The cumulative weights of $0.5L$, $1L$, and $2L$ sizes in suspensions producing mixed product are, therefore, 0.3, 1.6, and 14% respectively, and the comparable percentages for suspensions on classified product are 0.025, 0.4, and 6%, respectively. In actual practice crystal-size distributions will lie between these two limiting conditions since neither the mixed- nor classified-product removal systems will yield theoretical performance. The differences between the two systems will therefore tend to be less than those calculated above.

CRYSTAL-SIZE CONTROL

If it is assumed that the crystal geometry remains essentially constant as crystallizer conditions are varied over limited ranges, the seed rate S and reference size L must be interrelated to satisfy any given production rate. Thus as S increases, L must decrease. As L decreases, the rate of growth also decreases since the increase in total superficial crystal surface lowers the average degree of supersaturation. For constant draw-down time T the decrease in crystal size L is therefore accounted for by a slower rate of growth.

As an alternative, the increase in superficial surface associated with a decrease in crystal size may be offset by decreasing the total weight of crystals in suspension. The average supersaturation and rate of crystal growth are then unchanged and the decrease in L is accounted for by a decrease in draw-down time T. On the basis of these relations it may be inferred that for a fixed weight of crystals in suspension the maximum attainable production rate for crystals of constant quality should vary inversely as the crystal size.

SEED-RATE CONTROL

In cases where the nucleation rate is excessive, seed-rate control must be achieved by segregation and removal of excess nuclei. Since the weight of crystalline matter associated with these excess nuclei varies as the cube of the size, it is apparent that the earlier the nuclei are segregated and destroyed, the more efficient the operation.

For crystallizers operating with classified or semiclassified suspensions as illustrated in Figure 2A, excess nuclei segregate on top of the suspension below the circulating pump intake as soon as they are sufficiently large to subside. The subsided layer of fines may then be withdrawn and redissolved to destroy the excess nuclei. In this case both the excess nuclei removed from the upper layer and the product crystals removed from below are influenced by hydraulic classification so that the range of sizes is relatively narrow and both streams tend toward a similar distribution pattern. Comparisons may therefore be made directly on an l^3 basis. The ratio of fines removed to crystals produced is therefore represented as

$$\frac{N_f l_f^3}{N_p l_p^3}$$

where subscripts f and p refer to excess fines and product respectively. For

relatively large product crystals, fines may readily subside at one-tenth product size, and so a hundredfold excess of fines may readily be controlled with a fines-to-product weight ratio not exceeding 0.1.

Where fines are withdrawn from a mixed suspension into a fines trap, as shown in Figure 2B, the fines distribution is characterized more nearly by the distribution function $f(l/L)$ of Figure 5. If the product is also mixed, it will be characterized by the same distribution function and the weight of crystals in both cases will be proportional to L^3. The values of L_f and L_p, applicable to the fines and product, respectively, will be proportional to the respective draw-down times of the fines trap T_f and the product-removal system T_p. Thus, if the draw-down time of solution flowing through the fines trap is one-tenth the draw-down time of the product-removal system, it should be possible to absorb a hundredfold excess of nuclei without exceeding a fines-to-product ratio of 0.1 as in the case of classified fines and product. If, however, the fines are trapped in mixed distribution and the product is removed in classified form, the required seed rate is only one eleventh as great, and so a hundredfold fines excess for mixed product corresponds to a thousandfold excess for classified product. The draw-down time of the fines trapping system must therefore be less than one-twentieth that of the product-removal system to keep the fines-to-product ratio under 0.1. The foregoing examples are illustrative of typical cases only. In practice numerous other combinations or variations may actually be encountered.

OPERATING DATA COVERING SIZE CONTROL AND DISTRIBUTION

The most immediate application of this relation is in the design and evaluation of means for removal of excess fines. Thus without fines removal the size of ammonium nitrate crystals grown in the T.V.A. crystallizers with mixed suspensions has been reported to be predominantly 30 to 35 mesh (Tyler standard) in size (*6*, *7*). With fines removal the size increased to yield a major fraction of +20-mesh crystals of the type pictured in Figure 6. Operating conditions for these instances are tabulated below (*6*).

Screen analysis of fines removed:

Mesh size	+20	+28	+35	+48
Cumulative percentage	3	20	33	82

Screen analysis of suspension with no fines removed:

Mesh size	+16	+20	+28	+35
Cumulative percentage	0	1	38	72

Screen analysis of suspension for 15 lb./min. fines removal:

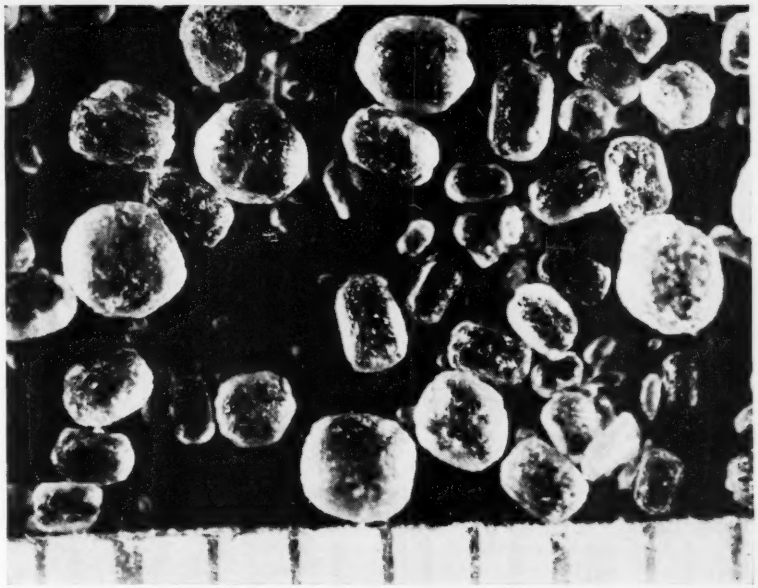

Fig. 6. Ammonium nitrate crystals produced by vacuum crystallization in T.V.A. plant (*7*) (millimeter scale shown along edge).

Mesh size	+16	+20	+28	+35
Cumulative percentage	12	62	89	94

The tests were made at a 140 lb./min. crystallization rate with 80,000 lb. of crystals in suspension (23,000 gal.). The suspension was circulated at 10,000 gal./min. to limit the maximum supersaturation to 0.014 lb./gal. Since the larger crystals produced in this instance are roughly twice the length of the smaller, fines removal has effected about an eightfold ($2^3 = 8$) reduction in the suspension seed rate. Inspection of the size distribution of fines removed shows the presence of substantial quantities of large crystals due to turbulent mixing between the main suspension and the trapped fines. Owing to this source of interference the full benefits of the fines trap were not realized.

The fact that 30–35-mesh (0.5 mm.) crystals were produced without fines removal serves as a definite index of the inherent nucleation rate of the system. If 2-mm. crystals were desired (fourfold size increase), the effective seed-rate requirement would be only one sixty-fourth as great. It would, therefore, be necessary to destroy sixty-three out of every sixty-four nuclei formed. To avoid loss of operating efficiency this large number would have to be isolated and redissolved at a very early age. Thus, where fines are segregated at an average size one fifth of product size, the volume of fines relative to product crystals would be about

$$63(1/5)^3 = 63/125, \quad \text{or} \quad 50\%$$

If, however, the fines system is designed to segregate excess nuclei at one-twentieth the average product size the percentage would be

$$63(1/20)^3 = 63/8{,}000, \quad \text{or about} \quad 1\%$$

Fines collection at ages one tenth to one twentieth of the average product size is within practical limits, and so size control by this means should be effective even though the inherent nucleation rate is about 100 times more than the requirements (fines removal on weight basis 1 to 10% of crystallization rate). The baffle system of fines segregation in the upper part of the T.V.A. Oslo-Krystal units (*7*) was reported to segregate fines from 1,000 to 2,000 gal./min. of solution (*6*), and the solution from the entire system (23,000 gal.) was passed through the fines segregation system on the average of 10 to 20 min. (10- to 20-min. fines draw-down time). The performance of the T.V.A. system was, however, handicapped by the asymmetric location of the baffle with respect to the currents in the suspension. Even though the fines subsided to a distinct level behind the barrier, this level fluctuated erratically and turbulence from below projected currents of larger crystals into the fines layer so that the over-all efficiency of the system was impaired. Further developments are required to improve the efficiency of this baffle design, as the fines draw-down time was one-thirtieth the product draw-down time; whereas in actual operation, with fines dissolved at 10% of the crystallization rate, the apparent fines draw-down time for an eightfold reduction in seed rate was about

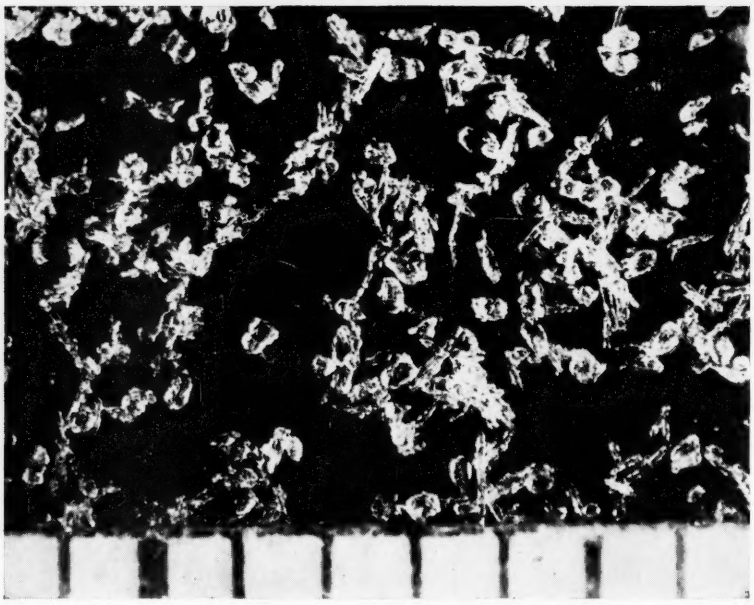

Fig. 7. Fines collected in fine-salt separator (*6*) (millimeter scale shown along edge).

1/4.1 of the product draw-down time ($7[1/4.1]^3 = 10\%$). This inefficiency is corroborated by the presence of substantial amounts of coarse crystals in the photograph of the fines collected as shown in Figure 7.

The foregoing estimates of nucleation rates are only approximate, as the crystal size, density of suspension, and turbulence in the system all affect the nucleation rate, as shown by a comparison of operating conditions applicable to mixed and semiclassified suspensions (*6*). In the latter case predominantly 8- to 12-mesh crystals were readily grown at a 55 lb./min. rate in a 45,000-lb. suspension (18,000 gal.) by use of a fines-removal rate of less than 0.5 lb./min. A circulation rate of 7,000 gal./min. was used to permit some classification within the system, and supersaturation was limited to 0.008 lb./gal. In this case fines segregation occurred on top of the suspension below the pump intake. Since this is possibly the most effective method of fines segregation known, associated with the mildest conditions for minimizing crystal attrition, it is highly advantageous to operate in this manner whenever crystal size serves as the most important criterion of plant performance.

IMPORTANT DESIGN CRITERIA AFFECTING CRYSTAL SIZE AND SIZE DISTRIBUTION

New crystallizer applications are often approached from the viewpoint that the most effective means for product-size control lies in size-classification devices (either hydraulic or mechanical) for the crystals withdrawn from the suspension. Regardless of the type of classification device used, it is readily apparent that it cannot put out large crystals unless conditions are maintained in the suspension which are conducive to the growth of large crystals. If proper conditions for the sustained growth of large crystals are maintained in the suspension, the crystal-size-distribution functions indicate that for most applications the smaller sizes are insignificant on a weight basis, and so there is no strong need for product classification.

Positive and direct means for size control lie largely in the provision of effective means for segregation and elimination of excess nuclei. Efficient segregation methods should be effective for the elimination of at least a hundredfold excess of nuclei relative to product crystals. This implies that the nuclei must be eliminated at an average age of one-tenth the product age or less. Thus the critical-performance requirement of the segregation system is the maximum solution rate through the segregation system relative to the total capacity of the crystallizer.

Secondary requirements that must be met are the establishment of a stable fines subsistence level free of fluctuations or turbulence, so that the fines-solution system will not inadvertently overload with relatively large intermediate-size crystals.

The design of the Oslo-Krystal crystallizers fulfills several of these objectives simultaneously in that nuclei, after reaching a critical size, subside to a stable layer on top of the suspension. For operation with a classified or semiclassified suspension all the solution in the system passes through the segregation zone on each pass through the crystallizer. For operation with mixed or circulating suspension the Oslo-Krystal units require the installation of extra baffles to permit effective fines segregation. In the latter case the ratio of solution flowing through the baffled area relative to the total circulation should be as great as possible consistent with the fact that the fines must subside to a stable level to permit efficient withdrawal of the fines. Since the basic principles governing crystal-size distribution and crystal-size control are equally applicable to Oslo-Krystal and single-body crystallizers, effective size control in the latter type can also be achieved by installation of means for the segregation and elimination of fines.

ACKNOWLEDGMENT

The assistance of V. E. Lyons of the Tennessee Valley Authority in suggesting constructive revisions of the original manuscript is gratefully acknowledged.

NOTATION

a = constant
D = density of crystal, lb./cu. ft.
e = base of natural logarithms
F = fines removal rate, lb./hr., no./hr.
k = constant
l = linear crystal size, ft.
L = crystal size at time T, ft.
n = number of crystals per unit size interval, no./ft.
N = cumulative number of crystals
P = production rate, lb./hr.
Q = suspension withdrawal rate, cu.ft./hr.
s = degree of supersaturation, lb./cu. ft.
S = suspension seed rate, no./hr.
t = time or crystal age, hr.
T = draw-down time, hr.
U = nucleation rate, no./hr.
v = volume of individual crystals, cu. ft.
V = volume of suspension, cu. ft.
w = weight, of individual crystals, lb.
W = cumulative weight of crystals in suspension, lb.
X = crystallization rate, lb./hr.

LITERATURE CITED

1. Jenkins, J. D., *J. Am. Chem. Soc.*, **47**, 903 (April, 1925).
2. McCabe, W. L., *Ind. Eng. Chem.*, **21**, 30, 112 (1929).
3. ———, and R. P. Stevens, *Chem. Eng. Progr.*, **47**, 168 (1951).
4. Miller, Philip, and W. C. Saeman, *Chem. Eng. Progr.*, **43**, 667 (1947).
5. Perry, J. H., ed., "Chemical Engineers' Handbook," 3 ed., pp. 1065–69, McGraw-Hill Book Company, Inc., New York (1950).
6. Saeman, W. C., paper presented at A.C.S. Southeastern Regional Meeting Wilson Dam, Ala. (Oct. 18–20, 1951).
7. ———, I. W. McCamy, and E. C. Houston, *Ind. Eng. Chem.*, **44**, 1912 (1952).
8. Seavoy, G. E., and H. B. Caldwell, *Ind. Eng. Chem.*, **32**, 629 (1940).
9. Svanoe, H., *Ind. Eng. Chem.*, **32**, 636 (1940).

Presented at A.I.Ch.E. Houston meeting

Properties of Evaporated Metal Films Related to Their Use for Surface Temperature Measurements

THEODORE B. SIMPSON and CHARLES C. WINDING

Cornell University, Ithaca, New York

Extension of the understanding of properties of films of metals produced on glass surfaces by vacuum evaporation has permitted the fabrication of film-resistance thermometers that with simple instrumentation accurately measure surface or average surface temperatures without altering the geography of that surface. Formerly unknown and unstable related properties of such films have been classified and may be anticipated or eliminated by recommended experimental procedures. Films of several of the most chemically inert and refractory metals 300 to 3,000 Å. thick have been shown to attain accuracies as high as 0.01°C. for practical periods of time. Their use, which is described, is developing satisfactorily, and the technique and equipment for their preparation are relatively simple.

Work on thin films as such, originating in 1889, has been extensive but has been directed principally toward the solution of problems related to solid state physics. Electrically and physically the behavior of thin films deviates considerably from that of bulk metal. Resistivities and temperature coefficients of resistivity frequently have no resemblance to those of the bulk metal. Film behavior is affected by the conditions under which it is formed. Tensile strength (*8*) and chemical inertness (*1*) generally increase as the film becomes thinner. This general subject is treated more extensively in reference *15*.

An interesting application of evaporated metal films has been their use as resistance thermometers for the measurement of surface temperatures. Not only may heat transfer studies and other specific situations require spot temperature measurements precisely at the surface, but also average values may be important in cases where temperature varies over a surface area. Many methods employed for such measurements have disadvantages that can be eliminated by the use of metal films. Optical methods of temperature measurements are incompatible with the thermal shielding that is frequently required. There is some disagreement regarding the effectiveness of the best designed thermocouples (*6, 9*). Techniques in which the wall of the conduit itself is used as a resistance thermometer (*2*) suffer from the need to measure extremely low resistances and the fact that the temperature measured is not precisely that of the surface. Coatings of temperature-sensitive phosphors (*5*) have a restricted range and require optical measurements. Though closer to the thin-film concept, use of a wrapping of tin foil over a surface (*14*) was only a first approximation.

The initial investigation by Winding, Baus, and Topper (*15*) of the use of evaporated metal films on glass for the measurement of surface temperatures indicated that this method showed promise in the range of room temperature to 125°C. Chromium films and, for short periods, nickel films 200 to 1,500 Å. thick were found suitable and were successfully used for the measurement of an average surface temperature in the calculation of coefficients of heat transfer for condensing organic vapors. The antecedents and advantages of film thermometers have been discussed by these authors. Included are essentially zero heat capacity, no change in surface geography, equivalency of the electrical resistance to an average surface value, and convenient values of electrical properties.

Recently a thick evaporated nickel film was used on steel as a thermocouple for the measurement of an instantaneous surface temperature in a gun barrel (*4*) in a manner similar to some earlier work (*7*). Precision of results was not reported. The need for a greater understanding of film behavior again appeared necessary for more general application of the principle.

In this study an effort was made to perfect the utilization of evaporated metal films for average surface temperature measurements. In both the preceding studies the necessity for random choice of film parameters and inexplicable film phenomena indicated the need for a more careful, fundamental investigation. Extension of the range of temperatures that might be measured by film thermometers, improvement in film stability and accuracy, introduction of greater variety of suitable metals, and greater understanding of their behavior have been attained.

EXPERIMENTAL

The technique and equipment required to produce evaporated metal films are relatively simple, but considerable care must be exercised to produce films with desirable properties. In general, a system capable of producing vacuums of 10^{-4}mm. Hg or better in a closure big enough to house the evaporation apparatus is required. Metal is vaporized from a high-temperature source and, because the residual pressure is low enough so that the mean free path of a gaseous metal atom is greater than the dimensions of the enclosure, travels in a straight line until it hits an obstruction, where it condenses and forms a film. Shadows completely free of deposited metal can be produced by introducing obstructions or shields in front of the desired area. Metal is distributed in thicknesses varying as the inverse square of the distance from the source.

Problems of technique include the need for evaporation temperatures of 500° to 3,500°C. and evaporator materials resistant to the extreme reactivity and solvent power of metals at high temperatures. Furthermore, pretreatment of the target surface and excellent vacuum must preclude contamination since evolution of gases from the target and other surfaces is one of the principal factors causing unsatisfactory films.

In this study a vacuum system of the bell jar and metal base-plate type and an oil-diffusion pump were used. Vacuum of 1×10^{-5}mm. Hg deteriorated to as high as 3×10^{-4}mm. during deposition of films owing to the outgassing of the system caused by radiated heat from the hot evaporator. In addition to those electrically heated refractory metal sources described in reference *15*, V-shaped refractory metal strips 3 in. long were used. For the evaporation of nickel or cobalt, conical baskets of tungsten wire lined with thorium oxide prepared as recommended by Swanger (*12*) were used.

Metals requiring a higher temperature or more inert source for evaporation were heated by bombardment with electrons from a heated tungsten filament. Where necessary, a crucible, for example graphite, was used. Filament-to-target voltages up to 4,000 v. D.C., unfiltered, and current to ½ amp. could be obtained. Despite the highly efficiently transmitted power of up to 2,000 w., evaporation rates were limited when ionization and consequent glow discharge of the locally concentrated metal vapor occurred. This electron bombardment technique appears useful for the fusion, where these limitations would not apply, of large quantities of a wide range of substances.

Films were deposited on a 1/16- by 2- by 1-in. Vycor or Pyrex glass or fused-quartz substrate. One-half-inch electric contacts were made by firing Hanovia platinum paste 13A on each end. Initially the slides were cleaned with a good detergent, hot

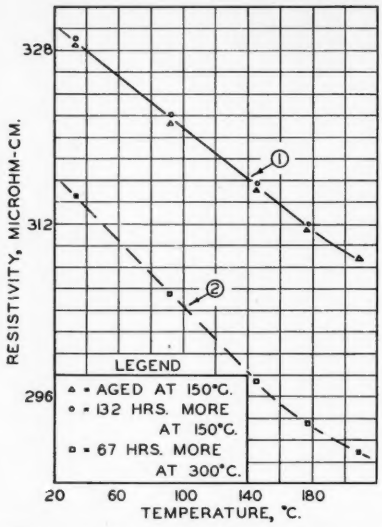

Fig. 1. Calibration of resistance of chromium films vs. temperature; (1) during 132 hr. aging at 150°C. and (2) after 67 hr. more at 300°C.

chromic acid, and boiling water. Following firing of the electrodes, the slides were cleaned with detergent and with boiling water. A shutter permitted the exclusion of all but the middle fraction of the evaporating metal vapors. The substrate could be heated in vacuum before or during the evaporation.

Films were removed from vacuum and electrical contact made through both a wire soldered to the surface of the platinum electrode and a tightly clamped brass plate. The effect of evaporation conditions and of various treatments on the electrical resistivity, temperature coefficient of resistivity, and appearance was then determined. A Wheatstone's bridge was used for the successive calibrations of the films while immersed in a Dowtherm-A bath.

EXPERIMENTAL RESULTS AND DISCUSSION

The types of metal films prepared, the method used for their evaporation, and the evaporation parameters resulting in films having the greatest stability and temperature coefficient of resistivity are listed in Table 1. Thickness was varied over the range 200 to 3,000 Å. in this study.

Thermal Properties

As a result of a large number of trial runs, a standardized procedure was adopted, and the data of Table 2 concerning the suitability of thoroughly aged films for average surface temperature measurements were obtained. Of these, nickel films are considered the most successful of the films developed. For short-term service, a few hours, they appear adequate for measurement of temperatures with accuracy approaching 0.01°C. No exceptions to good performance in the range to 200°C. were found for films 500 to 1,500 Å. thick, prepared as described on heated Vycor-glass slides. In the range up to 150°C. the performance of the tantalum film was considered the most satisfactory. The data show that further investigation is required to confirm the usefulness of platinum or molybdenum disilicide films for the measurement of higher temperatures than any of the other films measure. Since deterioration of the platinum-paste electrodes occurred at 450°C., use of chemically reduced platinum or elimination of special electrodes might improve performance. At this time use of films at temperatures in excess of 300°C. is not recommended.

Application of an evaporated magnesium fluoride film 600 Å. thick for the protection of some of these films proved moderately useful with some exceptions.

Table 2. Summary of Evaluation of Metals as Resistance Thermometers in Air

Metal	Performance up to 150°C.	220°C.	300°C.	400°C.
Au	m.s.	u.	u.	u.
Co	v.s.	s.	m.s.	u.
Cr	m.s.	m.s.	m.s.?	u.
Mo	?	u.	u.	u.
$MoSi_2$	?	?	?	?
Ni	v.s.	s.	m.s.	u.
Ni–Cr	s.	s.	u.	u.
Pt	m.s.	m.s.	m.s.	?
Ta	s.	?	u.	u.
Ti	m.s.	u.	u.	u.
Ti–Cr	u.	u.	u.	u.
V	s.	m.s.	u.	u.
W	u.	u.	u.	u.
Zir	u.	u.	u.	u.
Zir–Cr	u.	u.	u.	u.

v.s. indicates very satisfactory, < 1°C. calibration loss/32 hr. aging at indicated temperature.
s. indicates satisfactory, 1–3°C. calibration loss/32 hr. at indicated temperature.
m.s. indicates moderately satisfactory, 3–10°C. calibration loss/32 hr. aging at indicated temperature.
u. indicates unsatisfactory, >10°C. calibration loss/32 hr. aging at indicated temperature.

Mechanical and Chemical Properties of Films

Additional data were gathered in an effort to permit prediction of the behavior of these metal films under most conditions. The effect of abrasion of the films by the surface of a section of Kraft paper in a standardized procedure was determined by resistance measurement. Absolute changes in resistance and equivalent loss of temperature calibration were of interest. Suitable stability in the abrasion tests was considered indicative of probable satisfactory performance as a thermometer in gentle contact with solids. This test might also be considered to be a safe-side estimate of the calibration loss which would be caused by a rapid flow of water over the film. All the films were found to be at least satisfactory by this test. Tungsten, nickel, and cobalt suffered changes of resistance to 0.3%. Equivalent temperature-calibration loss for nickel or cobalt was, however, less than 1°C.

Films were immersed in Dowtherm-A at 190°C., 5% sodium sulfate at 90°C., and boiling water for periods of 2 hr. These liquids were chosen as typical examples of nonionic, strongly ionic, and weakly ionic systems respectively. There was no mechanical agitation of the test liquids.

Large initial changes, perhaps peculiar to the film state, were found and permitted to elapse prior to final evaluation. Performance was in specific cases disappointing. Cobalt was completely removed by boiling water; however it was not possible to distinguish between peeling of the film and chemical reaction. Vanadium suffered continual augmentation of its resistance in aqueous media. Tungsten proved highly sensitive to water and showed an unusual pattern of behavior. A platinum film which peeled in the water test was believed to have verged on nonadherence before immersion because of its thickness. The resistance of molybdenum also increased greatly in 5% sodium sulfate or water. However, zirconium, titanium, chromium, tan-

Table 1. Useful Films and Their Method of Preparation

Metal	Thickness, Å.	Evaporation method	Type of evaporator	Heated substrate	Resistivity ratio*	Temperature coefficient ratio*
Au over Bi_2O_3	450–2,500	Ohmic	Mo V	No	5.3	+0.45
Co	470–900	Ohmic	ThO_2 over W basket	Yes	2.2	+0.50
Cr	450–600	Ohmic	Ta V	No	21	−.051
			W basket	No		
Mo	≥770	Electron	None	Yes	14	+.043
$MoSi_2$	600	Electron	Mo crucible	Yes	19	−0.23
Ni	500–1,500	Ohmic	ThO_2 over W basket	Yes	2.0	+0.62
Ni	300–600	Ohmic	W wire	Yes	9	+0.15
Pt	400	Electron	ThO_2 over W basket	Yes	2.4	+0.30
Pt	1500	Electron	Graphite	Yes	2.4	+0.30
Ta	≥470	Electron	None	Yes	47	−.060
Ti	400–2,200	Ohmic	Ta V	Yes	4.3	−.032
Ti	700	Electron	Graphite	Yes	3.6	−.025
V	550	Electron	Graphite	Yes	9.3	−.001
V	500–3,500	Ohmic	Mo V	Yes	5.6	+.096
W	850	Electron	None	Yes	5.7	−.016
Zir	500–1,500	Ohmic	W wire	Yes	21	−.046

*Ratio of value of film to that of bulk.

talum, and nickel were found generally satisfactory.

The films were then subjected to a more rigorous series of specific chemical tests. The tests were performed by simple immersion of the films in the desired reagent with lead wires removed. The reagents were not agitated. Depth of penetration by the reagent was estimated from the change in electrical resistance of the film. Various concentrations of hydrochloric, sulfuric, nitric, acetic, and phosphoric acids were used as test reagents.

The general statement may be made that the films retain a corrosion resistance at least equal to that of the bulk metal. Platinum appeared to be the sole exception since a platinum film disintegrated in concentrated hydrochloric acid at room temperature within 4 hr. Most of the metals may be said to be moderately superior to the bulk metals in their resistance to acids. Chromium and titanium films proved greatly superior.

Important Film Variables

The principal portion of the behavior observed which was unique to the film state could be explained by the variations in properties associated with the film. These properties were found to be chemical inertness of the metal, thermal aging to which the film had been exposed, thickness of the film, temperature of the substrate during deposition, type of evaporator used, and the atomic number of the metal.

Necessarily, the chemical resistance of the particular metal was the most important factor in determining long-range film stability. The original choice of metals consequently was dictated largely by this consideration.

The severity and duration of the thermally accelerated aging to which a film has been exposed cause unexpected changes. What was presumed to be a structural instability of fresh films was rapidly eliminated by aging, as evidenced by resistance and resistance-temperature-coefficient changes. However, this appeared to be a resistance-driving-force relationship, for exposure to a new maximum temperature or a temperature close to the previous maximum caused elimination of an additional increment of structural instability. Nickel was typical of metals whose films showed an initial rapid resistance decrease resulting from structural stabilization. Vanadium was typical of another type showing a diminishing rate of resistance increase.

Figure 1 illustrates these processes for a chromium film. It can be seen that the next higher temperature range has introduced a large rapid decrease in resistance.

However, this steady state rate was not wholly dependent upon chemical resistance to the surroundings. For some metals slow evolution, presumably also structural, may oppose the increase in resistance caused by corrosion. It is not considered impossible that this slower resistance decrease, not detected with all metals, contributed to the high steady state stability of nickel.

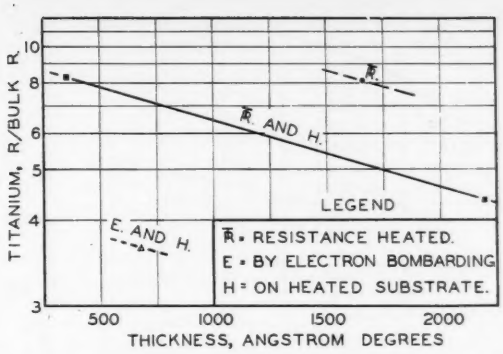

Fig. 2. Effect of varying deposition conditions on ratio of film resistivity to bulk-metal resistivity vs. thickness for titanium.

The magnitude of this slow type of evolution of properties was greatest for 400- to 700-Å. chromium films. With the extended knowledge of the behavior of these films (*10*), it is possible to obtain a stable film by using the foregoing decrease in resistance to offset oxidation-caused increases at temperatures varying with their age.

Protective magnesium fluoride films appear to reduce the rate of this slow type of evolution and may be used as a factor determining the range of greatest stability of the chromium films suggested above.

Variation of film thickness also permits unusual control over film behavior. Graphs presented in the prior publication (*15*) and the additional data obtained in this study have been combined to fit a curve by the method of least squares for ratio of resistance of film to that of the equivalent bulk metal vs. thickness with a correlation coefficient of 0.97. The relation becomes

$$\text{ratio} = 5{,}700(t)^{-0.85}; \quad 150 < t < 1{,}500 \text{ Å}.$$

and applies only to chromium films prepared on unheated substrates by evaporation from conical crucibles of tungsten wire. This exponential relation is typical of thin films. In a like manner most properties of thick films may be said to approach those of the bulk metal. The extent of the irreversible changes in the resistance of fresh thick films is less than that of thin films, for which the extreme case is evolution to an infinite resistance. The rapidity of the completion of this change in thick films is also favorable.

The behavior of a tantalum film particularly demonstrates the satisfactory fit of proposed concepts of structural evolution to this thickness-stability relation. This film had been found increasingly stable in successive aging periods at 220°C. The film was heated 2 hr. at 300°C. with minor resistance change. Heated again for 38 hr. at 300°C., it increased many hundredfold in resistance. According to current theory, structural evolution in the film proceeded at 300°C. to the point of agglomeration of the continuous film of metal into aggregates, forming a state found in electron microscope studies typical of films of thickness less than a maximum, dependent on the degree of annealing of the film. The maximum varied from 100 Å. for unannealed to 500 Å. for well-annealed films. This film was approximately 400 Å. thick. Utilization of a film several hundred Ångstroms thicker should permit aging to stability at 300°C. without agglomeration.

Table 3. Adherence Limits for Chromium Films

Type of evaporator	Substrate condition	Maximum thickness, Å
Tungsten cone	Unheated	1,100
Tantalum V	Unheated	>2,500
Tantalum V	Unheated	<3,100
Tungsten cone	Heated	1,650

When they were also found to have greater steady state stability, emphasis was shifted to the thicker films. Adherence then became a dominant problem, for although films of most metals are strongly adherent when thin, at greater thicknesses the film may peel spontaneously from the base.

Two-layer films from zirconium, titanium, or nickel over chromium were prepared, greater adherent thicknesses and better, more stable electrical properties being sought. Chromium is considered one of the most adherent of metals and hence was included in each pair. Though in general better electrical properties were not forthcoming, improvement in adherence was obtained, which was outstanding in the case of nickel.

Another variable, the substrate temperature during evaporation, is even more important in determining the maximum adherent thickness of a metal. Zirconium films of any thickness could be easily wiped off their substrates if they

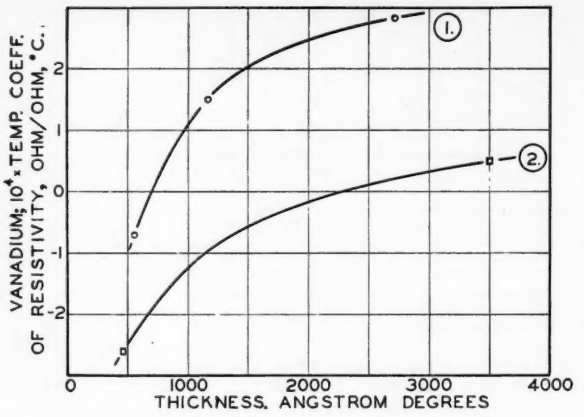

Fig. 3. Temperature coefficients of resistivity vs. thickness for vanadium films similar in all respects except that curve-1 films were deposited on heated substrates and curve-2 films on unheated substrates.

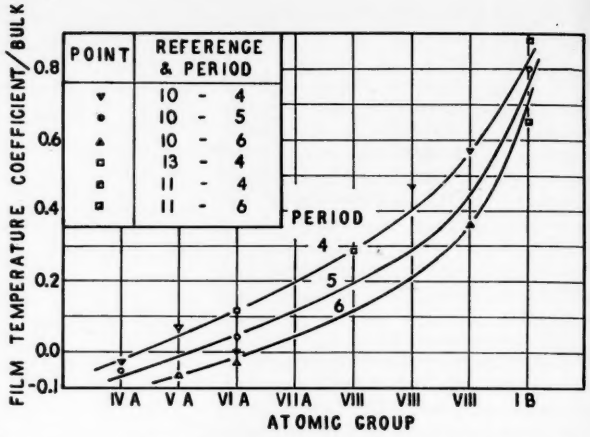

Fig. 4. Ratio of film temperature coefficient of resistivity to equivalent bulk-metal coefficient vs. atomic number.

had not been heated during deposition; on a heated substrate they became strongly adherent. Such improvement was true for many metals. The effect may be detected in Table 3.

This variable also strongly influences the film's electrical properties. Though the resistance of one reasonably thick film on an unheated substrate quickly became infinite and is not plotted, Figure 2 indicates that at equal thicknesses the film deposited on an unheated substrate has a greater resistance. The effect of this factor on the temperature coefficient of resistivity is best shown by the results for vanadium metal, presented in Figure 3. Coefficients may be seen to be significantly more positive for films prepared on heated substrates.

That these effects are not purely the result of the excellent outgassing achieved by heating the substrate is evidenced by the study of vanadium films. Substrates for some films were heated in vacuum and permitted to cool prior to deposition of the film. Only those deposited on hot substrates possessed the advantages enumerated above.

Film properties are strongly conditioned by the type of evaporator used in its preparation. This fact has led to the conclusion that contamination of the film occurs by evaporation of a minute portion of the refractory metal composing the evaporators. Outstanding is the dependence of the maximum adherent thickness on the type of evaporator. Chromium films, prepared by evaporation from tantalum V's, have a higher limiting thickness than those prepared from conical evaporators of tungsten wire. In all likelihood tantalum evaporators run hotter because of smaller contact area between them and the chromium and because of less likelihood of appreciable current flow through the chromium. Hence they are more suspect as sources of contamination. Table 3 clearly demonstrates this variation in limiting thickness.

Similarly the effect of type source on electrical properties appears to stem from contamination by the evaporator. In Figure 2 the curve of the ratio of the resistivity of the film to that of the bulk metal vs. thickness for titanium films prepared from tantalum evaporators lies above that for films prepared by electron bombardment of metal in a carbon crucible. In the latter case direct heating of the metal can be expected. Similar results were obtained for chromium, and, in addition, improvement in the temperature coefficient of resistivity for chromium occurred. Results for vanadium were uncertain.

An interesting correlation, presented in Figure 4, has been found between the temperature coefficients of resistivity of fresh films of this study and of other workers and the atomic number of the metal. Prediction of the temperature coefficient of unevaluated metals may be possible from this curve.

PRACTICAL USE OF FILMS

New techniques are available in assembling films as resistance thermometers and as elements in circuits. Evaporated films of chromium, molybdenum, cobalt, nickel, and molybdenum disilicide only 500 to 1,500 Å. thick on glass have been found satisfactory electrodes to which lead wires may be soft-soldered. It should be possible to increase the variety of metal films satisfactorily wetted by the use of solders of varying compositions. The chemical resistance of the films and ease of application as compared with fired platinum make them ideal for use as electrodes for the attachment of lead wires to a film of the same or different metal under severe or special conditions.

Protecting and insulating evaporated mineral films resulting in cumulative thicknesses exceeding the adherence limit of the metal have been successfully applied. Practical application of their properties should be possible in film circuits.

When the films are in use as thermometers, repeated complete calibration would not be necessary. During the aging of a film at temperatures below the maximum in its history, the successive calibration curves are simply displaced without affecting temperature coefficients. Since all the films considered for thermometers have linear or nearly linear calibration curves, a series of parallel lines results, each of which may be determined by a single new calibration point.

Where surface heaters of negligible bulk and known output or where resistances of low temperature coefficient are desired, evaporated metal films may be used. The near-zero temperature coefficients of resistivity of a wide range of thicknesses of chromium films prepared on heated substrates make them particularly suited for this purpose. Films of other metals fill this criterion when prepared in thicknesses at which their temperature coefficients change sign. Vanadium (*see* Figure 3) would be an unusually good metal of this type because its coefficient changes sign at a relatively great thickness and the stability associated with thick films would be retained.

SUMMARY

A number of types of evaporated metal films 400 to 3,000 Å. thick deposited on glass surfaces have been made that are useful as thermosensitive elements in air over ranges of temperature and periods of time far exceeding those previously offered. Nickel and cobalt films showed high sensitivity with usefulness at temperatures up to 300°C. as well as outstanding stability. Chromium, titanium, tantalum, gold, vanadium, and chromium over nickel films proved useful to intermediately high temperatures. Platinum and molybdenum disilicide films show promise of being suitable with further development at even higher temperatures.

These films as resistance thermometers may displace conventional devices lacking versatility and reliability.

The technique for evaporation by electron bombardment permitted the evaluation of the electrical properties of thick films of the refractories, molybdenum, tungsten, and tantalum.

The performance of films has been evaluated in three typical hot liquids, organic, weakly ionic, and strongly ionic in nature, to permit predictions of their behavior in other media. These and tests of their abrasion resistance indicate that suitable selected films should be rugged enough for service in most liquids, in gentle contact with solids, and in contact with gases and vapors.

Chemical behavior against mineral acids likewise has been compared with the behavior of the bulk metal. Generally films have been found to be moderately to markedly superior.

Data have been collected concerning the resistivities and temperature coefficients of resistivity of these films. The important variables causing behavior unique to the film state have been outlined. Deposition of metal on a substrate at 200°C. proved strikingly effective in producing films of superior adherence with greater stability and electrical properties closer to those of the bulk metal. The temperature coefficients of thick films show an interesting correlation with their atomic number.

Techniques and recommendations for the practical use of evaporated films have been outlined.

LITERATURE CITED

1. Aron, A., *Ann. phys.*, **1**, 361 (1946).
2. Baker, E. M., and U. Tsao, *Ind. Eng. Chem.*, **32**, 1115 (1946).
3. Baus, B., Ph.D. thesis, Cornell Univ., Ithaca, N. Y. (1949).
4. Bendersky, D., *Mech. Eng.*, **75**, 117 (1953).
5. Bradley, L. C., *Rev. Sci. Instr.*, **24**, 219 (1953).
6. Colburn, A. P., and O. E. Hougen, *Ind. Eng. Chem.*, **22**, 522 (1930).
7. Hackeman, P., Hermann Goring Air Research Inst., Germany (Jan. 27, 1941).
8. Lessing, L. P., *Sci. American*, **191**, No. 1, 37 (1954).
9. Othmer, E. G., and H. B. Coats, *Ind. Eng. Chem.*, **20**, 124 (1928).
10. Simpson, T. B., Ph.D. thesis, Cornell Univ., Ithaca, N. Y. (1954).
11. Suhrman, R., *Z. Physik*, **103**, 133 (1936).
12. Swanger, W. H., and G. R. Caldwell, *J. Research, Natl. Bur. Standards*, **6**, 1131 (1931).
13. Topper, L., Ph.D. thesis, Cornell Univ., Ithaca, N. Y. (1952).
14. Van de Waart, R., Ph.D. thesis, Cornell Univ., Ithaca, N. Y. (1940).
15. Winding, C. C., B. Baus, and L. Topper, *Ind. Eng. Chem.*, **47**, 386 (1955).

Presented at A.I.Ch.E. Louisville meeting

Chemical Reactor Stability and Sensitivity

II. Effect of Parameters on Sensitivity of Empty Tubular Reactors

OLEGH BILOUS and NEAL R. AMUNDSON

University of Minnesota, Minneapolis, Minnesota

In this paper extensive calculations on the quasi isothermal tubular reactor are presented. Temperature and concentration profiles were obtained on an analogue computer (R.E.A.C.). The calculations tend to show that there are regions of operation in which the reactor effluent is very sensitive to operating conditions. For example, it is shown that in some regions of operation a small change in the heat transfer coefficient at the reactor wall or a small dilution of the feed will produce large changes in the effluent. In such cases the reactor is said to exhibit *parametric sensitivity*. It is shown analytically that this sensitivity may be predicted by analyzing the frequency response or transient response of the reactor approximated by a local linearization. This linearization requires complete solutions of the steady state problem. Semiquantitative results are then obtained for the regulation required from a given specification of product limits. The frequency-response analysis should be useful in connection with the control problem.

If the reactor is fed partially with a recycle stream, then experience with electrical systems indicates that the possibility of instability exists. It is shown that at least theoretically these instabilities do exist, and a method based on the transfer function is developed for derivation of criteria of stability or instability.

In Part I of this paper the stability of the well-agitated reactor was examined in detail and criteria were developed based on the steady state values so that reactor behavior after perturbations, either small or large, might be predicted. This problem was not difficult because the transient behavior is described by ordinary differential equations. The treatment of stability problems for chemical systems exactly parallels the treatment of problems in nonlinear mechanics. This is fortunate as the theory therefore must only be restated in terms of the parameters of the chemical system. When one considers the tubular reactor, however, the problem is considerably more difficult, because transient reactor behavior is described by partial-differential equations which are nonlinear, and no adequate method of solution or estimate of the error in their linearization is available. Thus the treatment given in the following must be considered unsatisfactory from a rigorous point of view although it will be shown that machine solutions of the rigorous equations agree in a semiquantitative way with the solutions of the approximated equations. This may be

Olegh Bilous is at the Laboratoire Central des Poudres, Paris, France.

Part I of this article appeared in the December, 1955, issue of the *A.I.Ch.E. Journal*.

considered as a partial confirmation of the mathematical theory by the engineer.

The solutions to problems for the quasiisothermal tubular reactor have not been carried out in detail in the literature, although one recent paper (*4*) illustrated in a qualitative way some aspects of the problem. In general, in the past reaction systems have been assumed to be adiabatic or isothermal, the calculations for which are not difficult. In the quasiisothermal case there are two differential equations for the steady state, an energy balance and a mass balance. Even at the steady state these will be nonlinear and so calculation is not a simple task. As there seemed to be no general discussion of reactor behavior as the parameters of the system were varied, it was decided to make an extensive series of calculations in order to investigate anomalous behavior, if any. It should be stressed that the physical model used is a very simple one, all complicating factors having been neglected. This may seem rash, but the purpose of this paper is to show that complications may arise in very simple systems and to illustrate how such complications might be handled. Additional factors may be easily taken into consideration. It is generally true that if the basic problem has been well set, marginal corrections result from adding to the problem such factors as variation in velocity, heat capacities, heat transfer coefficients, pressure drop, and radial and longitudinal mixing. The addition of packing in the reactor, however, will increase the complications tremendously.

COMPUTER SOLUTIONS

The simple reaction $A \rightarrow B$, which is first order and irreversible, with heat of reaction ΔH, may be carried out in an unpacked tubular reactor whose ambient temperature is constant at T_W. The concentration of A at any point along the reactor may be x and the temperature y. Then a simple mass and heat balance will be

$$\frac{Dx}{D\theta} = \frac{\partial x}{\partial \theta} + v\frac{\partial x}{\partial \tau} = -pe^{-a/y}x \quad (1)$$

$$\frac{Dy}{D\theta} = \frac{\partial y}{\partial \theta} + v\frac{\partial y}{\partial \tau} = K(T_w - y) + Qpe^{-a/y}x \quad (2)$$

where

$$k = p\exp\left(-\frac{a}{y}\right), \qquad a = \frac{E}{R}$$

$$K = \frac{2h}{rc\rho}$$

$$Q = \frac{-\Delta H}{c\rho}$$

with reactor radius r, wall heat transfer coefficient (over-all) h, c the specific heat, and ρ the density. Equations (1) and (2) describe the transient behavior of the system. The steady state is described by

$$v\frac{dx_s}{d\tau} = -k_s x_s \quad (3)$$

$$v\frac{dy_s}{d\tau} = K(T_w - y_s) + Qk_s x_s \quad (4)$$

where the subscript s denotes the steady state value. k_s still depends upon the exponential variation of the temperature. Solutions to these equations may be found with the aid of the analogue computer (R.E.A.C.). Families of curves for different values of the parameters may be obtained without difficulty once the equations have been programmed for the machine, and these have been secured.

In Figure 1*a* is shown the effect of changes in the ambient temperature on the temperature profile, all other parameters being fixed. Over a small range of wall temperature the character of the profile changes appreciably. Figure 1*b* is the corresponding concentration profile. These two sets of plots were made with an activation energy of 11,250 cal./mole. The reaction is exothermic. In Figure 2*a* and *b* the same plots are made with doubled activation energy and frequency factor and with the other parameters changed somewhat. These changes have made the reactor behavior more pronounced. There is a critical change in the temperature and concentration profile as one moves from 335° to 337.5°K.

Figure 3*a* and *b* shows that the endothermic reaction displays no such unusual behavior when graphs with similar coordinates are prepared.

Figure 4*a* and *b* shows the effect of dilution of the feed on temperature and concentration profiles, and once again there is a critical value of the feed concentration above and below which reactor profiles are appreciably different. Figure 5 repeats the same graphs for an endothermic reaction but no unusual condition seems to exist.

Figure 6*a* and *b* shows the effect of small changes of the reactor-wall heat transfer coefficient. Small changes in the coefficients produce a marked change in the conversion. This effect is accentuated as the activation energy increases.

Thus from this rather extensive series of profiles one can see that certain conditions may occur under which reactor operation, without being unstable in the literal sense, will be extremely sensitive to small changes in the operating characteristics of the system. Changes such as gradual fouling of heat transfer surfaces or reactor surfaces or poor control of temperatures or concentrations might make continuous operation extremely difficult. Since these computations have shown that operation is very sensitive to the parameters of the system in some regions, this phenomenon will be referred to as *parametric sensitivity*.

To make a more formal study of the situation one can calculate the derivative of the temperature or concentration with respect to one of the parameters; for example,

$$v\frac{d}{d\tau}\left(\frac{dx_s}{dT_w}\right) = -k_s\frac{dx_s}{dT_w} - \frac{a}{y_s^2}k_s x_s\frac{dy_s}{dT_w}$$

$$v\frac{d}{d\tau}\left(\frac{dy_s}{dT_w}\right) = K - \left(K - Qk_s\frac{ax_s}{y_s^2}\right)\frac{dy_s}{dT_w} + Qk_s\frac{dx_s}{dT_w}$$

where these are differential equations in the derivatives with respect to the ambient temperature. These derivatives may be generated on the R.E.A.C. and this has been done in Figure 7. This plot corresponds to the temperature and concentration profiles given in Figure 2*a* and *b* and shows, quite naturally, that the dependence on wall temperature is most strong near the hot point.

In order to show that parametric sensitivity is not due to a mathematical change in the nature of the solution of the steady state equations, a phase space representation (*6*) of the temperature profiles was made for the case of feed dilution. This phase space representation was obtained by plotting the temperature gradient against the temperature. If there is a change in the nature of the solution a separatrix should exist between the two families of solutions if such exist. Figure 8*a* and *b* shows phase space trajectories which form a continuous family and there seems to be no evidence for a separatrix.

Parametric sensitivity in an industrial reactor might manifest itself in many ways. If a reactor is designed for a high conversion near a region of sensitivity, reactor-product quality might be difficult to control. On the other hand a side reaction to the one of interest might exhibit such a character, in which case yields of desired products would fall off. In a reaction such as a controlled oxidation it may be necessary to operate at a low temperature to produce a partially oxidized product. Sensitivity in this case might produce an overoxidized product.

ANALYTICAL TREATMENT OF PARAMETRIC SENSITIVITY

It is clear that it would be desirable to have methods for the prediction of parametric sensitivity without the necessity of plotting many reaction paths. The task of hand calculating reaction paths for the quasiisothermal reactor is not an easy one although on the analogue or digital computor it is not difficult. A numerical scheme, either by hand or on a digital

computer, inevitably involves a step-by-step integration down the reactor. This would not be difficult in the insensitive region but in the region of sensitivity the size of the steps would of necessity be small as by the very nature of parametric sensitivity the future course of the calculation depends strongly on small inaccuracies occurring during the course of the computation. Because of this difficulty in reproducing a multitude of reaction paths the problem will now be considered from an analytical point of view. The general method of attack is to calculate the response of the reactor to a sinusoidal input or to a step-function input. If this response can be calculated easily, then sensitivity may be predicted. It is the purpose of this section to show that such a computation is not difficult. From the different point of view of system engineering it is useful to know the harmonic response of a reactor. This has been investigated by Deisler and Wilhelm (*2*) and by Kramers and Alberda (*5*) but with a slightly different end in view.

If a first-order reaction is carried out isothermally in a tubular reactor, then

$$\frac{\partial x}{\partial \theta} + v\frac{\partial x}{\partial \tau} = -kx$$

If $\bar{x}$ is the Laplace transform of x and if the initial condition of the reactor is taken as zero,

$$\frac{d\bar{x}}{d\tau} = -(k+s)\frac{\bar{x}}{v}$$

where s is the transform variable.

If the input is sinosoidal and given by

$$x_i = A' \sin \omega\theta$$

then

$$\bar{x}_i = A'\mathfrak{L}(\sin \omega\theta) = A'S$$

and so

$$\bar{x} = e^{-kL/v}e^{-sL/v}A'S$$

It is clear from the property of inverse transforms that the amplitude ratio of input and output signals is

$$e^{-kL/v}$$

and that there is a phase lag in the sinusoidal output equal to

$$\frac{\omega L}{v}$$

The output may be written

$$x_0 = Ae^{-kL/v}\sin\left(\omega\theta - \frac{\omega L}{v}\right)$$

On the other hand if the input is a step function

$$x_i = \begin{cases} 0 & \theta < 0 \\ \epsilon & \theta > 0 \end{cases}$$

then

$$\bar{x} = e^{-kL/v}\frac{e^{-sL/v}}{s}\epsilon$$

and the reactor output is

$$x_0 = e^{-kL/v}\epsilon, \qquad \theta > \frac{L}{v}$$

In the language of control theory the function

$$\Omega(s) = e^{-(k+s/v)L}$$

is called the *transfer function.*

The generalization to more complicated isothermal systems is obvious and may be carried out by the matrix method (*1*). Instead, however, the quasiisothermal system considered in the earlier part of this paper will be treated. In Equations (1) and (2)

$$x = x_s(\tau) + X(\tau, \theta)$$

$$y = y_s(\tau) + Y(\tau, \theta)$$

where X and Y are the transient parts of x and y and satisfy, after the first-order linearization is taken about the steady state, the equation

$$\frac{\partial X}{\partial \theta} + v\frac{\partial X}{\partial \tau} = -k_s X - k_s\frac{ax_s}{y_s^2}Y \quad (5)$$

$$\frac{\partial Y}{\partial \theta} + v\frac{\partial Y}{\partial \tau} = Qk_s X + \left(Qk_s\frac{ax_s}{y_s^2} - K\right)Y \quad (6)$$

These equations are somewhat more complicated than might appear at first sight, as the coefficients of X and Y on the right-hand side are not constants but are complicated functions of the distance along the reactor as given by the steady state solutions. Thus on *a priori* grounds a simple solution might not be expected. Note also that the type of linearization used to derive Equations (5) and (6) does not involve a single linearization throughout the whole reactor but is a local linearization in which a new linearization is taken at each point along the reactor.

If the matrix $F(s, \tau)$ is defined by

$$\mathbf{F}(s, \tau) = -\begin{bmatrix} \dfrac{k_s + s}{v} & \dfrac{k_s a x_s}{v y_s^2} \\ \dfrac{-Qk_s}{v} & \dfrac{1}{v}\left[K - Qk_s\left(\dfrac{ax_s}{y_s^2}\right) + s\right] \end{bmatrix} \quad (7)$$

and if

$$\mathbf{M} = \ln \boldsymbol{\Omega}(s) = \int_0^L \mathbf{F}(s, \tau)\, d\tau$$

from which

$$\mathbf{M} = -\begin{bmatrix} \displaystyle\int_0^L \frac{k_s + s}{v}\, d\tau & \displaystyle\int_0^L \frac{k_s a x_s}{v y_s^2}\, d\tau \\ \displaystyle -\int_0^L \frac{Qk_s}{v}\, d\tau & \displaystyle\frac{1}{v}\int_0^L \left(K - Qk_s\frac{ax_s}{y_s^2} + s\right) d\tau \end{bmatrix} \quad (8)$$

---

then let it be assumed that the solution may be expressed in the form

$$\bar{\mathbf{V}}_o = \boldsymbol{\Omega}(s)\bar{\mathbf{V}}_i = e^{\mathbf{M}}\bar{\mathbf{V}}_i$$

where $\mathbf{V}_o$ and $\mathbf{V}_i$ are the matrices of the output and input, respectively, and $\bar{\mathbf{V}}_o$ and $\bar{\mathbf{V}}_i$ are their respective Laplace transforms. Thus

$$\mathbf{V}_0 = \begin{pmatrix} X_o \\ Y_o \end{pmatrix}, \qquad \mathbf{V}_i = \begin{pmatrix} X_i \\ Y_i \end{pmatrix}$$

In these formulas $\bar{\mathbf{V}}_o$ is the transform of the output for an arbitrary input. From transfer function theory the output signal caused by a sinusoidal input signal is given in complex form by

$$\mathbf{V}_o = \boldsymbol{\Omega}(j\omega)\mathbf{V}_i$$

and X_i and Y_i are complex sinusoidal inputs on the concentration and temperature of the same frequency but of different or the same amplitudes.

Because of the structure of the matrix M it can be separated into the sum of two matrices as

$$\mathbf{M} = \frac{-sL}{v}\mathbf{I} + \mathbf{N} \quad (9)$$

where $\mathbf{I}$ is the unitary matrix and

$$\mathbf{N} = -\begin{bmatrix} \displaystyle\int_0^L \frac{k_s}{v}\, d\tau & \displaystyle\int_0^L \frac{k_s a x_s}{v y_s^2}\, d\tau \\ \displaystyle -\int_0^L \frac{Qk_s}{v}\, d\tau & \displaystyle\frac{1}{v}\int_0^L \left(K - Q\frac{k_s a x_s}{y_s^2}\right) d\tau \end{bmatrix} \quad (10)$$

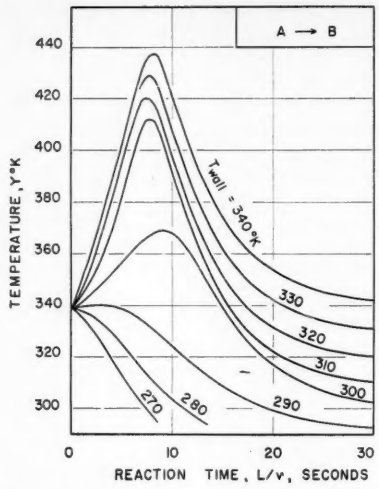

Fig. 1*a*. Temperature profiles in a tubular reactor; effect of wall temperature. E = 11,250, p = 1.59 × 10^{13}, x_i = 0.020, Q = 10,000, K = 0.20, T_i = 340°K.

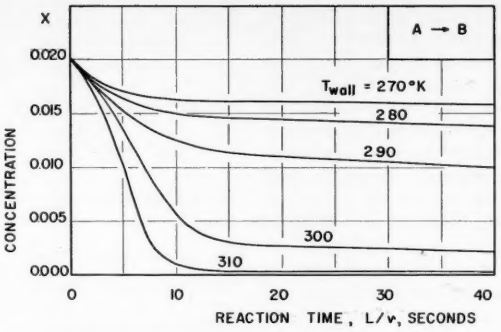

Fig. 1*b*. Concentration profiles in a tubular reactor; effect of wall temperature. Data are same as in Figure 1*a*.

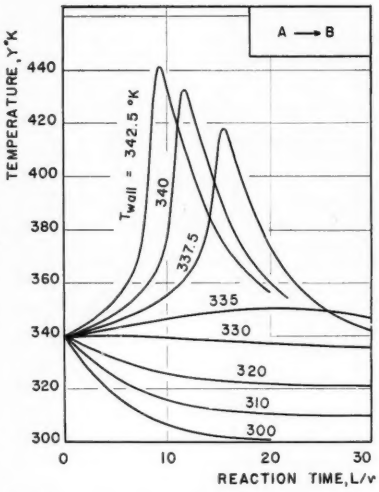

Fig. 2*a*. Temperature profiles in a tubular reactor; effect of wall temperature. E = 22,500, p = 3.94 × 10^{12}, x_i = 0.20, Q = 7,300, K = 0.20, T_i = 340°K.

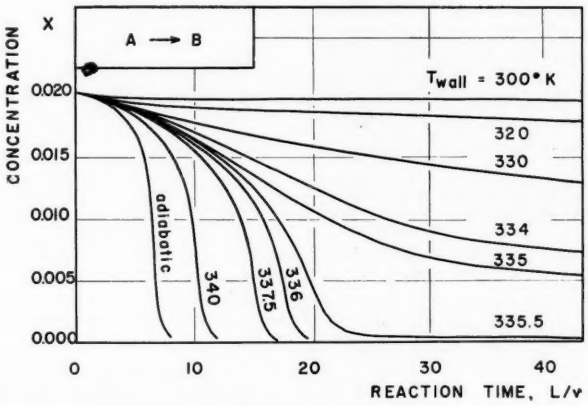

Fig. 2*b*. Concentration profiles in a tubular reactor; effect of wall temperature. Data are the same as in Figure 2*a*.

Now the matrix

$$\exp\left[\alpha\begin{pmatrix}1 & 0\\ 0 & 1\end{pmatrix}\right] \tag{11}$$

may always be written

$$e^{\alpha}\begin{pmatrix}1 & 0\\ 0 & 1\end{pmatrix} \tag{12}$$

and by Sylvester's theorem (*1, 3*) a second-order square matrix may be decomposed as

$$e^{\begin{pmatrix}A & B\\ C & D\end{pmatrix}} = e^{\frac{A+D}{2}}\frac{\sinh\Delta}{\Delta}\begin{bmatrix}\frac{A-D}{2}+\frac{\Delta}{\tanh\Delta} & B\\ C & \frac{D-A}{2}+\frac{\Delta}{\tanh\Delta}\end{bmatrix} \tag{13}$$

where

$$2\Delta = \sqrt{(A-D)^2+4BC}$$

Thus the function $\Omega(s)$ may be written in the form

$$\Omega(s) = e^{-sL/v}\begin{pmatrix}\alpha & \beta\\ \gamma & \delta\end{pmatrix} = e^{-sL/v}\mathbf{R}$$

where $\alpha, \beta, \gamma, \delta$ are implicitly defined by Equation (13). Therefore

$$X_0 = (\alpha X_i + \beta Y_i)e^{-j\omega L/v}$$

$$Y_0 = (\gamma X_i + \delta Y_i)e^{-j\omega L/v}$$

These are the complex responses X_o, Y_o to complex feed excitations X_i, Y_i of the feed concentration and temperature respectively. The phase angle is still $\omega L/v$, which is a lag behind the input signal. If the amplitudes of the input signals are θ and η, respectively, on concentration and temperature, then the amplitudes of the output signals are $\alpha\epsilon + \beta\eta$ and $\alpha\epsilon + \delta\eta$, respectively, and hence there is an interaction between the two signals. In complex form these are written

$$X_o = (\alpha\epsilon + \beta\eta)e^{-j\omega(\theta-L/v)}$$

$$Y_o = (\gamma\epsilon + \delta\eta)e^{-j\omega(\theta-L/v)}$$

Case A: 335°K.

L/v	0	5.04	12.60	21.50	30.20	35.20	40.50
x	0.0200	0.0190	0.0151	0.0107	0.0070	0.0065	0.0057
y	340	343	346	351	347	343	340

Case B: 337.5°K.

L/v	0	2.50	5.04	7.55	10.10	12.60	13.82	15.10	15.90
x	0.0200	0.0195	0.0190	0.0175	0.0158	0.0130	0.0105	0.0050	0.0012
y	340	342	346	350	355	365	377	410	418

If one supposes that the input is not sinusoidal but a step function, then

$$\overline{\mathbf{V}}_o = \frac{\boldsymbol{\Omega}(s)}{s}\mathbf{V}_i$$

in which $\mathbf{V}_i$ is the matrix of the two input steps. Then it follows that

$$\overline{\mathbf{V}}_o = \frac{e^{-sL/v}}{s}\begin{pmatrix}\alpha & \beta\\ \gamma & \delta\end{pmatrix}\mathbf{V}_i$$

and so

$$X_o = \alpha\epsilon + \beta\eta, \qquad \theta > \frac{L}{v}$$

$$Y_o = \gamma\epsilon + \delta\eta, \qquad \theta > \frac{L}{v}$$

with ϵ and η as steps in the influent.

Thus it is clear that there is no essential difference in the two methods; response to a sinusoidal or step input leads to the same conclusion.

	Case A	*Case* B
I	1.253	2.820
J	0.00135	0.001486

Case A

$$\boldsymbol{\Omega}(j\omega) = e^{-40.50j\omega}\begin{pmatrix}-1.267 & 0.000021\\ -142 & -1.308\end{pmatrix}$$

Case B

$$\boldsymbol{\Omega}(j\omega) = e^{-15.90j\omega}\begin{pmatrix}-35.0 & -.00924\\ 128{,}000 & 30.4\end{pmatrix}$$

In order to determine whether there is a basic difference between temperature profiles or concentration profiles at different parametric values two steady states will be treated, those at 335° and 337.5° in Figure 2*a* and *b*. The pertinent numerical data are

E = 22,500 cal./g. mole
p = 3.94×10^{12} min.$^{-1}$
Q = 7,300 (cu. cm.)(°C.)/mole
K = 0.200 min.$^{-1}$
T_i = 340°K. (feed temperature)
x_i = 0.020 mole/liter (feed concentration)

With a wall temperature of 337.5°K. the temperature of the reactant stream rises rapidly to 418°K., and at this point conversion is fairly complete. For a wall temperature of 335° there is only a moderate rise in temperature and the reaction proceeds slowly. From Figure 2*a* and *b* the data of cases *A* and *B* may be read:

Two integrals enter the expression for $\boldsymbol{\Omega}(s)$:

$$I = \frac{1}{v}\int_0^L k_s\,d\tau = -\frac{1}{v}\int_0^L \frac{v}{x_s}\,dx_s = \ln\frac{x_{initial}}{x_{final}}$$

$$J = \frac{1}{v}\int_0^L \frac{k_s a x_s}{y_s^2}\,d\tau = \int_{x_{final}}^{x_{initial}} \frac{a\,dx_s}{y_s^2}$$

With these definitions

$$\begin{pmatrix}A & B\\ C & D\end{pmatrix} = \begin{pmatrix}-I & -J\\ QI & -\dfrac{KL}{v} + QJ\end{pmatrix}$$

From the foregoing data

In order to illustrate better the meaning of the quantities thus obtained, the amplitudes of the output signals or, alternatively, the steady state value resulting from step inputs, caused by an input signal of 1% of the steady state values applied on either feed temperature or feed concentrations, was calculated. For simplicity the notation (Y_o, X_i) will designate the amplitude of the outlet temperature variation due to a 1% sinusoidal change in the feed concentration. The amplitudes are independent of the excitation frequency. (*See* Table 1.)

From an inspection of these values it is apparent that operation under Case *B* is highly sensitive to small variations in the operating conditions and that Case *A* has no unusual features. This was expected once the whole series of steady state profiles had been calculated. It seems therefore that sensitivity can be predicted from the calculation of a single profile. It should be remarked that the method presented here is a linearization and results are valid only for infinitesimal signal amplitudes on the steady state values. Thus the results in Case *B*, while they indicate correctly the amplification of an infinitesimally small input signal, should not be considered correct when applied to a 1% signal. However, the prediction of sensitivity even in a qualitative way, if one is not prepared to accept the quantitative result, is of some value.

TABLE 1

	Case *A*		Case *B*	
	Absolute value	%	Absolute value	%
(X_o, X_i)	2.53×10^{-4}	4.4	70.0×10^{-4}	580
(X_o, Y_i)	7×10^{-5}	1.2	0.0317	2,600
(Y_o, X_i)	0.028°K.	0.0	25.6°K.	6.1
(Y_o, Y_i)	4.45°K.	1.3	103°K.	25

In this illustration the output signals on temperature and feed reactant concentration resulting from a given input signal were found. From a design point of view it is much more interesting to determine the effect of temperature and feed concentration signals on the product concentration signal. Although the method described below is not needed on the example used, the method is needed on more complicated systems. If $Z(\tau, t)$ is the product signal, then the linearized equation for Z is

$$\frac{\partial Z}{\partial\theta} + v\frac{\partial Z}{\partial\tau} = k_s X + \frac{k_s a x_s}{y_s^2}\,Y \qquad (14)$$

The matrix $\mathbf{M}$ for this problem when Equations (5), (6), and (14) are combined is

$$\mathbf{M} = -\begin{pmatrix}\displaystyle\int_0^L \frac{k_s+s}{v}\,d\tau & \displaystyle\int_0^L \frac{k_s a x_s}{v y_s^2}\,d\tau & 0\\ \displaystyle\int_0^L -\frac{Qk_s}{v}\,d\tau & \displaystyle\frac{1}{v}\int_0^\tau \left(K - Q\frac{k_s a x_s}{y_s^2} + s\right)d\tau & 0\\ \displaystyle -\int_0^L \frac{k_s}{v}\,d\tau & \displaystyle\int_0^L \frac{k_s a x_s}{v y_s}\,d\tau & \displaystyle\int_0^\tau \frac{s}{v}\,d\tau\end{pmatrix} \qquad (15)$$

and

$$\boldsymbol{\Omega}(s) = e^{-sL/v}\begin{pmatrix}\alpha & \beta & 0\\ \gamma & \delta & 0\\ I\alpha + J\gamma & I\beta + J\delta & 1\end{pmatrix}. \qquad (16)$$

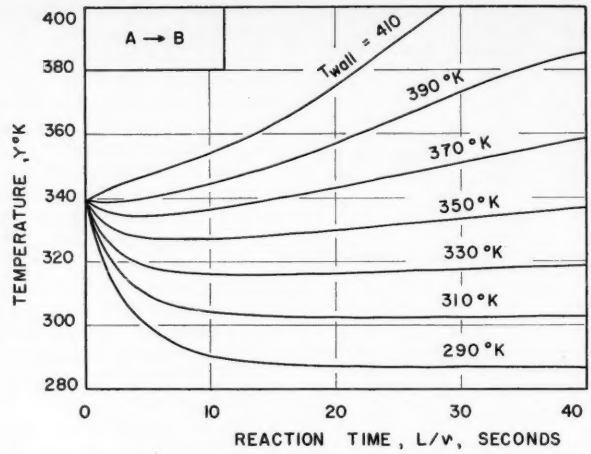

Fig. 3a. Temperature profiles in a tubular reactor; effect of wall temperature on an endothermic reaction. E = 11,250, p = 1.59 × 10^{13}, x_i = 0.20, Q = −10,000, T_i = 340°K., K = 0.20.

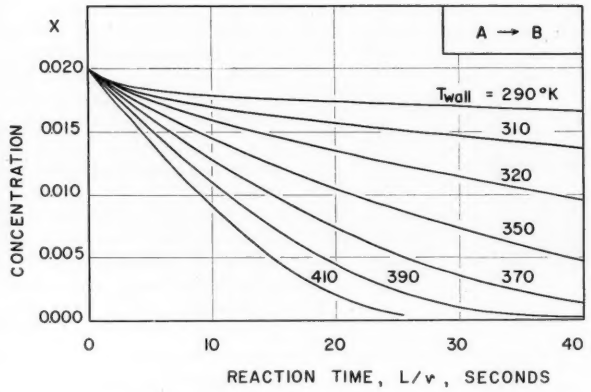

Fig. 3b. Concentration profiles in a tubular reactor; effect of wall temperature on an endothermic reaction. Data are the same as in Figure 3a.

where $\alpha, \beta, \gamma, \delta, I$, and J are as previously defined.

Thus the amplitude of the output signal on product concentration resulting from an input signal on feed concentration only or feed temperature only is given, respectively, by

$$|Z_0| = |I\alpha + J\gamma|\,|X_i|$$

$$|Z_0| = |I\beta + J\delta|\,|Y_i|$$

and with the data of the illustration

	Case A	Case B
$I\alpha + J\gamma$	1.776	91.4
$I\beta + J\delta$	0.00174	0.0218

Suppose now that it is required to keep the product stream quality within 5% of its steady state value. Assuming that this deviation is caused either by a variation in feed concentration alone or feed temperature alone, one may calculate the necessary percentage of regulation on the feed concentration or temperature; thus

	Case A	Case B
Feed concentration	2.02%	0.05%
Feed temperature	0.121% (0.4°)	0.013% (.04°)

It appears therefore that very stringent requirements on feed characteristics may be necessary under some operating conditions. The foregoing calculations are simple to carry out once the complete steady state profiles have been computed. Calculations such as these should give first approximations to the severity of the required process control and should give information in connection with the choice of control equipment.

A Complicated Example

The same example will be considered as was treated in Part I.

$$A + B \underset{k_2}{\overset{k_1}{\rightleftarrows}} C + F, \qquad \Delta H_{12}$$

$$C \xrightarrow{k_3} E, \qquad \Delta H_3$$

A, B, C, F, and E may be the unsteady state concentrations and A_s, B_s, C_s, F_s, and E_s the corresponding steady state concentrations. a, b, c, f, and e may be the unsteady state parts of the concentration and t the unsteady part of the temperature; then

$$A = A_s + a \qquad C = C_s + c$$

$$B = B_s + b \qquad F = F_s + f$$

$$T = T_s + t$$

If the kinetics are second and first order, respectively, the equations of the unsteady state are

$$\frac{DA}{D\theta} = -k_1AB + k_2CF \tag{17}$$

$$\frac{DB}{D\theta} = -k_1AB + k_2CF \tag{18}$$

$$\frac{DF}{D\theta} = k_1AB - k_2CF \tag{19}$$

$$\frac{DC}{D\theta} = k_1AB - k_2CF - k_3C \tag{20}$$

$$\frac{DT}{D\theta} = K(T_w - T) + Q_{12}(k_1AB - k_2CF) + Q_3k_3C \tag{21}$$

In order to obtain the steady state solution only Equations (17), (20), and (21) need be used, as there are some simple relations among the concentrations. If the column matrices

$$\mathbf{V} = \begin{bmatrix} a \\ b \\ c \\ f \\ t \end{bmatrix}; \quad \mathbf{V}_o = \begin{bmatrix} a_o \\ b_o \\ c_o \\ f_o \\ t_o \end{bmatrix}; \quad \mathbf{V}_i = \begin{bmatrix} a_i \\ b_i \\ c_i \\ f_i \\ t_i \end{bmatrix}$$

and the matrix

$$\mathbf{F}(s, \tau) = \mathbf{P} - \frac{s}{v}\mathbf{I}$$

are defined where I is the unitary matrix and

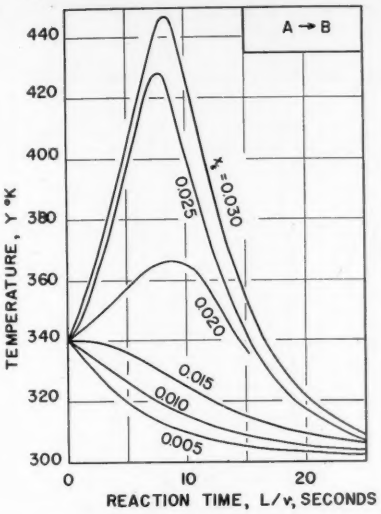

Fig. 4*a*. Temperature profiles in a tubular reactor; effect of feed dilution. $E = 11{,}250$, $p = 1.59 \times 10^{13}$, $Q = 10{,}000$, $K = 0.20$, $T_i = 340°K.$, $T_w = 300°K.$

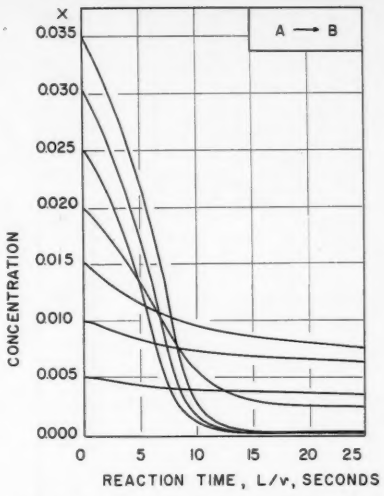

Fig. 4*b*. Concentration profiles in a tubular reactor; effect of feed dilution. Data are the same as in Figure 4*a*.

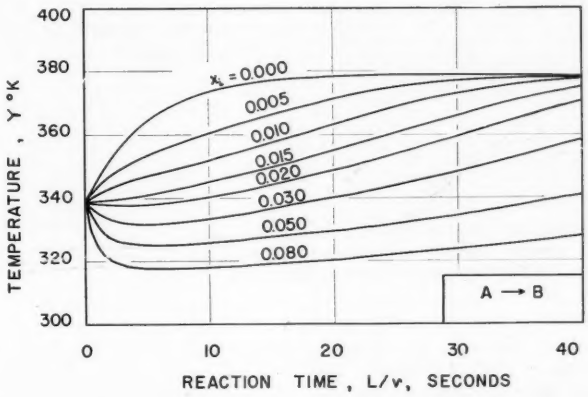

Fig. 5. Temperature profiles in a tubular reactor; effect of food dilution on an endothermic reaction. $E = 11{,}250$, $Q = -10{,}000$, $p = 1.59 \times 10^{13}$, $T_i = 340°K.$, $T_w = 380°K.$, $K = 0.200$.

$$\mathbf{P} = \frac{1}{v}\begin{bmatrix} -k_{1s}B_s & -k_{1s}A_s & k_{2s}F_s & k_{2s}C_s & -X_s \\ -k_{1s}B_s & -k_{1s}A_s & k_{2s}F_s & k_{2s}C_s & -X_s \\ k_{1s}B_s & k_{1s}A_s & -k_{2s}F_s - k_{3s} & -k_{2s}C_s & -Y_s \\ k_{1s}B_s & k_{1s}A_s & -k_{2s}F_s & -k_{2s}C_s & X_s \\ -k_{1s}B_s\dfrac{\Delta H_{12}}{c\rho} & -k_{1s}A_s\dfrac{\Delta H_{12}}{c\rho} & W_s & k_{2s}C_s\dfrac{\Delta H_{12}}{c\rho} & -Z_s \end{bmatrix} \tag{22}$$

where

$$X_s = k_{1s}A_sB_s\frac{E_1}{RT_s^2} - k_{2s}C_sD_s\frac{E_2}{RT_s^2}$$

$$Y_s = X_s - k_{3s}\frac{E_3}{RT_s^2}C_s$$

$$W_s = k_{2s}F_s\frac{\Delta H_{12}}{c\rho} - k_{3s}\frac{\Delta H_3}{c\rho}$$

$$Z_s = -X_s\frac{\Delta H_{12}}{c\rho} - K - k_{3s}\frac{E_3}{RT_s^2}C_s\frac{\Delta H_3}{c\rho}$$

then

$$\mathbf{M} = \ln \mathbf{\Omega}(s) = \int_0^L \mathbf{F}(s,\tau)\,d\tau = \int_0^L \left(\mathbf{P} - \frac{s}{v}\mathbf{I}\right)d\tau = \frac{-sL}{v}\mathbf{I} + \int_0^L \mathbf{P}\,d\tau$$

Note that $\int_0^L \mathbf{P}\,d\tau$ is the analogue of Equation (10) and that Equation (22) is identical with the matrix which appeared in Part I for the same chemical system. In order to evaluate the integrated matrix in numerical terms eight calculations based on the steady state must be made. Therefore it will be assumed that the solution may be expressed in the form

$$\bar{\mathbf{V}}_o = \mathbf{\Omega}(s)\bar{\mathbf{V}}_i$$

where $\bar{\mathbf{V}}_o$ is the Laplace transform of $\mathbf{V}_o$ and $\bar{\mathbf{V}}_i$ is the Laplace transform of $\mathbf{V}_i$. If $\mathbf{V}_i$ represents the matrix of a sinusoidal input, then the output in complex form is

$$\mathbf{V}_o = \mathbf{\Omega}(j\omega)\mathbf{V}_i$$

$$\mathbf{V}_o = \mathbf{R}\mathbf{V}_i e^{-j\omega L/v}$$

where $\mathbf{R}$ is a matrix derived from

$$\exp\int_0^L \mathbf{P}\,d\tau = \mathbf{R}$$

by Sylvester's theorem in the same manner as Equation (13) was derived. $\mathbf{R}$ will be a matrix of the form

$$\mathbf{R} = [a_{ij}] \qquad i,j = 1,2,3,4,5$$

and so

$$a_o = (a_{11}a_i + a_{12}b_i + a_{13}c_i + a_{14}f_i + a_{15}t_i)e^{-j\omega(\vartheta - L/v)}$$

$$c_o = (a_{31}a_i + a_{32}b_i + a_{33}c_i + a_{34}f_i + a_{35}t_i)e^{-j\omega(\vartheta - L/v)}$$

$$t_o = (a_{51}a_i + a_{52}b_i + a_{53}c_i + a_{54}f_i + a_{55}t_i)e^{-j\omega(\vartheta - L/v)}$$

where in this set of formulas a_i, b_i, c_i, f_i, and t_i are the amplitudes of the input signals and the a_o, b_o, c_o, f_o, and t_o are the output sinusoidal responses. The gain can be simply calculated from these formulas. If the input had been a step function rather than a sinusoid, the

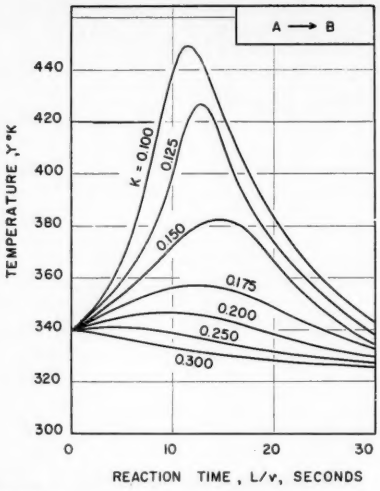

Fig. 6a. Temperature profiles in a tubular reactor; effect of heat transfer coefficient K. $E = 11{,}250$, $p = 7.89 \times 10^{12}$, $x_i = 0.020$, $T_i = 340$, $T_w = 320$.

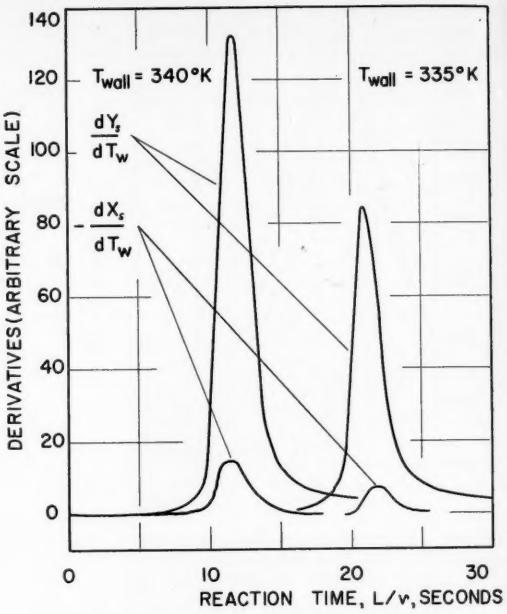

Fig. 7. Plot of derivatives of concentration and temperature with respect to the wall temperature against position in the reactor; effect of wall temperature. $E = 22{,}500$, $p = 3.94 \times 10^{12}$, $Q = 8{,}400$, $T_i = 340$°K., $K = 0.200$.

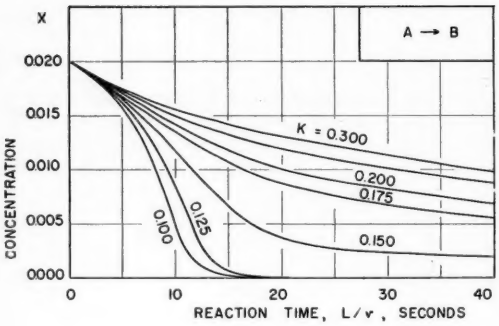

Fig. 6b. Concentration profiles in a tubular reactor; effect of heat transfer coefficient K. Data are the same as in Figure 6a.

exponential factors in these formulas would be missing, as if a_i, b_i, c_i, f_i, and t_i are steps in the input (small steps to be sure), then

$$\overline{\mathbf{V}}_o = \frac{\mathbf{\Omega}(s)}{s}\,\mathbf{V}_i$$

and the inverse of this is given by

$$a_o = (a_{11}a_i + a_{12}b_i + a_{13}c_i + a_{14}f_i + a_{15}t_i), \qquad \theta > \frac{L}{v}$$

with analogous formulas for b_o, c_o, f_o, and t_o. The quantity e_o may be computed as in the previous example and will not be repeated here.

STABILITY OF A TUBULAR REACTOR WITH A RECYCLE LOOP

Recycling is often used in industrial practice as a means of temperature control or to improve the yield if the yield per pass is low. The external feed and drawoff may be assumed to be q and the amount of recycle Q. The total internal flow is then $q + Q$. λ is defined as the recycle parameter

$$\lambda = q/Q$$

If by $\mathbf{V}_i$ the total feed matrix to the reactor is denoted, then

$$\overline{\mathbf{V}}_o = \mathbf{\Omega}(s)\overline{\mathbf{V}}_i$$

Also if $\mathbf{v}_i$ is the external feed (exclusive of recycle) and if differences in heat capacities are neglected, then

$$(Q + q)\overline{\mathbf{V}}_i = Q\overline{\mathbf{V}}_o + q\bar{\mathbf{v}}_i$$

where this is a combination energy and mass balance in matrix form.
Then

$$\overline{\mathbf{V}}_i = \frac{1}{1+\lambda}\,\overline{\mathbf{V}}_o + \frac{\lambda}{1+\lambda}\,\bar{\mathbf{v}}_i$$

and

$$\overline{\mathbf{V}}_o = \frac{1}{1+\lambda}\,\mathbf{\Omega}\overline{\mathbf{V}}_o + \frac{\lambda}{1+\lambda}\,\mathbf{\Omega}\bar{\mathbf{v}}_i$$

$$[(1+\lambda)\mathbf{I} - \mathbf{\Omega}]\overline{\mathbf{V}}_o = \lambda\mathbf{\Omega}\bar{\mathbf{v}}_i$$

with the result

$$\overline{\mathbf{V}}_o = \lambda[(1+\lambda)\mathbf{I} - \mathbf{\Omega}]^{-1}\mathbf{\Omega}\bar{\mathbf{v}}_i \quad (23)$$

where this is a matrix equation in which the order must be preserved and in which the exponent, -1, is standard notation for the inverse matrix. In Equation (23) the matrix

$$\mathbf{\Omega}_R = \lambda[(1+\lambda)\mathbf{I} - \mathbf{\Omega}]^{-1}\mathbf{\Omega}$$

is the transfer matrix for the recycle system. If $\mathbf{\Omega}$ is a matrix of the nth order, then it is clear that the transfer matrix is of the nth order each of whose terms consists of a quotient of sums of products of terms from $\mathbf{\Omega}$ and the adjoint of $[(1+\lambda)\mathbf{I} - \mathbf{\Omega}]$. Each of these sums of products will be divided by the determinant of $[(1+\lambda)\mathbf{I} - \mathbf{\Omega}]$.

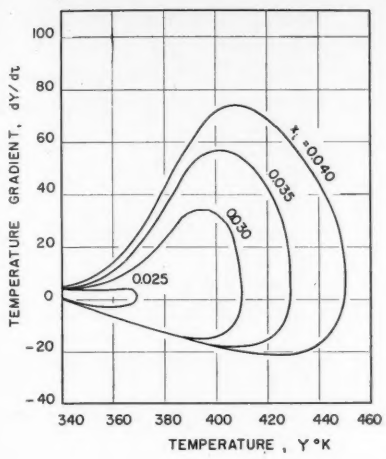

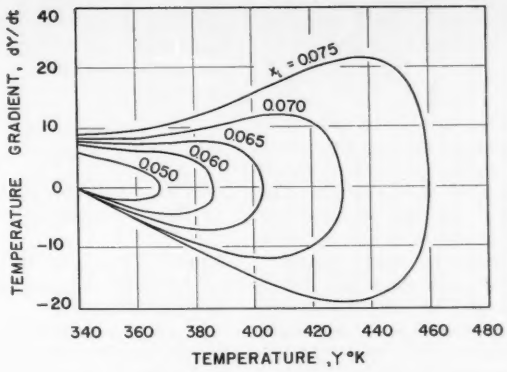

←Fig. 8*a*. Phase diagram of a tubular-reactor temperature profile. $E = 33{,}750$, $p = 7.89 \times 10^{12}$, $Q = 4{,}370$, $K = 0.300$

↑ Fig. 8*b*. Phase diagram of a tubular-reactor temperature profile. $E = 13{,}100$, $p = 7.89 \times 10^{12}$, $Q = 4{,}370$, $K = 0.300$, $T_i = T_w = 340°\text{K}$.

The details of a simple problem will now be carried out. Equation (16) gives the transfer function for the output product signal in terms of the input feed signals for the problem $A \rightarrow B$. Then

$$[(1+\lambda)\mathbf{I} - \boldsymbol{\Omega}(s)] = e^{-sL/v}\begin{bmatrix} (1+\lambda)e^{Ls/v} - \alpha & -\beta & 0 \\ -\gamma & (1+\lambda)e^{Ls/v} - \delta & 0 \\ -(I\alpha + J\gamma) & -(I\beta + J\delta) & (1+\lambda)e^{(L/v)s} - 1 \end{bmatrix}$$

Then

$$\boldsymbol{\Omega}_R(s) = \lambda\begin{bmatrix} (1+\lambda)e^{Ls/v} - \alpha & -\beta & 0 \\ -\gamma & (1+\lambda)e^{Ls/v} - \delta & 0 \\ -(I\alpha + J\gamma) & -(I\beta + J\delta) & (1+\lambda)e^{(L/v)s} - 1 \end{bmatrix}^{-1}\begin{bmatrix} \alpha & \beta & 0 \\ \gamma & \delta & 0 \\ I\alpha + J\gamma & I\beta + \delta J & 1 \end{bmatrix} \tag{24}$$

When one takes the inverse Laplace transform of $\bar{\mathbf{V}}_o$, he is concerned with the poles of the transform and their location. If there are poles in the right half of the s plane, then there is no finite steady state solution and the system is said to be unstable. It is clear from the analysis thus far that poles can enter only at the zeros of the denominator of terms in $\boldsymbol{\Omega}_R(s)$ or at the zeros of the determinant of $[(1+\lambda)\mathbf{I} - \boldsymbol{\Omega}]$, i.e., at the zeros of

$$[(1+\lambda)e^{(L/v)s} - 1][(1+\lambda)^2 e^{2Ls/v}$$

$$-(\alpha+\delta)(1+\lambda)e^{Ls/v} + \delta\alpha - \beta\gamma] = 0$$

The determinant will always be a product of

$$(1+\lambda)e^{(L/v)s} - 1$$

and a polynomial in $(1+\lambda)e^{Ls/v}$. With this in mind one finds that the remaining analysis will follow a general procedure rather than one which holds for the quadratic term only.

Since $\lambda > 0$

$$e^{Ls/v} = \frac{1}{1+\lambda}$$

can have a root in s only with negative real part. If σ_1 and σ_2 are the roots of the characteristic equation of the matrix $\boldsymbol{\Omega}$, in which

$$\sigma = (1+\lambda)e^{Ls/v}$$

then the system will be stable if the absolute values of the roots σ_1 and σ_2 are less than $1+\lambda$; i.e.,

$$|\sigma_1| < 1 + \lambda$$

$$|\sigma_2| < 1 + \lambda$$

or if the roots in σ of the equation

$$(1+\lambda)^2\sigma^2 - (1+\lambda)(\alpha+\delta)\sigma + \alpha\delta - \beta\gamma = 0$$

lie inside the unit circle.

The transformation

$$\sigma = \frac{1+\xi}{1-\xi}$$

maps the inside of the unit circle on the left hand of the ξ plane. Hence if the equation

$$[(1+\lambda)^2 + (1+\lambda)(\alpha+\delta) + \alpha\delta - \beta\gamma]\xi^2 + 2\xi[(1+\lambda)^2 - \alpha\delta + \beta\gamma] + [(1+\lambda)^2 - (1+\lambda)(\alpha+\delta) + \alpha\delta - \beta\gamma] = 0$$

has no roots in the right half of the ξ plane, the solution is stable. This will always be a polynomial in ξ to which the Routh-Hurwitz criterion (*see* Part I) may be applied. If

$$C_1 = [(1+\lambda)^2 - \alpha\delta + \beta\gamma][(1+\lambda)^2 + (1+\lambda)(\alpha+\delta) + \alpha\delta - \beta\gamma] > 0$$

$$C_2 = [(1+\lambda)^2 - \alpha\delta + \beta\gamma][(1+\lambda)^2 - (1+\lambda)(\alpha+\delta) + \alpha\delta - \beta\gamma] > 0$$

then by the Routh-Hurwitz criterion the system is stable. In the physical problem considered here the stability condition

may be obtained more simply from the characteristic equation of $\Omega(s)$

$$\sigma^2 - (\alpha + \delta)\sigma + \alpha\delta - \beta\gamma = 0$$

by writing that $\pm(1 + \lambda)$ be exterior to the root interval and that the product of the roots lies inside the circle of radius $(1 + \lambda)^2$ centered at the origin. The treatment which has been given above is more general and would apply to a characteristic equation of any degree.

If the same analysis is applied to an isothermal system it may be shown without difficulty that it is always stable in this sense. It may be noted that the aforementioned restrictions are lifted if λ becomes infinite; i.e., there is no recycle.

If the details of Equation (24) are carried out, it may be shown that

$$Z_o = \frac{\lambda(1 + \lambda)e^{Lj\omega/v}}{(1 + \lambda)^2 e^{2Lj\omega/v} - (\alpha + \delta)(1 + \lambda)e^{Lj\omega/v} + \alpha\delta - \beta\gamma}[UX_i + VY_i] \quad (25)$$

where X_i and Y_i are the complex feed signals on concentration and temperature and Z_o is the complex signal of the outlet product with

$$U = \frac{(I\alpha + J\gamma)(1+\lambda)e^{Lj\omega/v} + (\beta\gamma - \alpha\delta)I}{(1+\lambda)e^{Lj\omega/v} - 1}$$

$$V = \frac{(I\beta + J\delta)(1+\lambda)e^{Lj\omega/v} + (\beta\gamma - \alpha\delta)J}{(1+\lambda)e^{Lj\omega/v} - 1}$$

Example. A tubular reactor is assumed, with temperature and concentration profiles as in case A of the numerical example. The values of the elements for the matrix Ω have also been calculated. For a recycle parameter $\lambda = 0.70$ the expressions in the stability conditions C_1 and C_2 may be calculated and are

$$C_1 = 0.197 > 0$$

$$C_2 = 11.0 > 0$$

This loop system with this recycle ratio is therefore stable. Such a loop would require an external feed concentration $x_i = 0.0404$ and would give a product concentration $z_o = 0.0347$. The advantage of using a recycle loop in this case is that temperatures remain low, control is easy, and the ratio of concentrations B/A in the effluent has been increased by a factor of 2.43.

A discussion of the sign of the expressions C_1, C_2 shows in the present case that the loop is unstable for values of the recycle parameter $0 < \lambda < 0.308$ and stable if $\lambda > 0.308$.

The response of the system may be calculated on the assumption that an input signal frequency of $\omega = 0.01$. Equation (25) may be shown to reduce to

$$Z_o = (-0.606 + 0.500j)X_i + (-0.000623 + 0.000522j)Y_i$$

From this result the amplitude ratio and phase lag of output to input signal for an input signal on external feed concentration alone or feed temperature alone may be computed.

	Amplitude ratio	Phase lag
Z_o/X_i	0.785	130°
Z_o/Y_i	0.000814	130°

If the heat capacities of feed and product are markedly different, these quantities should be corrected.

Two or three calculations of this sort covering an adequate range of frequencies would usually give an idea of the control requirements. If more detailed information is required, Bode and Nyquist diagrams may be plotted in the usual way.

SUMMARY

In this paper an attempt has been made to analyze the quasiisothermal tubular reactor. This has been done by making extensive computations on the R.E.A.C., an analogue computer, for a simple mathematical model. These calculations reveal that regions of sensitivity exist in which slight changes in the operating conditions produce large changes in the yields. A method based on a local linearization was developed for the prediction of such sensitivity. This linearization requires for its use the calculation of the steady state temperature and concentration profiles. Small changes in the feed concentration or temperature may be transmitted through the reactor with accentuation or attenuation depending upon the region of operation. Numerical and theoretical examples were posed.

By analogy to electrical systems chemical systems with recycle or feedback should exhibit instability for some values of the parameters. These are shown to exist theoretically, and methods for prediction of the unstable regions are presented.

It should be pointed out clearly that the form of the solution is not exact for matrices. The quantity $\bar{\mathbf{V}}_0 = e^{\mathbf{M}\bar{\mathbf{V}}_i}$ after Equation (8) must be treated as an approximation of the true solution. The quantity appears to have the correct form but has not, because of the noncommutativity of some of the matrices involved.

ACKNOWLEDGMENT

A part of this paper was written while Neal R. Amundson was a Fulbright Scholar in the Department of Chemical Engineering, Cambridge University, England. The authors are indebted to the Computing Center of the University of Minnesota for advice and counsel in connection with the R.E.A.C. as well as for a considerable amount of computing time in the early stages of the work.

NOTATION

A, B, C, F, E, etc. = chemical species and concentrations of species

a, b, c, d, e, etc. = perturbations from steady state concentrations

c = specific heat of reactant stream

E = activation energy

h = over-all heat transfer coefficient

I, J = two calculated quantities defined in text

$\mathbf{I}$ = unitary matrix

$j = \sqrt{-1}$

$K = 2rh/c\rho$

k = reaction velocity constant, also k_1, k_2, k_3

L = reactor length

$\mathbf{M}$ = matrix defined in text, Equation (8)

$\mathbf{N}$ = matrix defined in text, Equation (10)

p = frequency factor in velocity constant

$Q = -\Delta H/c\rho$

q = feed rate in recycle problems

Q = recycle rate in recycle problems

r = reactor radius

T_W = reactor ambient temperature

v = velocity in reactor

$\mathbf{V}_0$ = reactor output signal

$\mathbf{V}_i$ = reactor input signal

x = concentration of feed in first problem

y = temperature in first problem

X, Y, Z = perturbations on x, y, z

z = concentration of product in first problem

Greek Letters

$\alpha, \beta, \gamma, \delta$ = matrix elements in first problem

ϵ, η = amplitudes or steps in concentration and temperature, respectively

λ = recycle parameter $= q/Q$

$\sigma = (1 + \lambda)e^{Ls/v}$

ΔH = heat of reaction

θ = time

ρ = density

τ = reactor-length variable

$\Omega(s)$ = open-loop transfer function

$\Omega_R(s)$ = recycle-loop transfer function

Sub- and Superscripts

s = steady state value

—(over symbols) = Laplace transform

LITERATURE CITED

1. Acrivos, A., and Neal R. Amundson, *Ind. Eng. Chem.*, **47**, 1533 (1955).
2. Deisler, P. F., and R. H. Wilhelm, *Ind. Eng. Chem.*, **45**, 1219 (1953).
3. Frazer, R. A., W. J. Duncan, and A. R. Collar, "Elementary Matrices," Cambridge University Press, Cambridge (1952).
4. Gee, R. E., W. N. Linton, R. E. Maier, and J. W. Raines, *Chem. Eng. Progr.*, **50**, 497 (1954).
5. Kramers, H., and G. Alberda, *Chem. Eng. Sci.*, **2**, 173 (1953).
6. Minorsky, N., "Introduction to Non-Linear Mechanics," J. W. Edwards, Ann Arbor, Mich. (1947).

Forces Acting in Flowing Beds of Solids

JOHN W. DELAPLAINE

University of Delaware, Newark, Delaware

Beds of granular solids flowing downward under the influence of gravity as a consolidated or dense phase have found wide application in recent years as media for effecting chemical and physical changes. Typical applications of the so-called "moving-bed" principle are the Houdriflow and TCC catalytic cracking units and the pebble heater. This technique provides a method for carrying out concurrent or countercurrent operations under controlled temperature gradients and has numerous applications in the chemical field.

This paper presents the results of a study of the stresses acting in beds of noncohesive granular solids flowing under steady state conditions in vertical vessels of constant cross section with no interstitial fluid flow relative to the solids. It is important to examine this relatively simple case of solids flow, which is of industrial significance, before systems involving solids acceleration and fluid pressure gradient can be effectively analyzed. The objectives of this study are to determine as many as possible of the fundamental laws governing solids flow by investigating the stress relationships and to explain the characteristics of flowing beds of solids.

The behavior of both static- and flowing-solids systems differs from that of comparable fluid systems. Solids systems have a finite angle of repose and the mechanism of stress distribution is by particle-to-particle friction. The stresses, or forces per unit area, are exerted by the particles on each other (local or internal stresses) and at the boundaries of the bed (boundary or wall stresses). Numerous investigators (*6*, *7*, *9*, *16*) have measured the boundary forces exerted by static beds of solids. They have shown that the stresses are not proportional to the bed depth but increase exponentially until asymptotic values are reached at bed-depth–to–tube-diameter ratios of about 5. In a flowing consolidated bed of Ottawa sand particles Brinn et al. (*3*) have shown that the velocity over approximately the central 80% of the bed was constant and the flow in this region was rodlike. Shear occurred in the outer region of the bed, and the velocity at the walls was found to be slightly lower than the average. This report will discuss how and why solids systems behave differently from fluids. It will also extend stress-relationship data from boundary stresses in static systems to both local and boundary stresses in flowing systems.

STRESS THEORY AND LITERATURE SURVEY

Equations of continuity of momentum are needed for the stress relationships in flowing beds of solids. The local stresses are related by balances around a differential volume of solids, $r\,dr\,d\theta\,dz$, shown in Figure 1, and the boundary and average stresses by a balance around a horizontal slab of $(\pi D_t^2/4)\,dz$ volume. Moment balances are used to simplify the local stress equations, and stress ratios are introduced to simplify both types of equations. Experimental data will be utilized to evaluate these stress ratios and the basic equations, so that all stresses may be calculated as functions of fractional radius, bed depth, pipe diameter, bulk density, and friction coefficients. Throughout this paper the buoyancy and local gravitational effects have been included in the term ρ_b for simplification, so that ρ_b represents a net force per unit volume of solids rather than a solids density.

Forces Acting on a Differential Volume

Figure 1 shows the stresses acting on an infinitesimally small volume in cylindrical coordinates, along with the areas on which these stresses act. There are three normal (compressive) stresses, σ_r, σ_θ, and σ_z, resulting from forces in the r, θ, and z directions acting on perpendicular planes. There are six shear stresses, τ_{zr}, τ_{rz}, $\tau_{\theta z}$, $\tau_{z\theta}$, $\tau_{\theta r}$, and $\tau_{r\theta}$, acting parallel to the plane of the stress in the direction of the second subscript and resulting from a normal force in the direction of the first subscript. If acceleration is absent and gravity is the only body force, the equations for these stresses are as follows, the downward, radial, and clockwise directions being taken as positive:

$$\frac{\partial \sigma_z}{\partial z} + \frac{\partial \tau_{rz}}{\partial r} + \frac{\partial \tau_{\theta z}}{r\,\partial \theta} + \frac{\tau_{rz}}{r} = \rho_b \tag{1}$$

$$\frac{\partial \sigma_r}{\partial r} + \frac{\partial \tau_{zr}}{\partial z} + \frac{\partial \tau_{\theta r}}{r\,\partial \theta} + \frac{\sigma_r - \sigma_\theta}{r} = 0 \tag{2}$$

$$\frac{\partial \sigma_\theta}{r\,\partial \theta} + \frac{\partial \tau_{z\theta}}{\partial z} + \frac{\partial \tau_{r\theta}}{\partial r} + \frac{\tau_{\theta r} + \tau_{r\theta}}{r} = 0 \tag{3}$$

These equations were obtained by direct substitution of the body forces in the classical equations for static equilibrium under nonuniform stress conditions given by Sechler (*12*), Westergaard (*17*), and others. If angular acceleration is absent, these authors show that moment balances around the radial, vertical, and tangential axes yield $\tau_{\theta z} = \tau_{z\theta}$, $\tau_{r\theta} = \tau_{\theta r}$, and $\tau_{rz} = \tau_{zr}$. For example, in the upper right-hand corner of Figure 1 the shear stresses $\tau_{r\theta}$ and $\tau_{\theta r}$ acting on the small square of the differential section must be equal and must give rise to opposite moments, or the particles will rotate around the vertical axis. If acceleration exists, the resultant force or moment from Newton's second law must be included in the appropriate equation.

Jaky (*5*) in a purely mathematical analysis of a static system of solids used two-dimensional stress differential equations. However, his final equations do not appear to be valid because of the numerous assumptions, such as the proportionality of both the shear stress and the coefficient of friction with bed depth.

The stress ratios used to simplify the force-balance equations for a differential volume are defined in the following table together with the ratios for a horizontal slab.

Present address: Cox and Weinrich, Washington, D. C.

TABLE 1

Local stress ratios, differential volume	Boundary and average stress ratios, horizontal slab
$\mu = \frac{\tau_{rz}}{\sigma_r}$	$\mu' = \frac{(\tau_{rz})_w}{(\sigma_r)_w}$ = friction coefficient
$k = \frac{\sigma_r}{\sigma_z}$	$k_a = \frac{(\sigma_r)_w}{(\sigma_z)_a}$
	$\alpha = \frac{(\sigma_z)_a}{4(\tau_{rz})_w} = \frac{1}{4k_a\mu}$

where the subscript w refers to the boundary or wall stress and $(\sigma_z)_a$ is the average vertical stress (i.e., total vertical force on a horizontal plane divided by its area). These ratios vary with the stress, bed depth, and radial distance.

Forces Acting on a Horizontal Slab

Figure 2*a* shows the boundary and average forces acting on a horizontal slab of solids within the bed. A vertical force balance on this horizontal slab of solids of thickness dz gives

$$\frac{d(\sigma_z)_a}{dz} = \rho_b - \frac{4(\tau_{rz})_w}{D_t} \qquad (4)$$

Substitution of the stress ratios yields

$$\frac{d(\sigma_z)_a}{dz} = \rho_b - \frac{4k_a\mu'(\sigma_z)_a}{D_t} = \rho_b - \frac{(\sigma_z)_a}{\alpha D_t} \qquad (5)$$

The classical solution to this equation was given by Janssen (*6*), who assumed k_a, μ', and α to be independent of bed depth and integrated from 0 to z bed depth. Thus

$$(\sigma_z)_a = \frac{\rho_b D_t}{4k_a\mu'}(1 - e^{-4k_a\mu' z/D_t}) = \alpha\rho_b D_t[1 - e^{-z/(\alpha D_t)}] \qquad (6)$$

Several investigators (*6, 7, 9, 16*) have found that at bed depths of less than about five tube diameters the stresses vary with bed depth, and at z/D_t ratios greater than about 5, stresses are independent of z. The bed therefore may be considered to be composed of these two sections. The subscript h will be used to refer to values of stress at high bed depths ($z/D_t > 5$). Figure 2*b* shows these stresses. In this region $d(\sigma_z)_{a,h}/dz = 0$; all the additional weight of solids is supported by the tube wall, and Equations (5) and (4) reduce to

$$\frac{(\sigma_z)_{a,h}}{\rho_b D_t} = \frac{1}{4k_{a,h}\mu_h'} = \alpha_h \qquad (7)$$

and

$$\frac{(\tau_{rz})_{w,h}}{\rho_b D_t/4} = \frac{(\sigma_z)_{a,h}}{\alpha_h\rho_b D_t} = 1 \qquad (8)$$

where α_h, $k_{a,h}$ and μ_h' are the stress ratios existing at high bed depths. Equation (7) shows that the maximum vertical force in a bed of solids equals its weight within the height αD_t. Equation (6) gives satisfactory values at relatively high bed depths if α or $k_a\mu'$ is measured at high bed depths.

Investigations of solids stresses have been limited essentially to boundary measurements in static systems. Most investigators (*7, 9, 16*) have correlated their stress measurements by the Janssen equation (5) using a constant value of k_a equal to the ratio of radial to horizontal stress in an unconfined bed of solids, which is a function of the coefficient of friction between particles. However, the available experimental data do not indicate that these assumptions are correct. Shaxby and Evans (*14*) developed a different equation for stress exerted by static powders, but a differentiation of their basic equation indicates that the slope of their $(\sigma_z)_a$-vs.-z curve at low bed depths differs by several hundred per cent from the solids density. These must be equal, as will be shown later. Caquot and Karisel (*4*) present an empirical equation for the variation of vertical stress with bed depth which involves an unknown constant. Since data are not available, they suggest that this constant is zero, and their equation reduces to the conventional Janssen equation (5).

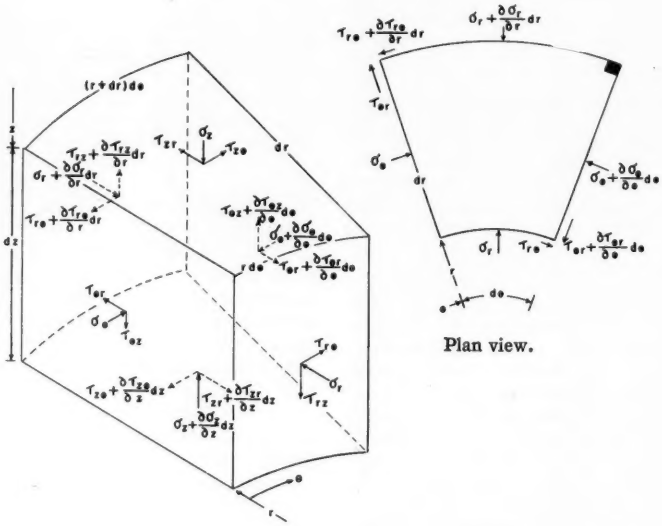

Fig. 1. Forces acting on a differential volume in cylindrical coordinates.

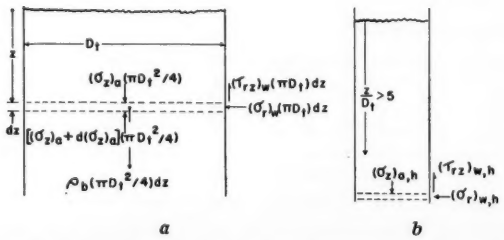

Fig. 2. Boundary and average stresses: *a*, force balance; *b*, stresses at high bed depth.

SCOPE OF WORK

In the previous section it was indicated that the basic differential equations for static systems are known but that satisfactory integrations have not been obtained. The present investigation is concerned with the determination of the stresses and evaluation of these equations in flowing-solids systems. The boundary stresses $(\sigma_r)_w$ and $(\tau_{rz})_w$, the average vertical stress $(\sigma_z)_a$, and the local stresses σ_z, σ_r, and σ_θ were measured, and the remaining shear stresses were calculated from the theoretical equations developed. In addition, the required solids properties,

density and friction coefficients, were determined. The relationships between the boundary and average stresses were developed from a force balance on a differential slab of solids. The relationships of the local stresses were determined from balances on a differential volume of solids.

To make the final correlations as general as possible, the tube-to-particle-diameter ratio was varied from about 10/1 to 400/1 and different solids materials were investigated. Runs were made in the following containers: (1) smooth steel tubing from 0.5 to 3.806 in. in diameter, (2) commercial (rusty) pipe 4.026 and 11.63 in. in diameter, and (3) a 5-ft.-diam. brick-lined vessel. The particle diameter varied from 0.009 to 0.14 in. The materials studied were spherical glass beads, ellipsoidal bead catalyst, and irregularly shaped, rounded Ottawa test sand particles. Their properties are listed in Table 2.

Table 2. Density Data

Material	Mesh	D_p, in.	ρ_p, g./cu. in.	ρ_b, g./cu. in. (flowing)
Sand	20–30	0.029	43.6	25.7
	30–36	0.022	43.6	25.1
	36–48	0.015	43.6	24.85
	48–55	0.012	43.6	24.35
	50–70	0.009	43.6	23.9
Glass beads	25–30	0.028	40.7	24.95
	35–40	0.0185	40.9	24.8
	50–60	0.011	42.5	25.7
Bead catalyst	3–10	0.125	19.3	12.1

EXPERIMENTAL METHODS

Apparatus

The equipment consisted of the system being studied, the pick-up gauge, the force transmission device, and the measuring circuit. The gauges and measurements will be discussed later in this section. Figure 3 is a photograph of the 3.80-in.-diameter apparatus which was similar to the other systems investigated. This picture shows the 6-ft. length of tubing, feed funnel, traversing mechanisms, and wall-forces gauge. A four-holed orifice located below the tubing maintained constant solids flow rate. This multi-holed orifice minimized the bed depth required to eliminate the effect of the orifice on the stresses by considerably reducing the height of stagnant solids below the height required above a single orifice.

The accurate transmission of each type of stress to the point of measurement required an instrument development program. The effect on the measurements of any stationary equipment in the bed had to be determined. It was necessary to hold the volume of any stationary internal device to a minimum. The internal stress measurements were made by hanging the plate or cylinder from a Statham transducer with 0.010-in.-diam. stainless hypodermic tubing, surrounded by a slightly larger stationary hypodermic shield to eliminate shear stress on the inner tube. The effect of the support tubing, shield, and thin alignment rods on the results was determined experimentally to be negligible.

In general, loads were measured with the Statham transducer, which contains a Wheatstone bridge the resistances of which vary with the load. This instrument was chosen because of its negligible deformation, linearity, sensitivity, and ease of calibration. A direct-current input was used and the output was recorded on a strip-chart self-balancing potentiometer. Direct calibrations with known weights were made after all runs.

Procedures

The variable in each run was bed depth. The system was "prerun" by allowing it to flow for a period of 10 min. to establish equilibrium stress conditions, and the level fell when feeding ceased at the beginning of the test period. It was necessary continually to level the top of the bed by hand during the run because of the lower velocity near the wall. The level varied linearly with time, an indication of constant density and velocity.

Wall-forces-gauge Measurements

This gauge, shown in Figure 4, simultaneously measured $(\tau_{rz})_w$ and $(\sigma_r)_w$ and μ', which equals $(\tau_{rz})_w/(\sigma_r)_w$. The horizontal force on a 1.245-in.-diam. curved disk in a 1.25-in. hole was transmitted through a pivoted shaft to a transducer. This shaft was supported by a spring steel strip from a vertical transducer, which measured the moment of the $(\tau_{rz})_w$ force about the pivot. This moment balance was verified by hanging weights from the disk surface. The reading of each transducer was unaffected by mechanical forces on the disk in the perpendicular direction.

The measured vertical load divided by the elliptical surface area equaled $(\tau_{rz})_w$. However, at low bed depths the center of radial pressure was below the disk centroid. This radial moment necessitated a small correction to $(\tau_{rz})_w$. The measured horizontal load divided by the projection of the area on a tangential plane (circle) equaled $(\sigma_r)_w$. The bed depth corresponding to the measurements was approximately equal to the distance from the free surface to the centroid of the disk. At low bed depths, only the disk area covered by solids is pertinent.

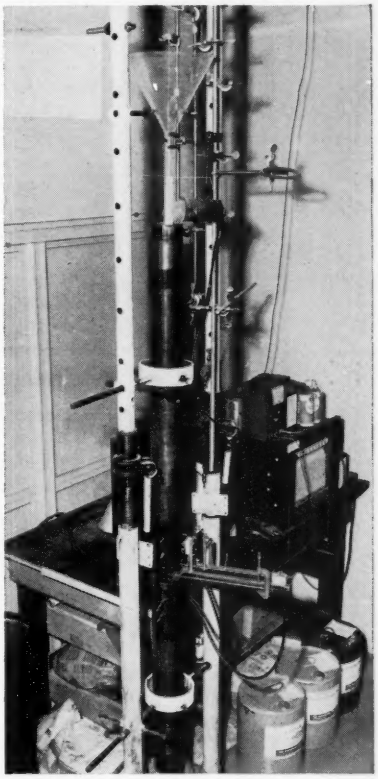

Fig. 3. Equipment.

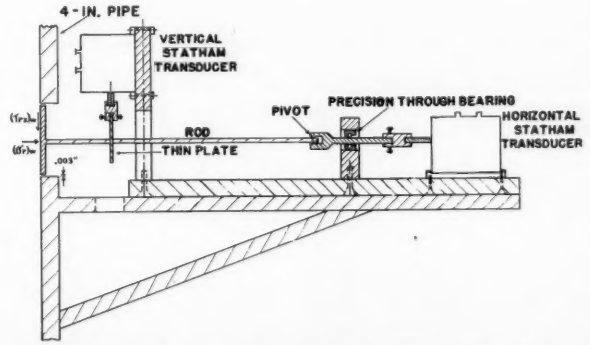

Fig. 4. Wall-forces gauge; 1.25-in.-diam. diaphragm forms extension of inner surface of 4-in. pipe.

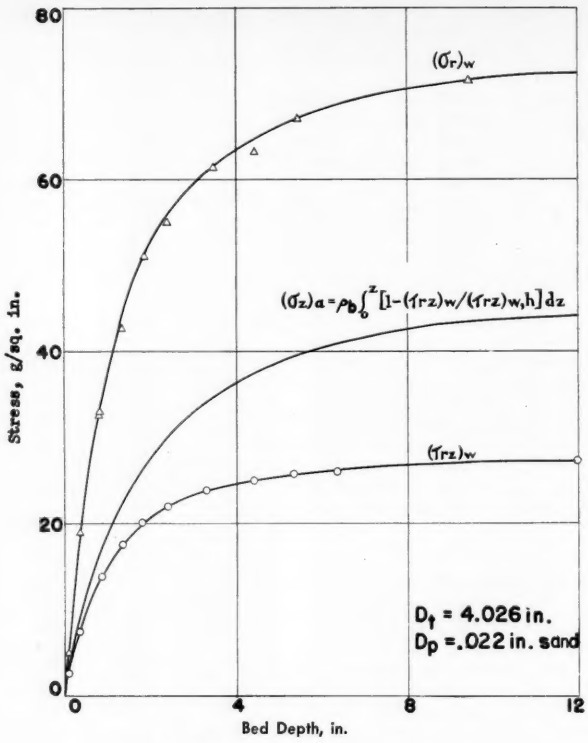

Fig. 5. Wall-forces-gauge measurements.

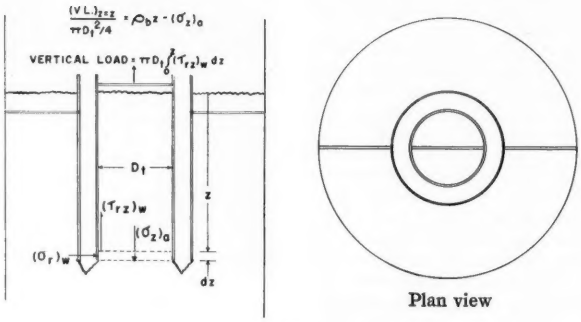

Fig. 6. Total-load measurements.

The validity of the measurements is demonstrated by the equality of the measured values of $(\tau_{rz})_{w,h}$ and the expected value from Equation (8) of $\rho_b D_t/4$. The average vertical stress at any bed depth was calculated from Equations (4) and (8) by graphical integration. Thus

$$(\sigma_z)_a = \rho_b \int_0^z \left[1 - \frac{(\tau_{rz})_w}{(\tau_{rz})_{w,h}}\right] dz \quad (9)$$

The stress ratios k_a, μ', and α were calculated at various bed depths from these stresses by the equations given in Table 1 and from Equations (7) and (8) at high bed depths. All stresses were found to be zero at zero bed depth. However, the limiting stress ratios at zero bed depth can be calculated by L'Hôpital's rule from the initial slopes of the appropriate stress-vs.-bed-depth curves. At zero bed depth (subscript 0), $(\sigma_z)_{a,0}$ equals zero, and from Equation (5)

$$\left[\frac{d(\sigma_z)_a}{\rho_b\,dz}\right]_0 = 1 \quad (10)$$

From Equation (10) and Table 1

$$k_{a,0} = \left[\frac{d(\sigma_r)_w}{\rho_b\,dz}\right]_0$$

$$\alpha_0 = \frac{1/4}{\left[\frac{d(\tau_{rz})_w}{\rho_b\,dz}\right]_0} \quad (11)$$

$$\mu_0' = \frac{\left[\frac{d(\tau_{rz})_w}{\rho_b\,dz}\right]_0}{\left[\frac{d(\sigma_r)_w}{\rho_b\,dz}\right]_0}$$

Figure 5 is a plot of the data from a typical wall-forces-gauge experiment.

Total-load Measurements

The vertical load, or total wall shear force $(\pi D_t) \int_0^z (\tau_{rz})_w\,dz$, was measured by suspending the tubing from a transducer, and $(\tau_{rz})_w$ was calculated from the slope of the load-vs.-bed-depth curve divided by πD_t. The most satisfactory results were obtained with the concentric-cylinder apparatus shown in Figure 6, along with the pertinent stresses on a controlled volume of solids. The solids velocity was controlled with the multiholed orifice located several feet below the cylinders. The annular space between the cylinders contained no solids, and so shear only from within the inner tube was measured. To calibrate the concentric-cylinder apparatus, similar experiments were carried out with both cylinders full. The limitation of these experiments is that $(\sigma_r)_w$ must be calculated as $(\tau_{rz})_w/\mu'$. The friction coefficient from wall-forces-gauge measurements was used.

From a force balance on the solids within the volume $(\pi D_t^2/4)z$,

$$(\sigma_z)_a = \rho_b z - \text{vert. load}/(\pi D_t^2/4)$$

Table 1 gives the equations for α and k_a. The validity of the method is demonstrated by the comparison in Figure 7 of $(\tau_{rz})_{w,h}/(\rho_b D_t/4)$ and $[d(\sigma_z)_a/\rho_b dz]_0$ with their expected value of 1.0 from Equations (8) and (10). Figure 7 is a plot of the data from a typical total-load experiment.

Average-vertical-stress Measurements

A grid of thin, perpendicular, vertical plates 2 ft. high with 6-in.-square openings and an effective cross section of (0.785) $(4.65)^2$ = 17 sq. ft. was suspended in a 5-ft.-diam. brick-lined vessel. The effective area was less than the total because the brick wall surrounding the grid carried part of the vertical force. Strain gauges were attached to the support rods and to a dummy rod. This method measures $(\sigma_z)_a$ by allowing all the vertical force across a horizontal plane to be exerted as shear on the grid except that transmitted by the solids flowing past the grid.

Figure 8*a* and *b*, for zero and finite bed depths above the top of the grid, shows the vertical force balances on the solids within the volumes $(\pi D_v^2/4)L$ and the stresses on a controlled volume within one of the grid openings. The experimental data indicate that at appreciable bed depths above an internal tube the stress ratio k_a within the tube has already attained its maximum (asymptotic) value. Therefore, in Figure 8*b*, k_a and α_g are constant at values of $k_{a,h}$ and $\alpha_{g,h}$ and Equation (5) can be integrated from M, where $(\sigma_z)_a = (\sigma_z)_{a,t}$, to N to give at the bottom of the grid

$$(\sigma_z)_a = \alpha\rho_b D_g[1 - e^{-z/(\alpha D_g)}] + (\sigma_z)_{a,t}[e^{-z/(\alpha D_g)}] \quad (12)$$

If the L/D_g ratio of the grid opening is large, Equation (12) reduces to $(\sigma_z)_a = (\sigma_z)_{a,h} = \alpha_{g,h}\rho_b D_g$. Similarly, in Figure 8*a* for zero bed depth above the top of the grid, $(\sigma_z)_a = (\sigma_z)_{a,h} = \alpha_{g,h}\rho_b D_g$. Therefore the average vertical stress exerted by the solids above the grid $(\sigma_z)_{a,t}$ multiplied by the total effective area of the grid equals the load carried by the grid minus the load carried at zero bed depth. Actually, from measurements at bed levels within the grid, $\alpha_g = 0.67$, and $e^{-L/(\alpha_g D_g)} = 0.0025$, and so a small correction to $(\sigma_z)_a$ was required. The measurements are believed to be reliable because $[d(\sigma_z)_a/\rho_b dz]_0 = 1.0$ (as is shown in Figure 20).

Concentric-cylinder-gauge Measurements

The local vertical-stress measurements used the concentric-cylinder gauge shown in Figure 9. The stresses on a controlled volume within the cylinders and the vertical forces on the solids within the volume $(\pi D_e^2/4)L$ are shown also. The principle is the same as described in the previous section. The equivalent area of the cylinders $(\pi D_e^2/4)$, divided into the difference between the load at finite and zero bed depths above the top of the cylinders, equals σ_z. In all concentric-cylinder experiments where D_a/D_p was greater than 20, $e^{-L/(\alpha D_a)}$ was negligible, and so the vertical stress transmitted through the cylinders was $\alpha_h \rho_b D_a$, by Equations (5) and (12), at zero and finite-bed depths above the cylinders. Therefore, all the vertical force exerted at the top of cylinders was exerted as additional shear stress on the tube surfaces.

The inner cylinder was suspended from a transducer which measured the load. The stationary outer cylinder absorbed its portion of the load in the annular zone plus the shear from outside the cylinders. Calibrating experiments with solids present only in the annular space between cylinders proved that the vertical shear force per unit area of surface was the same on both walls of the annular zone. These calibrating runs demonstrated also that the vertical force measured by the transducer in the actual concentric-cylinder runs was exerted over an area based on the geometric mean of the inner and outer cylinder diameters D_e. The following evidence demonstrated the validity of the concentric-cylinders measurements: (1) separate measurements of the loads on each cylinder were equal to those predicted from the geometry; (2) ρ_b equaled $\pi D_e^2/4$ divided into the maximum slope of the load-vs.-bed-depth curve at bed levels within the cylinders; and (3) $(\partial\sigma_z/\rho_b\,\partial z)_0 = 1.0$, at bed levels slightly above the cylinders, at 0 to 0.5 fractional radius (Figures 15 to 17). The point of application of the mean stress was calculated by graphical integration. With cylinders located at $r = 0$, the mean stress was exerted at $\frac{1}{3}D_e$. All σ_z data were plotted at the point of mean stress.

Thirteen cylinder arrangements were investigated. The best results were obtained with cylinders of 0.913- and 0.478-in. equivalent diameters. At cylinder-to-particle-diameter ratios below 20 erroneously high σ_z data were obtained.

Induced-shear-gauge Measurements

Radial stress σ_r was measured indirectly as a vertical shear force on a thin vertical plate suspended in a tangential plane from a transducer. The force per unit surface area of the plate equals the induced shear stress $(\tau_{rz})_i$, and $\sigma_r = (\tau_{rz})_i/\mu'$. However, $(\tau_{rz})_i \neq \tau_{rz}$, because the force on the plate can result from only a normal stress. Tangential stress σ_θ was measured from the induced force on a radial plane. The friction coefficient was taken from wall-forces-gauge measurements in the 3.8-in. tubing.

Reliable data were obtained with 0.0024-in. Sandvik stainless and 0.0033-in. spring steel plates. Figure 10 is a plot of the plate load as a function of width and length, at $r = 0$ and $z/D_i > 6$. It is apparent that the load caused by the disruption of flow around the top of the plate is appreciable. This effect was eliminated by use of data from plates of different plate lengths. Then $(\tau_{rz})_i$ equals the increment in load divided by the increment in total area (for both sides) of the plates. For plates ¼ in. or narrower $(\tau_{rz})_i$ is virtually independent of width as shown by a cross plot of $(\tau_{rz})_i$ vs. width.

Traverses of the bed were made with ¼- by ⅛- by 0.0024-in. and ¼- by 1- by 0.0024-in. plates. The incremental load/(μ') (incremental area = 7/16 sq. in.) = σ_r. The bed depth z was the distance from the free surface to the centroid of the lower ⅞ of the larger plate, or the portion covered by solids. However, z was obtained by graphical integration in the regions where the σ_r-vs.-z curve was not linear. The accuracy of the induced-shear measurements was shown by the constant values of σ_r in the center of the bed [as predicted by Equation (21) theory] and by a comparison of the extrapolated values of σ_r at the wall with $(\sigma_r)_w$ from wall-forces-gauge data (Figures 18 and 19).

Traverses were made in the 11.6-in. pipe with ½- by 1- by 0.0024-in. spring steel and ½- by 1- by 0.021-in. galvanized plates. The loads were divided by $\mu' = 0.28$ and $\mu' = 0.39$, respectively, and the results were extrapolated to zero plate thickness. Thus the method of determining σ_r in the 11.6-in. pipe is not the same as that used in the 4-in. equipment, but both techniques appear to be reliable.

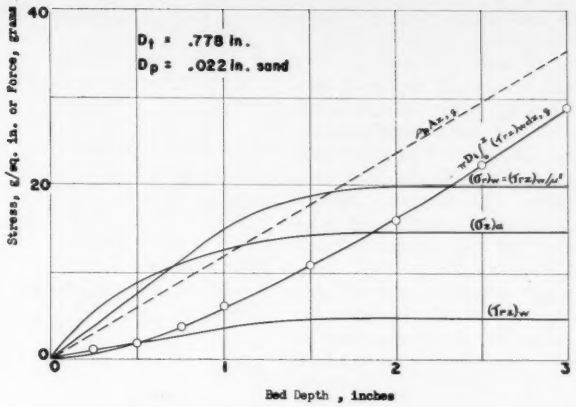

Fig. 7. Total-load-gauge measurements.

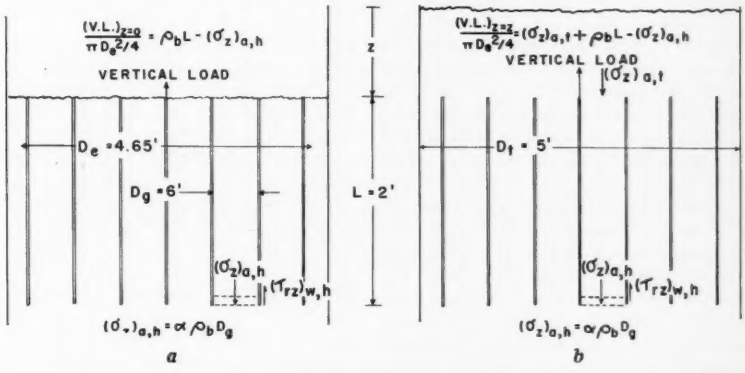

Fig. 8. Average-vertical-stress measurements: *a*, zero bed depth above grid; *b*, finite bed depth.

PROPERTIES OF SOLIDS SYSTEMS

The density or void fraction and the coefficients of friction were measured under flowing conditions. These properties depend on the particle and tube characteristics. A few static experiments were performed to develop methods for predicting the flowing-solids properties of unknown systems from static measurements.

Density and Void Fraction

The bulk density equals the particle density multiplied by one minus the void fraction. The flowing bulk density was determined by weighing the solids between two horizontal planes in the 3.8-in.

tubing after equilibrium flow conditions had been established. The same value of ρ_b was obtained from the weight of solids collected, divided by the change in bed volume during the same time interval. The particle- and flowing-bulk-density data are given in Table 2. The static loose and machine-packed bulk densities were measured also. The average density across a cross section ρ_b was found to be independent of bed depth, velocity (over a range of 0.001 to 0.9 ft./sec.), tube roughness, and tube diameter (D_t = 0.5–11.6 in.), unless the D_t/D_p ratio was less than about 20. By comparison, it can be shown from Adams' data (*1*) that the densities in an orifice and upstream are substantially equal, even though the velocities differ by a factor of 30.

The void-fraction data are presented in Figure 11. The void fraction ϵ was constant at a value of 0.39 for spherical particles and varied inversely with D_p for sand, because the small irregularly shaped particles were more difficult to compact. For irregularly shaped materials Figure 11 indicates that ϵ should be taken as 0.02 less than the static loose-packed void fraction. The data for bead catalyst indicate that a wide range of particle size decreases ϵ by about 0.02. The radial variation of ϵ was not measured. The data for static systems (*10, 11, 13, 18*) show that the high voidage necessitated by the presence of the wall exists for only a few particle diameters and has a negligible effect on the average value of ρ_b at D_t/D_p ratios greater than 20/1. However, in flowing systems shear occurs in the outer portion of the bed. The voidage is undoubtedly equal to or less than the loose-packed density in this region and is equal to the packed density in the central core. This would account for the higher flowing voidage of irregularly shaped particles compared with spheres.

Coefficients of Friction

Two coefficients are of interest: μ', the friction coefficient on the container, and μ, the coefficient of solids on solids. Both vary with the voidage (*15, 16*). In the outer region of a flowing bed, where solids-on-solids shear occurs, both the local voidage and μ should be the same as in conventional static tests where solids shearing is made to occur. Only static experiments to determine μ were carried out. Values of μ' were calculated from wall-forces-gauge measurements. These data are presented in Table 3. They were used in all calculations where a value of μ' was required. Table 3 shows that μ' is substantially independent of D_p but increases with the pipe roughness and solids roughness and/or irregularity of shape. Finally it was found that μ' was independent of the velocity of shear and the air humidity.

Because bead catalyst and sand apparently have the same value of μ' even though the shapes and sizes differ, it is believed that the values of μ' in Table 3 can be used for systems with similar surface characteristics. However, for unknown systems μ' may be predicted from static experiments. The values of μ_h' from flowing experiments (Table 3) were found to be about 80% of these measured by shearing solids over metal surfaces of comparable characteristics in essentially static tests [inclined-shear, horizontal-shear, annular-torsional-ring, and conventional shear-box (*15, 16*) experiments]. Thus $\mu_h' = 0.8\mu'_{static}$ approximately, where μ'_{static} is measured by inclined-shear tests or estimated from Figure 12, if only angle-of-repose data are available. Figure 12 was calculated from the data of Rausch (*10*). This is a plot of μ'_{static}/μ_{free} from inclined-shear experiments, where μ_{free} is the tangent of the angle of incline at which a free surface of solids starts to slide. Friction-coefficient data from inclined-shear tests are reported to show the relative values of the various coefficients from static experiments.

Table 3. Wall-forces-gauge Terminal Data

Material	D_p, in.	μ_0'	α_0	$k_{a,0}$	μ_h'	α_h	$k_{a,h}$
3.806-in.-diam. smooth steel tubing							
Sand	0.029	0.34	0.80	0.90	0.28	0.54	1.63
	0.022	0.35	0.71	1.01	0.25	0.52	1.93
	0.015	0.38	0.63	1.06	0.28	0.56	1.59
	0.012	0.28–0.38	0.52–0.72	1.27	0.28	0.52	1.74
	0.009			1.30	0.23		
Glass beads	0.028	0.19	0.92	1.40	0.17	0.73	2.00
	0.0185	0.24–0.30	0.73–0.93	1.13	0.17	0.70	2.21
	0.011				0.14		
Bead catalyst	0.125	0.5	0.56	1.01	0.28	0.50	1.72
4.026-in.-diam. commercial pipe (rough)							
Sand	0.022				0.35	0.43	1.67

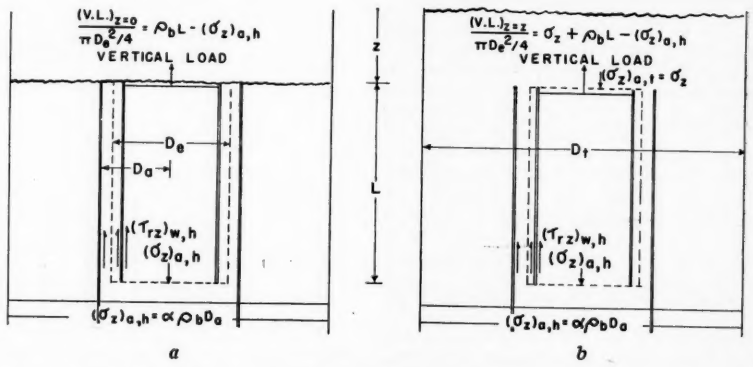

Fig. 9. Concentric-cylinder measurements: *a*, zero bed depth above cylinders; *b*, finite bed depth.

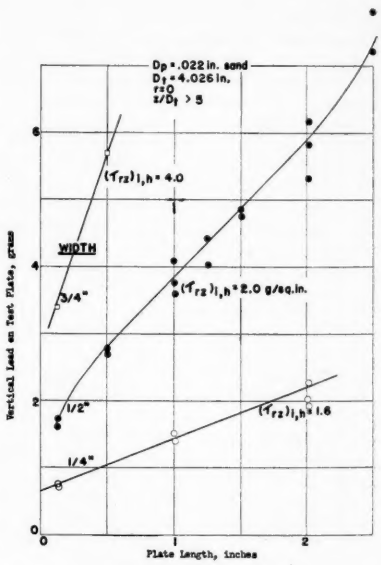

Fig. 10. Induced-shear-gauge data at center of bed.

	μ'_{static}		μ	μ_{free}
	Polished surface	Steel		
Sand	0.24	0.39	0.55	0.61
Glass bead	—	0.34		
Socony Vacuum beads	0.28	0.34		

Characteristic Properties of Flowing-solids Systems

This investigation confirmed the observations of Brinn et al. (3) of shear in approximately the outer 20% of the flowing bed and constant-velocity or rodlike flow in the remainder of the bed. The average velocity in the outer 10 to 20% of the bed was about 4% lower than the mean bed velocity, and the mean velocity was about 1% lower than the velocity in the central core. These observations are valid, however, only if the tube-to-particle-diameter ratio is greater than about 15 to 20.

The study further showed that all stresses, as well as ρ_b and μ', were independent of the rate of flow over the range of velocities studied. This would appear to indicate that motion introduces no new types of stress in solids systems and that the mechanism of stress distribution is entirely by particle-to-particle friction. There was neither tangential nor swirling motion nor torsional force in the systems studied.

All stresses vary appreciably with time, and vibration is present in all runs. Figure 13 is a photograph of the recorded variation of σ_z with time in a typical experiment. The vibration and variation of stress with time are believed to be caused by the characteristic stick-slip action described by Bowden and Tabor (2). This phenomenon occurs at the walls, in the region where shear occurs, and at the measuring-gauge surface. The percentage of variation of stress decreases as μ', D_t/D_p, and z/D_p increase.

PRESENTATION AND DISCUSSION OF STRESS DATA

In this section these data are discussed in detail. First the ratios of boundary and average stresses are presented; then the local values of stress and stress ratios are considered. The former are used in a later section to develop generalized equations for the boundary and average stresses, and the latter to develop equations for the local stresses and to explain the flowing-bed phenomena.

Stress Ratio k_a, $(\sigma_r)_w/(\sigma_z)_a$

The ratio k_a varies with bed depth and is relatively independent of D_p, $D_t(D_t/D_p > 20)$, solids material, and pipe surface. The effect of bed depth on k_a is shown in Tables 3 and 4. At zero and high bed depths, respectively, k_a is approximately 1.0 and 1.8. It must be 1.0 or less at low bed depths because free solids cannot exert a greater force than that caused by their weight, and $(\sigma_z)_a = \rho_b z$. The data indicate that k_a is about 1.4 at $(\sigma_z)_a/(\sigma_z)_{a,h} = 0.5$ and that the following equation is a fair representation of the experimental results:

$$k_a = 1.0 + 0.8\,\frac{(\sigma_z)_a}{(\sigma_z)_{a,h}} \qquad (13)$$

TABLE 4. TOTAL LOAD MEASUREMENTS

Single-cylinder measurements: $D_t = 1.053$ in.

Material	D_p, in.	α_0	$k_{a,0}$	μ_h'	α_h	$k_{a,h}$
Sand	0.022	1.1	0.8	*	0.6	1.6

Concentric-cylinder measurements: bed level within cylinders

Material	D_p, in.	D_a, in.	D_b, in.			
Sand	0.029	0.53	0.913	*	0.62	1.5
	0.022	0.53	0.913	*	0.69	1.3
	0.015	0.53	0.913	*	0.67	1.3
	0.012	0.53	0.913	*	0.43	2.1
	0.009	0.53	0.913	*	0.54	2.0
Glass beads	0.0185	0.40	0.547	*	0.9	1.6
	0.0185	0.40	0.633	*	1.0	1.5
	0.0185	0.53	0.726	*	0.9	1.6
	0.0185	0.53	0.913	*	1.5	1.0
	0.011	0.40	0.547	*	0.5	3.5

*μ' assumed from Table 3.

No uniform effect of D_p on k_a can be seen from Tables 3 and 4 at either low or high bed depths. This ratio is the same for 0.012- to 0.029-in. sands and 0.125-in. bead catalyst. Similarly, no uniform effect of D_t on k_a is noted over the range of 1 to 60 in. except at D_t/D_p ratios below 15, where k_a is considerably less than 1.0 at all bed depths. There must be no effect of D_t on $k_{a,0}$ because $(\sigma_r)_{w,0}$ is the equivalent to that produced by free solids acting on a flat plate, and $(\sigma_z)_a = \rho_b z$. The average value of $k_{a,h}$ is 1.6 to 1.8 for the small cylinders in Table 4, 1.8 for the 3.8- and 4.0-in. tubing and pipe in Table 3, and 1.45 from grid measurements in the brick-lined 60-in. vessel. The latter value was calculated from $(\sigma_z)_a$ measurements by estimating μ' for catalyst on brick from static measurements.

For sand, bead catalyst, and glass beads k_a is substantially the same. The higher values of k_a for glass beads in Table 3 are offset by the lower values in Table 4. Table 3 shows that $k_{a,h}$ is about 1.7 for sand in both smooth tubing and rough pipe, and $k_{a,h}$ in the brick-lined vessel is in the same order of magnitude.

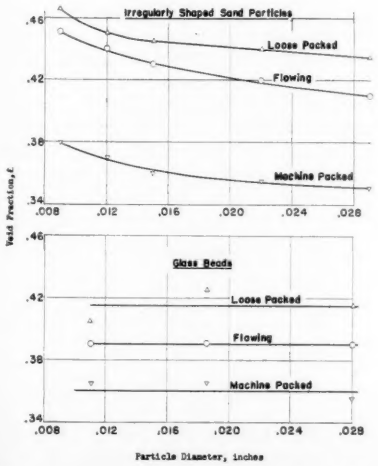

Fig. 11. Flowing- and static-void-fraction data.

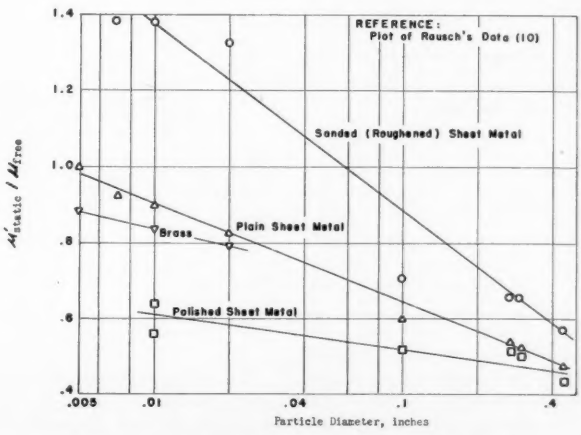

Fig. 12. Relationship between friction coefficients.

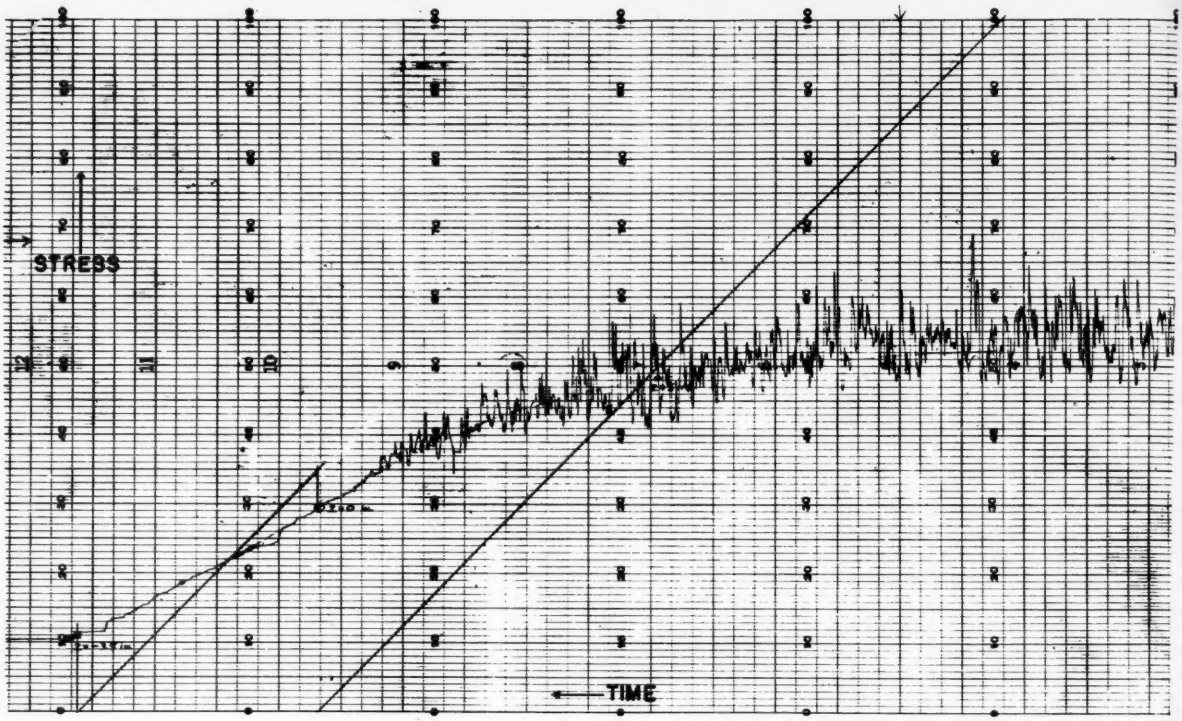

Fig. 13. Variation of vertical stress with time.

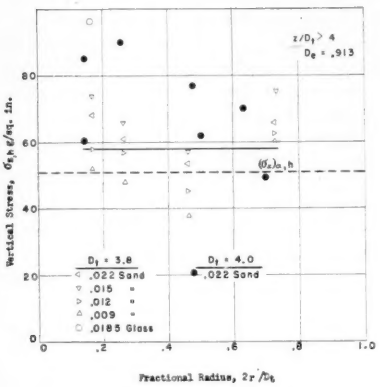

Fig. 14. Radial traverse of vertical stress at high bed depth.

Stress Ratio μ', $(\tau_{rz})_w/(\sigma_r)_w$

Table 3 indicates that μ_0'/μ_h' is approximately 1.2, and the decrease of μ' with z or $(\sigma_z)_a/(\sigma_z)_{a,h}$ is fairly rapid. The lowest value of μ' occurs at the highest normal (radial) stress, which is consistent with data for static systems (*15, 16*). Because μ'_{static} is about 20% higher than μ_h', it is suggested that the static condition is equivalent to that at zero bed depth. Table 3 shows that μ' is relatively independent of the D_t/D_p ratio ($D_t/D_p > 20$). This effect on μ' was discussed in the section on solids properties. Because the particles are actually shearing over a flat plate, μ' should be independent of D_t/D_p.

Stress Ratio α, $(\sigma_z)_a/(4)(\tau_{rz})_w$

Within the limits of accuracy of the experimental data, $k_a\mu'$, as well as k_a, varies linearly with $(\sigma_z)_a/(\sigma_z)_{a,h}$. From Equation (13) and the relationship $\mu_0'/\mu_h' = 1.2$, this linear relationship becomes

$$\frac{1}{4\alpha} = k_a\mu' = \mu_h'\left[1.2 + 0.6\,\frac{(\sigma_z)_a}{(\sigma_z)_{a,h}}\right] \quad (14)$$

The experimental and calculated values for α are listed below:

Material	μ_h'	α_0, exp.	α_0, Eq. (14)	α_h, exp.	α_h, Eq. (14)
Sand	0.28	0.7	0.74	0.55	0.5
Glass beads	0.17	0.9	1.2	0.7	0.8
Bead catalyst	0.28	0.56	0.74	0.5	0.5
Sand (rough pipe)	0.35	—	—	0.43	0.4

This agreement with Equation (14) is good, considering that Equations (13) and (14) involve no parameters other than μ_h'.

Vertical Stress, σ_z

Although the vertical stress data are less consistent than the other measurements, they indicate that $\sigma_{z,h}$ increases with decreasing friction coefficient, is independent of D_p and probably tube roughness, and is relatively constant in the center of the bed at a value higher than the average vertical stress, $(\sigma_z)_{a,h}$. No uniform effect on $\sigma_{z,h}$ of the fractional radius over the range $2r/D_t = 0.17$ to 0.74 can be seen from Figures 14 or 15. The average of the $\sigma_{z,h}$ values for sands from Figure 14 is 58, compared with $(\sigma_z)_{a,h} = 51$. The glass beads behave similarly. This indicates that $\sigma_{z,h}$ must be lower than $(\sigma_z)_{a,h}$ in the outer portion of the bed. The data for smaller cylinders in Figure 16 show σ_z is lower at a fractional radius of 0.8 than at 0.5.

The slightly higher values of $\sigma_{z,h}$ for the larger particles in Figure 14 may result from a greater disruption of the flow pattern of the larger particles past the cylinders. Table 3 shows no such effect

of D_p on $(\sigma_z)_{a,h}$. In any event this effect of D_p is small. The vertical stress for glass beads was 20 to 40% higher than for the sands in both the $\sigma_{z,h}$ and $(\sigma_z)_{a,h}$ experiments. This can be accounted for by the lower friction coefficients of glass beads. Figure 14 shows that $\sigma_{z,h}$ is slightly higher for rough pipe than for smooth tubing, but this does not appear to be consistent with the $(\sigma_z)_{a,h}$ data.

Figures 15 and 16 show the σ_z-vs.-z relationships at several radial positions. The initial gradient $(\partial\sigma_z/\rho_b\partial z)_0$ equals 1.0, 1.0, 0.5 and 0.5 at fractional radii of 0, 0.5, 0.74, and 0.8, respectively. Furthermore these gradients are constant in the outer portions of the bed from $z/D_t = 0$ to 1.0. This indicates high shear stress in this region. The distance required to transmit this shear to the center of the bed appears to be a function of the number of particle diameters of bed depth. Figure 17 shows the bed height required to reduce the vertical st. divided by $\rho_b z$ to a value of 0.75 near the center of the bed. The constancy of the z/D_p ratio at this point is shown below:

Materials	z/D_p for $\sigma_z = 0.75\rho_b z$
Sands (D_p = 0.009, 0.012, 0.015, 0.022, 0.029)	110, 100, 115, 140, 130
Glass beads (D_p = 0.011, 0.0185, 0.029)	90, 210, 150

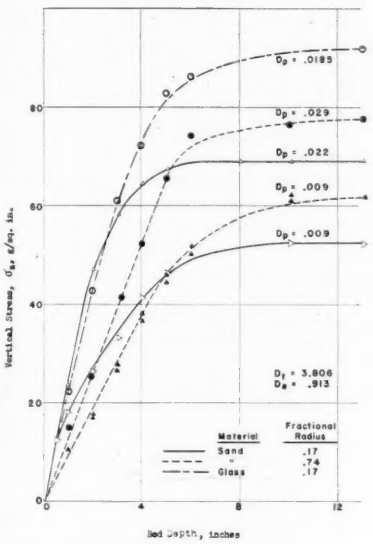

Fig. 15. Effect of bed depth on vertical stress.

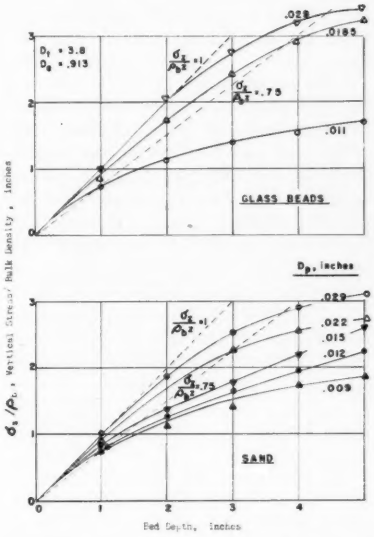

Fig. 17. Vertical stress at low bed depth.

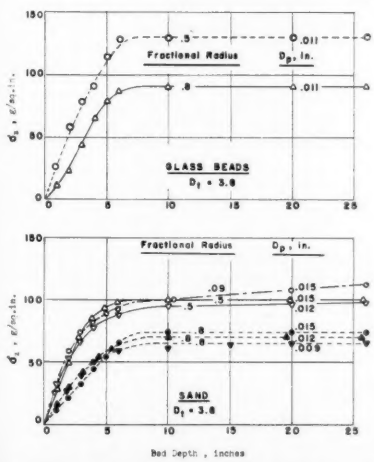

Fig. 16. Vertical stress traverse with small cylinders.

Radial Stress, σ_r

The induced-shear data presented in Figures 18 and 19 show that σ_r is constant in the center portion of the bed and increases rapidly in the region where shear is occurring, from a fractional radius of 0.8 to 1.0, at a slope $(\partial\sigma_r/\rho_b\partial_r)_h \geqq 5$. At the axis of the pipe $(\sigma_r)_h$ equals $0.06\rho_b D_t$ and $0.09\rho_b D_t$ for the 4.0- and 11.63-in. pipes, respectively. The $(\sigma_r)_w$ data are plotted in Figures 18 and 19 for comparison.

Figure 19 is a dimensionless plot of $\sigma_r/\rho_b D_t$ vs. z/D_t, so that the data for both pipes may be compared. The agreement is satisfactory considering the different types of traverses made. The initial gradient $(\partial\sigma_r/\rho_b\partial z)_0$ is approximately equal to 1.0 at all fractional radii and even at the wall, as indicated by Table 3. At intermediate bed depths, σ_r was lower at $r = 0.5$ and 0.7 than at the axis of the pipe.

Tangential Stress, σ_θ

Both σ_θ and σ_r data are included in Figure 18. The difference between these stresses appears to be negligible. It is concluded that the horizontal normal stresses on radial and tangential planes are equal and that horizontal stress is exerted

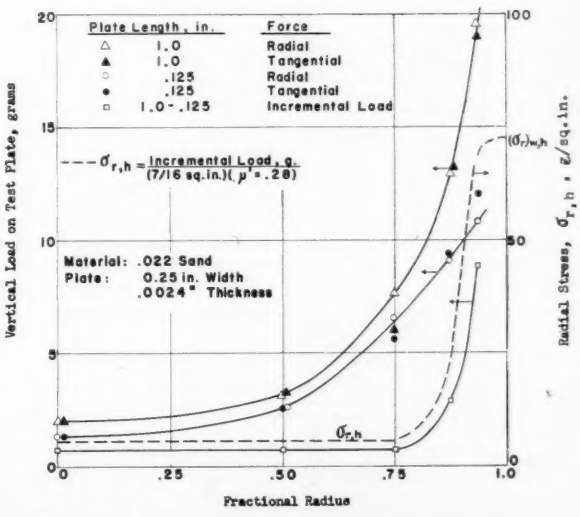

Fig. 18. Radial stress traverse at high bed depth.

equally in all directions at any given bed depth. This was further demonstrated by measuring the force normal to vertical planes inclined at various angles from a radial plane.

Stress Ratio k, σ_r/σ_z

The ratio k appears to be independent of radial position from a fractional radius of 0 to 0.7. In this region $k = (\partial\sigma_r/\rho_b\partial z)_0 = 1.0$ at low bed depths and k equals 0.1 to 0.15 at high bed depths. In the outer portion of the bed at high bed depths, k is large and equals 2 or more at the wall.

Internal Shear Stresses and Stress Ratios

The local shear stresses were not measured; however, equations will be developed in the next section which permit calculation of the shear stresses and the shear-stress ratio $\tau_{rz}/\sigma_r = \mu$.

ANALYSIS OF STRESS RELATIONSHIPS

Boundary and Average-stress Relationships

Because the solid particles flow without vertical acceleration, Equation (5) is valid for flowing systems. It can be integrated by using the relationship for k_a and μ' given by Equation (14). Substitution of Equations (7) and (14) in Equation (5) and integration from the free surface to a finite bed depth yields

$$\frac{(\sigma_z)_a}{(\sigma_z)_{a,h}} = \frac{(\sigma_z)_a}{\rho_b D_t/(4)(1.8)(\mu_h')} = \frac{1 - e^{-9.6\mu_h' z/D_t}}{1 + \frac{1}{3}(e^{-9.6\mu_h' z/D_t})} \quad (15)$$

The values of the boundary stresses can be calculated from Equations (13), (14), and (15). Thus when

$$\frac{(\sigma_z)_a}{(\sigma_z)_{a,h}} = Q$$

$$\frac{(\tau_{rz})_w}{(\tau_{rz})_{w,h}} = \frac{(\tau_{rz})_w}{\rho_b D_t/4} = \left(\frac{1.2 + 0.6Q}{1.8}\right)Q \quad (16)$$

$$\frac{(\sigma_r)_w}{(\sigma_r)_{w,h}} = \frac{(\sigma_r)_w}{\rho_b D_t/(4\mu_h')} = \left(\frac{1.0 + 0.8Q}{1.8}\right)Q \quad (17)$$

A similar relationship can be developed from the general Equation (18) for the variation of $k_a\mu'$ with Q rather than the specific Equation (14).

$$\frac{1}{4\alpha} = k_a\mu' = \mu_h'(B + CQ) \quad (18)$$

The final equation, comparable to the specific Equation (15), is

$$Q = \frac{1 - e^{-4\mu_h'(B+2C)z/D_t}}{1 + \left(\frac{C}{B+C}\right)e^{-4\mu_h'(B+2C)z/D_t}} \quad (19)$$

However B and C are constants which must be evaluated experimentally. To compare the average-vertical-stress data for different solids and vessels, $(\sigma_z)_a/\rho_b$ and bed depth were divided by $D_t/4\mu_h'$ and plotted in Figure 20. Equation (15) indicates that the data should fall on a single curve, having an initial slope of 1.0 and a maximum equal to the value of $1/k_{a,h}$. The discrepancies result from the difference between the measured value of $k_{a,h}$ and 1.8. The correlation could be improved by plotting $(\sigma_z)_a/(\sigma_z)_{a,h}$ as the ordinate, but this procedure does not permit prediction of $(\sigma_z)_{a,h}$. However, this method can be used to demonstrate the relationships between these stresses, as well as the accuracy of Equations (15) to (17). The fraction of the maximum shear and radial wall stresses, at $(\sigma_z)_a/(\sigma_z)_{a,h} = 0.5$, and the corresponding bed depth are given in the following table:

Material	$\frac{(\sigma_z)_a}{(\sigma_z)_{a,h}}$	$\frac{(\tau_{rz})_w}{(\tau_{rz})_{w,h}}$	$\frac{(\sigma_r)_w}{(\sigma_r)_{w,h}}$	$\frac{z}{D_t/\mu_h'}$
Sands ($\mu_h' = 0.28$)	0.5	0.44	0.40	0.09
Glass beads ($\mu_h' = 0.17$)	0.5	0.47	0.32	0.07
Bead catalyst ($\mu_h' = 0.28$)	0.5	0.48	0.42	0.12
Average	0.5	0.46	0.38	0.09
Calculated from Equations (15) to (17)	0.5	0.42	0.39	0.09

These equations are not valid at D_t/D_p ratios below about 15 because k_a is considerably less than 1 at all bed depths.

Local Stress Differential Equations

The experimental stress data can be employed to make Equations (1) to (3) useful for the study of solids flow. Because there is no linear acceleration in either the vertical or tangential direction, Equations (1) and (3) are valid in flowing systems. Equation (3) can be eliminated because all terms equal zero: σ_θ does not vary with θ, and all shear stresses in the tangential direction or resulting from a tangential force are zero. Because $\tau_{\theta z} = 0$, Equation (1) reduces to

$$\frac{\partial\sigma_z}{\partial z} + \frac{\partial\tau_{rz}}{\partial r} = \rho_b - \frac{\tau_{rz}}{r} \quad (20)$$

or

$$\frac{\partial\sigma_z}{\partial z} + \frac{\partial(r\tau_{rz})}{r\,\partial r} = \rho_b \quad (20)$$

In the central core of the bed (approximately 80%) there is no radial movement or acceleration and no rotation or angular acceleration. Therefore, in this region Equation (2) is valid and also $\tau_{zr} = \tau_{rz}$. Furthermore, the data show that $\sigma_\theta - \sigma_r$ equals zero. Hence

$$\left(\frac{\partial\sigma_r}{\partial r} + \frac{\partial\tau_{rz}}{\partial z}\right)_{core} = 0 \quad (21)$$

As discussed previously, at z/D_t ratios greater than about 5 all stresses including shear stresses are independent of z. Therefore, Equation (21) shows that $(\sigma_r)_{h,core}$ is independent of the radial position and is equal to $(\sigma_r)_{h,(r=0)}$. The radial stress data in the central core at high bed depths verify this deduction and hence indicate the validity of Equation (21).

In the outer portion of the bed the data show that $(\partial\sigma_r/\rho_b\partial_r)_h$ is equal to or greater than 5, rather than 0, as predicted by Equation (21). For there to be no radial acceleration in the outer section $(\partial\tau_{zr}/\rho_b\partial z)_h \leqq -5$, and τ_{zr} would reach impossibly high negative values at even moderate bed depths. It must be concluded that in the outer section of the bed there is a net transport of momentum in the radial direction by radial movement of particles. The equation in this region is

$$\left(\frac{\partial\sigma_r}{\partial r} + \frac{\partial\tau_{zr}}{\partial z}\right)_{outer\ section} = \frac{\text{radial acceleration force}}{\text{unit volume of solids}} \quad (22)$$

It should be noted that τ_{zr} is not necessarily equal to τ_{rz} in the outer section because particles are free to rotate about a tangential axis in this region.

Local Stress Relationships

At high bed depths

$$\frac{\partial\sigma_z}{\partial z} = 0$$

and Equation (20) integrates to

$$(\tau_{rz})_h = \frac{\rho_b r}{2} \quad (23)$$

where the arbitrary function of integration was evaluated as zero, either from Equation (8) or at $r = 0$, where $\tau_{rz} = 0$ from symmetry. Thus $(\tau_{rz})_h$ is independent of z, as predicted. From Equa-

TYPICAL VALUES OF $\tau_{rz}/(\tau_{rz})_{w,h} = \tau_{rz}/(\rho_b D_t/4)$

Fractional radius	$z/D_t = 0.25$	0.5	1	5
0	0	0	0	0
0.25	0.007	0.11	0.205	0.25
0.5	0.015	0.22	0.41	0.50
1.0 [Equations (15), (16)]	0.55	0.8	0.9	1.0

tion (20), $(\tau_{rz})_{0,core} = 0$, because Figures 15 and 16 show that $(\partial\sigma_z/\rho_b\partial z)_0 = 1.0$ from $r = 0$ to 0.5. At intermediate bed depths over the central portion of the bed, where $\partial\sigma_z/\partial z$ is approximately constant (i.e., $\partial\sigma_z/\partial z = (d\sigma_z/dz)_{core} =$ constant),

$$(\tau_{rz})_{core} = \frac{r}{2}\left[\rho_b - \left(\frac{d\sigma_z}{dz}\right)_{core}\right] \quad (24)$$

These equations show that the (vertical) shear stress, τ_{rz}, varies linearly with the radius if, and only if, the vertical stress σ_z does not vary radially. Similarly, the necessary condition for a linear-shear-stress distribution in a comparable fluid system is that the radial velocity gradient does not vary axially (*8*).

Equations (23) and (24) give τ_{rz} at any point in the core. Typical values of the dimensionless group $\tau_{rz}/(\tau_{rz})_{w,h} = \tau_{rz}/(\rho_b D_t/4)$ calculated from Figure 15 for 0.022-in. sand are given on page 136 to show how τ_{rz} varies throughout the bed.

At intermediate depths in the central portion of the bed

$$\frac{\partial\tau_{rz}}{\partial z} = -\frac{r}{2}\left(\frac{d^2\sigma_z}{dz^2}\right)_{core}$$

from Equation (24), and from Equation (21)

$$(\sigma_r)_{core} = (\sigma_r)_{(r=0)} + \frac{r^2}{4}\left(\frac{d^2\sigma_z}{dz^2}\right)_{core} \quad (25)$$

As $d\sigma_z/dz$ is continually decreasing, the second derivative is negative and σ_r is higher at the center of the bed at intermediate bed depths. This effect was observed experimentally. At very low bed depths $(d\sigma_z/\rho_b dz)_{0,core} = 1$, $(d\tau_{rz}/\rho_b dz)_{0,core} = 0$ from Equation (24), and $\partial\sigma_r/\partial r$ is again zero.

Approximate equations for the variation of σ_z and σ_r with bed depth in the central core can be developed from a force balance around the central core up to the plane of shear ($2r/D_t = 0.75$, approximately) by substituting $k\mu$, σ_z, and $0.75D_t$ into Equation (5). The experimental data show that k varies inversely with σ_z approximately according to the equation $1/k = 1 + 9\sigma_z/\sigma_{z,h}$, but the product $k\mu$ is relatively independent of bed depth at a value of ⅓ for sands. Therefore, very approximately,

$$\left(\frac{\sigma_z}{\sigma_{z,h}}\right)_{core} = \frac{\sigma_z}{\frac{\rho_b D_t}{1.8}} = 1 - e^{-1.8z/D_t} \quad (26)$$

and

$$\left(\frac{\sigma_r}{\sigma_{r,h}}\right)_{core} = \frac{\sigma_r}{\frac{\rho_b D_t}{18}} = \frac{1 - e^{-1.8z/D_t}}{1 - 0.9e^{-1.8z/D_t}} \quad (27)$$

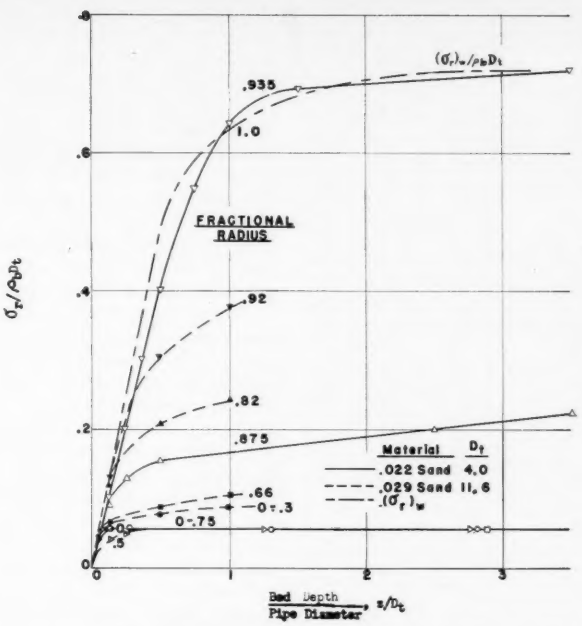

Fig. 19. Effect of bed depth and pipe diameter on radial stress.

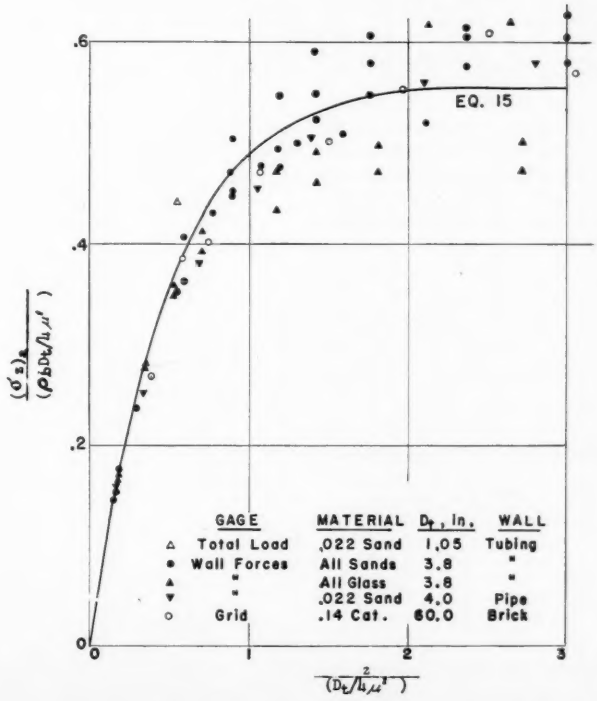

Fig. 20. Comparison of Equation (15) with experimental data.

For other materials 1.8 should be replaced by 1.8 ($\mu'_{material}/\mu'_{sand}$).

Stress Ratio μ, τ_{rz}/σ_r

The stress ratio μ equals a coefficient of friction of solids on solids only when shearing occurs at the point of measurement. The τ_{rz} and σ_r data in the central portion of the bed appear to indicate that μ increases continuously with both bed depth and fractional radius until μ_h is about two or three times as large as the fractional radius at high bed depth and a fractional radius of 0.7 or 0.8. The values of $(\tau_{rz})_{h,core}$ and $(\sigma_r)_{h,core}$ and hence their maximum ratio have not been established accurately, however. This high value of μ suggests that solids behave almost as a compact rigid body in the center of the bed, and they must either fracture or flow around each other. At a fractional radius of 0.7 to 0.8, μ equals the coefficient of friction required for this to occur, and increases in voidage, rotation, shear, and velocity gradient result. Beyond this point μ decreases rapidly to the value of about 0.5, as determined by conventional "static" friction tests, where the voidage at the shear plane is comparable. The stress ratio at the wall must decrease to μ', and therefore σ_r, which equals τ_{rz}/μ, increases with the fractional radius to the wall because $\tau_{rz}/\mu < (\tau_{rz})_w/\mu'$.

SUMMARY

In this study the local and boundary stresses in flowing beds of solids have been measured and found to be consistent with theoretical equations developed to relate these stresses, if the D_t/D_p ratio is greater than 20. Methods are presented to predict from static friction and density tests the solids properties required to evaluate the stresses in any given system.

All stresses are independent of the solids velocity and increase exponentially from zero to maximum values at bed-depth-to-particle-diameter ratios greater than about 5. The ratio of the wall radial stress to the average vertical stress increases with bed depth from 1.0 to 1.8, and μ', the wall friction coefficient, decreases about 20%. Equations are presented for calculation of the stresses and stress ratios as a function of bed depth, except in the outer portion of the bed, where solids-solids shear occurs.

The internal stresses are related to each other by the differential equations

$$\frac{\partial \sigma_z}{\partial z} + \frac{\partial (r\tau_{rz})}{r\,\partial r} = \rho_b$$

and

$$\frac{\partial \sigma_r}{\partial r} + \frac{\partial \tau_{rz}}{\partial z} = 0$$

except that the latter is not valid in the outer portion of the bed, where shear occurs and there appears to be a radial transport of momentum. In the central portion of the bed (1) the bulk density and velocity are constant; (2) the particles flow in a rodlike manner as a compact rigid body; (3) the radial-to-vertical-stress ratio k decreases with bed depth from 1.0 to about 0.1; (4) the shear stress τ_{rz} is not related to the radial stress σ_r but varies almost linearly with the fractional radius, and their ratio μ increases with both bed depth and fractional radius; and (5) the radial and vertical stresses are independent of the radial distance. The data appear to indicate that shearing occurs at the radial distance where μ_h has increased to a value greater than 2. This may be the maximum value of the coefficient of friction of solids on solids where the local density at the shear plane is high. At larger radial distances a velocity gradient is established, the voidage is increased as rotational shearing occurs, the radial stress increases rapidly with the fractional radius, and μ_h decreases to about 0.5, the friction coefficient where the voidage at the shear plane is approximately equal to that in static friction tests. At the wall $(\tau_{rz})_w/(\sigma_r)_w = \mu'$, which is considerably less than μ, and therefore σ_r increases with radial distance to the wall.

ACKNOWLEDGMENT

The author wishes to express his appreciation to C. G. Kirkbride for suggesting the problem, to J. J. Donovan for strain-gauge advice, to R. L. Pigford and J. A. Gerster for many helpful suggestions, to Sun Oil Company for permission to use the measurements in the 5-ft. kiln, and to Houdry Process Corporation for the use of the 11.63-in. equipment and for the static-density determinations.

NOTATION

Units are force, F; length, L; mass, M; and time, T.

A = area, L^2
B, C = constants
D_a = average opening diameter = one-half diameter of outer cylinder, L
D_e = equivalent diameter = geometric mean diameter of inner and outer cylinders, L
D_g = grid opening, L
D_p = particle diameter, L
D_t = tube diameter, L
g = acceleration of gravity, L/T^2
g_c = proportionality factor, ML/FT^2
k = ratio of radial stress to vertical stress = σ_r/σ_z
k_a = ratio of radial stress at wall to average vertical stress = $(\sigma_r)_w/(\sigma_z)_a$
L = length, L
Q = $(\sigma_z)_a/(\sigma_z)_{a,h}$ = fraction of maximum value of the average vertical stress
r = radial distance, L
z = vertical distance or bed depth, L
α = stress ratio 0.25 $(\sigma_z)_a/(\tau_{rz})_w = 1/(4k_a\mu')$
α_g = α within the grid
ϵ = void fraction
θ = angle, radians, or tangential direction
μ = stress ratio τ_{rz}/σ_r (= coefficient of solids friction only if shear occurs perpendicular to σ_r)
μ' = coefficient of friction of solids on pipe wall
μ_{static} = coefficient of friction of solids on metal from inclined shear tests
μ_{free} = coefficient of friction of solids on solids at a free surface = tangent of angle of repose
ρ_b = resultant body force per unit volume of solids = $[\rho_b' - (1-\epsilon)\rho_f]\,g/g_c$, F/L^3
ρ_b' = bulk density, M/L^3
ρ_f = fluid density, M/L^3
σ = normal stress acting on a perpendicular plane, F/L^2
σ_r = radial stress acting in a radial direction, F/L^2
$(\sigma_r)_w$ = radial stress at the wall, F/L^2
σ_z = vertical stress acting in a vertical direction, F/L^2
$(\sigma_z)_a$ = average vertical stress across bed at a given bed depth = $(1/A)\int_0^A \sigma_z\,dA$, F/L^2
$(\sigma_z)_{a,t}$ = average vertical stress at top of concentric cylinders, F/L^2
σ_θ = tangential stress acting in the tangential direction, F/L^2
τ = shear stress acting in a plane parallel to the stress, F/L^2
τ_{rz} = shear stress resulting from a radial force, in vertical direction, F/L^2
$(\tau_{rz})_w$ = τ_{rz} at the pipe wall, F/L^2
$(\tau_{rz})_i$ = induced shear stress on a test plate placed perpendicular to the stress being measured, F/L^2
τ_{zr} = shear stress resulting from a vertical force, in radial direction, F/L^2
$\tau_{z\theta}$ = shear stress resulting from a vertical force, in tangential direction, F/L^2
$\tau_{\theta z}$ = shear stress resulting from a tangential force, in vertical direction, F/L^2
$\tau_{r\theta}$ = shear stress resulting from a radial force, in tangential direction, F/L^2
$\tau_{\theta r}$ = shear stress resulting from a tangential force, in radial direction, F/L^2
$(d\sigma_z/dz)_{core}$ = constant value of $\partial\sigma_z/\partial z$ from $r = 0$ to $r = r$ in central core, F/L^3

Subscripts

h = value of stress at high bed depths, $z/D_t > 5$
o = value of stress at very low bed depths, $z = 0$
$(r=0)$ = value of stress at center line of bed, r = radial distance = 0
$core$ = value of stress in central core of bed at a given bed height

Presented at A.I.Ch.E. New York Meeting

BOOKS

Handbook of Engineering Materials. Douglas F. Miner and John B. Seastone, editors. John Wiley and Sons, Inc., New York (1955). 1,380 pages. $17.50.

The purpose of this new handbook is to provide the engineer with a rather extensive array of general information about the materials he may use in his work. The editors have compiled engineering data and descriptive subject matter for a wide variety of materials including those used in construction, manufacturing, production, and industrial research.

The contents of this volume include not only physical and chemical properties of materials, but also applications, engineering characteristics, testing procedures, availability of various types of materials, and biblographical references.

The handbook is somewhat arbitrarily divided into four sections, which cover the following topics: general information on materials, metals, nonmetals, construction materials. An authoritative presentation of data in concise, logical form has been accomplished by drawing on the skill of the fifty-one contributors to the handbook.

One of the groups for which this collection of information can be useful is those engineers who often use data in more than one particular field. The chemical engineer who requires specific information in fields such as mechanical, electrical, or civil engineering would find the handbook a good source of frequently used data. In addition, the bibliography that is given with each particular topic directs the reader to sources which supply more detailed treatments than the handbook is able to provide.

An obvious effort has been made to provide up-to-date information and to include data on materials which have only recently become of engineering importance.

ROBERT M. SECOR

Introduction to Chemical Engineering. Walter L. Badger and Julius T. Banchero. McGraw-Hill Book Company, Inc., New York (1955). 753 pages. $9.50.

Although the publishers do not say so on the jacket, this book is essentially a modernized version of a well-known earlier work, "Elements of Chemical Engineering," by W. L. Badger and W. L. McCabe, the most recent edition of which was published by the McGraw-Hill Book Company in 1936. The same topics are covered. A considerable part of the later book is a word-by-word reprint of the earlier text.

The present volume brings up to date the material of the older work. For example, binary distillation is now presented initially by the use of the enthalpy-concentration diagram, with the McCabe-Thiele method being subsequently developed as a special case. Although much of the old book remains in the new, large parts of this work have been completely rewritten. The growth of chemical engineering theory in the years since the issue of the earlier text is reflected in an increase in the number of pages from 660 to 753.

As an undergraduate text and a text for the engineer seeking a review of chemical

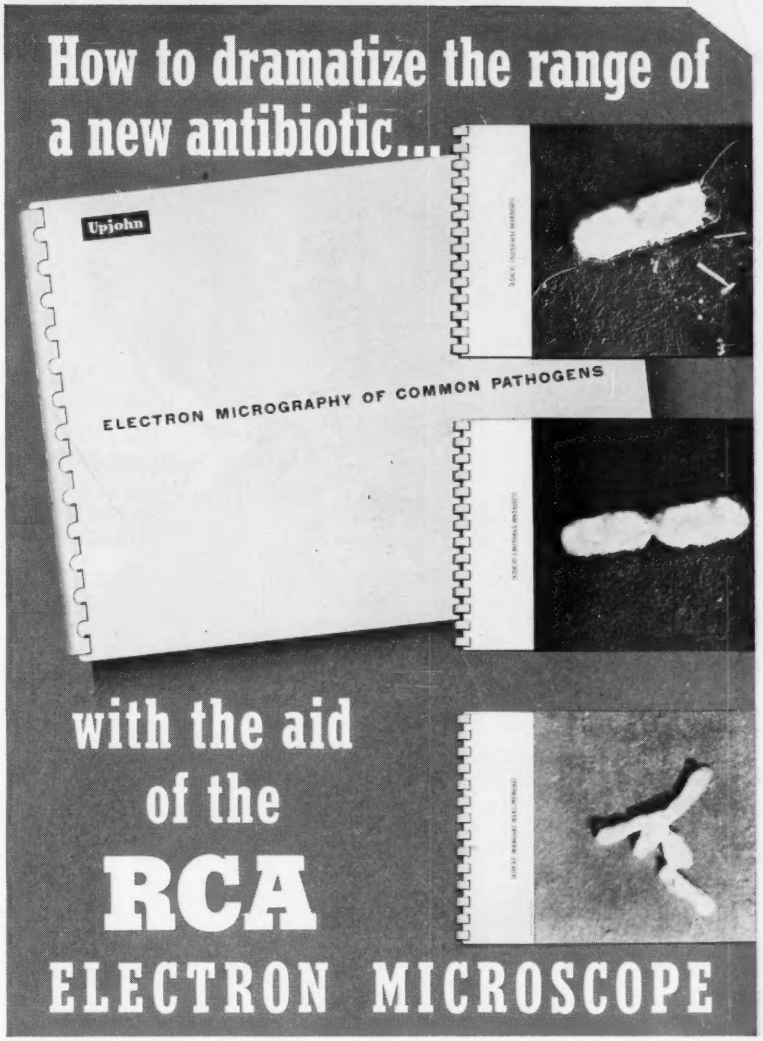

For almost ten years the physicists and microbiologists of the Upjohn Company have been using the RCA Electron Microscope to investigate disease-producing organisms and to develop new weapons against them. Recently, to demonstrate the range and effectiveness of its new broad-spectrum antibiotic, Panmycin* hydrochloride (Upjohn's brand of tetracycline hydrochloride), company scientists collaborated to produce a portfolio of electron micrographs of common organisms that are susceptible to Panmycin. Since photographs of many of these organisms at high magnifications were previously either rare or non-existent, Upjohn's brochure renders a real service to practicing physicians everywhere.

*TRADEMARK REGISTERED

RADIO CORPORATION of AMERICA

Photographic enlargements to over 300,000 diameters are now possible with RCA's new EMU-3 Electron Microscope. It is the ideal tool for advanced research requiring highest resolution, maximum magnification, and critical control. Find out how this vital instrument can be of service to you. Installation and service supplied by the RCA Service Company.

For information write to Dept. C-288, Building 15-1, Radio Corporation of America, Camden, N. J. In Canada: RCA VICTOR Company Ltd., Montreal

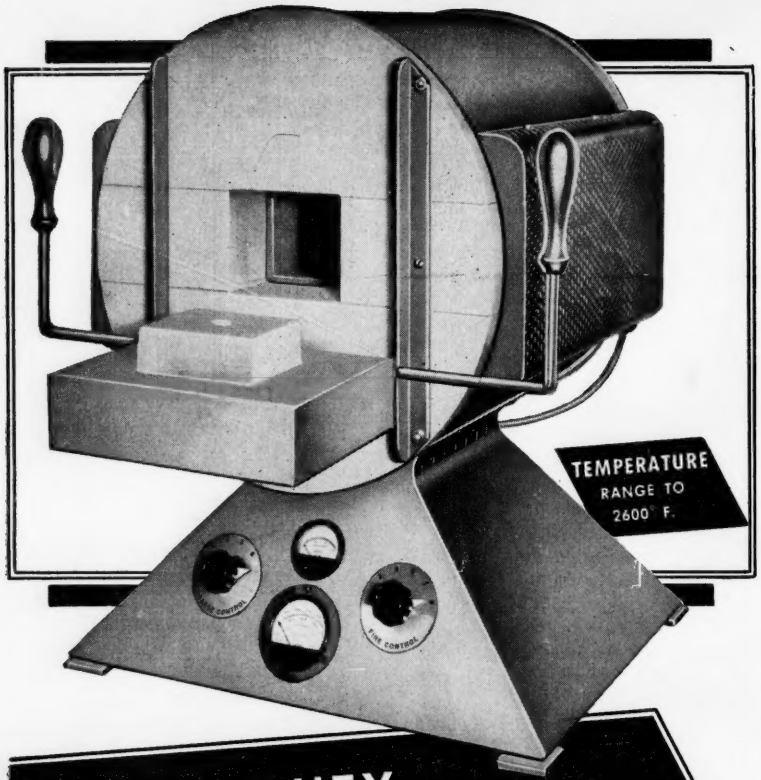

HEVI DUTY
LABORATORY
FURNACES

The Hevi Duty G-05-PT Furnace is a complete unit ready for use. All the temperature control and indicating devices are located in the furnace base. A tap-changing transformer equipped with two selector switches offers 48 steps of temperature control. This method allows close temperature regulation and means savings in power and maintenance. An indicating pyrometer and ammeter are mounted for easy observation.

Easily replaceable Silicon Carbide heating elements provide a uniform heat above and below a ceramic muffle which forms the heating chamber. Inside dimensions 4" wide, 3" high, 7" deep.

SEND FOR DETAILS IN BULLETIN 250-A.

Complete Self-Contained Furnace

Positive Temperature Control

Fast Uniform Heating

HEVI DUTY ELECTRIC COMPANY

LABORATORY FURNACES MULTIPLE UNIT ELECTRIC EXCLUSIVELY

MILWAUKEE 1, WISCONSIN

Continued from rid

engineering fundamentals, much to recommend it. A essential dipertinent equipment has been inclu with each topic covered. Many solved problems are included. Nearly every chapter contains a new set of problems for solution by the student. The development of the theory contains numerous references to pertinent recent research. Moreover, topics of which our knowledge is at present inadequate are brought to the attention of the student. Finally, the authors have, on the whole, succeeded in conforming to the notation adopted as standard by the American Institute of Chemical Engineers.

EDGAR W. SLOCUM

X-ray Diffraction Procedures for Polycrystalline and Amorphous Materials. H. P. Klug and L. E. Alexander. John Wiley and Sons, Inc., New York (1954). 716 pages. $15.00.

The phases of the subject emphasized by the present book are indicated in the title. First, it concentrates on the experimental or procedural aspects of the field; second, it is devoted entirely to polycrystalline or amorphous materials; i.e., it omits entirely single-crystal techniques, such as the Laue method and the rotating-crystal method. The authors contend that although the widest applications of X-ray diffraction are to polycrystalline materials, most previous treatments of this field are out of date or incomplete, especially with regard to the use of the Geiger counter spectrometer.

As a result of the concentration on techniques and on polycrystalline materials, this book is more suitable as a reference book for those who actually use X-ray diffraction methods in the laboratory rather than as a student textbook. Nevertheless, it is not entirely a reference book. In order to make the book as self-sufficient as possible, the authors have included introductory chapters on crystallography, the production and properties of X rays, and X-ray diffraction by crystals. These introductory chapters cover the first 160 pages of the book. They are well presented and in themselves constitute a handy little textbook for one who wishes to review these topics.

The principal parts of the book deal with the techniques and applications in the study of Debye-Scherrer diffraction patterns by both photographic and spectrometric methods. Topics include interpretation of powder-diffraction data, qualitative and quantitative analysis of crystalline powders, precision-lattice constant determinations, crystallite-size determination from line broadening, stress measurement in metals, and preferred orientation determination. A chapter on diffraction by noncrystalline materials is then given. The final chapter deals with small angle scattering.

The reader interested in metals may bemoan the brevity of the section devoted to preferred orientation determination and to the description of the use of the stereographic projection in such studies. Even more disturbing is the implication (page 556) that annealing removes rolling textures, without any mention of the existence of recrystallization textures.
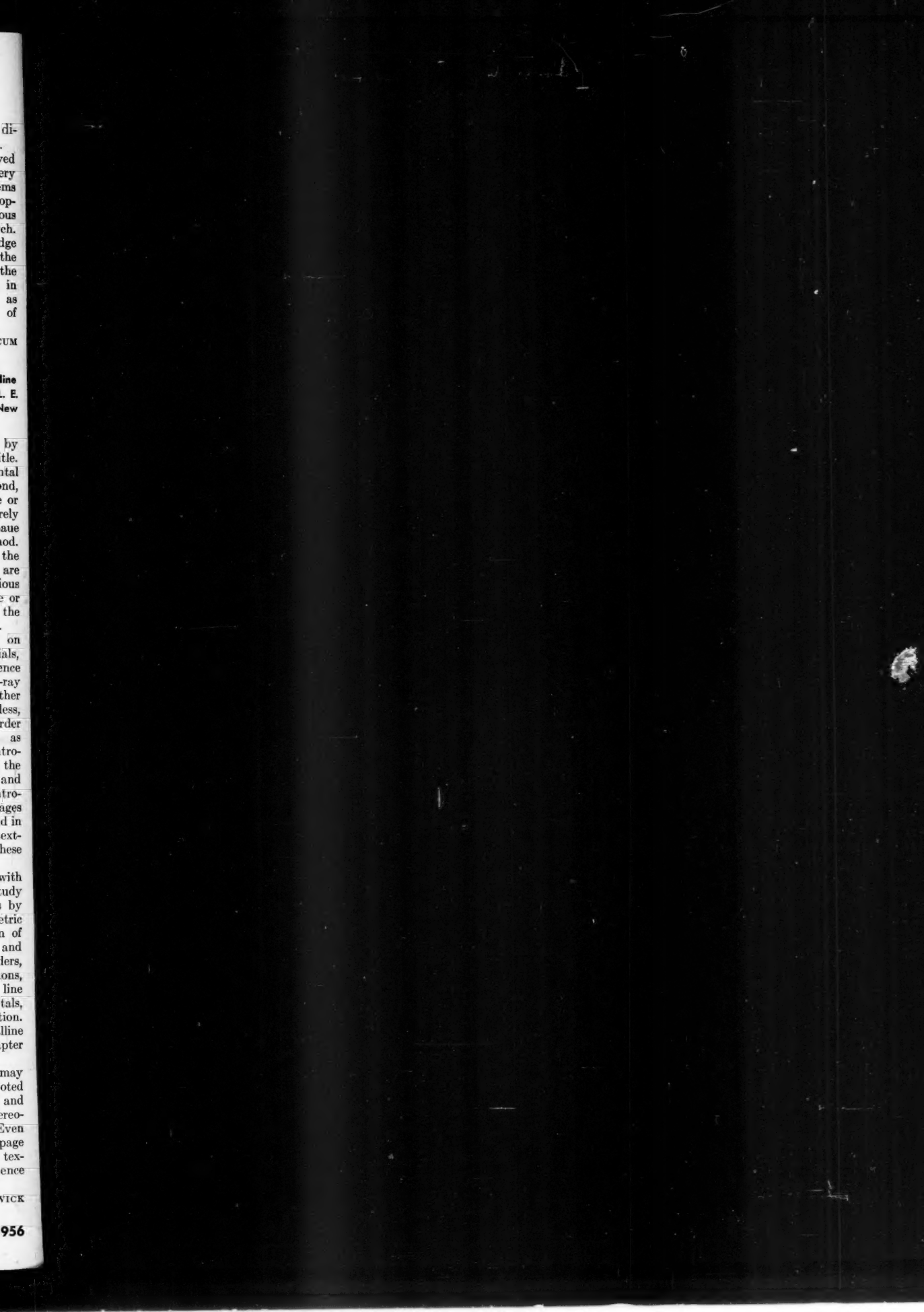
A. S. NOWICK